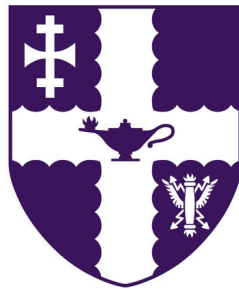


CFD Modelling of Gas Turbine Combustion Processes



A.R Uyanwaththa

Wolfson School of Mechanical Electrical and Manufacturing Engineering
Loughborough University

This dissertation is submitted for the degree of
Doctor of Philosophy

August 2018

I would like to dedicate this thesis to my parents . . .

Acknowledgements

Firstly, I wish to express my gratitude to my supervisor Professor W. Malalasekara for the guidance and continuous support he provided me during this PhD journey. I am thankful for the E.ON(UK) and EPSRC(UK) for providing granting me the iCASE scholarship for my doctoral research. I would also like to thank my other supervisors, Professor Graham Hargrave, Dr Mark Dubal, Mr David Graham who gave me invaluable advice and encouragement during this project. I am thankful to the lecturers at my home university at Peradeniya, especially Dr Prasanna Gunawardane, Prof Rajapakshe, and Prof Sivasegaram for their support and guidance for me to find higher education opportunities.

Besides my supervisor, I would like to thank Dr Yohshuke Matsushita of Tohoku University for generously introduced me to the art of CFD and mentoring me during his stay at Loughborough. I enjoyed the company of such a knowledgeable person, and I cherish all the discussions we had during his stay at Loughborough. At the same time, his student Satoki Yokoi's company also helped me and encouraged, I would like to hope both of their Japanese work ethic of never giving up has rubbed off on me as well. My sincere thankfulness also goes to Prof van Oijen of the Eindhoven University of Technology for hosting and helping me with CHEM1D code and FGM method, and Prof Håkan Nillson for providing valuable training on OpenFOAM. I am also thankful to my PhD examiners Mr Henk Versteeg and Dr Tariq Mahmud for providing valuable insight and suggestions to improve my thesis. I must be thankful to the OpenFOAM developers throughout the years who build up such a platform and made it available for new researchers to use freely. I must acknowledge the colleagues at Loughborough, Aravinda, Tom, Max, Joe, Brendon and Bo Liu with whom I had discussions on many topics and shared the difficulties of research. I would like to thank the small Sri Lankan community at Loughborough including Dr Hemaka Bandulasena and other families and individuals. Last but not least I am very thankful to my family who supported and understood me during this journey.

Abstract

Stationary gas turbines are under constant scrutiny to reduce environmentally harmful emissions and obtain efficient combustion. Numerical simulation tools have become an essential part of gas-turbine combustor development and optimisation to achieve reduced NO_x emissions and stable combustion. Computer simulations can provide accurate answers for many empirically determined parameters of combustor design processes. In this thesis work, the necessary computational tools to predict gas turbine combustion processes are developed and validated against experimental measurements. The gas turbine combustion process can be divided into two sub-processes namely air-fuel mixing and reaction, and in this thesis work numerical tools are developed and used to model both these sub-processes.

Air-fuel mixing can be considered as a turbulent passive scalar mixing phenomenon in the pre/mixing stage. In this thesis, the more common air-fuel mixing arrangement via jet in a cross-flow arrangement is numerically modelled. Two computational fluid dynamic codes STAR-CCM+ and OpenFOAM are used to model this problem using steady Reynolds Averaged Navier Stokes (RANS) methods to evaluate model performance and capabilities of each software. RANS results have shown reasonable agreement in mean velocity field, and scalar field predictions against experimental data, but the Reynolds stress field are under-predicted in general. In both software codes, the realizable $k - \varepsilon$ model has shown better agreement with experimental data in comparison to $k - \omega$ -SST model and the Reynolds Stress Transport model. Subsequently, the turbulent scalar mixing in a jet in cross-flow is modelled using the LES technique with different dynamic Sub-grid Scalar Stress (SGS) models and evaluated the model performance against experimental data from the literature. Locally dynamic Smagorinsky-Lilly model is implemented in OpenFOAM and Jet in cross-flow results are compared against experimental and two other dynamic SGS models. Large Eddy Simulation (LES) technique provides more insight into the turbulence velocity field, and the vortex structures present in the jet and cross-flow interaction zone are realised using this data. The presence of coherent vortex structures enhances the scalar mixing, and numerical simulations of these vortex structures are expected to improve the accuracy of scalar mixing modelling. But numerical modelling of scalar mixing process that is dominated by the scalar transport due to coherent vortex structures is computationally challenging. Therefore

in this endeavour, the LES approach is used in conjunction with a simpler scalar transport model, to take advantage of the resolved velocity field. LES results showed a significant improvement in Reynolds stress field predictions and scalar field predictions compared to RANS modelling, and well resolved LES showed negligible sensitivity to the SGS model used. Then the validated dynamic Smagorinsky model is used to model a twin-jet injection into the cross-flow problem to understand the twin jet interaction which is a vital design consideration of air-fuel pre-mixers and to investigate the applicability of extending the LES modelling for multiple jets in a cross-flow injection. The LES results exhibit good agreement with limited experimental data on the twin-jet in a cross-flow arrangement, and effects of two counter-rotating vortices from each jet propagating adjacent to each other as a result of Coanda effect can be seen in the velocity field results.

Understanding the problems of future gas turbine combustion, in this thesis, particular attention is paid towards numerical modelling of swirl stabilised flames. To understand the complex flow structures in a swirl stabilised burner non-reacting flow simulations of the Sydney swirl burner are performed. Two Non-reacting flow simulations with different swirl strengths are used to understand the vortex breakdown phenomenon of this burner arrangement which had a jet flow and a swirl flow surrounding the jet. LES have successfully reproduced the non-reacting velocity field and have resolved the bluff body recirculation zone and vortex breakdown structures induced by the swirl flow. Recently the investigations of the feasibility to use hydrogen in combination with natural gas in gas turbines to reduce emissions and to control lean flammability have shown promising results. In this endeavour, the numerical modelling of hydrogen-based fuel is also addressed. The Sydney swirl stabilised burner which operates with $CH_4 : H_2$ 1 : 1 fuel is a computationally challenging configuration that has not been modelled successfully in literature is also numerically modelled using the Steady Laminar flamelet method with a presumed probability density approach for the flame structure to evaluate the model performance. The velocity field predictions have captured the essential flow dynamics as the bluff body recirculation and toroidal flow reversal, but scalar field results have shown only moderate agreement with experimental measurements. Recognizing that the current and future gas turbine combustors operate on a mixed combustion regime during its full operational cycle, combustion simulations of premixed/partially premixed flames are also performed in this thesis work. Dynamical artificially thickened flame model is implemented in OpenFOAM and validated using propagating and stationary premixed flames. Low emission gas turbines predominantly operate in lean premixed conditions; however, on part load and transient conditions, the combustion mode can be best explained as stratified combustion. Flamelet Generated Manifold (FGM) methods are used in the modelling of turbulent stratified flames which is a relatively new

field of under investigation, and both experimental and numerical analysis is required to understand the physics. The recent experiments of the Cambridge stratified burner are studied using the FGM method in this thesis work, and good agreement is obtained for mixing field and temperature field predictions.

Table of contents

List of figures	xi
List of tables	xvi
Nomenclature	xvii
1 Introduction	1
1.1 Motivation	1
1.2 Research Methodology	4
1.3 Thesis Layout	5
2 Literature Review	8
2.1 Gas Turbine Air Fuel Mixing	8
2.2 Jet In Cross-Flow	11
2.2.1 Previous Experimental studies	15
2.2.2 Previous Numerical studies	18
2.3 Literature Review on reacting flow modelling	26
2.3.1 Flame types	26
2.3.2 Flame Stabilisation Using Flow Recirculation	32
2.4 Turbulent Combustion Modelling	37
2.4.1 Turbulent Premixed/Partially-Premixed combustion modelling	38
2.4.2 Turbulent Non-Premixed combustion modelling	44
2.5 Chapter Summary	49
3 Governing Equations	51
3.1 Basic Flow Equations	51
3.2 Turbulence modelling	52
3.2.1 RANS Turbulence models	53
3.2.2 Eddy viscosity models	54

3.2.3	Realizable $k - \varepsilon$ model	55
3.2.4	$k - \omega$ -Shear Stress Transport model	56
3.2.5	Lauder-Gibson Reynolds Stress Transport model	59
3.3	Large Eddy Simulations (LES)	60
3.3.1	Sub Grid Scale stress models	62
3.3.2	Dynamic Smagorinsky Model - DSM	63
3.3.3	Dynamic Mixed Model - DMM	64
3.3.4	Dynamic One Equation Model (DEOM)	65
3.4	Flow Solver	66
3.4.1	Wall treatment - RANS	66
3.4.2	Wall treatment for LES	72
3.5	Inlet boundary conditions for LES	73
3.6	Outflow Boundary Conditions	75
3.7	LES Accuracy and Errors	75
3.8	LES Resolution	78
3.9	Coherent Structures Identification	80
3.10	Passive scalar mixing modelling	82
3.11	Compressible - $k - \varepsilon$ model	82
3.12	Reacting Flows	83
3.12.1	Favre Averaged Transport Equations	87
3.12.2	Steady Laminar Flamelet Method	88
3.12.3	Presumed Probability Density Function Method	90
3.13	Flamelet Generated Manifold	92
3.14	Artificially Thickened Flame Model	94
3.15	Chapter Summary	97
4	RANS modelling of Jet in Cross-Flow	98
4.1	RANS modelling of Jet In Cross-Flow	98
4.1.1	Experimental Setup	98
4.2	RANS Simulations - STAR-CCM+	100
4.2.1	Simulation setup	100
4.2.2	RANS Results - STAR-CCM+	101
4.3	RANS simulation - OpenFOAM	118
4.3.1	Simulation set-up	118
4.3.2	RANS Results - OpenFOAM	119
4.4	Chapter Summary	128

5	LES modelling of Jet in Cross-Flow	129
5.1	LES of JICF	129
5.1.1	Velocity field results	132
5.1.2	Reynolds stress field results	135
5.1.3	Passive Scalar Mixing	142
5.1.4	Coherent Structures	147
5.1.5	LES Resolution	151
5.2	Twin Jet in Cross Flow	154
5.2.1	Experimental details	154
5.2.2	LES modelling of twin jet in cross-flow	154
5.2.3	Results	155
5.3	Chapter Summary	158
 6	 Non-Premixed flames	 161
6.1	Non Reacting Swirl Flows	162
6.1.1	Experimental setup	162
6.1.2	Simulation set up	164
6.1.3	Non-Reacting flow : Velocity Field	164
6.2	Reacting Flow Modelling	182
6.2.1	Validation Test : Sandia flames	182
6.2.2	Sydney Swirl Flame HMS1	185
6.3	Chapter Summary	193
 7	 Premixed/Partially Premixed Flames	 208
7.1	Thickened Flame Model Performance	208
7.1.1	Turbulent Flame kernel	209
7.1.2	Turbulent Premixed Flame in Backward Facing Step	215
7.2	Flamelet Generated Manifold test cases	224
7.2.1	2D Burner Stabilized Flame	224
7.2.2	Cambridge Stratified Burner	228
7.3	Chapter Summary	233
 8	 Conclusion and Future Work	 240
8.1	Jet in Cross-Flow modelling	240
8.2	Reacting flow modelling	242
 References		 244

Appendix A	263
A.1 Potential Flow JICF	263
A.2 Turbulent Schmidt number sensitivity	264
A.3 LES and RANS results of JICF	265

List of figures

2.1	NO_x and fuel unmixedness relationship	9
2.2	A typical gas turbine air-Fuel mixing arrangement	11
2.3	Vortex structures in JICF	13
2.4	Jet shear layer vortices and horseshoe vortices	14
2.5	One dimensional free propagating flame	27
2.6	Steady stretched counter flow flame	30
2.7	Partially premixed flame arrangements	32
2.8	Flame stabilisation using flow recirculation	35
2.9	Turbulent premixed flame characteristics	38
2.10	Concept of lower dimensional manifolds	42
3.1	Mean non-dimensional velocity against non-dimensional	69
3.2	Inlet turbulence generation methods for LES	74
3.3	Normalized transfer functions for filters	78
4.1	Jet In Cross-Flow : Test problem geometry	100
4.2	Jet In Cross-Flow : RANS inlet boundary conditions - STAR-CCM+	103
4.3	Jet In Cross-Flow : RANS Mean velocity components - STAR-CCM+	105
4.4	Jet In Cross-Flow : RANS Reynolds stress components - STAR-CCM+	106
4.5	Jet In Cross-Flow : RANS Mean velocity and Reynolds stress - STAR-CCM+	107
4.6	Jet In Cross-Flow : RANS Turbulence Kinetic Energy - STAR-CCM+	108
4.7	Jet In Cross-Flow : RANS Turbulence Viscosity Ratio STAR-CCM+	109
4.8	Jet In Cross-Flow : RANS Mean Velocity(U) contours - STAR-CCM+	111
4.9	Jet In Cross-Flow : RANS Mean Velocity(V) contours - STAR-CCM+	111
4.10	Jet In Cross-Flow : RANS Reynolds stress component $(\overline{u'u'})$ contours - STAR-CCM+	112
4.11	Jet In Cross-Flow : RANS Reynolds stress component $(\overline{v'v'})$ contours - STAR-CCM+	112

4.12	Jet In Cross-Flow : RANS Reynolds stress component $(\overline{u'v'})$ contours - STAR-CCM+	112
4.13	Jet In Cross-Flow : RANS Mean Passive Scalar - STAR-CCM+	115
4.14	Jet In Cross-Flow : RANS Mean Passive Scalar in z direction - STAR-CCM+	115
4.15	Jet In Cross-Flow : RANS Mean Passive Scalar in x direction - STAR-CCM+	116
4.16	Jet In Cross-Flow : RANS Mean Passive Scalar contours on $z = 1.5D$ - STAR-CCM+	117
4.17	Jet In Cross-Flow : Block Structured Grid - OpenFOAM	119
4.18	Jet In Cross-Flow : RANS inlet boundary conditions - OpenFOAM	120
4.19	Jet In Cross-Flow : RANS Mean velocity components - OpenFOAM	122
4.20	Jet In Cross-Flow : RANS Reynolds stress components - OpenFOAM	123
4.21	Jet In Cross-Flow : RANS Mean velocity and Reynolds stress components - OpenFOAM	124
4.22	Jet In Cross-Flow : RANS Turbulent viscosity - OpenFOAM	124
4.23	Jet In Cross-Flow : RANS Mean Passive Scalar in z direction - OpenFOAM	125
4.24	Jet In Cross-Flow : RANS Mean Passive Scalar in x direction - OpenFOAM	126
4.25	Jet In Cross-Flow : RANS Mean Passive Scalar contours - OpenFOAM	127
5.1	Jet In Cross-Flow : LES upstream flow	130
5.2	Jet In Cross-Flow : LES inlet boundary conditions	131
5.3	Jet In Cross-Flow : Mean velocity	133
5.4	Jet In Cross-Flow : LES stream lines and mean velocity	134
5.5	Jet In Cross-Flow : LES mean velocity(U) contours	136
5.6	Jet In Cross-Flow : LES mean velocity(V) contours	136
5.7	Jet In Cross-Flow : LES Reynolds stress magnitudes	137
5.8	Jet In Cross-Flow : LES Reynolds stress components variation	138
5.9	Jet In Cross-Flow : LES Reynolds stress component $(\overline{u'u'})$ contours	140
5.10	Jet In Cross-Flow : LES Reynolds stress component $(\overline{v'v'})$ contours	140
5.11	Jet In Cross-Flow : LES Reynolds stress component $(\overline{u'v'})$ contours	141
5.12	Jet In Cross-Flow : LES Reynolds stress and Mean velocity	142
5.13	Jet In Cross-Flow : LES Passive scalar distribution in z direction	144
5.14	Jet In Cross-Flow : LES Mean passive scalar and RMS	144
5.15	Jet In Cross-Flow : LES Mean passive scalar contours on $z = 1.5D$	145
5.16	Jet In Cross-Flow : LES Mean passive scalar contours on $y = 0D$	146
5.17	Jet In Cross-Flow : LES passive scalar distribution at $x = 3D, 6D$	147
5.18	Jet In Cross-Flow : LES passive scalar mixing index	147
5.19	Jet In Cross-Flow : LES stream lines from jet flow	148

5.20 Jet In Cross-Flow : LES Coherent structures	149
5.21 Jet In Cross-Flow : LES passive scalar iso-contours	149
5.22 Jet In Cross-Flow : LES Strauhal number	150
5.23 Jet In Cross-Flow : LES Turbulent energy spectrum	151
5.24 Jet In Cross-Flow : LES Resolved turbulent energy percentage	152
5.25 Jet In Cross-Flow : LES Turbulent viscosity ratio	153
5.26 Twin Jet In Cross-Flow : Geometry	155
5.27 Twin Jet In Cross-Flow : Mean velocity	156
5.28 Twin Jet In Cross-Flow : Passive scalar contours	156
5.29 Twin Jet In Cross-Flow : Stream lines	157
5.30 Twin Jet In Cross-Flow : Jet stream interaction	159
5.31 Twin Jet In Cross-Flow : Passive scalar variation	159
6.1 Sydney swirl burner : Geometry	163
6.2 Sydney swirl burner : Computational grid	165
6.3 Sydney swirl burner : Non-Reacting axial veocity	169
6.4 Sydney swirl burner : Non-Reacting tangential veocity	170
6.5 Sydney swirl burner : Non-Reacting radial veocity	171
6.6 Sydney swirl burner : Non-Reacting axial veocity RMS	172
6.7 Sydney swirl burner : Non-Reacting radial veocity RMS	173
6.8 Sydney swirl burner : Non-Reacting rotational veocity RMS	174
6.9 Sydney swirl burner : Non-Reacting Reynolds shear stress uv	175
6.10 Sydney swirl burner : Non-Reacting Reynolds shear stress uw	176
6.11 Sydney swirl burner : Non-Reacting stream lines	177
6.12 Sydney swirl burner : Non-Reacting axial velocity contours	177
6.13 Sydney swirl burner : Non-Reacting rotating velocity contours	178
6.14 Sydney swirl burner : Non-Reacting velocity contour comparison - High swirl	179
6.15 Sydney swirl burner : Non-Reacting velocity contour comparison - Low swirl	180
6.16 Sandia pilot burner : Geometry	183
6.17 Sandia pilot burner : Scalar Predictions	184
6.18 Sydney swirl burner : SMH1 Flame - Steady Laminar Flamelet construction	186
6.19 Sydney swirl burner : SMH1 Laminar flamelet relationship	186
6.20 Sydney Swirl burner : Laminar flamelets compared against turbulent flame composition	187
6.21 Sydney swirl burner : SMH1 Flame axial velocity	194
6.22 Sydney swirl burner : SMH1 Flame tangential velocity	195
6.23 Sydney swirl burner : SMH1 Flame axial velocity RMS	196

6.24 Sydney swirl burner : SMH1 Flame tangential velocity RMS	197
6.25 Sydney swirl burner : SMH1 Flame mixture fraction	198
6.26 Sydney swirl burner : SMH1 Flame mixture fraction RMS	199
6.27 Sydney swirl burner : SMH1 Flame mean tempearture	200
6.28 Sydney swirl burner : SMH1 Flame CO_2 mass fraction	201
6.29 Sydney swirl burner : SMH1 Flame CO mass fractoin	202
6.30 Sydney swirl burner : SMH1 Flame H_2O mass fraction	203
6.31 Sydney swirl burner : SMH1 Flame non unity lewis number	204
6.32 Syndey swirl burner : Reacting : velocity contours	205
6.33 Sydney swirl burner : Reacting : Scalar contours	206
6.34 Non-premixed Borghi diagram	207
7.1 Premixed/Partially Premixed Flames : Borghi Diagram	212
7.2 Turbulent Flame Kernel : Growth rate	212
7.3 Turbulent Flame Kernel : Reacting surface	213
7.4 Turbulent Flame Kernel : Reacting surface	214
7.5 Turbulent Backward Step Flame : Geometry	215
7.6 Turbulent Backward Step Flame : Recirculation zone	219
7.7 Turbulent Backward Step Flame : Non-reacting flow velocity field	220
7.8 Turbulent Backward Step Flame : Reacting flow velocity field	221
7.9 Turbulent Backward Step Flame : Progress variable	222
7.10 Turbulent Backward Step Flame : Shadowgraph	223
7.11 Turbulent Backward Step Flame : Scalar contours	223
7.12 Turbulent Backward Step Flame : Reacting sourface iso-contour	223
7.13 2D Burner Stablized Flame : Geometry	225
7.14 2D Burner Stablized Flame : Adiabatic premixed FGM	225
7.15 2D Burner Stablized Flame : Non-adiabatic premixed FGM	226
7.16 2D Burner Stablized Flame : Scalar comparision	227
7.17 Cambridge Stratified Burner : Geometry	229
7.18 Cambridge Stratified Burner : Adiabatic partially premixed FGM	230
7.19 Cambridge Stratified Burner : Mean Axial velocity	234
7.20 Cambridge Stratified Burner : Mean equivalence ratio	235
7.21 Cambridge Stratified Burner : Mean Temperature	236
7.22 Cambridge Stratified Burner : Mean CO_2 mass fraction	237
7.23 Cambridge Stratified Burner : Time mean scalar and velocity contours . . .	238
7.24 Cambridge Stratified Burner : Progress variable source term contours . . .	239

A.1	Pressure field distribution and stream lines in flow around cylinder calculated from potential flow	263
A.2	Jet In Cross-Flow : Turbulent Schmidt number effects - STARC-CCM+ . .	264
A.3	Jet In Cross-Flow : RANS and LES Velocity field - OpenFOAM	265
A.4	Jet In Cross-Flow : RANS and LES Reynolds Stress field - OpenFOAM . .	266

List of tables

1.1	US emmissions rates (lb/MWh) from fossil fuel electric power generation [1]	2
4.1	Measurement uncertainties JICF test case	99
4.2	Boundary conditions JICF test case	99
6.1	Sydney swirl burner : Boundary conditions	163
6.2	Boundary conditions for Sandia flame D	185
7.1	Turbulent Flame Kernel : Initial conditions	210
7.2	Cambridge Stratified Burner : Boundary Conditions	229

Nomenclature

Roman Symbols

a_{st}	Stoicheometric strain rate Eqn: 2.14
A_{fj}	Pre-exponential constant of reaction j Eqn: 3.96
A_o	Surface area of a laminar flame element Eqn: 2.16
A_t	Wrinkled flame area Eqn: 2.17
c	Progress variable Eqn: 3.119
c	Progress variable Eqn: 2.18
c	Speed of sound Eqn: 3.68
Da	Damköhler number Eqn: 2.12
E	Efficiency function
$E_{act,j}$	Activation Energy of reaction j Eqn: 3.96
$E_{(k)}$	Turbulent energy spectrum
F	Flame thicken factor
G_x	Axial flux of the axial momentum Eqn: 2.15
G_θ	Axial flux of the tangential momentum Eqn: 2.15
Ka	Karlovitz number based on laminar flame thickness Eqn: 2.12
Ka_δ	Modified Karlovitz number based on reaction zone thickness Eqn: 2.12
K_{fj}	Forward reaction rate of reaction j Eqn: 3.96

K_{rj}	Reverse reaction rate of reaction j Eqn: 3.96
l_t	Integral length scale Eqn: 2.12
Re_{cf}	Cross-flow based Reynolds number
Re_s	Swirl flow Reynolds number Table: 6.1
Re_t	Turbulent flame Reynolds number Eqn: 2.12
R_o	Outer radius of the annulus Eqn: 2.15
R_u	Universal gas constant Eqn: 3.96
S	Swirl number Eqn: 2.15
S_l	Laminar flame speed Eqn: 2.17
S_t	Turbulent flame speed Eqn: 2.17
St_w	Wake Strouhal number Eqn: 5.2
T	Temperature Eqn: 2.18
T_b	Burnt side temperature Eqn: 2.18
T_u	Unburnt side temperature Eqn: 2.18
β_j	Temperature exponent Eqn: 3.96
$T_{act,j}$	Activation temperature of reaction j Eqn: 3.96
U_e	Co-flow axial velocity Table: 6.1
U_n	Advection velocity Eqn: 3.68
u'	RMS velocity in the fresh gas side
u'	Fresh gas RMS velocity Eqn: 2.12
u'_{δ_e}	Sub-grid turbulent velocity
U_s	Swirl flow axial velocity component Table: 6.1
W_k	Molar mass of specie k
W_s	Swirl flow tangential velocity component Table: 6.1

$[X_k]$	Molar concentration of specie k
X_k	Molar fraction of specie k
Y_F	Fuel mass fraction Eqn: 2.18
Y_{Fb}	Burnt side fuel mass fraction Eqn: 2.18
Y_{Fu}	Unburnt side fuel mass fraction Eqn: 2.18
Y_k	Mass fraction of specie k
ΔZ_f	Diffusion layer thickness

Greek Symbols

χ	Scalar dissipation rate
χ_q	Scalar dissipation rate at quench limit
χ	Stoichiometric scalar dissipation rate Eqn: 2.14
δ_l	Laminar flame thickness Eqn: 2.12
δ_r	Reaction zone thickness Eqn: 2.12
γ	Specific heat ratio Eqn: 3.68
γ	Resolved turbulent kinetic energy percentage
κ	Flame stretch Eqn: 2.16
ν'	Stoichiometric coefficients in reactant side
ν''	Stoichiometric coefficients in product side
Ω_{ij}	Vorticity tensor Eqn: 3.76
$\dot{\omega}_k$	Mass reaction rate of specie k
ϕ'	Scalar fluctuations Eqn: 2.13
ψ	Compressibility Eqn: 3.68
σ^2	Scalar variance Eqn: 2.13
τ_t	Turbulent time scale Eqn: 2.12

τ_k	Kolmogorov time scale Eqn: 2.12
τ_c	Chemical time scale Eqn: 2.12
Ξ	Flame wrinkling factor Eqn: 2.17

Acronyms / Abbreviations

ATF	Artificially Thickened Flame
CFD	Computational Fluid Mechanics
CIVB	Combustion Induced Vortex Breakdown
CVP	Counter Rotating Vortex Pair
DMM	Dynamic Mixed Model
DNS	Direct Numerical Simulation
DOEM	Dynamic One Equation Model
DSM	Dynamic Smagorinsky Model
EBU	Eddy Break-Up
EDC	Eddy Dissipation Concept
FGM	Flamelet Generated Manifold
FPV	Flamelet Progress Variable
FSD	Flame Surface Density
FVM	Finite Volume Method
GDH	Gradient Diffusion Hypothesis
GS	Grid Scale
ILDm	Intrinsically Lower Dimensional Manifold
JICF	Jet In Cross-Flow
LDA	Laser Doppler Anemometry
LES	Large Eddy Simulation

PIV	Particle Image Velocimetry
PLIF	Planar Laser Induced Fluorescence
PVC	Precessing Vortex Core
RANS	Reynolds Averaged Navier-Stokes
RST	Reynolds Stress Transport
SGS	Sub-Grid Scale
SLFM	Steady Laminar Flamelet Method
SST	Shear Stress Transport
VB	Vortex Breakdown

Chapter 1

Introduction

1.1 Motivation

In a world with ever-increasing demand for electrical power generation, fossil fuel combustion devices are under increasing pressure to reduce harmful emissions and achieve efficient performances. Consequences of power generation from fossil fuel burning were understood many decades ago, yet most of the countries are still struggling to cope with energy demand associated with rising population, urbanisation, and development. According to the World Energy Council (WEC) survey in 2013, 80% of world energy sources are fossil fuel based, with coal accounting for about 40% of electric power, oil and natural gas accounting 32% and 20% respectively [2]. Due to clean combustion technologies and efficient Combined Cycle Gas Turbine (CCGT) power plants, natural gas-based power plants shows a higher growth compared to other fossil fuel power sources. International Energy Agency (IEA) estimated that global energy demand increases by one third from 2011 to 2035, with demand for natural gas increasing by 48%, coal by 17%, oil by 13%, nuclear by 66% and renewable sources by 77% [3]. The IEA report estimated energy-related CO_2 emissions to increase by 20%. Moreover, even on an energy plan towards bringing the CO_2 emissions to limit the global temperature rise to less than $2^\circ C$ in the long term, the demand for natural gas is expected to rise by one-third based on the current trend. Furthermore, it showed the remaining limited fossil energy sources would not restrain the projected energy sector growth. At the current production rates, 142 years of coal, 61 years of natural gas and 54 years of oil are estimated. Total remaining recoverable coal sources amounts to 3050 years, natural gas resources for about 233 years and oil resources for 178 years. Therefore, for the foreseeable future, the fossil fuel generated power is expected to drive the world through development, especially the developing countries in Asia, Africa, and South America. With the exploration of shale gas reservoirs the price of natural gas is expected to reduce, and once the

Table 1.1 US emissions rates (lb/MWh) from fossil fuel electric power generation [1]

	NO_x	SO_2	CO_2
Coal	2.1	6.5	2146
Oil	3.1	6.5	1878
Gas	0.48	0.13	944

upfront investment on exploration, gas transportation infrastructures are completed natural gas use will continue to grow in predictable future.

The international understanding of the climate change resulted in the Paris climate agreement a legal binding which was signed by major industrial countries, to reduce the global warming to less than $2^\circ C$ of the pre-industrial era and has come to enforcement. Therefore further restrictions on Greenhouse gases can be expected in addition to prevailing clean air protocols. Table:1.1 shows the US emissions from electricity generation using fossil fuels. CO_2 emissions from gas combustion is nearly 50% lesser than coal and oil, and NO_x emissions from gas combustion is lower by a magnitude of order. The comparative advantage of using natural gas as a power source compared to other fossil fuels is therefore clearly substantiated from the emission reduction point of view and near future economic sustainability.

Even though the renewable energy technologies are on a rapid rise, still intermittent power supply and large-scale storage methods are unresolved issues associated with renewable energy technologies. Gas power generation can be used in conjunction with renewable energy sources, which are susceptible to fluctuating power sources like wind turbines, the tidal power to generate Hydrogen gas by electrolysis. This method is derived from the *Power-to-Gas* concept, which provides an option to store and transport Hydrogen in the natural gas grid as an energy storage method. Hydrogen can be used as a blended fuel in Lean Premixed burners to stabilise lean flames [4]. So use of Hydrogen as a gas turbine fuel, and as a blended fuel with natural gas has stirred interest in the energy industry. In addition, Hydrogen generated by bio-degradation will also join the renewable and clean gas power stream in the near future. Therefore the use of Hydrogen based blended fuels can be expected only to grow in commercial power generation. Due to this ability of gas turbines to work efficiently with many different types of current and future fuels, it is introduced as an *omnivorous* machine [5].

Natural gas combustion is mainly associated with four emissions namely CO_2 , CO , NO_x and particulates or soot. The NO_x , emission level, is directly proportional to fuel residence time in the burner and sensitive to the maximum temperature. However, CO emissions are inversely proportional to the residence time. This intrinsic relationship between NO_x

production and complete combustion requires an optimization to trade off between NO_x and CO . Lean premixed gas turbines are designed to work efficiently and to comply with low emission standards. However, as discussed above the future gas turbines will require cleaner combustion and more efficient combustor designs. Air-fuel mixing plays a vital role in these premixed burners in which the air-fuel mixing quality has a profound effect on the combustion performance and emission levels. In addition, lean premixed burners are susceptible to combustion flashback which is a primary operational concern. In the design process, the lower cost of repeatability of numerical studies is the most prominent advantage of numerical simulations compared with experimental studies which are expensive due to high operational pressures. Due to the increase of computing power in recent years, numerical simulations of turbulent reacting and non-reacting flows of combustion devices have become a design tool and an analysis method.

Outline of the present investigation

The essence of this thesis is numerical simulations and analysis of air-fuel mixing methods and stabilised flames which are of practical use to the gas turbine combustion processes. Gas turbine combustion involves many contributory processes as air-fuel mixing, reacting flow, quenching flows, exhaust gas recirculation etc. These processes can be categorised based on the region, as air-fuel mixing region and reaction zone. Although air-fuel mixing is a molecular process, this process can be enhanced by turbulence and gas turbine designers employ different approaches to achieve proper air-fuel mixture. However, extended air-fuel mixing zones cause pressure drop and increase both the risk of flame flashback and overall size of the combustor. Therefore even though the air-fuel mixing is an essential design requirement, the design of air-fuel mixing arrangement is constrained by other design criteria. The reaction zone is further sub-categorised into three zones. The primary zone, where flow recirculation mixes hot combustion products with incoming fresh gases and stabilise the flame, and in some configurations exhaust gas recirculation also enters this zone. The intermediate zone where excess air is introduced to attenuate thermal dissociation due to high temperatures (2000K). The dilution zone where dilution gases are injected to reduce the temperature to the Rotor Inlet Temperature (RIT) $\sim 1850K$. Heat transfer from wall cooling, cooling due to dilution gas injection and radiation also play essential roles in the heat transport process. Also, flow instabilities coupled with combustion acoustics also needed to be combined into a comprehensive understanding of the combustion process. Therefore, computational modelling tools are very much an integral part of the design process of future gas turbine combustion chambers and fuel mixers.

In this work, the air-fuel mixing arrangement is studied initially without the effect on combustion (cold flow simulations) mainly due to the inadequacy of comprehensive combined mixing data and reacting flow data for comparison and validation of numerical tools. As introduced in Section 1.1, injection of Hydrogen into natural gas network provides an energy storage method for renewable energy sources, and study of the combustion of this fuel mixture is also a part of this work. Therefore turbulent combustion modelling methods were used to numerically model the Sydney swirl stabilised swirl burner with CO_2 and H_2 fuel mixtures. Finally, turbulent premixed/partially-premixed combustion modelling techniques were investigated for modelling premixed and stratified flames.

1.2 Research Methodology

In this thesis work, the well-established flow simulation technique Computational Fluid Dynamics (CFD) using Finite Volume Method (FVM), which solves partial differential equations that describe conservative equations and transport equations was used. The commercial CFD package STAR-CCM+ and the open source C++ code OpenFOAM were used for numerical modelling in this thesis. Three-Dimensional flow equations which are commonly known as Navier Stokes Equations and other scalar transport equations were solved by making necessary assumptions according to the problem. Two turbulent flow modelling techniques namely Reynolds Averaged Navier Stokes (RANS), and Large Eddy Simulation (LES) techniques were used in this thesis. Direct Numerical Simulation (DNS) technique resolves all turbulent length scales up to Kolmogorov scales, hence provides the most accurate flow field. However, this method is still computationally expensive due to the grid resolution required scales with a higher order of Reynolds number ($Re^{9/4}$). Direct Numerical Simulations of scalar mixing studies have been performed by some researchers [6] on similar problems with lower Reynolds number flows, but this thesis work is mostly focused on the LES method.

In RANS technique the full turbulent energy spectrum is modelled by firstly time averaging the Navier-Stokes equations, and secondly by using physical relationships of turbulent length scales and time scales to close the turbulent flux terms. RANS method is computationally less demanding compared to DNS method but has not been able to predict complex turbulent flows such as swirl flows, and recirculation flows accurately. Particularly due to the effects of eddy viscosity assumption used in RANS technique, the scalar mixing results are highly dependent on the model coefficients used, and this will be discussed in this thesis. Despite these shortcomings for complex geometries, RANS method is still used in industrial applications primarily due to the lesser computational demand. In contrast to RANS, DNS

method resolves the full energy spectrum at an extremely high computational cost. Therefore as an intermediate technique between RANS and DNS methods, LES method has been developed in which turbulent length scales larger than a defined grid scales are solved, and sub-grid energy levels are modelled. The LES method has proven to predict industrially relevant reacting and non-reacting flows of gas turbines to agree well with experimental measurements [7]. Hence LES studies were performed in this study to investigate relevant combustion problems associated with gas turbine combustion.

The combustion and flame stabilisation process of the gas turbine is the most critical process of the overall gas turbine power production. Modelling of the turbulent combustion is still considered a challenge among the practitioners of computational fluid dynamics, predominantly because of the highly non-linear chemical source term and temperature relationship and the smaller chemical time scales compared to the flow time scales. The development and advancements of new turbulent combustion models and the evaluation of existing combustion models under challenging test cases are of equal importance to the turbulent reacting flow modelling community. Even the most advanced turbulent combustion endeavours of engineering applications use combustion models instead of direct chemistry solution due to prohibitive computational expenditure associated. In this thesis, turbulent combustion modelling approaches are divided along the axis of non-premixed and premixed/partially premixed flames. In the most advanced turbulent non-premixed combustion models of today, the effects of reactants mixing are accounted for by explicitly calculated probability density functions; in the most advanced premixed combustion modelling approaches level set methods are used to track the flame surface propagation. Both these methods are computationally expensive as well as require complex mathematical implementations. Therefore in this thesis more established presumed probability density methods and progress variable based are used in modelling of turbulent combustion.

1.3 Thesis Layout

Chapter 1 : Introduction

Introduction and motivation of the thesis work are provided in this chapter.

Chapter 2: Literature Review

Previous work related to theoretical studies of the air-fuel mixing process and turbulent combustion modelling are discussed. In this chapter Jet In Cross-Flow (JICF) arrangement

is considered as the generic air-fuel mixing technique. Hence previous experimental and numerical studies of JICF studies are discussed in detail.

As the second half of this thesis work is comprised of reacting flow modelling, which can be used in stabilised gas turbine flames, the literature on reacting flow modelling are also discussed. Basics of turbulent flames, flame stabilisation method and turbulent combustion models used in general practice and their relative advantages are discussed.

Chapter 3: Governing Equations

Governing equations used in the numerical modelling of turbulent reacting and non-reacting flows are introduced here. Equations of Reynolds Averaged Navier-Stokes (RANS) method and the Large Eddy Simulation method (LES) are introduced since both techniques are used in this thesis. Turbulent Non-Premixed combustion modelling techniques using Steady Laminar Flamelet Method (SLFM), and Premixed combustion modelling using Flamelet Generated Manifold and Thickened Flame combustion models are also introduced. Previous and recent prominent advancements in turbulent combustion modelling are also mentioned.

Chapter 4: RANS modelling of Jet in Cross-Flow

To understand the flow dynamics and scalar mixing quality variations associated with a JICF arrangement, a test case from literature is modelled and validated against a comprehensive experimental dataset. RANS simulation results using the commercial CFD software packages STAR-CCM+ and OpenFOAM are compared and discussed.

Chapter 5: LES modelling of Jet in Cross-Flow

LES simulation results of JICF problem with several Sub-Grid Stress (SGS) models are presented, and results are discussed. Coherent structures in this flow were realized using LES solution field to look into the effects of turbulent structures in air-fuel mixing. Mixing quality quantification methods are also discussed in this chapter. Then the developed LES modelling strategy is used to model twin jet in a cross-flow interaction test case.

Chapter 6: Non-Premixed flames

The stationary gas turbine combustion process utilises different combustion modes during its operational cycle. Flames inside the combustion chamber switch to non-premixed modes during part load and start-up stage of a low NO_x premixed burner. Therefore, the numerical

modelling of non-premixed flames are important in the numerical modelling treatment of gas turbine combustion process. In addition, the recent interests of the use of Hydrogen blended fuels have motivated the efforts of modelling CH_4 , H_2 blended fuel based flame in this Chapter. In this chapter non-premixed flames are modelled using adiabatic Steady Laminar Flamelet Method (SLFM). LES modelling of two test cases from Sydney Swirl burner studies for the non-reacting flow cases are modelled, and results are discussed. Vortex structures are essential in turbulent flame stabilisation. Before discussing reacting swirling flows it is necessary to understand the non-reacting swirl flow field. Hence a low swirl test case with a Swirl Number ($S = 0.54$), and a high swirl case ($S = 1.59$) are studied. Sandia-flame D is also modelled under RANS context to validate the solver performance. Then, Sydney Swirl Burner test case SMH1, which used a CH_4 - H_2 fuel mixture is simulated, and results are compared against experimental data.

Chapter 7: Premixed/Partially Premixed Flames

Artificially Thickened Flame (ATF) model and Flamelet Generated Manifold (FGM) model are used in this chapter to model premixed/partially-premixed flames. ATF model is validated using a simulation of the growth of a turbulent flame kernel at two different turbulent intensities, and a mixing layer flame behind a backward facing step. FGM model is used to model the Cambridge stratified swirl burner test cases.

Chapter 8: Conclusion and Future Work

In this chapter principal conclusions of the numerical modelling of air-fuel mixing using Jet in Cross-Flow studies and turbulent combustion, modelling are discussed. The shortcomings of numerical simulations are outlined, and identified steps to improve the accuracy of numerical predictions are suggested as future work.

Chapter 2

Literature Review

2.1 Gas Turbine Air Fuel Mixing

Development of first stationary gas turbines was encouraged because of the need to eliminate the indirect heat transfer between source and working fluid in steam turbines. Although the first patent for a gas turbine dates back to 1871 by the Englishman John Barber, the first electricity generation power plant was built in 1939 at Neuchâtel, Switzerland [8]. The early stationary gas turbines operated with blast furnace oil like heavy oils as the fuel until the oil crisis in the 1970s, consequently gas turbines were developed to use natural gas. In early designs of Sir Frank Whittle's engines, a fuel atomizer with a wide spray cone angle was used, and an air swirler provided toroidal flow reversal to recirculate combustion products to stabilize the flame [9]. Early gas turbines were predominantly operating in non-premixed mode, and due to their inherent high temperature that occurs in the stoichiometric air-fuel composition, high levels of NO_x from the oxidation of atmospheric nitrogen was generated. As an attempt to reduce NO_x emissions levels to comply with strict emission restrictions, Lean Pre-Mixed (LPM) combustion was introduced by gas turbine manufacturers where air and fuel are mixed before the combustor to result in a fuel lean combustible mixture. In LPM combustion mode a fuel-air mixture with fuel/air ratio close to half of the stoichiometric ratio is used, and in such mixtures atmospheric nitrogen act as a diluent because resulting flame temperatures are not sufficient to oxidise nitrogen. However, during operation, the burner may operate as diffusion flame during transient loading conditions and start-up and shutdown stages. When the idea of Lean Premixed/Pre-vaporized burner concept was introduced [10] with the intention to reduce NO_x by lowering the flame temperature, most of the design considerations were compared against aero-engines which had established fuel pre-evaporation and premixing methods, and the need for investigation of different air-fuel mixing injectors was highlighted. Subsequently, the effect of air-fuel mix-

2.1 Gas Turbine Air Fuel Mixing

ing non-uniformity on NO_x production was studied theoretically and experimentally using simplified well-stirred reactor assumptions [11], [12].

The NASA swirl can combustor study which used Kerosene as fuel was studied by Mikus et.al[11] and they developed a model to predict NO_x production in gas turbines. They defined fuel non-uniformity index s as the ratio of standard deviation of fuel mass fraction to mean fuel mass fraction, and the NO_x emission index (E_{NO_2}) was defined as NO_x emissions equivalent to NO_2 per 1000 kg of fuel. The model showed that as the fuel non-uniformity index s was increased the rate of change of NO_x emission index increased E_{NO_2} as it is shown in Figure: 2.1. Also, their model was used with reasonable success in predicting NO_x level prediction of the Kerosene burner. The model also showed that with increased pressure ratio the fuel non-uniformity effect on NO_x emissions further worsened producing more NO_x . Furthermore, Lyons [12] conducted a study on the Lean Pre vaporized

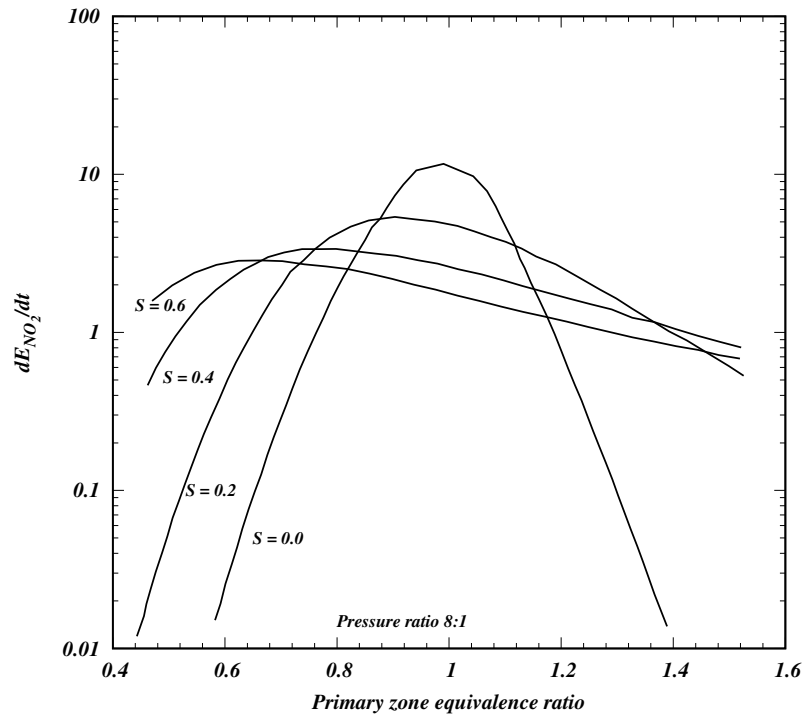


Figure: 2.1 NO_x emissions index predicted by the Mikus et.al model for a kerosene combustor at different fuel non-uniformity levels (Reproduced from [11]).

Premixed (LPP) burner to investigate the relationship between fuel non-uniformity and NO_x emissions, and two theoretical models for NO_x productions were developed and validated against exhaust gas analysis. Their study also showed that fuel non-uniformities have a significant influence on NO_x production. To further understand the effect of spatial and tem-

polral nonuniformities of air-fuel mixing on NO_x emissions, a jet in co-flow arrangement was studied by Fric [13] at atmospheric pressure. In his work a parameter for the “level of unmixedness (U)” was used which was based on fuel concentration variance (c'^2) and time mean fuel concentration (\bar{c}) as,

$$U = \frac{c'^2}{\bar{c}(\bar{c} - 1)} \quad (2.1)$$

Their results showed that even if small temporal fluctuations ($c'/\bar{c} = 10\%$, $U \approx 0.0004$) can double the NO_x level from a purely premixed mixture. Hence, temporal fluctuations of air-fuel mixing quality is a vital parameter in the design of low emission gas-turbine combustors. Furthermore, their work concluded with the emphasis on the need for investigating the effect of air-fuel mixing on NO_x production at elevated pressures, because at higher pressure the possibility to obtain prior mixing is further restricted if reaction rates increase faster than mixing time scales.

Barnes and Mellor [14] have developed a Characteristic Time Model (CTM) to estimate the NO_x emissions per fuel mass for a piloted lean premixed burner and summarised a series of studies on investigations of fuel unmixedness on NO_x emissions. Their CTM predicted values were compared with a CFD simulation and showed the need to modify the empirical CTM model. Also, their work reviewed contemporary studies which had shown an increase in NO_x emissions due to spatial unmixedness and temporal fuel unmixedness. Furthermore, their work assumed a Gaussian distribution of equivalence ratio compared with CFD results and commented that there were significant discrepancies between CFD results and experimental measurements. However, the reported CFD simulation was a coarse simulation; hence there is much more scope for improvement.

By using a swirl mixing arrangement Kräemer et.al [15] achieved nearly 30% NO_x reduction for the temperature range 1300 - 1650 °C. Moreover, their study showed that the relative advantage of premixing is reduced at very lean mixtures with lower flame temperature when compared to high-temperature lean flames. However, reduction of flame temperature conflicts with other major gas turbine design requirements such as increased thermal efficiency and reduced unburnt hydro-carbon emissions. Frey et al. [16] also investigated the quality of fuel distribution in circumferential and axial direction on varying the pre-mixer length and inlet turbulence level by using a pre-mixer that consisted of a swirler and radial fuel rods with injection holes. Their results showed that better mixing was obtained by increasing the residence time (pre-mixer length) compared to inlet turbulence intensity. These studies showed the effect of air-fuel mixing quality on NO_x emissions and the importance of obtaining spatially and temporally uniform mixing quality. Consequently, lean premixed burner approach has shown promising results compared to other NO_x reduction

methods such as flame quenching method in which flame is quenched by quenched air or water injected into the high-temperature zones. However, to increase the mixing quality and residence time the premixing region cannot be extended without conflicting with thermal efficiency and unburnt hydrocarbon levels because if the mixture is closer to lean extinction limit the unburnt fuel mass increases. Therefore, computational modelling techniques are extensively used in optimization and modelling of air-fuel mixing arrangement designs.

Gaseous fuel jet injection into cross-flowing air stream is one of the widely used techniques in gas turbine fuel injection methods. This fuel injection method is usually used in combination with a swirl flow that further enhances mixing by increasing flow entrainment and helps to stabilize the flame via hot combusted products recirculation. Figure 2.2 depicts this method of fuel injection from swirl vanes, which can be simplified as a fuel jet injected to a cross-flow. Radially placed fuel rods with injection holes and swirl vanes with fuel injection nozzles are such common fuel injection methods, and these methods are viewed as an ensemble of multiple fuel jets injected into cross-flow. One objective of this study is to use the current numerical turbulent flow modelling techniques to model the Jet In Cross-Flow (JICF) arrangement thus model the air-fuel mixing of JICF arrangement. In next section, previous experimental and numerical studies on JICF air-fuel mixing arrangements are reviewed.

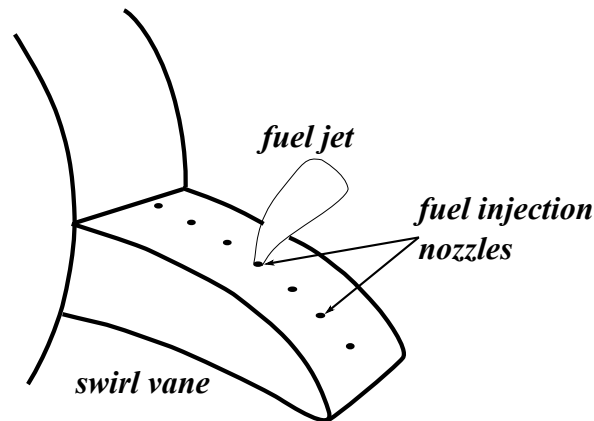


Figure: 2.2 A gas turbine air-fuel mixing arrangement using jet in cross-flow

2.2 Jet In Cross-Flow

Earliest research works on the Jet In Cross-Flow (JICF) studies were encouraged by the research and development work on Vertical and/or Short Take Off/Landing (VOSTL) air craft applications [17]. In gas turbine context, air-fuel mixing applications and combustor wall

cooling applications also use the JICF arrangement, and in other engineering applications like exhaust gas plumes, mixing applications also use this arrangement. In recognition of the importance of JICF studies, in 1993 the Advisory Group for Aerospace Research and Development (AGARD) held a symposium on computational and experimental assessment of Jet In Cross-Flow, in which the research findings to that date were presented [18].

Some definitions must be declared that are used in the classification of JICF problems. Two basic flow parameters, Momentum ratio (J) and Velocity ratio (R) are defined using jet flow bulk velocity (U_j), cross-flow bulk velocity (U_c), jet fluid density (ρ_j) and cross-flow fluid density (ρ_c). Reynolds numbers (Re) of jet and cross-flow, characteristic length scales of the jet nozzle and channel cross-section are also used to scale the turbulence intensity and eddy length scales. Reynolds number is mostly defined based on the circular jet flow pipe diameter (d).

$$\begin{aligned} J &= \sqrt{\frac{\rho_j U_j^2}{\rho_c U_c^2}} \\ R &= \frac{U_j}{U_c} \\ Re_d &= \frac{\rho U d}{\mu} \end{aligned} \tag{2.2}$$

For example, thin wall cooling applications encounter low Re number flows in contrast to mixing applications where high Re flows are used [19]. In fuel mixing applications the fuel jet must penetrate sufficiently into the cross-flow stream to generate turbulence and entrainment; therefore typical mixing applications have velocity ratio between 1 - 10. In flows with low-velocity ratios ($R < 1.0$), the jet stream is weak to penetrate into the cross-flow, hence can be assumed only boundary layer of the cross-flow is affected thus used in wall cooling applications like gas turbine blade cooling. JICF arrangements with very high-velocity ratios ($R > 10$) are mostly used in impingent cooling applications.

JICF generates complex flow structures from jet and cross-flow interaction, and from wall interactions. Four distinct vortex structures are found as it is shown in Figure: 2.3. These vortex structures are named as,

1. Counter-rotating Vortex Pair (CVP)
2. Horseshoe vortices
3. Wake vortices
4. Jet shear-layer vortices

Many early JICF studies were focused towards understanding the mechanism behind these flow structures formation. However, from an engineering point of view, the velocity field and scalar field distribution are more important. Therefore in this endeavour, the currently understood flow structure formation mechanisms are only briefly discussed. Jet shear layer vortices are weak in vorticity strength and unsteady, and these are formed as a Kelvin-Helmholtz instability due to the flow shear between jet flow and cross-flow, and an annular shear layer can be observed to separate from the nozzle orifice and propagate on the mean jet flow. As the jet evolves downstream, these vortices grow in size and eventually lose the annular structure as it can be seen from Figure: 2.4a

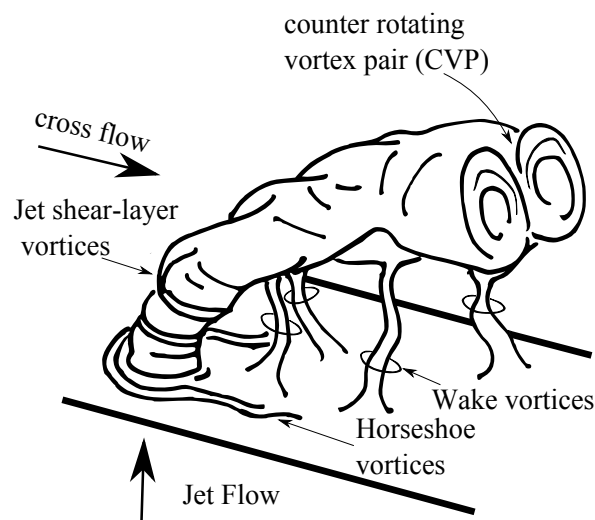


Figure: 2.3 Vortex structures in JICF - redrawn from Fric and Roshko [13]

The horseshoe vortices that can be seen as wrapped around the base of jet flow are distinct flow structure resembles the same structures formed in a flow around a cylinder. These vortices have shown periodicity similar to wake vortex structures under certain flow regimes[20]. Figure: 2.4b shows the formation of horseshoe vortex on the upwind side of the jet, it is understood that the incoming wall boundary layer meets an adverse pressure gradient ahead of the jet and separate to form these horseshoe vortices [13]. Kelso and Smit [21] performed an experimental analysis on a laminar jet and laminar boundary layer of a cross-flow interaction for different conditions, and concluded that the horseshoe vortex system exhibit steady, oscillating or coalescing nature depending on the flow conditions.

During early studies of JICF, the velocity fluctuations in the wake which are periodic and oscillatory were compared with vortex shedding of flow behind cylinder. Work using smoke wire flow visualization by Fric and Roshko [13] shed light on the formation of vertical vortex structures, by systematic analysis of flow visualization studies and hot-wire anemometry methods. Prior to their work it was assumed that wake vortices formation was similar to

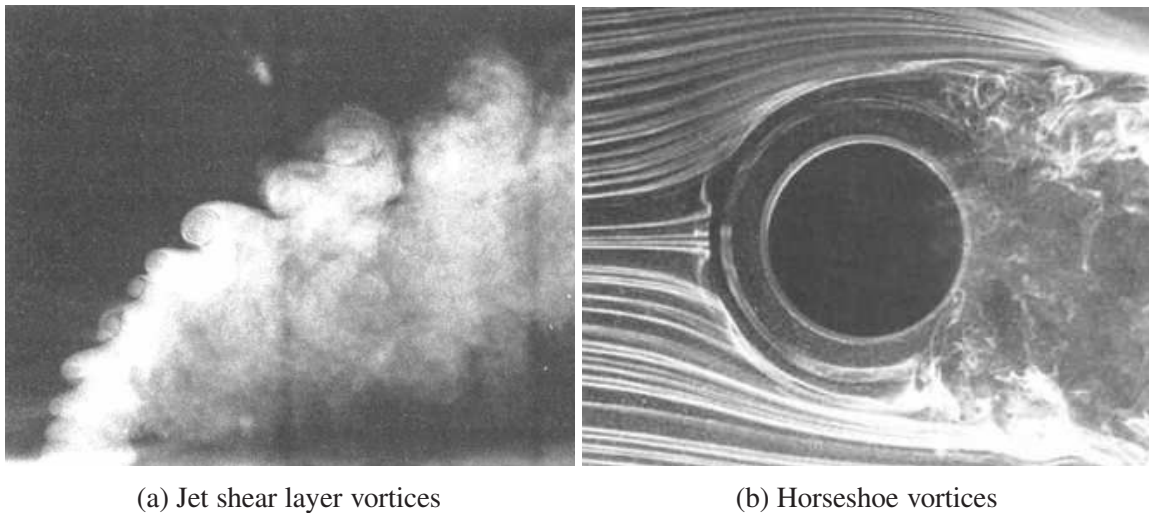


Figure: 2.4 Jet shear layer vortices and horseshoe vortices - copied under permission from Fric and Roshko [13]

the wake formation in flow past a cylinder problem, however this investigation showed that no analogy between vortex shedding in JICF and flow past cylinder could be established. However, these wake vortices show similarities with vortices behind solid bodies, but the main difference with regard to wake vortices formation comes from the difference that solid body acts as a permanent obstacle compared to jet flow. In addition the wake is defined as the region downstream between the jet and the wall, therefore in contrast to bluff-body wake these vortices has a termination point on the wall and the other termination occurs on the jet itself. Therefore, they concluded that these wake vortex are formed downstream beside the jet by the cross-flow boundary layer separation due to the adverse pressure. This separation occurs alternatively on each side and causes boundary layer fluid vorticity to erupt. These tornadoes like vorticity structures have one end on the wall boundary layer while other ends are attached to the jet hence jet flow is entrained to the cross-flow.

The Counter-Rotating Vortex Pair (CVP) is the most dominant flow structure and shows distinct mean flow characteristics that develop downstream. There seems to be no universally accepted mechanism of the CVP formation, and different authors have postulated different mechanisms. Broadwell and Breidenthal [22] considered that the CVP is formed from the momentum impulse provided by the transverse jet on the cross-flow. Later with more experimental evidence, it was suggested that the vortex sheet emanated from the pipe causes the CVP formation [23]. After the extensive experimental investigation by Kelso et al. [20] postulated that two processes contribute to the formation of CVP, firstly they observed that the shear layer of the jet folded and rolled up very close to the nozzle exit and secondly they observed the mean reorientation of the shear layer vorticity. Thus, they proposed that

the superposition of these two processes as the CVP formation mechanism. In a subsequent numerical study this CVP mechanism was confirmed, hence currently accepted as the CVP formation mechanism [24]. However, through numerical simulations, Yuan et al.[25] showed a different view on the CVP formation mechanism. So it is inconclusive what the exact mechanism of CVP formation is, but in an engineering context, the CVP structures are present even in laminar JICF and under certain conditions could exhibit Vortex Breakdown (VB) structures as well.

The jet flow acts as an obstruction to the cross-flow, therefore comparable to flow past a solid cylinder. The potential flow solution of flow around a cylinder is shown in Figure: A.1, and it shows the generated pressure gradients variation. Therefore, by extension, it can be inferred that due to this pressure gradient the emanating jet flow deforms into an oval shape, and along the jet trajectory the jet flow cross-section evolves to a kidney-shaped cross-section that can be identified as a Counter-rotating Vortex Pair (CVP).

2.2.1 Previous Experimental studies

Margason [17] reviewed the previous fifty years of research work on JICF. According to this review in early studies, the similarity between flow around a cylinder and JICF was used to explain and understand the flow field and wake vortex structures. This analogy was supported by the observation of periodic fluctuations in the wake flow, which appeared to be similar to vortex shedding behind the cylinder. Although in subsequent researches this analogy of wave vortex shedding was proved to be flawed and dismissed, this analogy explains the jet flow deformation and the pressure distribution around the jet nozzle. Additionally, his review summarised early research endeavours to find empirical relationships for the jet path, vortex path, deflection angle and other flow parameters for different velocity ratios. These empirical relationships were used during times before computational fluid dynamics came to research forefront, yet with the increase of computational powers in recent decades the empirical relationships can now be substituted by more comprehensive flow simulation data. However formation mechanisms of these vortical structures were not established at the time, only hypotheses were made using the similarity of flow around the cylinder.

Keffer and Baines [26] carried out one of the earliest analysis of JICF flow field based on experimental observations using hot-wire measurements and smoke visualizations. Their analysis followed the methods of free jet analysis and hence defined a natural coordinate system to find the self-similarity of the flow field. Their observations showed that JICF problem is not entirely self-preserving as turbulent free jet, especially because of the vortical structures generated are much stronger than a free jet in the downstream region. However, in the near jet nozzle region where the vortices are weak in strength, a mean excess velocity

similarity was observed, but this self-similarity region was limited to 3.46, 3.20 and 3.10 diameters for velocity ratios 4,6 and 8 respectively. Thus, it is clear that as the velocity ratio increases the self-similar region shortens, therefore in subsequent JICF studies researchers worked on selected velocity ratios instead of seeking self-similar profiles of velocity field statistics.

Ramsey et al. [27] performed a series of JICF experiments using air to air injection for low-velocity ratio flows that related more to film cooling applications. In this study, the authors investigated the cooling of a flat plate below the jet and the temperature profiles obtained by this study has been used in subsequent numerical validation studies. Kamotani and Greber [28] used a hot-wire anemometry and hot wire probe to measure velocity and turbulence for JICF experiment that was designed to investigate combustor wall cooling applications. They used a heated air jet and measured the temperature distribution for many momentum ratios, and obtained self-similarity for transverse temperature distribution on the symmetry plane. More accurate measurements near the initial jet developing region using Laser Doppler Anemometry (LDA) were obtained by Crabb et.al [29] for low velocity ratios of $R = 1.15, 2.3$. They addressed the need for experimental measurements for the validation of numerical computations, therefore used a tracer gas (Helium) to measure the jet concentration field as well. Because this experiment provided both mean velocity and Reynolds stress data, many numerical simulations have been validated later using this data set. Andreopoulos and Rodi reported experimental data for JICF experiments with $R = 0.5, 1, 2$ and mean velocity and fluctuating components were measured using an anemometer and a three sensor hot-wire probe method [23]. From three instantaneous velocity component measurements, they evaluated turbulent kinetic energy, turbulent shear stress components. Additionally, their study showed that at low-velocity ratios, jet flow inside the pipe is influenced by the cross-flow interaction. In their experiment, three regions of turbulent kinetic energy field were identified. First the region over the jet exit where high-velocity gradients and flow curvature was present, second the immediate downstream zone where the velocity gradients in the recirculation zone generated turbulent kinetic energy was present, and third the downstream zone where gradually velocity gradients attenuated. This experimental dataset has also been used extensively for numerical validation purposes because of the detail velocity data measurements.

Recognizing the need to investigate the scalar mixing in JICF arrangement Smith and Mungal [30] conducted experiments for different velocity ratios varying from $R = 4$ to 14, using Planar Laser-Induce Fluorescence (PLIF) method. Later, they extended their work, and velocity ratios from $R = 5$ to 25 were experimentally investigated using both velocity field and scalar field measurements while keeping $R \times d$ a constant where d is the jet diam-

eter [31]. In this experiment, the high Reynolds number flows were studied varying from $Re_d = 8400$ to 41500 . Interestingly their experiments for JICF with $R > 10$ found that the near-field maximum centreline scalar decaying can be characterized by $s^{-1.3}$ which is different from free jet (s^{-1}), and far-field which is characterized by a decay rate of $s^{-0.66}$ where s is the jet centreline coordinate, and the branching of these two zones occur at $s = 0.3R^2d$. Therefore, by looking at the maximum centreline scalar decay rates they identified the near-field region where CVP is formed and the scalar mixing is enhanced compared to a free jet. In far-field, the CVP is fully developed, and the mixing is not enhanced comparatively, thus concluded that the CVP formation mechanism is responsible for enhanced mixing. Their study confirmed the existence of boundary layer separation and vortex roll-up in the near field vortex interaction region, and scale similarity was observed in this region with respect to jet diameter d , They reported that for test cases where $R > 10$ jet fluid was found in wake vortex structures via entrainment, and Gopalan et al.[32] reported in their experimental work that for $R < 2$ the wake vortices were not present or weak in strength. Moreover, they found that the CVP formation is delayed as velocity ratio increased and the jet concentration was asymmetric about the symmetric plane. Later, based on the above work Su and Mungal [33] performed measurements of the scalar field and 2-D velocity field using PLIF and Particle Image Velocimetry (PIV) for a lower velocity ratio of $R = 5.7$, and measured scalar variance, scalar flux components and Reynolds stress tensor as well. The experimental data from this research group has been used in subsequent numerical validation and simulations [19, 6].

Most of the academic studies have been focused on a single jet in a cross-flow interaction, however, in practical applications like of air-fuel mixing multiple fuel jets are injected. These multiple fuel jets have interactions with each other as well; therefore the understanding of these interactions are important for the optimisation of mixing process. Toy et al. [34] performed a series of twin jets side by side interactions with changing the nozzle spacing and velocity ratios. They found that the flow field is dominated by a single vortex pair formed from both jets. However, their study concluded with the emphasising the need to perform more comprehensive measurements of the velocity field. In a more recent study Naik-Nimbalkar et al. [35] inlined twin jet in cross-flow mixing, where they changed the nozzle distance. From their study, they found that because of the shielding effects of the first jet the second jet showed more penetration, and for higher velocity ratios the first jet was pulled towards the second jet. Although there have been some other studies on multiple jets, in the context of gas turbine air-fuel mixing application these vortex interactions have not been studied with sufficient experimental measurements.

In a more recent series of studies Cárdenes et al. [36] conducted 2D-LIF and PIV measuring techniques to obtain 2D scalar fluxes and Reynolds stress contours for a velocity

ratio of $R = 3$. The same setup was extended with simultaneous PIV/LIF measurements for a JICF of $R \simeq 4$ and mean scalar and velocity field measurements, Reynolds stress, scalar flux measurements were discussed with numerical modelling using RANS and LES techniques [37]. Further experimental data were reported for different velocity ratio test cases in subsequent work [38]. Then to further improve the inlet boundary conditions and scalar measurements accuracy the same experimental set up was used by Cárđanes et al. [39]. This experimental data-set was prepared in the context of air-fuel mixing investigations, and high Reynolds number flows were studied, and in many subsequent numerical studies, these data were used [40, 41, 37, 42]. Therefore, in this thesis, the experimental data from this particular test cases were used.

2.2.2 Previous Numerical studies

Early numerical studies on JICF have been performed using empirical jet flow penetration profiles [43]. Earliest flow field simulations using partial differential equations solving was performed by Patankar et al. [44] using the Reynolds Averaged Navier Stokes (RANS) method, in which the standard $k - \epsilon$ model was used to model turbulence. In their study mean streamwise velocity component and jet penetration were compared against experimental measurements and obtained good agreement. A more comprehensive computational study of JICF was performed by Alvarez et al. [45] using the $k - \epsilon$ model and a second-moment closure model, in which they numerically modelled the experimental test cases by Andreapolous and Rodi [23], Ramsey and Goldstein [27]. In their work scalar transport was modelled using the scalar flux transport closure method proposed by Launder and Samaraweera [46]. Their results showed that both models predicted reasonable agreement with mean streamwise velocity and the second-moment closure model predicted an over-predicted recirculation zone. The streamwise normal stress prediction also showed that second-moment closure model over-predicted the stress when compared to the $k - \epsilon$ model. The scalar field predictions showed similar patterns in general, but the second-moment closure approach showed marginal improvement over the $k - \epsilon$ model result. In modelling of the Andreopoulos et al.'s experiment showed that the mean velocity components were predicted similarly by both models and agreed well with experimental data, yet the second-moment closure method slightly over-predicted the recirculation zone. However, the turbulent stress field predictions showed a clear difference in the performance of two models, where it was seen that the $k - \epsilon$ model results showed significantly greater magnitude compared to second-moment closure model and experimental results in general. Therefore, even though neither turbulence models calculated the Reynolds stress terms sufficiently, they concluded that the second-moment closure model performance was comparatively better than the $k - \epsilon$ model.

Marking the earliest use of Large Eddy Simulation (LES) methods Jones and Wille [47] compared three Sub-Grid Scale (SGS) models namely the Standard Smagorinsky model, a dynamic model that calculates the Smagorinsky constant, and a model with one transport equation for sub-grid kinetic energy to model the experimental case by Chan and Hwang [48] which was a plane jet in cross-flow problem. Their work used both adaptive and non-adaptive grids and found that mesh adaptation did not result in a significant improvement of results, and all three SGS models performed nearly the same way in predicting velocity field despite differences in turbulent eddy viscosity values. It was seen that the model with a transport equation for sub-grid kinetic energy produced the largest eddy viscosity while the dynamic model produced the smallest amount. However, the model with the transport equation for sub-grid kinetic energy showed marginally improved results in the prediction of turbulent quantities. The mesh resolution in this simulation was insufficient to comment on the performance of these SGS models. Later, a LES study on JICF was conducted by Yuan et al. [49] for two velocity ratios of 2.0 and 3.3 in which the experimental case of Sherif and Pletcher [50] was modelled using a locally dynamic SGS model that had shown the ability to model transitional flows and the energy backscatter from unresolved sub-grid scales to resolved scales. In addition, their study showed that the upstream condition of jet flow pipe has significant influence over the mean flow field results.

LES of JICF was performed by Schlüter and Schönfeld [19] to investigate gas turbine air-fuel mixing arrangements. They compared standard Smagorinsky model and Filtered Smagorinsky model using the experimental data by Andreopoulos et al. [23] experiments and Smith and Mungal's [31] experiment, to model the scalar mixing as well. Their simulation reproduced the flow structures of JICF and showed reasonable agreement with mean velocity field experimental data, but the filtered Smagorinsky models showed better agreement with experimental data near field than the standard Smagorinsky model. Similarly, the mean passive scalar field results prediction also showed superior performance of the filtered Smagorinsky model. Furthermore, their simulation using different Schmidt number showed that LES results showed miniscule dependency on Schmidt number. They then extended the simulation setup to model the twin jet-in cross-flow interaction experiment by Toy et al. [34] and obtained good agreement with limited experimental data. Finally, they extended their modelling approach to model a gas turbine fuel premixing arrangement which used a swirl vane with fuel injection nozzles.

Wegner et al. [51] used LES technique to investigate the JICF flow modelling and the effect of jet angle on scalar mixing, using the experimental data of Andreopoulos and Rodi [52],[23]. Their study used a velocity ratio $R = 0.5$ JICF arrangement with perpendicular jet and two cases where the jet was inclined by 30° in the direction of the cross-flow and in

opposing direction to the cross-flow. Lilly's dynamic Smagorinsky model [53] was used for sub-grid stress terms closure. Their mean streamwise velocity comparison with experimental data showed reasonable agreement, but wall-normal velocity prediction (jet direction) showed consistent over prediction. Turbulent kinetic energy comparison also showed good agreement with experimental data closer to the jet inlet, but further downstream LES results showed significant overprediction of turbulent kinetic energy. From different injection angles, they found that the fuel injection towards the incoming cross-flow enhances the mixing and could reduce the pre-mixer length.

Majander and Siikonen [54] modelled the experimental test of Crabb et al. [29] using standard Smagorinsky model, and steady and unsteady inlet boundary conditions at the jet were tested. According to the mean streamwise velocity predictions, both steady inlet and unsteady inlet boundary conditions produced similar results, and as the downstream distance increased LES results overpredicted the velocity. Although LES results showed some numerical discrepancies, a good qualitative agreement was obtained for turbulent fluctuation predictions. Furthermore, they commented on the need for more high-resolution data of the recirculation zone to understand the velocity field and scalar mixing field better. Salewski et al. [55] also conducted numerical and experimental studies to investigate mixing in circular and noncircular jets in cross-flow in a water channel. Their LES method did not involve an explicit SGS model; instead, an assumption of negligible sub-grid energy levels have been used, and reasonable agreement was obtained between Numerical results and experimental results. From their study, it was suggested that nozzle shapes that introduce more small-scale structures into the cross-flow enhance scalar mixing. Further, their experiments and simulations revealed that nozzles with a higher aspect ratios (blunt) provide better mixing, this is contradictory to the argument presented by Holdeman et al. [56], and Liscinsky et al. [57] where they studied different aspect ratio nozzles and found using time mean values that the global mixing quality is independent of the nozzle shape. Therefore, the shape of jet nozzle influence on mixing quality is debatable and more studies should be carried out, and LES can be used to investigate the optimization of mixing quality using different arrangements. Cavar and Meyer [58, 59] simulated the experimental test case of Oslash et al. [60] using Smagorinsky, Dynamic Smagorinsky and Mixed Scale Model with varying mesh resolutions and numerical schemes. All SGS models produced good LES results that agreed with experimental data. However, all models showed discrepancies very close to the jet nozzle. They attributed these discrepancies to the shear layer vortices created at the upwind side of the jet that was not accurately produced by LES. Also, in their work Proper Orthogonal Decomposition (POD) of 3D velocity field data from LES were used to explain the formation of Counter-rotating Vortex Pair (CVP) and wake vortices. Using the

POD analysis they proposed the idea that CVP originates from the hanging vortices that are formed at the lateral sides of the jet, and wake vortices originate from vortex shedding caused by the oscillating vortex core.

In a series of studies using the experimental data of Cárdenes et.al [61, 39] numerical investigations were carried out by Galeazzo et.al [37],[62] and Ivanova et.al [40, 63, 41]. Ivanova et al. [63] conducted a numerical study of JICF using RANS, Unsteady RANS and Scale-Adaptive Simulation (SAS) methods using the $k - \omega - SST$ model and $k - \omega - SST$ -SAS model. In RANS simulations, the problem was assumed to be symmetric around the symmetric plane of the cross-flow. This study showed that unsteady simulations produced marginally better agreement with experimental measurements than steady simulations, and URANS method reached grid independence sooner than SAS simulations. With regard to SAS model, they showed that further studies are required to understand the model performance comprehensively, but the model showed good promising results in predicting mean velocity profiles but overpredicted the fluctuation quantities and the scalar field predictions. Ivanova et al. [40] presented LES and URANS simulations of JICF using $k - \omega - SST$ model and Wall Adaptive Large Eddy (WALE) model, where they investigated the effect of turbulent Schmidt number using URANS and LES. In addition, they modelled the passive scalar variance using another transport equation. From their results, it can be seen that for time-mean velocity field statistics the difference between URANS and LES was minimal. However, in turbulent scalar flux predictions, URANS showed a significant dependence on turbulent Schmidt number when compared with LES results. Ivanova et al. [41] performed a study on the effect of turbulent Schmidt number in JICF modelling and concluded that a low turbulent Schmidt number of $Sc_t \sim 0.2 - 0.3$ only helps the scalar mixing by artificial diffusion and do not resemble the physical reality of scalar mixing. Further, they concluded that the for the particular problem the Schmidt number varies around 0.5 which they found by deducing the turbulent scalar diffusivity using LES data. Galeazzo et al. [37] performed LES and RANS on the same experimental set-up using $k - \epsilon$, $k - \omega - SST$ models and standard Smagorinsky model respectively. Their results showed that RANS results agreed very well with mean velocity field but turbulent fluctuating components were not predicted sufficiently, and LES results showed better agreement with experimental data in both mean and fluctuating components prediction. In another study by Galeazzo et al. [42], the same experimental set up was modelled using LES and RANS modelling results using the Smagorinsky model and $k - \epsilon$, $k - \omega$ -SST models. Furthermore, they showed that LES captures the coherent structures very well that reflects as better agreement with experimental measurements when compared with RANS method in which coherent structures are not captured sufficiently.

Moreover, Denev et.al [64], Prière et.al [65] have also conducted LES analysis of JICF scalar mixing problem. Direct Numerical Simulation (DNS) of JICF were carried out by Hahn and Choi [66] and Muppadi and Mahesh [6] for low Re number flows. However, during this thesis work, DNS works of JICF were excluded from the discussion.

Scalar mixing modelling

In this thesis work numerical modelling of air-fuel mixing is one of the main objectives, therefore in this sub-section, the previous literature on turbulent scalar transport modelling is discussed. The scalar mixing process can be considered as a process with three stages, entrainment, dispersion, and diffusion occurs at all turbulent scales. Providing an overview of previous studies of turbulent mixing Dimotakis [67] sub categorized scalar mixing into three levels,

Level I : Scalar mixing is not coupled with flow dynamics, examples are equal density gas mixing, dispersion of non-reacting tracer gases or particles, small temperature differences, small particle/cloud smoke or ink mixing.

Level II : Mixing is coupled with flow dynamics such as Rayleigh-Taylor instabilities caused by different density flows.

Level III : Mixing produces changes to the fluid properties such as density, composition. Chemically reacting flows, detonations and supernova explosions can be considered as examples for this mixing level.

Furthermore, Dimotakis stated that most of the scalar mixing studies are limited to the first level of mixing, where the scalar can be considered as a passive scalar. In numerical analysis of passive scalar mixing, a passive scalar transportation is derived using a Reynolds' transport theorem. A scalar transport equation is a transport quantity of rank zero tensor, and if the scalar imposes no influence on the fluid flow or any other transport quantity, such a scalar is known as a passive scalar. The passive scalar transport equation hence is a conserved scalar equation with no source term in the transport equation. In this thesis work, the air-fuel mixing is also treated as the mixing of a passive scalar, because the air and fuel density can be assumed approximately equal in these applications.

In the passive scalar transport equation the turbulent scalar flux term $(\overline{u'c'})$, requires closure and the most common method of closure is to use the Gradient Diffusion Hypothesis (GDH). The turbulent scalar flux closure using turbulent diffusivity (D_t) and turbulent Schmidt number (Sc_t) as Eqn 2.3.

$$\overline{u'c'} = D_t \frac{\partial C}{\partial x_i} = -\frac{\mu_t}{Sc_t} \frac{\partial C}{\partial x_i} \quad (2.3)$$

This simple method assumes isotropic turbulence, therefore in practical situations where highly anisotropic eddies are present, this model fails to encapsulate counter gradient scalar transport [68]. Combest et.al[69] reviewed other closure methods for turbulent scalar flux term, these methods are mainly categorized into algebraic models and scalar flux transport models. An algebraic method to incorporate anisotropic mixing effect an anisotropic turbulent diffusivity tensor (D_{ij}^t) was introduced by Batchelor [70].

$$\overline{u'c'} = -D_{ij}^t \frac{\partial C}{\partial x_i} \quad (2.4)$$

Daly and Harlaw improved on this method, and the turbulence diffusivity tensor was replaced using an algebraic model that assumes the proportionality of Reynolds stresses to turbulent scalar flux as Eqn 2.5, where C_θ is a positive model constant [71].

$$\overline{u'c'} = -C_\theta \frac{k}{\varepsilon} \overline{u'_i u'_j} \frac{\partial C}{\partial x_i} \quad (2.5)$$

Following the same assumption, Fox [72] introduces a closure method that includes turbulent Schmidt number,

$$\overline{u'c'} = \frac{k}{Sc_t \varepsilon} \overline{u'_i u'_j} \frac{\partial C}{\partial x_i} \quad (2.6)$$

In scalar flux transport methods, an additional transport equation for turbulent scalar flux is solved as Eq 2.7,

$$\frac{\partial \overline{u'c'}}{\partial t} + \overline{U} \frac{\partial \overline{u'c'}}{\partial x_j} = \frac{\partial \left(J_{ij} - \overline{u'_i u'_j c'} - \frac{1}{\rho} \overline{p' c'} \delta_{ij} \right)}{\partial x_j} + P_i + R_i - \varepsilon_i \quad (2.7)$$

where J_{ij} is the molecular diffusion component, P_i closed production, R_i unclosed pressure gradient and ε_i scalar flux dissipation term. It can be seen that solving an additional transport equation is not only computationally expensive but also introduces new terms to be closed.

Turbulent Schmidt number Effect

The turbulent scalar diffusion analysis uses similarity with the molecular diffusion process, and hence the relationship between kinematic molecular viscosity (ν) and molecular diffusivity of scalar (D) is extended into defining a relationship between kinematic eddy viscosity ν_t and turbulent scalar diffusivity D_t . In the practice of CFD, the turbulent Schmidt number is usually considered as a global parameter to control turbulent scalar diffusion. Turbulent scalar mixing depends on the integral scalar length scales which are considerably larger and

anisotropic than Kolmogorov scales, whereas molecular diffusion process is a homogeneous and uniform process that occurs at a much smaller length scale than turbulent length scale in most engineering applications [72]. Therefore a representing turbulent Schmidt number as a global parameter is understood to be the underlying reason for inaccurate representation of scalar field diffusion.

Reynolds [73] reviewed previous attempts on modelling turbulent Schmidt number and Prandtl number and observed that these dimensionless numbers depend on the molecular Schmidt number and Prandtl numbers respectively, and on the position in the flow, hence local turbulent intensity and for wall-bounded flows the distance from the wall. Following those observations, he introduced an empirical relationship between molecular Schmidt number and turbulent Schmidt number in the form of,

$$Sc_t = C_1 \exp \left[-C_2 Sc^m \left(\frac{v_t}{\nu} \right)^n \right] \quad (2.8)$$

where C_1 , C_2 , m , n are model constants. In this model, the Schmidt number variation based on position is implicitly accounted through eddy viscosity, and turbulent Schmidt number is reduced with the increase of the turbulent viscosity ratio (v_t/ν), allowing the opportunity for more scalar mixing.

Combest et.al[69] reviewed recent efforts on modelling Schmidt number and Prandtl number since the work of Reynolds and concluded that regardless of numerous effort to model the turbulent diffusivity variation, a constant turbulent Schmidt number varying from 0.1 to ≥ 1 is used in mainstream CFD modelling of scalar mixing. However it is noteworthy to mention the efforts by Guo et al. [74] to include a variable Schmidt number by the use of genetic algorithms, which can be identified as an effort to address future turbulence models where artificial intelligence will be used to refine model constants. He et al. [75] conducted a parametric study on the effects of turbulent Schmidt number in JICF arrangements by varying Schmidt number from 0.2 to 1.5 and momentum ratios from 8 to 72 with the use of $k - \epsilon$ model. They modelled the experimental setup of Crabb et al. and Kamotani and Greber [28]. Furthermore, they developed an empirical correlation between turbulent Schmidt number and the position by using the empirical correlations of Kamotani and Greber [28] for the temperature profiles of JICF (Eqn: 2.9 in which X is the direction in cross-flow from the centre of the jet and d is the jet flow pipe diameter).

$$asSc_t = \frac{v_t}{D_t} = 0.82J^{0.05} \left(\frac{\rho_j}{\rho_c} \right)^{0.11} \left(\frac{X}{D} \right)^{-0.07} \quad (2.9)$$

This relationship shows with the increase of momentum ratio (J) Schmidt number increases indicating a reduced scalar spread rate, while with distance in jet evolution Schmidt number reduces indicating an increase of scalar mixing. Furthermore, this relationship shows the necessity of interpreting the dependency of density difference on turbulent scalar mixing. Concluding their work He et al. proposed a value of $Sc_t = 0.2$, even though such a small value is understood to be artificially enhancing the scalar spread rate.

Ivanova et al. [76] estimated Sc_t for a JICF arrangement using LES data and found it to fluctuate around 0.5, and hence proposed for RANS simulations a similar numerical value for Sc_t to be used. Nevertheless, during their work, they emphasized on the influence turbulence kinetic energy on turbulent Scalar diffusion. In RANS simulations turbulent kinetic energy is proportional to the produced eddy viscosity hence implicitly influences on the turbulent diffusivity $D_t = \nu_t/Sc_t$. Further, their work agreed that the current practice of RANS modelling of turbulent scalar mixing in CFD is to artificially enhance or minimize the turbulent scalar diffusion by either decreasing or increasing the Sc_t value. The modelling work of the same setup using RANS by Galeazzo et al.[37] used $Sc_t = 0.9$. Furthermore, Tominaga and Yoshihide [77] conducted a series of atmospheric dispersion simulations using RANS and postulated that in a problem with multiple flow dynamics, the local turbulent flow characteristics should be taken into consideration in determining a global Schmidt number value. Therefore in addition to research mentioned above and other work by many other researchers as [6],[78], a consistent method of determining turbulent Schmidt number was not found.

As discussed in this section the modelling of turbulent scalar flux using a Gradient Diffusion Hypothesis based model with a constant turbulent Schmidt number method do not conform with the physical process of mixing with vortical structures. However, more advanced modelling requires measurements of higher order scalar statistics for validation, and the closure problem becomes more complex with the introduction of additional model constants. Due to these reasons, in engineering practice, the constant turbulent Schmidt number approach is widely used for the closure of turbulent scalar flux. Hence, the value of turbulent Schmidt number has been selected on a problem based on the amount of eddy viscosity produced by the RANS model according to the application in consideration. However, in LES method since the large vortical structures that transport scalar, are resolved the deficiencies of GDH can be minimised, as the sub-grid scalar flux can be explained using constant turbulent Schmidt number with reasonable accuracy if the sub-grid eddies are of isotropic range. Therefore in this thesis, the turbulent scalar flux modelling is achieved using a constant turbulent Schmidt number and GDH.

2.3 Literature Review on reacting flow modelling

In the second half of this thesis (Chapter 6,7) numerical simulations of turbulent flames are presented. Turbulent flames that resemble gas turbine combustor flames, namely the Sydney swirl stabilized burner, Cambridge stratified burner are simulated in this thesis. These experiments were conducted using natural gas and blends of natural gas and hydrogen, therefore only numerical simulation of gaseous fuels are considered. In this section, the literature on turbulent flames and combustion modelling strategies are reviewed.

2.3.1 Flame types

Most commonly used flame types in gas turbines are non-premixed flames or diffusion flames in which fuel and oxidiser are mixed at the flame interface. The characteristic nature of these flames is to have fast chemical time scales capable of burning at a wide range of equivalence ratios. Thus a more stable flame is achieved. However, the non-premixed flames have this inherent disadvantage of creating high-temperature zones at the stoichiometric composition, producing NO_x emissions. There are many NO_x reduction methods used in gas turbine combustor design such as staged combustion, and water injection to reduce the flame temperature. It is known that fuel-lean mixtures produce low-temperature flames, thus using this ability to achieve low NO_x emission standards, lean premixed flames are now widely used in industrial gas turbines [9] In this type of flames fuel and oxidiser is mixed to a combustible mixture before reacting stage. However, the operation of purely premixed flames is not only a safety concern but presents many operational issues such as combustion induced instabilities, flame flashback, and flame extinction. Therefore in the design of gas turbine combustors, the flame stability of non-premixed flame mode is used in part load operations, and startup stages [79], thus introduce different equivalence ratios in a gas turbine combustor. Therefore the partially premixed flames or stratified flames are also necessary for gas turbine combustor modelling applications. In this endeavour, all three modes of flames were numerically simulated and discussed the performance of these combustion models.

Premixed Flames

A mixture of fuel and oxidiser capable of sustaining a chemical reaction can be ignited to obtain a premixed flame, and in contrast to non-premixed flames, premixed flames exhibit a propagating nature because of the availability of the combustible mixture. In a laminar premixed flame of hydrocarbon fuel the laminar flame speeds (S_l) are usually of the order

2.3 Literature Review on reacting flow modelling

of 10-100 m/s and the laminar flame thickness δ_l is around 0.1mm scale. Free flow flame is the canonical premixed flame, and in Figure: 2.5 a one-dimensional laminar free flame problem is shown with the definitions used in this thesis. The laminar flame thickness (δ_l) is calculated using the relationship Eqn:2.10

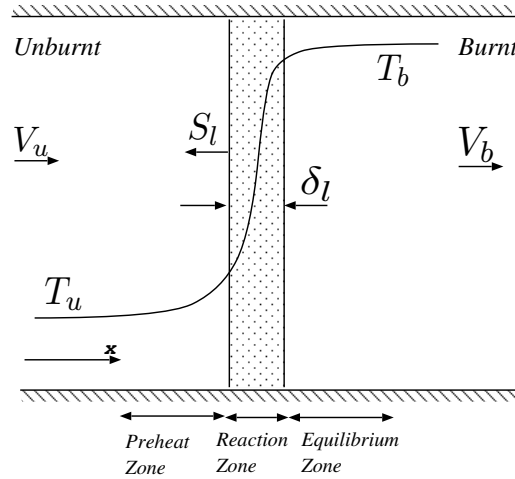


Figure: 2.5 One dimensional free propagating flame

$$\frac{1}{\delta_l} = \frac{1}{T_b - T_u} \frac{dT}{dx} \quad (2.10)$$

A one-dimensional free flow flame can be solved with detail chemical reactions using different software packages, and in this thesis work Cantera [80] and Flame-Master [81] were used. It is known that the turbulent flame speeds S_t increase with increasing turbulence (velocity fluctuations u'). Similarly, turbulent flame brush thickness also grows more than the laminar flame thickness as a result of intense mixing. Using experimental observations Gülder [82] developed this relationship between laminar flame speed and turbulent flame speed as,

$$\frac{S_t}{S_l} = 1 + \frac{u'}{S_l} \quad (2.11)$$

In turbulent combustion due to the laminar reaction zone interaction with eddies, the reaction zone deforms hence causing a wrinkled flame front. Flame wrinkling is considered to be the primary mechanism that increases the reaction rates in turbulent flames, as increased surface area enhances the fuel consumption rate. However, the above proportional relationship between turbulent flame speed and turbulence is only valid until the flame quenching occurs due to extensive flame stretch or heat loss. In literature, there are multiple variants of relationships provided for turbulent flame speed and RMS velocity [83, 84]. However, no universal relationship has been found due to the inherent problem of turbulence and only

2.3 Literature Review on reacting flow modelling

semi-empirical models valid for different regions of turbulence are presently available for the turbulent flame speed. Therefore discussion of premixed flames are subjected to the flame regime defined by Damköhler (Da), Karlovitz number (Ka) and turbulence Reynolds number (Re_t) which are given in Eqn: 2.12 (unity Prandtl number is assumed).

$$\begin{aligned}
 Da &= \frac{\tau_t}{\tau_c} = \frac{l_t/u'}{\delta_l/S_l} \\
 Ka &= \frac{\tau_c}{\tau_\kappa} = \frac{\delta_l/S_l}{\nu/\varepsilon} \\
 Re_t &= \frac{u'l_t}{\nu} = \left(\frac{u'}{S_l}\right)\left(\frac{l_t}{\delta_l}\right) \\
 Ka_\delta &= \frac{\delta_r/S_l}{\sqrt{\nu/\varepsilon}} = \delta_r^2 Ka
 \end{aligned}
 \tag{2.12}$$

Different premixed flame regimes are drawn in diagrams as functions of velocity scale ratios and timescale ratios, such diagrams are known as Borghi diagrams [85]. On a Borghi diagram, different premixed flame regimes can be represented as shown in Figure: 7.1 (The test cases simulated in Chapter 7 are also placed in the flame regime diagram). Laminar flames are shown in the region below $Re_t < 10$, this is the region where normalised length scale and normalised turbulent velocity scale show values similar to a laminar flame regime. Larger values of Damköhler number ($Da \gg 1$) corresponds to much faster chemical reactions than eddy time scales, therefore turbulence has a negligible effect on flame structure, and this limit is called flamelet limit where the flame is thinner than all eddies hence only wrinkled. On the opposite limiting case when chemical time scales are larger than eddy time scales ($Da \ll 1$), the reaction-rate is controlled by chemistry therefore, referred as stirred reactor regime. In terms of modelling approach, at the flamelet limit the reaction rate is modelled by multiplying the laminar reaction rate by wrinkled flame surface area, and in the stirred reactor limit reaction rate can be modelled by Arrhenius type chemical reaction-rate expression.

In the $Ka < 1$ region where chemical time scale is smaller than even the smallest eddy time scale, the flame structure is closer to a laminar flame and thin and can be wrinkled by the turbulence eddies hence known as the thin flame regime. The thin flames regime which falls under laminar flamelet regime can be further categorized into wrinkled flamelet regime ($u' < S_l$), and corrugated flamelet regime ($u' > S_l$). In the wrinkled flamelet region strength of turbulence is insufficient to induce turbulence flame interactions hence the laminar flame is moderately wrinkled, and in the corrugated flamelet regime turbulent velocities become

2.3 Literature Review on reacting flow modelling

larger than laminar flame speed hence not only wrinkles the flame front but produce regions of fresh and burnt gases in the flame front.

When $Ka > 1$, turbulent eddies have sufficient time to interact with the laminar flame structure since chemical time scales are larger than the smallest eddy time scale. Therefore this region ($Ka > 1, Da > 1$) is referred to as the thickened flame regime or the distributed reaction zone. The extent of turbulence interaction is indicated by how much the turbulence disrupts the laminar flame thickness of preheat, reaction and equilibrium zones. The modified Karlovitz number (Ka_δ) provides a limit on the extent of turbulence interaction, if $Ka_\delta < 1$, then the turbulence interaction only reaches the depth of the preheat zone but not interact with the reaction zone. Therefore up to $Ka_\delta < 1$ region can be considered as a sub-regime of laminar flamelet regime, but significantly affected by turbulence. Beyond $Ka_\delta > 1$ region shows that turbulence has penetrated to the reaction zone of the laminar flame structure, hence known as the broken reaction zone. In this region, local quenching and flame extinction could occur due to excessive local flame stretch. For most combustion applications the pre-mixed flames operate in corrugate or thin reaction zone regimes, and the flames analysed in this thesis also fall into these regimes.

Non-Premixed Flames

As introduced earlier the non-premixed or diffusion flames are preferred in many combustion devices due to the simplicity of arranging two streams of oxidiser and fuel separately and combust at the mixing interface. Non-propagating nature, sensitivity to flame stretch and quenching from flame stretch are the important characteristics of non-premixed flames. The canonical problem of non-premixed flame is a counter-flow flame arrangement as shown in Figure: 2.6. In diffusion flames, the reaction zone is stabilized closer to the stoichiometric air-fuel ratio, and the flame thickness is not a characteristic of the fuel as in premixed flames, and the reaction zone depends on the level of mixing of fuel and oxidiser. Therefore, stretched non-premixed flame can have a range of flame thickness depending on flow conditions. Furthermore, in diffusion flames, the time scale of chemical species diffusion is more important in the determination of the combustion process because when compared to the much smaller chemical time scales, therefore combustion rate is determined by the rate at which oxidiser and fuel are mixed by diffusion. If the local molecular diffusion timescale reaches the chemical timescales local quenching could occur and flame blow-off can be seen as a result.

Air and Fuel mixing process is important in non-premixed flame analysis especially when chemical reaction rates are relatively faster the overall reaction progress is controlled by the rate of air-fuel mixing at the molecular level. Calculation of molecular mixing is com-

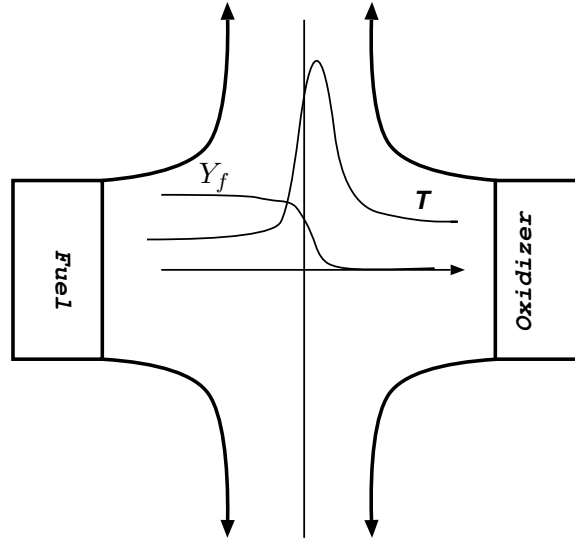


Figure: 2.6 Steady stretched counter flow flame

putationally is far beyond the reach in conventional CFD methods, but it is understood that turbulent mixing helps the molecular mixing process by stirring reactants. Since molecular mixing occurs at the smallest turbulent scales it manifests as a sink term in the Reynolds averaged scalar variance transport equation Eqn:2.13, (similar in LES context as well) in which σ^2 is the scalar variance and ϕ' is the scalar fluctuation.

$$\frac{\partial \sigma^2}{\partial t} + \frac{\partial \bar{u}_j \sigma^2}{\partial x_j} = D \frac{\partial^2 \sigma^2}{\partial x_j^2} - \overline{2\phi' u'_j \frac{\partial \phi'}{\partial x_j}} - 2 \overline{\phi' u'_j \frac{\partial \bar{\phi}}{\partial x_j}} - 2 \underbrace{D \left(\frac{\partial \phi'}{\partial x_j} \right)^2}_{\text{scalar dissipation rate}} \quad (2.13)$$

Modelling of scalar dissipation rate will be discussed in the Section:2.4.2, but it is established here that the scalar dissipation rate (χ) is used as a governing parameter of the reaction progress and inequilibrium and greater scalar dissipation rates result in faster reaction rates [86]. Turbulent non-premixed flames also show sensitivity to turbulence levels thus different turbulent flame regimes are identified based on the interaction of turbulence and chemical effects. However, in non-premixed flames identification of distinct flame regimes is difficult because non-premixed flames do not show intrinsic length scales, but the flame scales are highly dependent on flow parameters. Therefore strain rate of the flame or scalar dissipation can be used as a characteristic molecular timescale, and mixture fraction gradient can be used to estimate the diffusion layer thickness. For the counter-flow diffusion flame the stoicheometric strain rate a_{st} and stoicheometric scalar dissipation rate χ_{st} are related

as,

$$\chi_{st} = \frac{2a_{st}}{\pi} \exp -2[erfc^{-1}(2Z_{st})] \quad (2.14)$$

where $erfc^{-1}$ is the inverse of error function [87]. Peters [87] suggested to obtain the diffusion layer thickness $((\Delta Z)_F)$ using the relationship $((\Delta Z)_F = 2Z_{st})$. Further, Peters proposed a non-premixed flame regime diagram as shown in Figure: 6.34, that shows for larger mixture fraction variances $(\overline{Z'^2}) > (\Delta Z)_F$, the reaction zone are separated. This is understood as, in highly fluctuating mixture fraction zones there exist the possibility for the flame to extend to leaner and richer zones. For smaller mixture fraction variances $\overline{Z'^2} < (\Delta Z)_F$ caused by good air-fuel mixing or premixing, the reaction zones are connected. Further, it shows that when mean scalar dissipation rate is larger than the quenching limit of scalar dissipation rate $(\overline{\chi}_{st} > \chi_q)$ the flame does not exist.

In practical burners after ignition, the flame must be stabilised using the mixing of oxidiser and fuel, and this is referred as flame stabilisation mechanisms. There are different flame stabilisation methods as rim stabilised flames, triple flames, piloted flames and recirculation stabilised flames. These different methods are used accordingly to the inlet flow speed to premixed flame speed ratios, where for smaller ratios simpler stabilisation methods like rim stabilised flames are used and for larger ratios stabilisation using hot combustion products recirculation methods are used. In most gas turbine combustors the flame stabilisation is achieved via flow recirculation methods and a pilot flame mechanism; therefore the simulated flames in this thesis also had swirl stabilisation or flow recirculation stabilisation. In section Section: 2.3.2 flame stabilization using recirculation flows are discussed.

Partially Premixed Flames

When a flame operates on a combination of a combustible premixed mixture and unmixed oxidiser and fuel, the flame is said to operate as a partially premixed flame. The Lifted flame (Figure: 2.7a) is the canonical problem of partially premixed flame in which air and fuel are supplied from different streams, and flame front is stabilized at an elevated height from the burner face. Closer to the burner outlet due to high velocities the flame is extinguished but as the flow velocity is reduced flame stabilised downstream where air and fuel are mixed, and both fresh reactants are meeting. Therefore in this problem, the flame operates on both premixed and non-premixed state. The stratified flame arrangement as shown in Figure: 2.7b, the central fuel rich flow provides stable combustion region, and the surrounding lean flow provides a low emission flame. Stratified flame arrangements are widely used in modern low emission combustors.

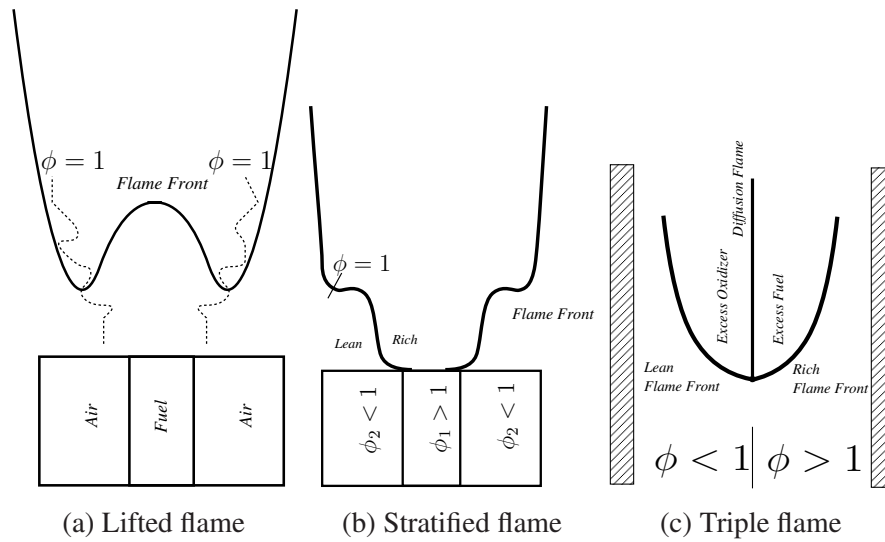


Figure: 2.7 Partially premixed flame arrangements

In stratified equivalence ratio mixtures, triple flames can be observed as shown in Figure: 2.7c. Triple flame has the propagating character associated with premixed flames, and maximum flame speed occurs closer to the stoichiometric air-fuel ratio, hence as shown the shape of the flame surface is determined by the equivalence ratio. In the triple flame, a secondary diffusion flame can be observed inside the burned gas region as a result of excess oxidiser and excess fuel from the lean side and rich side of the domain. Since all three forms of combustion namely fuel rich, fuel lean and diffusion flame occur in this arrangement, hence the name triple flame. In contrast to premixed flames where a homogeneous mixture is present, the partially premixed mixtures can be both homogeneous and inhomogeneous. Therefore in the homogeneously premixed regions, the reaction is controlled by chemical kinetics while in the inhomogeneous region reaction is controlled by the mixing process. To mathematically model a partially premixed flame structures, the homogeneous mixture reaction is described by a reaction progress variable, and the inhomogeneous mixture reaction is represented by a mixture fraction variable.

2.3.2 Flame Stabilisation Using Flow Recirculation

As explained earlier, turbulent premixed and non-premixed flames are susceptible to extinction because of turbulence and changes in equivalence ratio. Therefore, stable operation of gas turbine flames require a flame stabilisation mechanism, and in this section, flame stabilisation using flow recirculation is discussed. The principle of flame stabilisation using flow recirculation is to create and sustain a hot combustible environment using the high-

2.3 Literature Review on reacting flow modelling

temperature combustion products and, enhance air-fuel mixing using turbulence. Bluff body stabilisation and swirl stabilisation are the two most commonly used methods to create a stable flame using flow recirculation. A sudden expansion geometry as shown in Figure: 2.8a, in which a recirculation zone occurs in the wake of the bluff body is used as flame stabilisers in bluff body stabilised burners. In bluff body stabilised flames the flame stability limits are increased by greater residence time in the recirculation zone [88]. Therefore, the flame stabilisation is geometry dependent in this approach of flame stabilisation. The recirculation zone behind a backwards-facing step flame, dump combustor geometry are examples of bluff body stabilised flames.

Swirl stabilised burners are the most widely used flame stabilisation method in industrial non-premixed flames because swirl induced recirculation zone generate strong flow shear with highly turbulent flow structures that enhance mixing [79]. A typical swirl stabilised flame is illustrated in Figure: 2.8b in which a swirl is introduced upstream of the combustor to the reactant stream via swirl vanes or lateral injection, and the flame is stabilised away from the nozzle in a flow recirculation zone. Swirl flows are introduced with an axial jet in most burner designs, and swirl flow increases the jet width, entrainment rate, and rate of decay as the swirl strength is increased [89]. In addition to flame stabilisation, swirl flames reduce combustion chamber length and minimise flame impingement with burner walls [90]. In the analysis of swirl flows the dimensionless Swirl Number (S) introduced by Chiger and Beer [91] has been used,

$$S = \frac{G_{\theta}}{R_o G_x} \quad (2.15)$$

Where G_{θ} is the axial flux of the tangential momentum, G_x is the axial momentum flux, and R_o is the outer radius of the annulus. In a swirling flow, a radial pressure gradient exists due to centrifugal forces, and an axial pressure gradient is generated because of the swirl decay caused by the intense flow shear. For small swirl strength the axial pressure gradient does not couple the axial and tangential velocities, but for stronger axial pressure gradients a coupling occurs, and toroidal reverse flow is created. It has been found to occur at swirl strengths beyond $S > 0.6$ [89]. Therefore, in typical gas turbine burners, the use of swirl flows with swirl number varying from 0.6 to 2.5 is common [90]. This flow reversal structure acts similar to a bluff body in the flow passage creating an aerodynamic stagnation zone that facilitates flame stabilisation. Since this flow reversal changes the original axial to rotational momentum ratios, it is known as a Vortex Breakdown (VB) structure [92]. The increase of swirl strength is limited by several other combustion flow dynamics such as flame flashback, vortex breakdown and combustion instabilities. The toroidal flow reversal zone in a swirl flow is a result of *bubble* type vortex breakdown and thus referred to as recirculation bubble. In a review of swirl flames Lilley [89] showed that by changing the

2.3 Literature Review on reacting flow modelling

inlet swirl degree, the mean residence time of the combustor could be changed. The review stated that from early studies it was known that the position of the recirculation could be controlled by swirl intensity, relative swirl direction, and jet velocity ratio. Furthermore, it showed that at higher working pressures swirl flow introduces local high-temperature zones producing NO_x in a liquid propane burner.

In addition to the recirculation bubble, another instability occurs above the recirculation zone as a result of spiral vortex breakdown at higher swirl numbers [93]. This instability causes the vortex core to oscillate about the central axis, thus named the Precessing Vortex Core (PVC) and this is also another vortex breakdown structure [94]. As a result of PVC, the recirculating flow zone also displaces from the geometric centre and starts to precess [94]. The effects of PVC has been extensively studied by Syred [95] and showed that occurrence of PVC is essentially a function of swirl number and burner geometry in isothermal conditions, but in reacting flows, this is a more complicated phenomenon that depends on many other conditions like mode of fuel entry, equivalence ratio etc. More importantly, his review showed experimental evidence that demonstrated premixed or partially premixed combustion produce a stronger PVC structure than diffusion flames. Therefore, this strong PVC structures could generate self-excited thermo-acoustic instabilities in premixed/partially premixed burners. Furthermore, according to this review, he showed that in burner designs with a central fuel jet or a bluff body the generation of PVC can be seen at much lower swirl number flows than previously understood. In addition to the above two vortex structures, another vortex structure was reported to emanate to the flow from the jet exit. This eddy was observed in the radial-axial plane, inside the vortex core path and named thus radial-axial eddy [89]. This eddy creates alternating rich and lean combustion zones near the jet exit and contributes towards forming combustion oscillations. In Syred's review, he postulated this eddy is probably formed as a result of the flame wobble caused by the PVC.

It is clear that in both bluff-body stabilisation and swirl stabilisation involves complex flow dynamics, and in reacting swirl flows this turbulence-chemistry interaction produces intense combustion, vortex breakdowns and combustion instabilities. Therefore, in this thesis numerical simulations are used in the investigation of physics of both swirl stabilised flames and flame stabilised behind bluff-bodies. However, in addition to numerical challenges of turbulent combustion modelling, the recirculation zone makes this problem an elliptic flow field, hence require iterative numerical solution techniques. Moreover, because of the PVC axisymmetric assumptions also cannot be used in modelling of swirl flames.

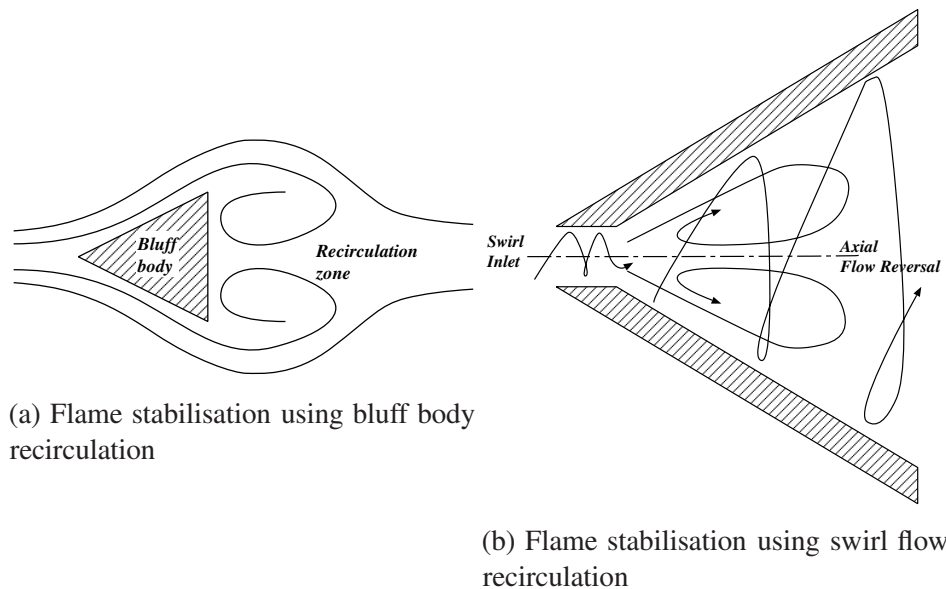


Figure: 2.8 Flame stabilisation using flow recirculation

Modelling of Swirl Flows and Vortex Breakdown

After investigating many other VB structures, Sarpkaya categorized three basic types of stationary vortex breakdowns, double helix, spiral and axisymmetric [96]; he characterised a vortex breakdown as an abrupt change in the structure of the core of a swirling flow. These findings were subsequently supported by other research work but found that, depending on the Reynolds number and inlet swirl strategy there could be more than three modes of VB modes and the double helix separation mode was questioned [97]. However from the experimental evidence, it is clear that propensity to create VB is increased with swirl strength, but geometrical parameters also contribute towards shaping the swirl flow domain and affect the VB structure formation. Many subsequent researchers experimentally attempted to describe the VB structure formation mechanisms, and Lucca and O'Doherty [98] provided an extensive review of previous research work. However, in the context of combustion devices, VB structures are important because of two fundamental combustion phenomenon, combustion induced vortex breakdown (CIVB) structures and flame stabilization. The heat release of combustion dampens the ability for vortex breakdown formation in the main reacting zone [89]. However, combustion also could instigate vortex breakdowns in a propagating flame in vortex [99]. While large toroidal flow reversal helps flame stabilisation, CIVB structures are not necessarily controllable by design and could act adversely and cause flame instabilities. Because VB creates a stagnation point, these structures could potentially instigate flame flashback upstream of the stagnation point [100]. It has been found that the

2.3 Literature Review on reacting flow modelling

propagating flame speed in a vortex is dependent on the circumferential velocity. Although in a stationary gas turbine flame is not designed to operate in propagating flame mode, in the operational cycle propagating flames in a vortex must be considered. Therefore, to understand the effects of vortex breakdown in combustion numerical combustion simulation tools can be used.

In one of the earliest numerical investigations of swirling flows Kopecky and Torrance [101] assumed steady axisymmetric and independent of upstream flow influence flow field, and solved transport equations for vorticity and circulation to reproduce the recirculating zone created as a vortex breakdown bubble. Then Shi [102] carried out unsteady axisymmetric simulations and showed that the solution reaches steady state if no vortex breakdown occurred, and reproduced a recirculating zone near the axial centre line. Spall and Gatsky [103] performed the first fully three-dimensional simulation of VB structures. Their simulation reproduced weak helical, double helix, spiral and bubble-type VB structures; however, their work was limited to laminar flow situations. Nejad et al. [104] compared numerical simulations using $k - \epsilon$ model with two component LDV measurements of an isothermal swirl/non-swirl flows inside a dump combustor. From their results, it can be seen that $k - \epsilon$ model results agreed very well with mean axial and mean tangential velocity components even though the turbulent kinetic energy predictions were severely underpredicted. Thus they concluded that the $k - \epsilon$ model requires modifications to improve the prediction of the turbulent kinetic energy of the swirl flow test cases. Weber et al. [105] assessed the performance of three different RANS turbulence models a Reynolds stress model, $k - \epsilon$ model and an algebraic stress model in the modelling of isothermal swirl flow near a combustion chamber burner zone. According to their results, Reynolds stress model and algebraic stress models showed similar and better agreement with experimental results, whereas the $k - \epsilon$ model produced increased eddy viscosity thus reduced turbulence levels. Moreover, the anisotropic turbulence generation and the radial distribution tangential momentum was not produced well by the $k - \epsilon$ model.

As established and computationally inexpensive RANS turbulence models showed poor results in modelling of strong swirl flows, and VB structures, more advanced turbulence modelling techniques were used in more recent studies. Wang and Bai [106] used LES technique to model isothermal swirl flow in a dump combustor geometry with Scale similarity SGS model, and time mean velocities and velocity fluctuations showed good agreement with experimental data. Malasekara et al. [107] also analysed the isothermal swirl flow of the Sydney swirl burner using LES technique with dynamic Smagorinsky model and results showed very good agreement with experimental measurements. Bulat and Jones [108] investigated an industrial combustor under pressurised conditions and showed that LES results

agreed very well with time mean and fluctuating components of velocity measurements. Furthermore, they showed that LES results captured the PVC and vortex breakdown structures. Also, many other researchers have reported excellent agreement of LES and experimental measurements of turbulent swirl flow and recirculation zones, and vortex breakdown structures [109][110]. Therefore, considering the need for studying different swirl flow arrangements in flame stabilisation, swirling flows and swirl stabilised flames were investigated in this thesis work using the LES method.

2.4 Turbulent Combustion Modelling

On review of turbulent combustion modelling approaches, these methods can be categorized into three main categories.

- Geometrical analogy: The reacting surface or the flame front is considered as a convected surface, and combustion progress is estimated using displacement speed and consumption speeds/rates. Flame surface density and G-equation models are examples of this approach.
- Statistical analogy: The instantaneous value of any scalar can be estimated as a function of temperature, species mass fractions, reaction rate, and other turbulence flow parameters. Mean scalar quantities and their second moments can be calculated using the Probability Density Functions (PDF) of each variable, probability density can be assumed (presumed PDF) or determined by a PDF transport equation [111]. PDF transport methods are computationally expensive but have shown to capture the unsteady combustion dynamics such as flame extinction due to quenching, and reignition [112]. However, in this thesis work, PDF transport methods are not discussed because of the expensive computational cost associated with that model.
- Mixing analogy: High Damköhler number analogy is used in this, where chemical time scales are faster than the mixing time scales. Hence the determination of reaction rates is predominantly determined by the turbulent mixing (scalar dissipation rate).

Large Eddy simulations have shown very good results in predicting the unsteady physics of gas turbine combustion, especially combustion instabilities because LES provides a better description of turbulence and it is heuristically the turbulence combustion interactions are also predicted better with LES than RANS methods. Although the combustion modelling strategies for non-premixed flames and premixed flames share similar theoretical basis, in practice due to the nature of flame propagation of premixed flames and stationary non-premixed flames these models are discussed separately.

2.4.1 Turbulent Premixed/Partially-Premixed combustion modelling

It is known that premixed laminar flame burning velocity (flame speed) is a function of the air-fuel composition, reactants pressure, temperature and product temperature. Turbulence increases the effective flame surface area by flame wrinkling, therefore increases the fuel consumption rate and this is reflected as an increase of flame speed, this is illustrated in Figure: 2.9a. Similarly, the increase heat release from reaction also induces flow accelerations, and this is known as flame generated turbulence, and in some cases, due to increased temperature, the viscosity increases causing these flow fluctuations to attenuate which is referred to as re-laminarization due to combustion. Larger eddies or increased turbulence intensity disturb the flame structure. The turbulent flame speed initially increases with turbulent intensity (u') and reaches a steady state as a result of the balance between the effects of increased flame area and effects of flame structure alteration by turbulence. When turbulence intensity is further increased flame extinction occurs as a result of quenching, and this is shown in Figure: 2.9b. Moreover, counter-gradient transport of products is also critical in premixed combustion because the more common gradient diffusion hypothesis fails to capture this phenomenon. Therefore, modelling these two-way flame turbulence interaction and highly non-linear chemical reactions in a computationally feasible grid requires complex mathematical modelling and assumptions according to the flame regime.

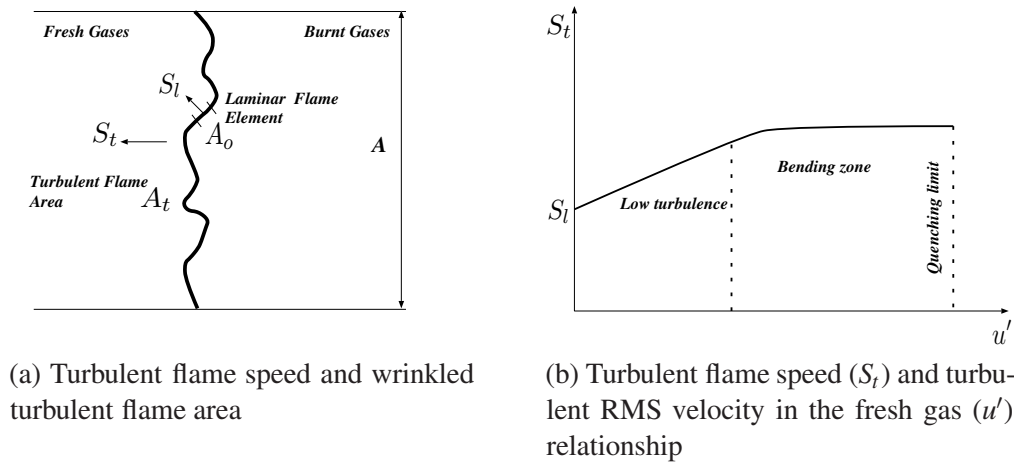


Figure: 2.9 Turbulent premixed flame characteristics

The flame stretch κ is defined as fractional rate of flame surface area change for a laminar flame surface element A_o Eqn: 2.16, and the wrinkling factor Ξ is defined as the ratio of available flame area (A_t) to its projection in the propagating direction (A) as Eqn: 2.17.

$$\kappa = \frac{1}{A_o} \frac{dA_o}{dt} \quad (2.16)$$

$$\Xi = \frac{S_t}{S_l} = \frac{A_t}{A} \quad (2.17)$$

The Eddy Break Up (EBU) model was developed by Spalding [113] which assumed the mixture is only either burnt or unburned state. The mean rate of reaction is expressed as a function of eddy dissipation rate (ϵ), turbulent kinetic energy and the variance of product species concentration. This model assumed high Reynolds number and high Damköhler number flow and a model constant of the order of unity was used according to the problem. Since no additional transport equations for species are solved this model is computationally affordable even for very complicated three-dimensional geometries. Since the original model did not involve any chemical kinetics, later the model was modified to include chemical reactions [114], but this approach increases the computational cost for complex geometrical problems. Following the EBU model, the Eddy Dissipation model (EDC) model was developed by Magnussen [115] to incorporate single-step reaction chemical kinetics and later extended to include finite rate chemistry modelling [116]. However, since both these models were based on the idea that the turbulent motions determine the reaction rate these models over predict the reaction rate in highly strained areas. Therefore, the turbulence model performance and combustion model performance are coupled strongly in this modelling approach thus the near wall predictions become highly sensitive to the turbulence modelling approach.

Bray Moss Libby model [117][118] provided the basis of premixed combustion models based on the flamelet assumption, which assumed burned and fresh mixture are separated by a thin continuous layer. This is a reasonable assumption under moderately distorted flames where the local flame structure remains similar to a laminar flame element. The advantage of assuming the combustion occurs at high Damköhler number limit is that under this condition laminar flamelets preserve the laminar flame structure, therefore allows to mathematically decouple the chemical structure and effect of turbulence. In this model, a reaction progress variable (c) is introduced that monotonically increases from zero in the unburned side to unity in the burnt side, by further assuming incompressible flow assumptions and unity Lewis number and no heat loss. They introduced the concept of calculating transport properties using probability density functions of the progress variable. The physical argument behind this approach is that inside the flame brush properties equals to either unburned state, burned state or the reacting gas. Another advantage of this model is that from the PDF-based calculation method counter-gradient transport of products can be included in the mathematical modelling. However, the Bray-Moss-Libby model assumptions do not close out the mean turbulent reaction rate, flame front crossing frequency at the sampling

point was used to model the reaction rate [119, 120]. Modelling the reaction rate by considering flame crossings presents practical difficulties thus alternative approaches were used to estimate mean reaction rate.

$$c = \frac{T - T_u}{T_b - T_u} = \frac{Y_F - Y_{Fu}}{Y_{Fb} - Y_{Fu}} \quad (2.18)$$

One such way of calculating the mean reaction rate was to use the flame surface area per volume, referred to as Flame Surface Density (FSD denoted by Σ). An algebraic derivation of FSD was provided by Goulding et al. using fractal theories [121] and a balanced equation for the FSD was also used in literature [122] [123]. The algebraic FSD model has been used in modelling of stationary burner flames, and dynamic FSD models also have been used by calculating the wrinkling factor based on resolved flame characteristics [124],[125]. The established FSD modelling approach was initially used in the RANS context, and later Hawkes and Cant [126] extended the modelling method to LES technique using a transport equation for sub-grid FSD. An alternative method to FSD method was proposed by Weller et al. [83], in which a flame wrinkling density function was used along with a transport equation for the perturbed laminar flame speed to account for the flame stretch and curvature effects. Ma et al. compared many FSD models by comparing simulations of three test cases and provided a comprehensive overview of the FSD model performances [127]. Turbulent Flame speed closure uses a transport equation for the reaction progress variable with a chemical source term that is closed using a turbulent flame speed closure model and tested for a gas turbine combustor test case [128]. Their model considered effects of fuel, flame front thickening and distortion, flame quenching by stretch and local preferential species diffusion effects. Flohr and Pitsch [129] extended the Zimont's turbulent flame speed closure model [128] and, proposed a turbulent flame speed closure model. Another approach for modelling premixed flames is to follow the position of the flame which is called the G equation model. Iso-surface defined by the well known G -Equation [130] is considered to represent the flame surface. Although many G -equation formulations were presented previously, a physically consistent formulation of the G equation for both corrugated flamelet zone and thin reaction zones was introduced by Pitsch [131]. This formulation is a level set method based formulation and the equation requires two closure models, which are mathematically complicated to define due to flame propagation velocity relative to flow velocity is difficult to calculate. Such an approach is complicated but considered one of the advanced combustion models [132].

Artificial Thickened Flame (ATF) Model

In this thesis work, the Artificial Thickened Flame model is used for premixed flame modelling with dynamic flame thickening, and the detailed model implementation is described in Section: 3.14. The principal idea behind the method is to multiply the diffusion coefficient by a thickening factor and divide the reaction rate by the thickening factor to maintain the same laminar flame speed yet thicken the laminar flame thickness. Butler and O'Rourke [133] developed the early framework of this model, however in the LES modelling framework this model became more popular because an Arrhenius type equation can be used to represent chemical kinetics of the fuel that is resolvable in an LES grid. Colin et.al [132] introduced the ATF method in LES framework via an efficiency function formulation. They outlined that this model has the advantages of not requiring a Sub-Grid Scale model or ad-hoc sub models to represent combustion phenomena such as ignition, flame stabilisation and flame-wall interactions. Furthermore, this model can extend to detail chemistry analysis, and the artificial thickening method does not alter the flame response to unsteady phenomena. Legier et.al[134] introduced a flame sensor to identify the reaction zone and change the diffusion coefficient only in the region where reactions occur, thus removing the effects of the increased diffusion coefficient on mixing and heat transfer in other areas of the problem domain. Charlette et al. derived another wrinkling factor model that claimed to operate better under weaker turbulence regions [135][136]. In subsequent studies, ATF has been combined with flamelet methods with tabulated chemistry to enhance the turbulence-chemistry interaction of flamelet assumption based models and will be discussed in next sections.

Flamelet Generated Manifolds (FGM)

Chemical reduction techniques can be theoretically developed based on the physical observation of the time scale difference in multi-step chemical reactions, where some reactions are much faster than others. Especially intermediate species generation and destruction or radical formation have small time scales in the order of nanoseconds. Therefore, in most engineering applications these fast chemical reaction time scales can be assumed to have a negligible effect on the total turbulent reaction rate. However, for accurate predictions of chemically reacting flow problems the chemical reaction mechanism should be described sufficiently, therefore reduced chemical mechanisms are introduced with three or four steps. In reduced chemical mechanisms some reactions are assumed to be in partial equilibrium while some others are in steady state [137]. Therefore these reduced chemical kinetic mechanisms have drawbacks such as requiring more pre-processing time to develop such models

for each fuel-oxidizer system, and the above assumptions of partial-equilibrium and steady-state are only valid for some compositions and mixture states. In addition, these multiple step reaction mechanisms can lead to a stiff system of equations and with the increase of the number of reaction steps the solution of this system of equations also become difficult. A comprehensive mathematical review of the status of chemical mechanism reduction techniques available is presented by Guasiss and Mass [138]. In this thesis work, the combustion model Flamelet Generated Manifold (FGM) which is based on the chemical reduction method Intrinsically Lower Dimensional Manifold (ILDM) is used, therefore in this section an overview of that method is provided.

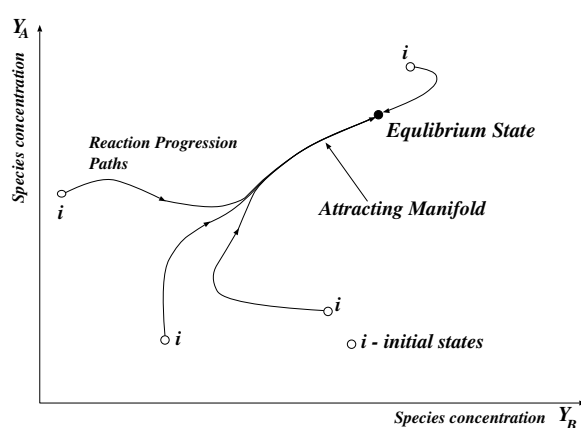


Figure: 2.10 Concept of lower dimensional manifolds

The principle concept of ILDM is explained in Figure: 2.10, where reaction trajectories are shown for a hypothetical homogeneous adiabatic isobaric reaction system with different initial conditions of the two species A and B . If initial compositions had specific element mole numbers, the reaction system reaches unique equilibrium state as shown. It can be seen that for a reaction system as this, reaction paths converge and form an attracting manifold before it reaches the final equilibrium. Therefore for a system with multiple species on a multidimensional state space this attracting manifold represents a low dimensional manifold, therefore referred as the Intrinsic Low-Dimension Manifold (ILDM). Most importantly the reaction system progress along the attracting manifold is governed by slow time scale reactions, and the branches represent fast time scale reactions, therefore instead of solving the complete chemical system, only the lower dimensional manifold can be resolved to obtain the final state of the system with lesser computational resources. Mass and Pope proposed a method of local eigenvalue analysis of the source terms of the chemical system of equations [137]. However, their method is computationally complicated for larger carbon chain fuels and, also at lower temperature mixtures because in these conditions both diffusion, and

convection effects are equally dominant, and this method neglects convection and diffusion effects.

Van Oijen [139] proposed a simpler method by assuming that thermochemical states in a laminar flamelet represent a one dimensional manifold in thermochemical state space. This manifold is parametrized by a number of control variables which varies gradually during the combustion process, and for combustion modelling, the manifold can be used as a tabulated lookup table as a function of these control variables. In their method, 1D flamelet solutions were generated using 1D freely propagating flat flames, and the ability to use available 1D flame solvers is also another advantage over the method of Mass and Pope [137]. These 1D laminar flamelet solutions are parameterized by reaction progress variable in premixed combustion cases, and a linear combination of selected mass fractions or states from the flamelet solution can be used as the progress variable. For an adiabatic premixed flame a single flamelet is sufficient, and for a non-adiabatic flame different flamelet solutions are generated using different initial mixture temperatures; therefore two control variables are used in describing the lower dimensional manifold. For partially premixed flames also this method has been extended with mixture fraction and progress variable are used as control variables [140].

Vreman et al. [141] investigated progress variable based laminar flamelet models performance on both premixed and non-premixed flames. They compared non-premixed flamelet (counterflow) based manifold and a premixed flamelet (free propagating) based manifold for the well known Sandia Flame D, which is a partially premixed flame. A similar ILDM method was used in non-premixed flame modelling using non-premixed flamelets by Pierce and Moin [142] (Section:2.4.2). The laminar flamelets calculated from two approaches showed remarkable differences, especially because the non-premixed manifold did not produce steady flamelet solutions after a certain scalar dissipation rate value that contributed towards a significant portion of the zone where reaction rate was active. Although the premixed manifold also failed to generate a steady flamelet solution below some small mixture fraction value, this did not contribute towards the loss of reaction information in critical regions. Furthermore, in addition to the presumed PDF method to obtain mean quantities over sub-grid scales, using the Artificially Thickened Flame concept only source terms were modified. Their results showed an improvement of predictions by using combined ATF model and premixed flamelet method (Premixed FGM) especially for Sandia Flame F, and the study found that premixed flamelets and non-premixed flamelets produced very similar results below the rich flammability limit. When rich flammability limit was slightly exceeded, minor disparities appeared. In a similar study Kuenne et al. [143] used ATF concept combined with FGM to use tabulated chemistry instead of reduced chemistry for the

ATF method. In their study, they used CO_2 mass fraction as the reaction progress variable. They modelled the Tecflam premixed swirl burner configuration and obtained good agreement with experimental measurements for the velocity field, temperature field and major species mass fractions. Furthermore, their implementation used separate time integration for scalar and velocity to increase the computational efficiency.

Following this combined ATF-FGM method Proch and Kempf [144] also used the same approach to model the Cambridge swirl burner stratified flame series successfully. However they used a different linear combination of species as the reaction progress variable ($Y_{CO_2} + Y_{H_2O} + Y_{CO}$). To model stratified flames they used many 1D free propagating flame solutions with different mixture fractions, with unity Lewis number assumption. Moreover, they used dynamic flame thickening in combination with a smooth transition of thickening factor from the reacting zone to non-reacting zone. The study assumed a top-hat Filter Density Function instead of more commonly used β probability density function distribution for the two control variables, mixture fraction and progress variable. Their work can be considered as the state of the art of LES turbulent premixed/partially premixed modelling approach with flamelet and presumed PDF assumptions. In this thesis work, initial attempts are taken towards a combustion model with combined thickened flame and FGM model where a dynamic thickened flame model is successfully implemented and validated in the OpenFOAM framework. Validation studies of the FGM model implementation by Kroger et al. [145] are performed using both pre-mixed/partially premixed flames.

2.4.2 Turbulent Non-Premixed combustion modelling

When compared to premixed combustion modelling, the non-premixed combustion modelling methods need to address the oxidizer fuel mixing. Therefore, to incorporate the effects of air-fuel mixing, the conserved scalar mixture fraction Z is used. In the most basic non-premixed laminar combustion problem, the computation reduces to find a solution of the mixing problem, and find the *flame structure* $(T(Z,t), Y_k(Z,t))$ as a function of mixture fraction. In turbulence, flame modelling the theoretical developments of laminar flame can be extended in the time-averaged RANS context or spatially averaged LES context, but this introduces unclosed mean reaction rate terms and turbulent scalar flux terms. Similar to premixed combustion models the principal problem of turbulent non-premixed combustion modelling is also the means of calculating mean reaction rate. The turbulent flame structure can be expressed as conditional expressions of mixture fraction (Z) as $(Y_k||Z^*), (\dot{\omega}_k||Z^*), (T||Z^*)$, because the laminar flamelet relationships (laminar flame structure is a function of Z) do not strictly convert into turbulent flame structures. This conditional notation $(T||Z^*)$ is used because, in addition to mixture fraction Z , many other

turbulent parameters influence the turbulent flame structure, such as its higher order statistics of the mixture fraction and nonequilibrium parameters like the scalar dissipation rate.

The non-premixed combustion modelling approaches can be categorized into two categories according to the way how these conditional relationships are sought. In the primitive variable approach the turbulent flame structure $(\overline{Y_k||Z^*}), (\overline{T_k||Z^*})$ is sought after. The well known Steady Laminar Flamelet Method (SLFM) and Conditional Momentum Closure (CMC) models fall into the primitive variable modelling approach. In CMC method a balanced equation for conditional mass fraction $(\overline{Y_k||Z^*})$ corresponding to the mean mass fraction of each species is developed and solved [146][147]. There are several advantages of this method because conditional mass fractions can be measured, and combustion phenomena such as ignition and diffusion flame surface can be easily identified as an iso-surface of mixture fraction [148]. However, additional transport equations for each species and closure values makes this method computationally very expensive, therefore in this thesis work, such methods are not employed. In contrast, the reaction rate modelling approach resolves balance equations for species mass fractions and temperature equations, thus the mean reaction rates for species $(\overline{\omega_k})$ are modelled, and the conditional relationship $(\overline{\omega_k||Z^*})$ is used to close the mean reaction rates. The reaction rate modelling approach has the advantage of including compressibility and non-adiabatic effects easily into the model, but the primitive variable methods are significantly computationally more efficient because species transport equations are not solved. Eddy Dissipation Concept (EDC) models, Eddy Break-Up (EBU) models can be understood as simplest models of infinite rate chemical reactions based modelling methods of this approach. However, in this thesis, only SLFM method is used for non-premixed flame modelling due to better compromise between computational efficiency and detail chemical analysis.

In the flamelet assumption, it is assumed that the turbulent flame structure can be locally one-dimensional thus a function of only mixture fraction and time. To conform with this assumption flame must be very thin compared to the turbulence eddy scales. These local flame structures are assumed to be similar to a laminar flame structure thus named laminar flamelets. The existence of such flame elements has been experimentally confirmed [149],[150]. In the infinitely fast chemistry limit, conditional averages can be approximated as,

$$\begin{aligned} \overline{Y_k||Z^*} &= \rho(Z^*)Y_k(Z^*) \\ \overline{T_k||Z^*} &= \rho(Z^*)T(Z^*) \end{aligned} \tag{2.19}$$

To calculate the averaged species and temperatures the Probability Density Function (PDF) of the mixture fraction ($p(Z^*)$) is used as,

$$\begin{aligned}\bar{\rho}\tilde{Y}_k &= \int_0^1 \rho(Z^*)Y_k(z^*)p(Z^*)dz^* \\ \bar{\rho}\tilde{T} &= \int_0^1 \rho(Z^*)T(z^*)p(Z^*)dz^*\end{aligned}\tag{2.20}$$

Therefore, the flame structure calculation reduces to a determination of mixture fraction PDF, and in the approach used in this thesis, probability density functions are assumed. It is known that the infinitely fast chemistry of equilibrium assumption is far from realistic in practical combustion devices with conventional hydrocarbon fuels, therefore in addition to the chemistry independent conserved scalar (mixture fraction), another parameter is required to represent the non-equilibrium effects. Peters[151] introduced the stoichiometric scalar dissipation rate χ_{st} as the non-equilibrium parameter, and his work is considered as the start of Steady Laminar Flamelet Method (SLFM). In SLFM method the turbulent flame structures $\tilde{T}(Z, \chi_{st}), \tilde{Y}_k(Z, \chi_{st})$ are calculated using pre-calculated steady one dimensional flame structures, and then integrating assuming PDF distributions of Z and χ as,

$$\begin{aligned}\bar{\rho}\tilde{Y}_k &= \int_0^\infty \int_0^1 \rho Y_k(Z, \chi_{st}) dZ d\chi_{st} \\ \bar{\rho}\tilde{T} &= \int_0^\infty \int_0^1 \rho T(Z, \chi_{st}) dZ d\chi_{st}\end{aligned}\tag{2.21}$$

The implementation of SLFM method is described in detail in Section:3.12.2

The first record of SLFM method successfully applied for turbulent non-premixed jet flames is by Liew et al. [152], in which he predicted reasonable agreement in CH_4, CO, T predictions using RANS turbulence modelling. However, in contrast to Peter's suggestion to use χ_{st} , Liew et al. had used χ_{max} as the non-equilibrium parameter. Nevertheless, when compared to experimental data, the numerical simulation showed residual O_2 on the flame axis. This was understood to have caused from the local quenching as evident by high scalar dissipation rates, thus allowing the O_2 to travel through the stoichiometric surface without reacting. Lentini [153] tested three jet flame test cases, a Syngas-air flame, and two methane-air flames were tested using multiple laminar flamelets and showed improved results compared to Liew et.al.

Furthermore, many numerical simulation tests have been conducted under RANS turbulence modelling paradigm, and SLFM method and local flame stretch caused extinction were not accurately represented sufficiently by these modelling approaches [154]. Varnos et al. [155] used SLFM method in NO modelling context for a methane-hydrogen jet flame,

and their results showed significant discrepancies between numerical predictions and experimental measurements. Similar results were reported by other researchers [156][157], and Chen and Chang [158] also conducted studies on *NO* production and found that radiative heat loss needed to be addressed especially downstream of the jet flame. Based on the enthalpy defect concept of Bray and Peters [159] a non-adiabatic flamelet model was developed by Marracino and Lentini [160] that used a flamelet library parameterized by enthalpy defect (the difference between adiabatic and actual enthalpy). This model was used in modelling turbulent jet flames and showed improved performance in *NO* predictions [161][162]. Following the studies of Haworth et al. [163] that showed the importance of time dependency of the laminar flamelet equations, Ferreira [154] developed a transient laminar flamelet model that used a complex flamelet library which was parameterised using two additional variables, reaction progress variable and a flamelet residence timescale. Pitsch et al. [164] developed an unsteady SLFM model and studied a hydrogen flame and observed inclusion of radiation effects improve the mean *NO* prediction.

Cook and Riley [165] carried out the first SLFM simulations in LES context, where they used a presumed β Probability Density Function (PDF) formulation of the mixture fraction. They used scale similarity assumption to obtain mixture fraction variance. Based on their approach many other researchers have conducted SLFM simulations under LES context with different PDF shapes [166] and solving transport equations for mixture fraction [167]. Pierce and Moin [168] proposed a dynamic model to calculate the mixture fraction variance and scalar dissipation rate instead of previous algebraic models and tested with LES of swirling jet flames and confined coaxial jet flames and reported good agreement with experimental measurements. An LES study of a methane-air jet flame was conducted by Kempf et al. [169] using a flamelet library compiled from detail chemistry analysis and showed that SLFM results agreed sufficiently with experimental measurements except for *CO* prediction which was overpredicted in the fuel rich zone.

Pierce and Moin [142] developed a non-premixed combustion model, especially for LES context using the flamelet assumptions, namely Flamelet Progress Variable method (FPV). Instead of using scalar dissipation rate to represent the non-equilibrium chemistry in this method they used a reaction progress variable (a linear combination of species mass fraction) to parametrise the laminar flamelets, and this method is known as Flamelet Progress Variable (FPV) method. In this method an additional transport equation for progress variable is solved instead of an algebraic approach to calculating the scalar dissipation rate, hence computational overload increases slightly with this method because for the progress variable source term a runtime look-up procedure is required. Preintegrated look-up table is used to look up the progress variable source term. They claimed this method has the advantage

of capturing local flame extinction and reignition phase of the flamelet. They modelled a dump combustor geometry for their modelling and showed improved predictions when compared to SLFM method in the flame stabilisation region. Ample experimental evidence has been found showing the differential diffusion of H_2 and other species near jet nozzle in low Reynolds number and high Reynolds number flames. Therefore Pitsch [170] extended SLFM model to include differential diffusion of species and obtained good agreement with experimental data. However, in this thesis work, only steady adiabatic laminar flamelet modelling approach is used.

In this thesis work the Sydney swirl burner is studied using LES and SLFM methods, and two previous studies on this particular burner are reported in Ranga-Dinesh et al. [171], Kempf et al. [172]. Ranga-Dinesh et al. [171] performed SLFM calculations of SMH1 flame which was a swirl flame with swirl number $S = 0.42$ using a single flamelet solution that fitted the turbulent flame structure on average. GRI 2.11 mechanism was used to calculate the single flamelet solution at $\chi = 500s^{-1}$. Their mean velocity field and RMS values of velocity components showed reasonable agreement with experimental data at most locations. Furthermore, their results showed slight underprediction of mixture fraction, and they attributed this to the velocity prediction discrepancies near the recirculation zone. Although, there were numerical discrepancies in temperature and species predictions as CO_2 and CO , predicted scalar patterns followed the experimental observations. Then in the study of Kempf et al. [172], comparisons of two studies of SLFM approaches by the Imperial College research group (IC) and the Loughborough University research group (LU) were presented for the Sydney burner flame series (non-swirl - SM1, swirl - SMH1, SMH2). In this research two groups used different solvers and different approaches in the calculation of scalar dissipation rate. LU group used a single flamelet approach which was calculated using GRI 2.11 mechanism while IC group used Lindstedt and Sick et al. [173] mechanism. Moreover, LU group used a Cartesian coordinate system whereas IC group used a cylindrical computational domain which suited well with the annular inlet profiles of the computational geometry. There were significant differences between the two computational codes used as well. Authors have reported that swirl burner flames were harder to simulate when compared with the non-swirl test case and this was predominantly due to complex vortex structures in swirl flame and the high velocity associated with the jet flow. However, simulations of both groups showed similar results, while velocity field was predicted to be with good agreement in experimental data, scalar predictions showed discrepancies.

2.5 Chapter Summary

In this chapter, the previous studies on the effects of air-fuel mixing on gas turbine combustion performance were introduced first. Many studies have shown that spatial and temporal fluctuations of air-fuel mixing quality have an adverse effect on the production of NO_x emissions. The Jet In Cross-Flow (JICF) arrangement, which is a widely used technique in gas turbine air-fuel mixing is selected as the analytical problem investigated in this thesis. Previous experimental and numerical simulation studies of JICF were introduced in this Chapter, and it can be seen that most of these studies have been more focused on the investigation of flow features rather than the scalar mixing in this arrangement. In numerical modelling of this problem Large Eddy Simulation technique has been used in literature with successful results in the prediction of the velocity field. These LES modelling efforts have been performed mostly with a single Sub-Grid Scale model with a user-specified model constant; therefore an opportunity to investigate the SGS stress models using dynamic models that is independent of user-specified model constant is identified. DNS studies have been performed for very low Reynolds number JICF arrangements and even using these data there has not been a conclusive mechanism for the formation of counter-rotating vortex pair. Most of the previous studies have been focused on a single jet in cross-flow studies only, and there is a need for more studies on multiple jets in cross-flow interactions and jet in cross-flows with a swirl flow component is also important in understanding the air-fuel mixing in a gas turbine pre-mixer. Therefore, in this thesis numerical modelling of a single jet in a cross-flow test case is extended to a side by side twin jets in a cross-flow arrangement. Turbulent mixing modelling methods were also discussed in this Chapter, and the shortcomings of the more commonly used turbulent scalar flux closure method were addressed. Although there are complex turbulent scalar flux closure methods, these methods require more careful validation using homogeneous turbulence tests before applying for an inhomogeneous turbulent flow problem like JICF, therefore in this thesis, the constant Schmidt number and gradient diffusion hypothesis based approach is used for the jet in cross-flow mixing modelling.

Different flame types and flame stabilisation methods used in gas turbine combustion chamber were discussed in this Chapter. Recirculation of the high-temperature products are used as a means to stabilise the flame and computational modelling of toroidal flow reversal using RANS methods have not resulted in good results. Therefore LES method is used in recent endeavours to model swirl stabilised flames. There has been increased attention to use Hydrogen as a gas turbine fuel as a means of flame stabilisation and energy storage method from renewable energy sources. Numerical model development in the modelling of hydrogen blended fuel combustion has not been explored extensively by considering the special attributes of Hydrogen, but instead, the existing combustion models are being used in

the CFD community to model hydrogen blended fuels. Therefore, the ability of established non-premixed combustion modelling techniques based on laminar flamelet assumptions is investigated in this thesis. In the literature review, non-premixed combustion models are reviewed but focused more on the steady laminar flamelet method due to the computational simplicity and the ability to incorporate chemical kinetics and chemical nonequilibrium dynamics. In the most advanced laminar flamelet method based models the turbulence effects on the flame structure are explicitly calculated via a transported probability density function method; however, this method is computationally still expensive. The presumed probability steady laminar flamelet based methods are computationally affordable for computations with complex flows, and the literature review showed that to capture the swirling flow features LES can be used, and this method will be used in the modelling of Sydney swirl burner with Hydrogen and Methane based fuel.

Premixed/Partially-Premixed combustion modelling methods and difficulties of obtaining the accurate turbulent flame speeds and increased reaction rates as a result of increased turbulence were discussed in this Chapter. In premixed combustion modelling the use of reaction progress variable approach is the simpler and more commonly used method and in this thesis work the artificially thickened flame model is used in conjunction with a progress variable equation. Although the artificially thickened flame method has the advantage of resolving the chemical source terms explicitly, the inclusion of complex chemical mechanisms is computationally expensive. However, to use the artificially thickened flame model in partially premixed flames, another constitutive equation will be required to express the mixing process and reaction. Therefore, the flamelet generated manifold method which incorporates a chemical reduction method in combination with a progress variable equation and optional mixture fraction transport equation will be explored in modelling of premixed and partially-premixed stratified flames in Chapter 7.

Chapter 3

Governing Equations

This chapter provides an overview of the mathematical formulation of the governing equations and discusses the assumptions that are used in this thesis work. Both chemically reacting and non-reacting turbulent flows are numerically simulated in this thesis work. Only the governing equations are introduced in this chapter because solution methods are extensively discussed in general Finite Volume Method (FVM) based literature [174, 175]. Governing equations for turbulent non-reacting flows are introduced firstly and modelling chemically reacting flows are explained later.

3.1 Basic Flow Equations

The physical problems addressed in this thesis involves only gaseous phase; hence the working fluid is assumed to be a single phase continuum. In non-reacting flow problems the flow incompressibility is assumed, and for both reacting and non-reacting flows the fluid is assumed to behave as a Newtonian fluid. By following Reynold's Transport theorem for any fluid property Φ , a general transport equation for the intensive property $\phi = \Phi/\rho$ can be derived for a control volume CV with a control surface CS and a control mass CM as,

$$\left(\frac{d\Phi}{dt}\right)_{CM} = \int_{CV} \frac{\partial}{\partial t}(\rho\phi) + \int_{CS} \phi\rho V \cdot n ds \quad (3.1)$$

V, n are the velocity vector, and surface normal vector, and ρ is the fluid density in usual notation. The mass conservation equation for a control volume can be derived in Cartesian coordinates as Eqn: 3.2 by combining the mass conservation law and Reynolds transport theorem for the mass flux.

$$\frac{\partial \rho}{\partial t} + \frac{\partial}{\partial x_j}(\rho u_j) = 0 \quad (3.2)$$

The linear momentum transport equation for the i^{th} momentum component can be written in Cartesian coordinate format as Eqn: 3.3 where f_b denotes the body force per control volume. In this thesis work gravity force and Coriolis forces acting on a control volume mass are neglected.

$$\frac{\partial}{\partial t}(\rho u_i) + \frac{\partial}{\partial x_j}(\rho u_i u_j) = -\frac{\partial p}{\partial x_j} + \mu \frac{\partial^2 u_i}{\partial x_i x_j} + f_b \quad (3.3)$$

In addition, for any scalar ϕ the transport equation can be written as,

$$\frac{\partial \phi}{\partial t} + \frac{\partial}{\partial x_j}(\rho u_j \phi) = \frac{\partial}{\partial x_j} \left(\Gamma \frac{\partial \phi}{\partial x_j} \right) + S_\phi \quad (3.4)$$

where S_ϕ is the source term.

3.2 Turbulence modelling

Three main turbulence flow modelling methods are in current practice; namely Direct Numerical Simulations (DNS), Large Eddy Simulations (LES) and Reynolds Averaged Navier Stokes (RANS). From these three methods the DNS method provides the most accurate representation of the turbulence field by resolving the non-linear governing equations to the smallest resolvable length scales (*Kolmogorov length scale*) and timescales. For DNS method the spatial resolution required is of the order $N^3 \simeq Re^{9/4}$ and similar temporal resolution is also required. Therefore spatial and temporal resolution requirements for DNS method is still beyond available computational resources. The LES method resolves the anisotropic and geometric dependent flow structures while mathematically isotropic and smaller eddies are modelled. RANS method models the whole turbulent energy spectrum by time averaging, therefore, requires comparatively less computational resources than both LES and DNS methods. However, for industrial applications and collaborative research work, Reynolds Averaged Navier Stokes (RANS) simulations are still used even if the whole turbulence energy spectrum is modelled by the same universal modelling approach. RANS methods have the advantage of the lower demand for computational resources and fewer results for post-processing when compared with the LES method. Therefore, in this thesis, both RANS and LES methods were employed for numerical modelling work, but more emphasis is made on the LES method.

3.2.1 RANS Turbulence models

In this section, the RANS models used in this thesis are introduced. RANS models are predominantly used in non-reacting flow modelling hence flow incompressibility is assumed in this context. Turbulent flows are considered to have a mean flow characteristic and a fluctuating nature as well. Therefore turbulent flows are neither structured nor completely random. This analogy leads to the well known Reynolds decomposition where any turbulence quantity ϕ can be decomposed into a time mean component $\bar{\phi}$ and a fluctuating component ϕ' as $\phi = \bar{\phi} + \phi'$, with the property $\overline{\phi'} = 0$. Reynolds decomposed values of velocity, and any scalar can be used in the same transport equations discussed in Section: 3.1, that leads to the incompressible RANS equations as Eqn 3.5 where $\bar{u}, \bar{\phi}$ are time mean quantities.

$$\begin{aligned} \frac{\partial \bar{u}_i}{\partial x_i} &= 0 \\ \frac{\partial \bar{u}_i}{\partial t} + \frac{\partial}{\partial x_j} (\bar{u}_i \bar{u}_j) &= -\frac{1}{\rho} \frac{\partial \bar{p}}{\partial x} + \frac{\partial}{\partial x_j} \left(\nu \frac{\partial \bar{u}_i}{\partial x_j} \right) + \left[\frac{\partial (-\overline{u'_i u'_j})}{\partial x_j} \right] \\ \frac{\partial \bar{\phi}}{\partial t} + \frac{\partial (\bar{\phi} \bar{u}_j)}{\partial x_j} &= \frac{1}{\rho} \frac{\partial}{\partial x_j} \left(\Gamma_\phi \frac{\partial \bar{\phi}}{\partial x_j} \right) + \left[\frac{\partial (-\overline{u'_i \phi'})}{\partial x_j} \right] \end{aligned} \quad (3.5)$$

When compared to the transport equations of instantaneous quantities, RANS equations include additional second order fluctuating terms $\overline{u'_i u'_j}$ and $\overline{\phi' u'_i}$, which are known as Reynolds stress tensor (τ_{ij}) and turbulent scalar flux term. The Reynolds stress tensor and turbulent scalar flux terms require closure to solve the systems of equations. Reynolds stress components are closed using the Boussinesq hypothesis, which assumes that Reynolds stresses are proportional to the mean rate of flow strain S_{ij} , and effects of eddies are considered isotropic. Further by introducing the eddy viscosity (μ_t) via the assumption that turbulent Reynolds stresses show Newtonian fluid-like behaviour, the problem of calculating Reynolds stress reduces to the calculation of eddy viscosity and turbulent kinetic energy k .

$$\begin{aligned} \tau_{ij} &= -\rho \overline{u'_i u'_j} = \mu_t \left(\frac{\partial \bar{u}_i}{\partial x_j} + \frac{\partial \bar{u}_j}{\partial x_i} \right) - \frac{2}{3} \rho k \delta_{ij} \\ \tau_{ij} &= 2\mu_t S_{ij} - \frac{2}{3} \rho k \delta_{ij} \\ S_{ij} &= \frac{1}{2} \left(\frac{\partial \bar{u}_i}{\partial x_j} + \frac{\partial \bar{u}_j}{\partial x_i} \right) \end{aligned} \quad (3.6)$$

3.2.2 Eddy viscosity models

The concept of eddy viscosity (turbulent viscosity) was first introduced by Ludwig Prandtl in his studies [176], in which it was hypothesised that eddy viscosity can be expressed using the product of turbulent length scale (l_t) and turbulent velocity scale ($u_t \sim \sqrt{k}$) and a dimensionless model coefficient (C) as,

$$v_t = Cl_t \times u_t = Cl_t \sqrt{k} \quad (3.7)$$

In the most simple eddy viscosity model, velocity scale is calculated using the mean velocity gradient, and such models are known as zero-equation models, these models provide a reasonable agreement for canonical flow arrangements.

In one-equation models of Spalart's [177] and Baldwin-Barth model [178] a single transport equation is solved to compute eddy viscosity. These models are not in mainstream turbulence modelling practice and limited to specific flow problems. It is intuitive to use a transport equation for the turbulent kinetic energy which is a representation of the velocity fluctuations to determine a turbulent velocity scale, Eqn: 3.8.

$$k = \frac{1}{2} \overline{u'_i u'_i}$$

$$\frac{\partial \rho k}{\partial t} + \frac{\partial (\rho k \bar{u}_j)}{\partial x_j} = \frac{\partial}{\partial x_j} \left(\mu \frac{\partial k}{\partial x_j} \right) - \frac{\partial}{\partial x_j} \left(\frac{\rho}{2} \overline{u'_j u'_i u'_i} + \overline{p' u'_j} \right) - \rho \overline{u'_i u'_j} \frac{\partial \bar{u}_i}{\partial x_j} - \mu \left(\frac{\partial u'_i}{\partial x_j} \frac{\partial u'_i}{\partial x_j} \right) \quad (3.8)$$

The sink term $\mu \left(\frac{\partial u'_i}{\partial x_j} \frac{\partial u'_i}{\partial x_j} \right)$ of the equation Eqn: 3.8 represents the dissipation of turbulent energy into internal energy, and in the class of two-equation RANS models this sink term is modelled by using another transport equation. Two-equation models which employ two transport equations for solving eddy viscosity have been established as the prominent method of turbulence modelling in industrial problems due to computational efficiency and the well-established practices. Reynolds Stress Transport (RST) models are based on direct closure of all second order fluctuating terms (Reynolds stress terms), hence involves six additional transport equations, and there are different approaches of modelling Reynolds stress tensor resulting different RST models. RST models have shown promising results without using the eddy viscosity assumptions for certain problems like swirl flows and shown poor results for some. Therefore much academic interest has been drawn towards RST models. Such turbulence models have proven computationally expensive and difficult to solve due to the numerical stiffness of additional transport equations. The use of RST models in in-

dustrial applications has been very limited when compared with two-equation models. The two-equation models namely the Realizable $k - \varepsilon$ model, $k - \omega - SST$ model, and the RST model proposed by Gibson-Lauder [179] are used in this thesis for JICF modelling work to understand the model performance in modelling such three-dimensional turbulence flow fields.

3.2.3 Realizable $k - \varepsilon$ model

The standard $k - \varepsilon$ model of Launder and Spalding [180] used two transport equations for turbulent kinetic energy and turbulent kinetic energy dissipation rate (ε). The definition of turbulent kinetic energy dissipation was derived from fluctuating deformation rates s'_{ij} , hence the turbulent kinetic energy dissipation term of Eqn: 3.8 is modelled as,

$$\varepsilon = 2\nu \overline{s'_{ij} s'_{ij}} = 2\nu \left(\mu \left(\frac{\partial u'_i}{\partial x_j} \frac{\partial u'_i}{\partial x_j} \right) \right) \quad (3.9)$$

In addition, the turbulent diffusion term of Eqn: 3.8 is also modelled using gradient diffusion hypothesis as,

$$- \left(\frac{\rho}{2} \overline{u'_j u'_i u'_i} + \overline{p' u'_j} \right) \approx \frac{\mu_t}{\sigma_k} \frac{\partial k}{\partial x_j} \quad (3.10)$$

and the rate of turbulent kinetic energy production term (P_k) is modelled as,

$$P_k = - \overline{\rho u'_i u'_j} \frac{\partial \bar{u}_i}{\partial x_j} \approx \mu_t \left(\frac{\partial \bar{u}_i}{\partial x_j} + \frac{\partial \bar{u}_j}{\partial x_i} \right) \frac{\partial \bar{u}_i}{\partial x_j} \quad (3.11)$$

Therefore, once the turbulent kinetic energy (k) transport equation and turbulent energy dissipation (ε) equations are solved, the eddy viscosity is calculated using the relationship,

$$\nu_t = C_\mu \frac{k^2}{\varepsilon} \quad (3.12)$$

Although the standard $k - \varepsilon$ model has been widely used in many turbulence flow problems, it has shown anomalies in the prediction of planar and circular jet spread rates due to inaccurate length scales predicted by ε equation [181]. Also flows with high mean shear strains and separation have shown poor performances due to overprediction of eddy viscosity [182]. The standard $k - \varepsilon$ model fails to assure the positivity of normal Reynolds stress components and Schwarz's inequality ($\overline{u_i u_j^2} \leq \overline{u_i^2 u_j^2}$) for Reynolds shear stress components at larger mean strain rates ($Sk/\varepsilon > 3.7, S = \sqrt{2S_{ij} S_{ij}}$). Therefore, Shih et al. [182] attempted to derive a new ε equation from vorticity fluctuations and related the global model constant C_μ to the local strain rate. Realizable $k - \varepsilon$ formulation ensures positivity of nor-

mal Reynolds stress components and satisfies the Schwarz's inequality for Reynolds shear stress components. Hence the realizability of Reynolds stress tensor is conserved. Turbulent kinetic energy equation used in the standard $k - \varepsilon$ model is used without any modifications in the realizable $k - \varepsilon$ model Eqn: 3.13.

$$\frac{\partial \rho k}{\partial t} + \frac{\partial(\rho k \bar{u}_j)}{\partial x_j} = \frac{\partial}{\partial x_j} \left[\left(\mu + \frac{\mu_t}{\sigma_k} \right) \frac{\partial k}{\partial x_j} \right] + 2\mu_t S_{ij} \cdot S_{ij} - \rho \varepsilon \quad (3.13)$$

ε is calculated from the transport equation Eqn: 3.14,

$$\frac{\partial \rho \varepsilon}{\partial t} + \frac{\partial(\rho \varepsilon \bar{u}_j)}{\partial x_j} = \frac{\partial}{\partial x_j} \left[\left(\mu + \frac{\mu_t}{\sigma_\varepsilon} \right) \frac{\partial \varepsilon}{\partial x_j} \right] + \rho C_1 S \varepsilon - \rho C_2 \frac{\varepsilon^2}{k + \sqrt{\nu \varepsilon}} \quad (3.14)$$

$$\begin{aligned} \mu_t &= \rho C_\mu \frac{k^2}{\varepsilon} \\ C_\mu &= \frac{1}{A_0 + A_s \frac{k U^*}{\varepsilon}} \\ U^* &= \sqrt{S_{ij} S_{ij} + \tilde{\Omega}_{ij} \tilde{\Omega}_{ij}} \end{aligned} \quad (3.15)$$

$$A_s = \sqrt{6 \cos \phi} \quad \phi = \frac{1}{3} \cos^{-1}(\sqrt{6}W) \quad W = \frac{S_{ij} S_{jk} S_{ki}}{\tilde{S}^3} \quad \tilde{S} = \sqrt{S_{ij} S_{ij}}$$

$$\tilde{\Omega}_{ij} = \Omega_{ij} - 2\varepsilon_{ijk} \omega_k \quad \Omega_{ij} = \overline{\Omega_{ij}} - \varepsilon_{ijk} \omega_k$$

$\overline{\Omega_{ij}}$ is the mean rate of rotation tensor viewed in a rotating reference frame with the angular velocity ω_k . Model constants are implemented as,

$$A_0 = 4.0, \quad C_1 = \max\left(0.43, \frac{\eta}{5 + \eta}\right), \quad \eta = S \frac{k}{\varepsilon}, \quad C_2 = 1.9, \quad \sigma_k = 1.0, \quad \sigma_\varepsilon = 1.2$$

3.2.4 $k - \omega$ -Shear Stress Transport model

$k - \varepsilon$ models have shown better performance in modelling free shear flows, but have shown poor performance in modelling adverse pressure gradient flows. To improve the eddy viscosity hypothesis based model performance near shear stress dominated flows, Wilcox used turbulence dissipation frequency ($\omega = \varepsilon/k$) to estimate the turbulent length scale as $l_t \sim \sqrt{k}/\omega$ [183][184]. The Wilcox $k - \omega$ model solves a transport equation for ω . Therefore this model is also a two-equation model. Additionally, the $k - \omega$ model can be used without a wall-damping function to integrate through the viscous sub-layer and shows more robustness under weak adverse pressure gradients. However, this model has shown sensitivity to

the free stream value of ω . Therefore, model performance depended on the imposed boundary conditions [185]. Menter combined the $k - \varepsilon$ and $k - \omega$ models to obtain the effects of respective advantages of each model [186], by multiplying the $k - \omega$ equation with a blending function $F1$ and the transformed $k - \varepsilon$ model by $1 - F1$. The objective of this blending was to obtain $k - \omega$ model behaviour near walls and $k - \varepsilon$ behaviour away from the walls, and this model was named the Baseline Model. Then following the baseline model the $k - \omega$ -Shear Stress Transport ($k - \omega$ -SST) model was proposed which showed significant improvements in modelling adverse pressure gradient flows [187]. In this new model, two modifications were made to the baseline $k - \omega$ model. The $k - \omega - SST$ model satisfies Bradshaw's assumption [188], which states that the principal wall shear stress follows a linear relationship with boundary layer kinetic energy,

$$\tau_{xy} \propto k = \rho a_1 k \quad (3.16)$$

. However in adverse pressure gradient flows where turbulent production and wake regions turbulent kinetic energy production is much greater than dissipation this assumption is violated. Therefore for the $k - \omega$ -SST model to satisfy the Bradshaw's assumption, a modification to the turbulent viscosity calculation is introduced as,

$$\mu_t = \frac{\rho a_1 k}{\max(a_1 \omega, \sqrt{2S_{ij}S_{ij}F2})} \quad (3.17)$$

where $a_1 = 0.31$. Secondly, the turbulent kinetic energy production term P_k is modified as

$$P_k = \min(P_k, c_1 \beta^* k \omega) \quad (3.18)$$

The transport equations for k and ω are as Eqn: 3.19 Eqn: 3.20

$$\frac{\partial \rho k}{\partial t} + \frac{\partial(\rho \bar{u}_j k)}{\partial x_j} = \frac{\partial}{\partial x_j} \left(\mu_{eff,k} \frac{\partial k}{\partial x_j} \right) + P_k - \beta^* \rho k \omega \quad (3.19)$$

$$\frac{\partial \rho \omega}{\partial t} + \frac{\partial(\rho \bar{u}_j \omega)}{\partial x_j} = \frac{\partial}{\partial x_j} \left(\mu_{eff,\omega} \frac{\partial \omega}{\partial x_j} \right) + C_\alpha \frac{\omega}{k} P_k - C_\beta \rho \omega^2 + 2(1 - F1) \sigma_{\omega,2} \frac{\rho}{\omega} \frac{\partial k}{\partial x_i} \frac{\partial \omega}{\partial x_i} \quad (3.20)$$

$$\mu_{eff,k} = \mu + \frac{\mu_t}{\sigma_k}$$

$$\mu_{eff,\omega} = \mu + \frac{\mu_t}{\sigma_\omega}$$

The blending function $F1$,

$$F1 = \tanh(\gamma_1^4)$$

$$\gamma_1 = \min \left[\max \left(\frac{\sqrt{k}}{\beta^* \omega y_c}, \frac{500\nu}{y_c^2 \omega} \right), \frac{4\rho\sigma_{\omega,2}k}{CD_{k\omega}^2} \right] \quad (3.21)$$

The cross diffusion term ($CD_{k\omega}$) in the blending function is modelled as,

$$CD_{k\omega} = \max \left(\left(2\rho\sigma_{\omega,2} \frac{1}{\omega} \frac{\partial k}{\partial x_j} \cdot \frac{\partial \omega}{\partial x_j} \right), 10^{-10} \right)$$

The function $F2$ is modelled as,

$$F2 = \tanh(\gamma_2^2)$$

$$\gamma_2 = \max \left(\frac{2\sqrt{k}}{\beta^* \omega y_c}, \frac{500\nu}{y_c^2 \omega} \right) \quad (3.22)$$

Model coefficients (C) are calculated using a blending function in the form, $C = C_1 F1 + C_2(1 - F1)$.

$$C_{\alpha 1} = 0.5532, C_{\beta 1} = 0.075, \sigma_{k1} = 2, \sigma_{\omega 1} = 2$$

$$C_{\alpha 2} = 0.4403, C_{\beta 2} = 0.0828, \sigma_{k2} = 1, \sigma_{\omega 2} = 1.186 \quad (3.23)$$

$$\beta^* = 0.09, c1 = 10$$

y_c is the nearest distance from cell to the nearest wall.

3.2.5 Launder-Gibson Reynolds Stress Transport model

Instead of using Boussinesq hypothesis for Reynolds stress closure, each Reynolds stress component can be solved using a transport equation. In addition, a transport equation for the turbulence dissipation rate (ε) is also solved, hence increasing the computational cost than other RANS models. In this work, the RST model implementation by Launder-Gibson [179] is used, and in this model, the eddy viscosity is expressed as,

$$\nu_t = C_\mu \frac{k^2}{\varepsilon} \quad (3.24)$$

Transport equation for Reynolds stress tensor $\tau_{ij} = \overline{u_i u_j}$ is as,

$$\begin{aligned} \frac{\partial \rho \tau_{ij}}{\partial t} + \frac{\partial}{\partial x_k} (\rho \tau_{ij} \bar{u}_k) &= D_t + D_m - P_{ij} + \phi_{ij} - \varepsilon_{ij} \\ P_{ij} &= \left(\overline{\rho u'_i u'_k} \frac{\partial U_j}{\partial x_k} + \overline{\rho u'_j u'_k} \frac{\partial U_i}{\partial x_k} \right) \\ D_t &= -\frac{\partial}{\partial x_k} \left(\overline{\rho u'_i u'_j u'_k} + p (\delta_{ij} u'_i + \delta_{ik} u'_j u'_k) \right) \\ D_m &= \frac{\partial}{\partial x_k} \left(\mu \frac{\partial}{\partial x_k} (\overline{u'_i u'_j}) \right) \\ \phi_{ij} &= p' \left(\frac{\partial u'_i}{\partial x_j} + \frac{\partial u'_j}{\partial x_i} \right) \\ \varepsilon_{ij} &= 2\mu \frac{\partial u'_i}{\partial x_j} \frac{\partial u'_k}{\partial x_k} \end{aligned} \quad (3.25)$$

In contrast to other two-equation models, the production term P_{ij} does not need modelling in this approach. Contribution of turbulent diffusion transport of Reynolds stress was modelled as,

$$D_t = C_1 \frac{\partial}{\partial x_k} \left(\rho \frac{\overline{k u'_k u'_l}}{\varepsilon} \frac{\partial \overline{u'_i u'_j}}{\partial x_l} \right); C_1 = 0.22 \quad (3.26)$$

The pressure strain term ϕ_{ij} is modelled by linear approximation, hence this method is known as Linear Pressure-Strain model as well. The pressure strain is further linearly decomposed into slow pressure strain (ϕ_{ij}^s), rapid pressure strain (ϕ_{ij}^r) and wall reflection term (ϕ_{ij}^w). In Eqn. 3.27 the decomposed pressure strain terms modelling is shown (n_k is the k component of the wall normal unit vector and the coefficient f is calculated as a function of

the normal distance to the nearest distance y_c).

$$\begin{aligned}
 \phi_{ij} &= \phi_{ij}^s + \phi_{ij}^r + \phi_{ij}^w \\
 \phi_{ij}^s &= -C_s \rho \frac{\varepsilon}{k} \left(\overline{u'_i u'_j} - \frac{2}{3} \delta_{ij} k \right), \quad C_s = 1.8 \\
 \phi_{ij}^r &= -C_r \left[\left(P_{ij} - \frac{1}{3} \delta_{ij} P_{kk} \right) \right], \quad C_r = 0.6 \\
 \phi_{ij}^{s,w} &= C_{s,w} \frac{\varepsilon}{k} \left(\overline{u'_k u'_m n_k n_m} \delta_{ij} - \frac{3}{2} \overline{u'_k u'_i n_k n_j} - \frac{3}{2} \overline{u'_k u'_j n_k n_i} \right) f, \quad C_{s,w} = 0.5 \\
 \phi_{ij}^{r,w} &= C_{r,w} \left(\tilde{\phi}_{km} n_k n_m \delta_{ij} - \frac{3}{2} \tilde{\phi}_{ik} n_k n_j - \frac{3}{2} \tilde{\phi}_{jk} n_k n_i \right) f, \quad C_{r,w} = 0.18 \\
 \tilde{\phi}_{ij} &= P_{ij} - \frac{1}{3} \delta_{ij} P_{kk} \\
 f &= \frac{C_\mu^{0.75} k^{1.5}}{\kappa y_c \varepsilon}, \quad \kappa = 0.41, C_\mu = 0.09, k = 0.5 \left(-\rho \overline{u'_i u'_i} \right) \\
 y_c &= \text{nearest wall distance}
 \end{aligned} \tag{3.27}$$

The turbulent kinetic energy dissipation equation Eqn: 3.28 has the same model constants as $k - \varepsilon$ model.

$$\frac{\partial \rho \varepsilon}{\partial t} + \frac{\partial \rho \varepsilon \bar{u}_j}{\partial x_j} = \frac{\partial}{\partial x_j} \left[\mu + \frac{\mu_t}{\sigma_\varepsilon} \left(\frac{\partial \varepsilon}{\partial x_j} \right) \right] + \frac{\rho \varepsilon}{k} (0.5 C_{\varepsilon 1} P_{kk} - C_{\varepsilon 2} \varepsilon) \tag{3.28}$$

3.3 Large Eddy Simulations (LES)

Turbulent flow can be explained as an energy cascade process in which the larger eddies with more turbulent energy transfers energy to the smaller eddies with lesser energy. Larger eddies with lower wave numbers are anisotropic and problem specific, whereas smaller eddies are isotropic and problem independent and hence universal. The essence of Large Eddy Simulation technique is based on the notion that problem dependent physics are explicitly calculated, while problem independent universal phenomenon is mathematically modelled. In LES method spatial averaging operation is used to retain eddies larger than resolving grid scale (GS), and filter out eddies smaller than grid scale (Sub Grid Scale) eddies. In LES method the governing transport equations are obtained by filtering time-dependent flow equations. For a general space time variable $\phi_{(x,t)}$ the filtered variable $\bar{\phi}_{(x,t)}$ over a convolution filter kernel G is given by the relationship,

$$\bar{\phi}_{(x,t)} = \int_{-\infty}^{+\infty} \int_{-\infty}^{+\infty} \phi_{(\xi,t')} G(x - \xi, t - t') dt' d^3 \xi \tag{3.29}$$

3.3 Large Eddy Simulations (LES)

The filter characteristics are associated with the filter type and its spatial and temporal cut-off limits $\bar{\Delta}$, $\bar{\tau}_c$. In this thesis and most of LES modelling a top-hat filter (box filter) is used which characteristics are given as,

$$G(x - \xi) \begin{cases} \frac{1}{\Delta} & \text{if } |x - \xi| \leq \frac{\Delta}{2} \\ 0 & \text{otherwise} \end{cases} \quad (3.30)$$

The filter cut off scale Δ is calculated using cube root of the finite volume cell as $\Delta = \sqrt[3]{\Delta x \Delta y \Delta z}$. Filtered governing equations for incompressible flows results as Eqn 3.31.

$$\begin{aligned} \frac{\partial \bar{u}_i}{\partial x_i} &= 0 \\ \frac{\partial \bar{u}_i}{\partial t} + \frac{\partial \bar{u}_i \bar{u}_j}{\partial x_j} &= -\frac{1}{\rho} \frac{\partial \bar{p}}{\partial x_i} + \frac{\partial}{\partial x_j} \left[\nu \left(\frac{\partial \bar{u}_i}{\partial x_j} + \frac{\partial \bar{u}_j}{\partial x_i} \right) \right] \end{aligned} \quad (3.31)$$

The second order non-linear term appears in the filtered momentum equation ($\overline{u_i u_j}$) requires special treatment to be solved using FVM. It is decomposed into resolved stress ($\overline{u_i u_j}$) and Sub-Grid Scale (SGS) stress (τ_{ij}) and other stress terms as Eqn: 3.32.

$$\begin{aligned} \overline{u_i u_j} &= \overline{u_i u_j} + \underbrace{\overline{u_i u_j} - \overline{u_i u_j}}_{\tau_{ij}} \\ \tau_{ij} &= L_{ij} + C_{ij} + R_{ij} \\ L_{ij} &= \overline{\overline{u_i u_j}} - \overline{u_i u_j} \\ C_{ij} &= \overline{\overline{u_i u_j'}} - \overline{u_i' u_j'} \\ R_{ij} &= \overline{u_i' u_j'} \end{aligned} \quad (3.32)$$

L_{ij}, C_{ij}, R_{ij} are named as Leonard stress term, Cross stress term and Sub-Grid Scale Reynolds stress respectively, and only R_{ij} component is independently Galilean invariant, yet as a whole, the term τ_{ij} must be Galilean invariant. hence by following Germano's modification [189] modified stress terms are obtained as Eqn: 3.33. However, in practice of Sub-Grid Scale stress closure, all three terms are lumped into SGS stress and modelled.

$$\begin{aligned} L_{ij}^m &= \overline{\overline{u_i u_j}} - \overline{\overline{u_i u_j}} \\ C_{ij}^m &= \overline{\overline{u_i u_j'}} - \overline{\overline{u_i u_j'}} - \left(\overline{\overline{u_i u_j'}} - \overline{\overline{u_i u_j'}} \right) \\ R_{ij}^m &= \overline{u_i' u_j'} - \overline{u_i' u_j'} \end{aligned} \quad (3.33)$$

3.3.1 Sub Grid Scale stress models

In this section brief introduction to the used SGS models are presented. Earliest remarkable work on Modelling of Sub Grid Scale (SGS) stress was performed by Smagorinsky in 1963[190]. Following the Boussinesq hypothesis, sub-grid viscosity (ν_{sgs}) was derived as a function of filter cut off length (Δ), filtered strain rate (\overline{S}_{ij}) and the Smagorinsky model constant (C_s) as Eqn: 3.34.

$$\begin{aligned}
 \tau_{ij} &= -2\nu_{sgs}\overline{S}_{ij} + \frac{1}{3}\tau_{ij}\delta_{ij} \\
 \nu_{sgs} &= C_s^2\Delta^2|\overline{S}|, \quad C_s \simeq 0.17 - 0.21 \\
 |\overline{S}| &= \sqrt{2\overline{S}_{ij}\overline{S}_{ij}} \\
 \overline{S}_{ij} &= \frac{1}{2}\left(\frac{\partial\overline{u}_i}{\partial x_j} + \frac{\partial\overline{u}_j}{\partial x_i}\right)
 \end{aligned} \tag{3.34}$$

Local equilibrium in production and dissipation of sub-grid scale turbulent kinetic energy and isotropic sub-grid eddies were assumed in the derivation of the theoretical Smagorinsky SGS model constant $C_s = 0.173$ [191]. Complex turbulent flows do not fully conform with above model assumptions, hence model constant is adjusted case by case, and this approach is considered as a major drawback of the standard Smagorinsky model. LES modelling of boundary layer problems have shown that the Smagorinsky model constant has to be reduced to minimise the viscosity, and this is usually done manually or by using a damping function near the wall like van Driest function[192]. Additionally, the boundary layer eddies are highly anisotropic near the wall. Hence a highly anisotropic grid is required to resolve these eddies, and this could increase the numerical errors associated with LES. The Smagorinsky model predicts the energy transfer from grid-scale turbulent kinetic energy to sub-grid kinetic energy because the eddy viscosity remains positive, yet in reality, in certain physical problems, energy transfer from sub-grid scales to grid scales (inverse energy cascade) is important in modelling. Nevertheless, the Smagorinsky model has been widely used in LES modelling due to the simplicity and robustness of the model.

Scale Similarity Models

The smallest resolved eddies and the largest modelled eddies can be considered similar in length scales and time scales, and this idea was used in deriving the scale similarity model by Bardina et al.[193]. Mathematically the Sub-Grid turbulence velocity scale u'_i is given by the difference between unfiltered velocity and filtered velocity scales, $u'_i = u_i - \overline{u}_i$. Filtering the Sub-Grid velocity scale (\overline{u}'_i) yields large-scale fluctuations at sub-grid scale

level, therefore filtering the above relationship $\overline{u_i'} = \overline{u_i} - \overline{\overline{u_i}}$ shows that the difference between grid scale velocity and double filtered grid scale velocity denotes the smallest resolved scale fluctuations (RHS). Based on the scale similarity hypothesis Bardina et.al [193] developed the well known Bardina model, in which the SGS stress tensor is calculated as,

$$\tau_{ij} \approx \overline{\overline{u_i u_j}} - \overline{\overline{u_i}} \overline{\overline{u_j}} \quad (3.35)$$

Compared to eddy viscosity models Bardina model does not use any assumptions on principal SGS stress components to be in align with principal strain rates. Hence this model has shown better correlations with DNS data. However, the model does not introduce any energy dissipation term, hence subjected to numerical instabilities and a method to include dissipation eddy viscosity based model and scale similarity model can be combined resulting in a mixed model by Zang et al. [194].

$$\tau_{ij}^a = (\overline{\overline{u_i u_j}} - \overline{\overline{u_i}} \overline{\overline{u_j}})^a - 2(C_s \Delta)^2 |\overline{\overline{S}}| \overline{\overline{S}}_{ij} \quad (3.36)$$

As a result mixed model incorporates the dissipation effects of sub-grid eddies, and interaction between larger sub-grid eddies and smaller resolved eddies (τ_{ij}^a denotes the asymmetric part).

3.3.2 Dynamic Smagorinsky Model - DSM

Due to the disadvantages of using a global Smagorinsky constant over complex turbulent flow, a locally varying Smagorinsky model constant was proposed by Germano et al. [189] by extending the scale similarity model to include a test filtering approach. In this method, a filter larger than the grid filter ($-$) is used as a test filter (\sim) to obtain test filtered equations as Eqn: 3.37. T_{ij} represents the residual stress after test filtering.

$$\begin{aligned} \frac{\partial \tilde{u}_i}{\partial t} + \frac{\partial (\tilde{u}_i \tilde{u}_j)}{\partial x_j} &= \frac{1}{\rho} \frac{\partial \tilde{P}}{\partial x_i} + \frac{\partial}{\partial x_j} \left(-T_{ij} + 2\nu \tilde{S}_{ij} \right) \\ T_{ij} &= \overline{\overline{u_i u_j}} - \tilde{u}_i \tilde{u}_j \end{aligned} \quad (3.37)$$

Germano et al. presented the idea that resolved turbulence stress \mathcal{L}_{ij} represent the contribution of eddies which are of the size difference between test filter and grid filter; this concept is known as the Germano identity.

$$\begin{aligned} \mathcal{L}_{ij} &= \overline{\overline{u_i u_j}} - \tilde{u}_i \tilde{u}_j = T_{ij} - \tilde{\tau}_{ij} \\ \mathcal{L}_{ij} &= T_{ij} - \tilde{\tau}_{ij} \end{aligned} \quad (3.38)$$

Lilly [53] proposed a least square procedure to calculate the Smagorinsky model coefficient using the Germano identity, and in this thesis, Lilly's implementation is used. The anisotropic components of SGS stress tensor τ_{ij} and test filtered stress tensor T_{ij} relationships can be given as,

$$\begin{aligned}\tau_{ij}^a &= \tau_{ij} - \frac{1}{3}\tau_{kk}\delta_{ij} = -2C\Delta^2|\bar{S}|\bar{S}_{ij} \\ T_{ij}^a &= T_{ij} - \frac{1}{3}T_{kk}\delta_{ij} = -2C\widetilde{\Delta}^2|\widetilde{S}|\widetilde{S}_{ij}\end{aligned}\quad (3.39)$$

and the relationship for \mathcal{L}_{ij} can be written as,

$$\begin{aligned}\mathcal{L}_{ij}^a &= (-2C\widetilde{\Delta}^2|\widetilde{S}|\widetilde{S}_{ij}) - (-2C\Delta^2|\bar{S}|\bar{S}_{ij}) = -2C\Delta^2M_{ij} \\ M_{ij} &= \frac{\widetilde{\Delta}^2}{\Delta^2}(|\widetilde{S}|\widetilde{S}_{ij}) - (|\bar{S}|\bar{S}_{ij})\end{aligned}\quad (3.40)$$

Lilly's proposed method uses the error minimization of Eqn 3.40 as $e = \mathcal{L} - (-2C\Delta^2M_{ij})$ and obtained the dynamic Smagorinsky model constant C as,

$$C = \frac{-1}{2\Delta^2} \frac{L_{ij}M_{ij}}{M_{ij}^2}\quad (3.41)$$

The ratio between test filter and grid filter ($\widetilde{\Delta}/\Delta$) is set to 2.0 during the work presented in this thesis. Subgrid viscosity μ_{sgs} was clipped by negative molecular viscosity $\mu_{sgs} = \min(-\mu, \mu_{sgs})$, to artificially include turbulent kinetic energy backscatter.

3.3.3 Dynamic Mixed Model - DMM

Following the Germano identity, a similar procedure was proposed to calculate the mixed model constant by Zang et al. [194]. However, the model by Zang et.al used a modified Leonard stress term ($L_{ij}^m = \overline{\overline{u_i u_j}} - \overline{\overline{u_i}} \overline{\overline{u_j}}$) that is Galilean invariant and used resolved velocity field in contrast to the other sub-grid stress terms. Due to this mathematical inconsistency Vreman et al. [195] proposed an alternative method (T_{ij} as) in calculating the model constant dynamically known as the Dynamic Mixed Model (DMM) and in this work that implementation is also used. Calculation of mixed model coefficient of Eqn:3.36 is performed as

Eqn:3.42,

$$\begin{aligned}
 C &= \frac{M_{ij}(L_{ij} - H_{ij})}{M_{ij}} \\
 M_{ij} &= -2\Delta^2 |\widetilde{S}| \widetilde{S}_{ij} + 2\Delta^2 |\widetilde{S}| \widetilde{S}_{ij} \\
 H_{ij} &= \widetilde{\widetilde{u_i u_j}} - \widetilde{\widetilde{u_i}} - \widetilde{\widetilde{u_j}} - (\widetilde{\widetilde{u_i u_j}} - \widetilde{\widetilde{u_i u_j}})
 \end{aligned} \tag{3.42}$$

The DMM model implemented by Rostock University ([196]) was used in this thesis for modelling of JICF.

3.3.4 Dynamic One Equation Model (DEOM)

Similar to RANS modelling methods transport effects of sub-grid turbulent kinetic energy can be incorporated to close the SGS stress term using the relationship ($k_{sgs} = \frac{1}{2}(\overline{u'_i u'_i} - \overline{u'_i u'_i})$). In LES method the energy containing eddies are resolved hence sub-grid turbulence contains a significantly less amount of energy to influence the flow. Therefore the development of such models has been not come to the research forefront. Nevertheless, in flows where sub-grid scales contain significant energies or in problems where a purely uniform grid is difficult to obtain, a model with an additional transport equation for turbulence kinetic energy can be used to include the effects of sub-grid turbulent fluctuations. Additionally, in this model, the turbulent kinetic energy production is directly calculated, instead of assuming local equilibrium between energy production and dissipation. Therefore non-local history effects can be incorporated. According to channel flow simulation study using different SGS stress models by Fureby et al. [197], one equation model outperformed algebraic SGS models because of independent velocity scale provided by the sub-grid kinetic energy and inclusion of non-equilibrium effects. First work on this sub-grid kinetic energy transport modelling was done by Yoshizawa and Horiuti [198], and then following the dynamic procedure of Ghosal and Moin [199] a model where model constants (C_k, C_ϵ) are calculated by the procedure outlined by Furbey et al. [200]. Sub-grid viscosity is calculated as,

$$\nu_{sgs} = C_k \Delta k^{1/2} \tag{3.43}$$

In this model the transport equation for sub-grid turbulent kinetic energy and the SGS tensor are as Eqn: 3.44

$$\begin{aligned}\frac{\partial k_{sgs}}{\partial t} + \frac{\bar{u}_j \partial k_{sgs}}{\partial x_j} &= -\tau_{ij} \frac{\partial \bar{u}_i}{\partial x_j} + \left[(\mathbf{v} + \mathbf{v}_{sgs}) \frac{\partial k_{sgs}}{\partial x_j} \right] - \varepsilon \\ \tau_{ij} &= -2\nu_{sgs} \bar{S}_{ij} + \frac{2}{3} \delta_{ij} k_{sgs} \\ \varepsilon &= \frac{C_\varepsilon k_{sgs}^{3/2}}{\Delta}\end{aligned}\tag{3.44}$$

3.4 Flow Solver

In this thesis two CFD solver packages are used, STAR-CCM+(v 8.06) and OpenFOAM C++ package (v 2.3.x). Both packages use the Finite Volume Method based solution approach for the governing equations and, able to employ fully unstructured computational grids. However, in this work, OpenFOAM simulations were performed based on block-structured grids generated using the *blockMesh* utility. Both packages use segregated equation solving approach to solve the pressure and three momentum equations, and in STAR-CCM+ simulations the *SIMPLE* algorithm was used. In the OpenFOAM simulations however in addition to *SIMPLE* algorithm, the *PISO* algorithm and the *PIMPLE* algorithm which is a combined algorithm of *PISO* and *SIMPLE* was used for unsteady simulations. *PISO* algorithm can be used with smaller time steps whereas the *PIMPLE* algorithm can be used with comparatively larger time step simulations. During STAR-CCM+ simulations residuals for continuity and momentum equations were brought down 5 magnitudes of order (10^{-5}) and grid independence was assured after grid refinement. Similar measures were taken in OpenFOAM to ensure the systems of equations were solved sufficiently.

3.4.1 Wall treatment - RANS

Wall treatment - STAR-CCM+

In the jet in cross-flow simulations in Chapter 4 using STAR-CCM+ a combined wall treatment methods were used. In this method, if the near wall-cell falls within the logarithmic region high y^+ wall treatment methods are used, and if the near wall-cell falls within the viscous sublayer, low y^+ wall treatments are used. STAR-CCM+ wall treatment assures that wall treatment is formulated to produce reasonable results when wall-cell falls within

the buffer layer.

$$\begin{aligned} y^+ &= \frac{yu^*}{\nu} \\ u^* &= \frac{u}{u^+} \end{aligned} \quad (3.45)$$

Reference velocity definition $u^* = \sqrt{\tau_w/\rho}$ is replaced by an iterative process of the wall functions that returns u^+ as a function of y^+ .

$$u^+ = \begin{cases} y^+, & y^+ \lesssim 1 \\ \frac{1}{\kappa} \ln(Ey^+), & y^+ > 30 \end{cases} \quad (3.46)$$

y^+ is the non-dimensional wall distance, and default values for model coefficients $E = 9.0$ and $\kappa = 0.42$ were used. In the case of wall-cell lies in the buffer layer a Reichardt blended wall function [201] is used to blend the viscous sub-layer and logarithmic regions.

$$\begin{aligned} u^+ &= \frac{1}{\kappa} \ln(1 + \kappa y^+) + C \left[1 - \exp\left(-\frac{y^+}{D}\right) - \frac{y^+}{D} \exp(-by^+) \right] \\ D &= y_m^+ \\ C &= \frac{1}{\kappa} \ln E \kappa \\ b &= \frac{1}{2} \left(\frac{D\kappa}{C} + \frac{1}{D} \right) \end{aligned} \quad (3.47)$$

For Reynolds Stress Transport model wall treatment uses additional treatment. A blending function g is introduced to calculate u^* , and turbulence production (P_k) and turbulence dissipation (ϵ) in the wall cell is calculated. A blending function g is defined as,

$$\begin{aligned} g &= \exp\left(-\frac{Re_y}{11}\right) \\ Re_y &= \frac{\sqrt{ky}}{\nu} \end{aligned} \quad (3.48)$$

Reference velocity is calculated as,

$$u^* = \sqrt{g\nu u/y + (1-g)C_\mu^{1/2}k} \quad (3.49)$$

The normal gradient of velocity of wall cell is calculated using P_k using the relationship,

$$\frac{\partial V}{\partial n} = \frac{P_k}{\tau_w} \quad (3.50)$$

Turbulent kinetic energy production rate P_k ,

$$P_k = \tau_w \left(g \frac{u}{y} + (1 - g) \frac{u}{u^+ \kappa y} \right) \quad (3.51)$$

Wall-cell turbulence dissipation ε is calculated using,

$$\varepsilon = \frac{k^{3/2}}{l_\varepsilon} \quad (3.52)$$

Specific Reynolds stress tensor (R) at the wall is calculated using Neumann boundary condition with zero gradient $\partial R / \partial n|_w = 0$, and each stress component production is imposed by a special method [202] to agree with the wall function approach [203].

Wall treatment - OpenFOAM

In OpenFOAM simulations in Chapter 4, also high-Re number modelling approach was used with wall functions especially because the low-Re number modelling near the jet flow and cross flow interaction is computationally expensive. The jet flow direction and the cross-flow direction are perpendicular to each other, thus maintaining a finer grid near the cross-flow channel boundary is computationally expensive given that the jet flow velocity is greater in magnitude than the cross-flow velocity. Turbulence modelling near the wall requires particular attention, because as flow reaches a wall mean velocity and velocity fluctuations attenuate causing turbulent kinetic energy to become null at the wall. Therefore near the wall, Reynolds stresses can be assumed as isotropic and in magnitude equal to molecular viscous stresses. To resolve such steep gradients in turbulent kinetic energy requires very high spatial resolution in the region closer to the wall, and Low-Reynolds number models use the approach of using a higher resolution grids near the wall. $k - \varepsilon$ family models use a different approach of modelling the near wall behaviour by the use of wall functions (High Re number modelling), this modelling method is computationally less demanding than Low-Reynolds number modelling.

Turbulent boundary layer can be divided into three regions characterized according to dimensionless wall distance y^+ as, viscous layer $0 < y^+ < 5$, buffer layer $5 < y^+ < 30$, inertial layer $30 < y^+ < 200$. y^+ is defined as a function of normal distance from wall y_c and friction velocity u_τ (wall shear stress τ_w) and molecular kinematic viscosity ν .

$$y^+ = \frac{y_c u_\tau}{\nu} \quad (3.53)$$

$$u_\tau = \sqrt{\frac{\tau_w}{\rho}}$$

In the viscous sub-layer viscous effects are dominant, and turbulence effects are minuscule, whereas in inertial sub-layer turbulence effects are dominant, and in the buffer layer both viscous effects and turbulence effects are present and maximum turbulence production is reported to be around $y^+ = 12$ according to experimental and numerical investigations. As Figure 3.1 shows DNS data by Kim et.al[204] and experimental data by Eckelmann [205] for turbulent mean velocity profiles for a boundary layer over a flat plate. Empirical rela-

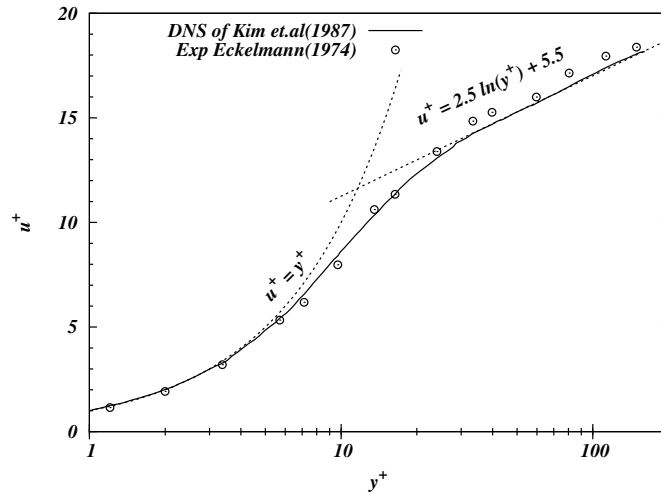


Figure: 3.1 Mean non-dimensional velocity against non-dimensional

tionships for dimensionless turbulence quantities in the viscous sub-layer can be given as Eqn:3.54.

$$\begin{aligned}
 u^+ &= \frac{u}{u_\tau} = y^+ \\
 k^+ &= \frac{k}{u_\tau^2} = 0.1y^{+2} \\
 \varepsilon^+ &= \frac{\varepsilon}{u_\tau^4/\nu} = 2\left(\frac{k^+}{y^+}\right) \sim 0.2 \\
 \omega^+ &= \frac{\omega}{u_\tau^2} = \frac{6}{\beta 1y^{+2}}, (\beta 1 = 0.075)
 \end{aligned}
 \tag{3.54}$$

In the inertial sub-layer, the velocity follows a logarithmic function of the wall distance as shown in Eqn:3.55.

$$\begin{aligned}
 u^+ &= \frac{u}{u_\tau} = \frac{1}{\kappa} \ln(y^+) + B \\
 k^+ &= \frac{1}{\sqrt{C_\mu}} = \frac{1}{\sqrt{\beta}} \\
 \varepsilon^+ &= \frac{\nu}{u_\tau \kappa y^+} \\
 \omega^+ &= \frac{\nu}{u_\tau \kappa y^+ \sqrt{\beta}}
 \end{aligned} \tag{3.55}$$

$$\kappa = 0.4, B = 5.5, C_\mu = \beta = 0.09.$$

In RANS turbulence modelling practice placing the first cell in the buffer layer is avoided to evade the high turbulence production term in the kinetic energy equation. Instead, the first cell is placed either in viscous sub-layer (Low Re number approach) or in inertial sub-layer (High Re number approach). Computation of numerical values at the wall is done on the wall-cell centre, which is placed at y_c (normal distance from the wall) away from the wall. Non dimensional wall cell centre distance y_c^+ is estimated using the definitions of non dimensional wall distances, and if $y_c^+ < y_{lim}^+ = 11$ the wall cell is considered to be in the viscous sub-layer and if $y_c^+ > y_{lim}^+ = 11$ the first cell is considered to be placed in the inertial layer. Estimation of friction velocity u_τ can be achieved considering zero-pressure gradient boundary layer,

$$\begin{aligned}
 k_c^+ &= \frac{k_c}{u_\tau^2} \\
 u_\tau &= c_\mu^{1/4} k_c^{1/2}
 \end{aligned} \tag{3.56}$$

In the first case ($y_c^+ < 11$), viscosity at the wall is considered as molecular viscosity, and the turbulence production term P_k in the k equation is modified by assuming a constant shear stress over the wall cell control volume. Turbulent kinetic energy at the wall cell is set to zero, as Eqn: 3.57.

$$\begin{aligned}
 P_k &\simeq \tau_w \frac{\partial U_c}{\partial y} = \mu U / y_c \\
 k_c &= 0
 \end{aligned} \tag{3.57}$$

Moreover, eddy dissipation rate and frequency in the wall cell are also estimated using the relationships for viscous sub-layer Eqn: 3.58.

$$\begin{aligned}\varepsilon_c &= \frac{c_\mu \rho k_c^2}{\mu} \\ \omega_c &= \frac{6\nu}{C_{\beta_1} y_c^2}\end{aligned}\tag{3.58}$$

In the second case ($y_c^+ > 11$) first cell viscosity is modified, and wall shear stress is calculated by considering that first cell centre lies in the logarithmic region of the boundary layer,

$$\begin{aligned}\mu_w &= \frac{\rho U_\tau y_c}{\frac{1}{\kappa} \ln(y_c^+) + B} \\ \tau_w &= \frac{\mu_w}{U_c} / y_c\end{aligned}\tag{3.59}$$

In solving k equation near the wall, zero gradient condition is imposed, and the turbulence production term P_k is modified assuming cell shear stress is equal to the wall shear stress, while the velocity gradient in wall normal direction is calculated from wall functions.

$$\begin{aligned}P_k &= \frac{|\tau_w| U_\tau}{\kappa y_c} \\ \frac{\partial k}{\partial x} &= 0 \\ \frac{\partial U}{\partial n} &= \frac{u_\tau}{\kappa y_c}\end{aligned}\tag{3.60}$$

In solving ε equations, the wall cell value is not solved by transport equations, yet it is modelled by the values from Eqn :3.58. Although there are many options in use for the implementation of wall boundary conditions for RANS simulations, OpenFOAM implementation is to identify the first cell location, either within the viscous layer ($y^+ \leq y_{lim}^+ = 11$) or within inertial sub-layer y^+ . An iterative process is usually used to estimate friction velocity from given velocity of cell u_p , using Eqn:3.61.

$$F = \frac{u_p}{u_\tau} - \frac{1}{\kappa} \ln y_p - B = 0\tag{3.61}$$

3.4.2 Wall treatment for LES

As LES technique resolves eddies to the level of cut off length scale, theoretically the effects of the dissipative viscous sub-layer are possible to resolve yet requires nearly DNS grid resolution near the wall boundary. When non-slip boundary conditions are imposed at wall boundaries, the mean velocity gradient still introduces sub-grid fluctuations at the wall boundary which violates the non-slip boundary condition. Therefore, in practical LES endeavours a wall treatment method is used to model the sudden velocity gradients near the wall. A review of applicable wall treatment methods for LES is provided by de Villers [206]. In OpenFOAM package wall functions for instantaneous filtered velocity can be used to model the wall boundary layer, even though in the strict sense wall functions are only applicable for mean velocity. For LES simulations of a jet in cross-flow in Chapter 5, Spalding's continuous wall function approach [207] was used in LES simulations as shown in Eqn: 3.62. The continuous wall function is more suitable in practical LES applications with complex geometries because the first grid cell can be placed in either viscous sub-layer or buffer-layer.

$$F(u_\tau) = u^+ - y^+ + \frac{1}{E} \left[e^{\kappa u^+} - 1 - \kappa u^+ - \frac{1}{2}(\kappa u^+)^2 - \frac{1}{6}(\kappa u^+)^3 \right] \quad (3.62)$$

Model constants $\kappa = 0.42$ and $E = 9.8$ were used and by substituting the relationships of $y^+ = y_c u_\tau / \nu$, $u^+ = \bar{u}_c / u_\tau$ a non linear equation for friction velocity u_τ is obtained. The initial estimation of the friction velocity is obtained via the relationship as in Eqn: 3.63, and corrected eddy viscosity from the friction velocity is obtained from the relationship Eqn:3.64.

$$u_\tau = \left\{ (v_{sgs} + \nu) \left| \frac{\partial \bar{U}}{\partial x_j} \right| \right\}^{1/2} \quad (3.63)$$

$$v_{sgs} = \max \left(\frac{u_\tau^2}{\left| \frac{\partial \bar{U}}{\partial x_j} \right|} - \nu, 0 \right) \quad (3.64)$$

The friction velocity u_τ is calculated using Newton Raphson iterative method and using this value eddy viscosity is corrected at the near wall cell.

$$u_\tau = u_\tau^{n-1} + \frac{F(u_\tau)}{F'(u_\tau)} \quad (3.65)$$

$$F'(u_\tau) = \frac{\partial F(u_\tau)}{\partial u_\tau}$$

The near wall centre velocity \bar{u}_c can be calculated in several ways, but OpenFOAM implementation uses the magnitude of the filtered velocity. Another well-known way to circumvent the wall eddy viscosity generated by the shear is to use a damping function for viscosity, and van Driest damping function is used in this thesis [192]. The model coefficient C_s^o is altered as,

$$C_s = C_s^o \left(1 - \exp \left(- \frac{y^+}{A^+} \right) \right) \quad (3.66)$$

The model constant $A^+ = 26$.

3.5 Inlet boundary conditions for LES

Since LES technique resolves turbulent fluctuations in the system, accurate representation of turbulent inflow structures is a vital factor in obtaining an accurate prediction of the flow field in the solution domain. In problems where a dominant turbulence generation mechanism is available like vortex shedding problems, the exact representation of incoming turbulence structures can be neglected. Inlet turbulent structures for LES should be stochastically varying size from filter size to integral length scale at the inlet and should satisfy the governing equations to result in non-divergent velocity field. In addition, these fluctuations should be coherent to reproduce characteristics of turbulent flows (energy cascading and spatial and temporal correlations). Adhering to above requirements and specifying the mean flow velocities and fluctuations without increasing the computational overhead is a considerable challenge in LES framework [208]. During this thesis, several methods of inlet boundary specifications were employed and discussed below.

Random Velocity Fluctuations

Randomly generated velocity fluctuations can be superimposed on the mean velocity distribution to generate inlet velocity fluctuations. However, these fluctuations do not have the spatial or temporal coherence to produce the effects of turbulent energy cascade. Instead, these velocity fluctuations create same energy for all wavelengths. Hence low-frequency eddies have comparatively smaller energy causing them to diminish inside the flow field. Some studies have reported successful results by using this method [209][210], and it can be expected that in problems which the inlet boundary is specified closer to another dominant turbulence generating mechanism like a swirl flow this method can be used without losing the inlet turbulence effects. However, some studies have shown that due to insufficient eddies from the upstream flow, reattachment length on the canonical problem of backward

facing step has overpredicted [211]. The simplicity of specifying the boundary values and minimal additional computational overload added are the main advantages of this method.

Synthetic turbulence generation

Spatially and temporally correlated velocity fluctuation generation algorithms have been developed to produce inlet turbulence with physically realistic turbulence energy spectrum. Klien et al. [212] used digital filtering of random noises to create more accurate first order and second order statistics and a local autocorrelation function, and this technique is widely used in LES work. Kornev et.al[213] used *random spot method* to create inlet turbulence structures and this method holds few advantages over the earlier method proposed by Klien et.al. Random spot generation method generates fluctuations with prescribed spatial integral length scales, integral time scales, two-point spatial and one-point temporal autocorrelations, as well as one-point cross-correlations between fluctuating velocity components. Korneve's method can be applied on a non-uniform grid and with variable time steps compared to digital filtering technique, and this is important in complex inflow geometries, and also not only homogeneous turbulence but inhomogeneous turbulence structures can be generated.

Mapped Velocity

In this approach velocity field is mapped from an internal mapping plane with scaling applied to ensure the bulk flow rate is conserved, the idea is shown in Figure 3.2b. Since the section to generate initial turbulence structures is a section of the same problem domain, this approach is computationally less demanding than the use of a previously computed database. If downstream flow perturbations propagate in the upstream direction up to the mapping surface, then these perturbations will be mapped into the inlet. Therefore mapping surface must be placed sufficiently away from the main problem domain.

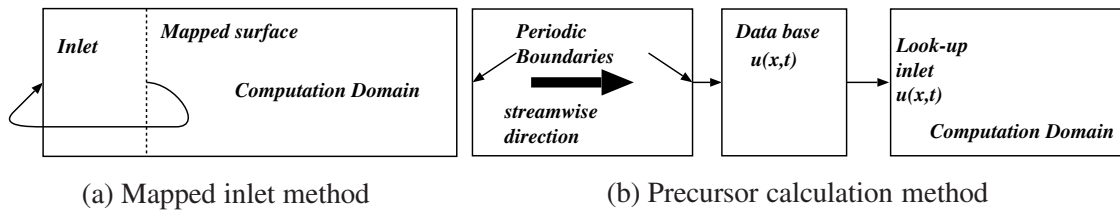


Figure: 3.2 Inlet turbulence generation methods for LES

Precursor-computation

A pre-computed simulation to obtain turbulent inlet fluctuations can be carried out and stored in a database in an auxiliary simulation and looked up by the main computational domain (Figure 3.2a illustrates the concept). Although this method could provide higher order moments of velocity very accurately, the computational overhead is more expensive to be used in complex geometrical simulations, hence in this method was not considered.

3.6 Outflow Boundary Conditions

In compressible flow LES calculations with implicit pressure solution techniques, acoustic waves can propagate across the computational domain. In a numerical sense, these waves impose as another noise similar to turbulence, flame generated turbulence or discretisation errors. Non-reflecting boundary conditions are used to avoid numerical instabilities arising from reflected pressure waves from outlet boundaries OpenFOAM library provides a non-reflecting pressure boundary condition which is a simplified form of the boundary condition proposed by Poinso and Lelef [214]. In this method the boundary value is found by solving the advection equation Eqn:3.67, the advection velocity (U_n) is calculated by considering the speed of sound (c) and flow velocity (U) at the outlet boundary. Pressure wave speed at the outlet is calculated by using compressibility (ψ) and specific heat ratio ($\gamma = C_p/C_v$).

$$\frac{\partial \phi}{\partial t} + U_n \frac{\partial \phi}{\partial n} = 0 \quad (3.67)$$

$$\begin{aligned} U_n &= U + c \\ U_n &= U + \sqrt{\frac{\gamma}{\psi}} \end{aligned} \quad (3.68)$$

3.7 LES Accuracy and Errors

Computational fluid dynamic methods are always associated with a myriad of numerical errors, and these errors are mostly mutually non-exclusive; therefore reliability of the answer depends on how these numerical errors are treated. To understand and interpret the LES results and discrepancies the error sources are important. In this section, the common error sources are discussed, and more in detail discussions are found in literature [206, 215, 216].

Mainly numerical errors in LES can be classified into three groups as, discretisation errors, modelling errors and filtering errors.

Discretisation errors

Discretisation errors are not unique to LES method, but all numerical approximations of continuum mechanics are subjected to discretization errors as a result of approximating a continuous field variable as a discrete variable. Truncation errors associated with the first order and second-order accuracy of the spatial and temporal approximation is an inherent feature of FVM. Discretization errors can be minimized by increasing the spatial and temporal resolution. However, increased grid resolution does not necessarily guarantee grid independence in LES because the implicit filtering does not ensure the smallest resolvable scales are fully resolved [215]. In addition, the SGS stress models responses have shown grid dependent characteristics [216]. Cell non-orthogonality and skewness introduce errors because of the unboundedness, and the limiter schemes used in the approximation of convection term also introduce local first-order or second-order accuracies based on the limiting level. Since these numerical errors and high-frequency turbulent fluctuations are inseparable, the LES method requires very good orthogonal grids.

Modelling errors

LES method requires modelling of sub-grid scale physical phenomena like turbulent kinetic energy dissipation to internal energy, scalar dissipation, chemical reactions. Therefore, the shortcomings of these mathematical models also appear as errors in the final numerical solution. Most of the SGS models in use assume sub-grid scale eddy isotropy, but this assumption is far from realized in complex inhomogeneous turbulence fields such as shear-layers, swirling flow or near boundary layers. In SGS models that require resolved strain field to derive the SGS stress field are subject to this error caused by anisotropic turbulence and provides erroneous feedback to the resolved velocity field. Since dynamic SGS models incorporate the similarity between largest filtered eddies and smallest un-filtered eddies, the erroneous assumption of isotropic turbulence could exacerbate the modelling error. The isotropic assumption is detrimental to boundary layer modelling, and use of an anisotropic grid or extremely fine filter to conform with isotropy are used in accurate boundary layer modelling endeavours.

Turbulent energy transfer from SGS eddies to Grid-Scale (GS) eddies is known as backscatter or inverse energy transfer which is a physical phenomenon needed to be modelled. However, using computationally expensive explicit backscatter modelling strategies

have only shown marginal improvements [139]. In this work, the dynamic Smagorinsky model can accept negative eddy viscosity to artificially accommodate energy backscatter. Turbulent kinetic energy transfer from GS to SGS and the SGS dissipation is assumed in Smagorinsky and other zero equation (algebraic) SGS models. Although this assumption is satisfactory in many applications, in large turbulence generating locations this assumption fails to conform with the physics, hence turbulent kinetic energy accumulation occurs and affects laminar to turbulent transition predictions [217]. One equation SGS stress models consider the non-equilibrium effects through modelling sub-grid kinetic energy, hence capable of realizing the non-equilibrium effects. However even one equation models the source term is unable to distinguish between stresses derived from fluctuations and mean flow gradients; therefore even velocity gradients laminar flow regions could trigger an SGS response causing inaccuracies in laminar flow regions [206]. Although dynamic algebraic SGS models use the resolved turbulent fluctuation information to calculate the model coefficients they could be adversely affected by local non-equilibriums; therefore dynamic one-equation models are used for the more accurate representation of local turbulence production modelling [218].

Filtering Errors

Implicit filtering of governing equations also introduces errors. Namely *Aliasing error* and *Commutation error* are major errors caused by filtering operation. Aliasing error is related to the process of filter truncation of eddies smaller than cut off length. As Figure: 3.3 illustrates, the response of top hat filter in physical space shows a sharp cut-off, but the frequency space response shows that only spectral cut-off filter provides a sharp cut off in frequency space. From the top hat filter response, it can be seen that frequencies higher than cut-off frequency will exist in LES solution. Moreover, some lower frequencies are not fully resolved due to discretization errors as described earlier. Therefore these under-resolved eddies will manifest as redundant turbulence energy into the resolved eddies introducing an error, and in flows where a significant percentage of turbulence energy is contained in smaller resolved eddies, the presence of these unresolved eddies can be detrimental to the solution. Aliasing error is more critical in dynamic models because smallest resolved eddies are used in determining local model constants.

Commutation error is the errors arising due to grid size (filter size) variation. In the derivation of filtered Navier Stokes equations commutative property of filtering was assumed, however if the filter size is not constant the filtering operation is not necessarily commutative with differential operator ($\overline{\frac{\partial \phi}{\partial x}} \neq \frac{\partial \overline{\phi}}{\partial x}$). Implicit LES uses the implicit top-hat filtering operation, but due to physical considerations of complicated geometries, a uni-

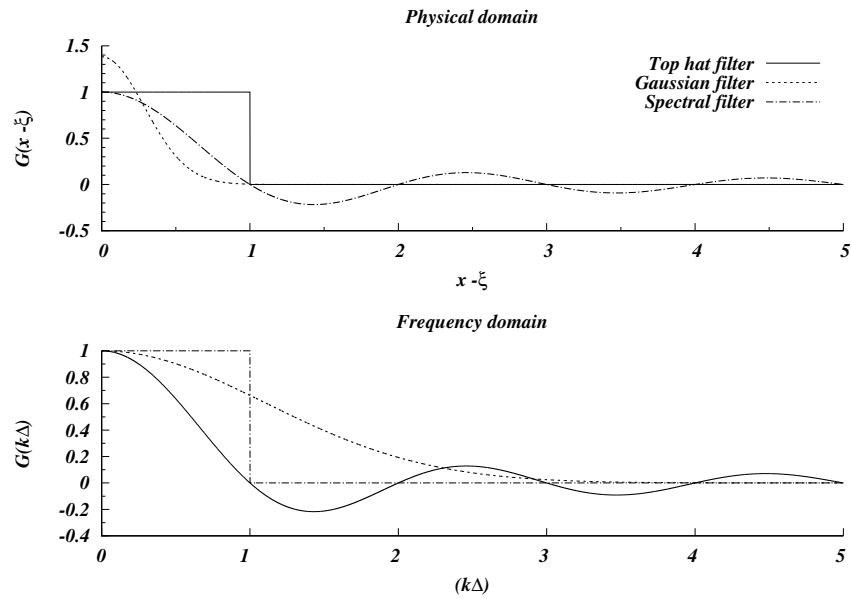


Figure: 3.3 Normalized transfer functions for filters

formly spaced grid is virtually impossible without increasing the computational overhead immensely. Implicit filtering on a non-uniform grid requires additional terms into the filtered Navier Stokes equations, but in practice, these terms are neglected; thus commutation error must be acknowledged in LES with non-uniform grids. To minimize the commutation error, a grid with minimal grid size gradients should be used. Nevertheless, near the wall boundaries, grid size variation is inevitable hence the commutation error influences the modelled SGS stresses near walls.

Considering all three major error sources in LES method increasing the grid resolution is the most pragmatic method of minimizing these errors. However, the required accuracy must be compared to the additional computational cost of increasing the grid resolution. Thus trial and error methods are used to find the required compromise between accuracy and computational cost. However this practice itself further extends the process of LES simulations.

3.8 LES Resolution

LES technique assumes that the SGS stress model cut-off scale falls in the range of isotropic turbulence and low energy eddies, and filter cut-off width is a grid dependent variable. Thus LES resolution can be considered as a direct reflection of the grid resolution. However, prior to the simulation, there is no technique to estimate if the filter cut-off scale falls in the

dissipative scales range. One of the simplest ways to investigate where the filter cut-off scale is positioned in the energy cascading spectrum is to generate the turbulent energy spectrum using resolved velocity recordings and identify the presence of inertial range. On a turbulent energy spectrum plotted in logarithmic scales, the inertial range can be identified from the characteristic slope of turbulent energy with respect to wave number ($k = 2\pi f/U$) as given by Eqn: 3.69.

$$E_{(k)} \propto k^{-5/3} \quad (3.69)$$

However, this method neither represents the full computational domain, nor all turbulent flow regimes show this spectral characteristic where boundary layer, transitional flows and low turbulence flows show different energy spectrum distributions.

The concept that modelled stress components should be smaller in magnitude itself can be used to verify the LES resolution by inspecting the percentage of modelled stress magnitude in a post-processing stage. Pope [219] proposed that to confirm the LES solution field is resolved sufficiently, the percentage of resolved turbulent kinetic energy (γ)(Eqn: 3.70) should be larger than 80 %. ($\langle \rangle$ denotes time averaging)

$$\begin{aligned} \gamma &= \frac{k_{resolved}}{k_{resolved} + \langle k_{modelled} \rangle} \\ k_{resolved} &= \frac{1}{2} \langle \overline{u'_i u'_i} \rangle \\ \overline{u'} &= \overline{u} - \langle \overline{u} \rangle \\ k_{modelled} &= \frac{1}{2} \tau_{ii} \end{aligned} \quad (3.70)$$

For statistically steady flows the time mean of LES solution can be considered as equivalent to the ensemble average, and experimental measurements which are averaged over significantly larger sampling times can be used for comparison and validation of LES models. To obtain statistically independent mean field solutions, the time averaging process must be conducted over sufficient time period (larger than integral timescale $T_{avg} \gg T'_{int}$). The relationship between error percentage and time average span (T_{avg}) can be shown as Eqn: 3.71, with the use of variance (σ^2) and number of samples (N) As Eqn: 3.71 shows that the statistical error minimizes with increasing number of samples and with increasing the averaging timespan.

$$Error = \left| \frac{U_{true} - U_{est}}{U_{true}} \right| = \frac{\sigma}{U_{true}} \frac{1}{N^{1/2}} = \frac{\sigma}{U_{true}} \left(\frac{T'_{int}}{T_{avg}} \right)^{1/2} \quad (3.71)$$

3.9 Coherent Structures Identification

Coherent structures in turbulent flows are understood without strict definitions as flow structures with vorticity and distinguishably repeating over time. Therefore coherent structures amalgamate spatial and temporal correlations to the turbulence flow definition, which is otherwise a completely random phenomenon. Since larger eddies exhibit structural coherence, air-fuel mixing applications like mixing applications utilise this attribute to enhance and control scalar mixing. Experimentally these structures are visualized using smoke or other particles as a standout flow feature from the background flow, for numerical visualisation vorticity can be considered as the primary identifier [220]. Especially in the JICF problem four major vortex structures have been identified as introduced in Section:2.2, and swirling flows that are discussed in this thesis also involves coherent flow structures. Since scalar mixing and transport in JICF is dominated by the counter-rotating vortex pair, identification of these vortex structures sheds light into understanding the scalar mixing process. Effects of coherent structures have been studied and reviewed by several authors [221, 222], and in this section coherent structure identification techniques used in this thesis are outlined.

Primarily the coherent structure identification problem reduces to a vortex identification problem, thus the objective of the definition of vortex arises. Addressing the difficulty of objectively defining a vortex Lugt [223] defined a vortex as a mass of fluid rotates around an axis. In an effort to develop a method to identify vortex Jeong and Hussain [224] concluded that using only the Lugt's notion of rotating fluid mass, and hence looking for a pressure gradient created by the rotating flow to locate a vortex core was not always reliable. Therefore Jeong and Hussain outlined two requirements for a vortex core as,

- i At the vortex core a net vorticity and net a circulation must be present.
- ii Vortex core of the identified geometry should be Galilean invariant.

One of the earliest vortex detection methods was to search for closed or spiral path lines [223], but this method is not a comprehensive method because particles do not complete full cycles during a vortical movement, and other situations where this method fails were explained by Jeong and Hussain [224]. Another intuitive method of locating a vortex is to observe the vorticity field ($\text{curl}(\mathbf{U})$) on free flows, yet this approach is inapplicable for shear flows. Furthermore, Jeong and Hussain reviewed the method of identifying vortices based on the definition given by Hunt et al. [225] for an eddy, that a positive second invariant (Q) of velocity gradient must exist with a lower pressure, this method is known as Q -criterion of identifying vortex structures.

Q -criterion

The velocity gradient tensor can be decomposed into symmetric strain rate S_{ij} and anti-symmetric vorticity Ω_{ij} as,

$$\frac{\partial u_i}{\partial x_j} = S_{ij} + \Omega_{ij} \quad (3.72)$$

and the second invariant of velocity gradient Q is defined as a balance between vorticity and strain,

$$Q = \frac{1}{2} \left[\left(\frac{\partial u_j}{\partial x_j} \right)^2 - \frac{\partial u_i}{\partial x_j} \frac{\partial u_j}{\partial x_i} \right] = \frac{1}{2} \left(|\Omega|^2 - |S|^2 \right) \quad (3.73)$$

$$|S| = |\text{tr}(SS^t)|^{1/2}$$

$$|\Omega| = |\text{tr}(\Omega\Omega^t)|^{1/2}$$

Then the necessary condition for a vortex to exist was defined as $Q > 0$. Q -criterion is applicable for shear flows in contrast to previously mentioned methods.

λ_2 -criterion

Jeong and Hussain proposed a method based on the local pressure extremes across the vortex named λ_2 - criterion [224]. Local pressure extrema can be found in Hessian of pressure (p_{ij}) which is given by the gradient of the Navier-Stokes equations as,

$$a_{i,j} = -\frac{1}{\rho} p_{ij} + \nu u_{i,jkk} \quad (3.74)$$

The acceleration gradient $a_{i,j}$ can be decomposed into symmetric and antisymmetric part (Eqn: 3.75), and since the p_{ij} is symmetric, only the symmetric part of acceleration gradient is considered in calculation of pressure minimum.

$$a_{i,j} = \underbrace{\frac{DS_{ij}}{Dt} + \Omega_{ik}\Omega_{kj} + S_{ik}S_{kj}}_{\text{symmetric}} + \underbrace{\frac{D\Omega_{ij}}{Dt} + \Omega_{ik}S_{kj} + S_{ik}\Omega_{kj}}_{\text{antisymmetric}} \quad (3.75)$$

The necessary condition for a vortex is to have two negative eigenvalues of the pressure (hessian matrix). Since unsteady term and viscous effects do not make any significance to the presence of a vortex, two negative eigenvalues of $S.S + \Omega.\Omega$ are sought, where S and Ω are the symmetric and antisymmetric of velocity gradient tensor. Once these eigenvalues are orderd in magnitude $\lambda_1 \geq \lambda_2 \geq \lambda_3$, the condition for two negative eigenvalues can be reduced

to $\lambda_2 < 0$

$$\frac{\mathbf{D}S_{ij}}{\mathbf{D}t} - \nu S_{ij,kk} + \Omega_{ik}\Omega_{kj} + S_{ik}S_{jk} = -\frac{1}{\rho}p_{ij} \quad (3.76)$$

3.10 Passive scalar mixing modelling

In RANS context the scalar transport equation Eqn: 3.5 requires closure of the turbulent scalar flux term $\overline{u'\phi'}$. The turbulent scalar flux is closed by using Gradient Diffusion Hypothesis (GDH), and eddy diffusivity concept which results in RANS passive scalar transport equation Eqn: 3.77. In this thesis, a constant turbulent Schmidt number was used to model the eddy diffusivity of passive scalar Γ_t , and the modelling assumptions were discussed in Section 2.2.2.

$$\begin{aligned} \overline{u_i'\phi'} &= \Gamma_t \frac{\partial \bar{\phi}}{\partial x_i} \\ \Gamma_t &= \frac{\mu_t}{Sc_t} \\ \frac{\partial \bar{\phi}}{\partial t} + \frac{\partial (\bar{u}_j \bar{\phi})}{\partial x_j} &= \frac{\partial}{\partial x_j} \left[\left(\frac{\mu}{Sc} + \frac{\mu_t}{Sc_t} \right) \frac{\partial \bar{\phi}}{\partial x_j} \right] \end{aligned} \quad (3.77)$$

In LES method the filtered passive scalar transport equation is given by Eqn: 3.78, and the sub-grid scalar flux $(\widetilde{u_j \phi} - \tilde{u}_j \tilde{\phi})$ is modelled using gradient diffusion hypothesis as in Eqn: 3.79. Therefore, when compared with RANS method the passive scalar modelling in LES method is only different from the way in which the sub-grid viscosity is calculated.

$$\frac{\partial \tilde{\phi}}{\partial t} + \frac{\partial (\tilde{u}_j \tilde{\phi})}{\partial x_j} = \frac{\partial}{\partial x_j} \left(\frac{\mu}{Sc} \frac{\partial \tilde{\phi}}{\partial x_j} \right) - \frac{\partial (\widetilde{u_j \phi} - \tilde{u}_j \tilde{\phi})}{\partial x_j} \quad (3.78)$$

$$(\widetilde{u_j \phi} - \tilde{u}_j \tilde{\phi}) = -\frac{\mu_{sgs}}{Sc_{sgs}} \frac{\partial \tilde{\phi}}{\partial x_j} \quad (3.79)$$

3.11 Compressible - $k - \varepsilon$ model

During this thesis work, RANS turbulence models were used to investigate turbulent combustion model performance and more commonly used $k - \varepsilon$ model was used because of the ease of use. However, the standard $k - \varepsilon$ model was developed for incompressible flows,

therefore for compressible flows, additional terms are included.

$$\mu_t = \rho C_\mu \frac{k^2}{\varepsilon}$$

$$\frac{\partial(\rho k)}{\partial t} + \frac{\partial}{\partial x_i}(\rho k \bar{u}_i) = \frac{\partial}{\partial x_j} \left[\left(\mu + \frac{\mu_t}{\sigma_k} \right) \frac{\partial k}{\partial x_j} \right] + P_k + P_b - \rho \varepsilon \quad (3.80)$$

$$\frac{\partial(\rho \varepsilon)}{\partial t} + \frac{\partial}{\partial x_i}(\rho \varepsilon \bar{u}_i) = \frac{\partial}{\partial x_j} \left[\left(\mu + \frac{\mu_t}{\sigma_\varepsilon} \right) \frac{\partial \varepsilon}{\partial x_j} \right] + C_{1\varepsilon} \frac{\varepsilon}{k} P_k - C_{2\varepsilon} \rho \frac{\varepsilon^2}{k} + C_{3\varepsilon} \rho \varepsilon \frac{\partial \bar{u}_i}{\partial x_j} \quad (3.81)$$

P_k : Turbulent Kinetic Energy Production

$$P_k = -\rho \overline{u'_i u'_j} \frac{\partial \bar{u}_j}{\partial x_i} = -\rho \left[\left(\frac{\partial \bar{u}_i}{\partial x_j} + \frac{\partial \bar{u}_j}{\partial x_i} \right) - \frac{2}{3} \frac{\partial \bar{u}_k}{\partial x_k} \right] \frac{\partial \bar{u}_j}{\partial x_i} \quad (3.82)$$

P_b : Effect of buoyancy in turbulent kinetic energy transport equation is neglected for reacting flow given the magnitude of inertial forces. In the energy dissipation equation energy dissipation equation due the compressibility effects are represented by the $C_{3\varepsilon} \rho \varepsilon \frac{\partial u_i}{\partial x_j}$ term in Eqn 3.81. The $C_{3\varepsilon}$ has been found to be equal to -0.33 by a order of magnitude analysis of the dissipation equation [226]. Model constants are set as, $C_{1\varepsilon} = 1.44$, $C_{2\varepsilon} = 1.92$, $C_{3\varepsilon} = -0.33$, $C_\mu = 0.09$, $\sigma_k = 1.0$, $\sigma_\varepsilon = -1.3$.

3.12 Reacting Flows

In this section, the instantaneous governing equations for a turbulent reacting flow are discussed alongside the important assumptions made in derivation and simplifications, that are used in this thesis. In this thesis, all non-premixed, premixed, partially premixed flames have been considered. In modelling of non-premixed flames adiabatic steady laminar flamelet model is used, and in modelling of premixed flames flamelet generated manifold method and artificially thickened flame model is used.

In addition to the mass conservation and momentum conservation principals used in incompressible flow simulations, species mass conservation and energy conservation are solved in reacting flow simulations. The density changes occur due to temperature changes, and composition changes are taken into consideration by assuming the mixture of gases are ideal gases and hence by using the ideal gas thermodynamic state equation. In OpenFOAM solver, the compressibility of the gases is taken into consideration by estimating the gas compressibility (ψ) [227].

Species Mass conservation equation is given by,

$$\frac{\partial \rho Y_k}{\partial t} + \frac{\partial \rho (u_i + V_{k,i}) Y_k}{\partial x_i} = \dot{\omega}_k \quad \text{for } k = 1 : N \quad (3.83)$$

$V_{k,i}$ is the i^{th} component of the diffusion velocity of species k and the source term $\dot{\omega}_k$ is the consumption rate of species k. Since the direct calculation of species diffusion velocity is a numerically challenging task. The Ficks law which relates the diffusion velocity to the concentration gradient as Eqn: 3.84 leads to the simplified species mass conservation Eqn: 3.85.

$$V_k Y_k = -D_k \frac{\partial Y_k}{\partial x_i} \quad (3.84)$$

$$\frac{\partial \rho Y_k}{\partial t} + \frac{\partial \rho u_i Y_k}{\partial x_i} = \frac{\partial}{\partial x_i} \left(\frac{\partial \rho D_k Y_k}{\partial x_j} \right) + \dot{\omega}_k \quad (3.85)$$

In the specific enthalpy transport equation 3.86, radiation source term is usually neglected in non-sooting flames, and in addition for low Mach number reacting flows viscous energy dissipation neglected and acoustic interactions are also neglected [68]. Specific enthalpy transport Equation is given by,

$$\frac{\partial (\rho h)}{\partial t} + \frac{\partial}{\partial x_i} (\rho u_i h) = \frac{\partial}{\partial x_i} \left[\frac{\mu}{\sigma_h} \frac{\partial h}{\partial x_i} + \mu \left(\frac{1}{Sc_k} - \frac{1}{\sigma_h} \right) \sum_{k=1}^n h_k \frac{\partial Y_k}{\partial x_i} \right] + \frac{\partial p}{\partial t} + S_{rad} \quad (3.86)$$

The Prandtl number σ_h is calculated as,

$$\sigma_h = \frac{c_p \mu}{k}$$

Diffusion coefficients D_k is used to calculate thermal diffusivity D_{th} by using the Lewis number relationship

$$Le_k = \frac{D_{th}}{D_k}$$

in addition a constant Lewis number is assumed for many flames.

$$Le_k = \frac{D_{th}}{D_k} = \frac{k}{\rho c_p D_k}$$

$$Sc_k = \frac{\mu}{\rho D_k} = Le \sigma_h$$

Assuming a unity Lewis number the enthalpy transport equation can be further simplified,

$$\frac{\partial \rho h}{\partial t} + \frac{\partial \rho u_i h}{\partial x_i} - \frac{\partial}{\partial x_i} \left[\frac{\mu}{\sigma_h} \frac{\partial h}{\partial x_i} \right] = \frac{\partial p}{\partial t} + S_{rad} \quad (3.87)$$

In order to relate the thermodynamic state variables, perfect gas law is assumed as,

$$p = \rho \frac{R}{M} T \quad (3.88)$$

The perfect gas definition for specific enthalpy as $dh = c_p dT$ can be represented as a solution of polynomials of $c_p(T)$ as Eqn: 3.89 to calculate enthalpy as a polynomial function of temperature[228] in the form,

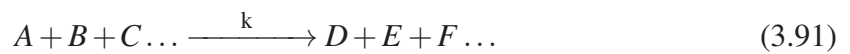
$$\begin{aligned} c_p(T) &= \frac{R}{M} [a_0 + a_1 T + a_2 T^2 + a_4 T^4] \\ h(T) &= h_0 + \frac{R}{M} [a_0 T + \frac{a_1}{2} T^2 + \frac{a_2}{3} T^3 + \frac{a_3}{4} T^4 + \frac{a_4}{5} T^5] \end{aligned} \quad (3.89)$$

In the flameletFoam solver which is used in non-premixed SLFM calculations the density is calculated using the compressibility ψ before the pressure velocity coupling is solved. Therefore, the flameletFoam solver implicitly addresses the compressibility of the flow.

$$\begin{aligned} \rho &= \rho_o + \psi \times p \\ \psi &= \frac{1}{R_u T} \end{aligned} \quad (3.90)$$

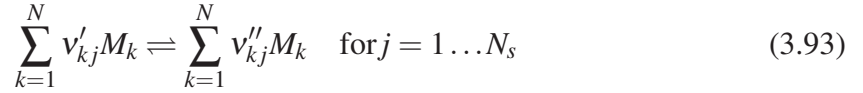
Chemical Reactions

In chemically reacting systems, the species conversion occurs through activated chemical reactions while conserving the element mass and total system mass. Interms of numerical computation of chemically reacting systems the chemical kinetics are important especially if reaction time scales are comparable with turbulence time scales or intermediate chemical species are of special interest. Oxidation of natural gas or other typical fuels go through a series of interemediate chemical reactions and these reactions can be expressed as elementary reactions. For an elementary reaction as Eqn: 3.91 the reaction rate \dot{q} is given as function of the reaction orders ($a, b, c \dots$) and the rate coefficient k (Eqn: 3.92)



$$\dot{q} = \frac{d[A]}{dt} = -k[A]^a[B]^b[C]^c \quad (3.92)$$

In calculation of reaction rates of elementary reactions the reaction order is generally taken to be same as the stoicheometric coefficients of the specie. Therefore, a chemically reacting system with N species and a total of N_s elementary reactions in forward and reverse directions is shown in Eqn: 3.93, where v'_{kj} and v''_{kj} are the stoicheometric coefficients of the species k in the reaction j , on the reactants side and the products side respectively.



The reaction progress rate of intermediate reaction j (Q_j) is given as a function of species concentrations $[X_k]$, forward reaction rate K_{fj} and reverse reaction rate K_{rj} as,

$$Q_j = K_{fj} \prod_N^{k=1} [X_k]^{v'_{kj}} - K_{rj} \prod_N^{k=1} [X_k]^{v''_{kj}} \quad (3.94)$$

However, in CFD calculations of reacting flows the species transport equations that calculate the mass fractions of species (Y_k) are solved, the mass reaction rates for specie k ($\dot{\omega}_k$) is important and given by the relationship as a summation of reaction rates of each reaction (Q_j) as Eqn: 3.95

$$\begin{aligned} \dot{\omega}_k &= \sum_{j=1}^{N_s} \dot{\omega}_{kj} = W_k \sum_{j=1}^{N_s} v_{kj} Q_j \\ v_{kj} &= v''_{kj} - v'_{kj} \end{aligned} \quad (3.95)$$

The chemical reaction rate constant for each chemical reaction is given by the well known Arrhenius equation, where A_{fj} is the pre-exponential coefficient, and $T^{\beta j}$ is the weak temperature dependence of the pre-exponential coefficient, and $T_{act,j}, E_{act,j}$ are the activation temperature and activation energy respectively.

$$k_{fj} = A_{fj} T^{\beta j} \exp\left(\frac{-T_{act,j}}{T}\right) = A_{fj} T^{\beta j} \exp\left(-\frac{E_{act,j}}{R_u T}\right) \quad (3.96)$$

Due to highly non-linear chemical source terms and smaller chemical timescales compared to turbulent timescales, a three-dimensional direct numerical solution of turbulent species transport equations is still computationally expensive. Therefore combustion models are used, or reduced chemical mechanism with a number of major species and reactions are used.

Detail chemistry solver

The detailed chemistry reacting flow solver reactingFoam available with OpenFOAM is used for FGM simulation validations in Section: 7.2.1. Instead of calculating the exponential source term of chemical species, this solver uses a modelled source term evaluated by using the Partially Stirred Reactor concept, using a reactive fraction (κ_k) [229],

$$\tilde{\omega}_k = \kappa_k \dot{\omega}_k \quad (3.97)$$

However, in the laminar flame condition $\kappa = 1$, and the species transport equations represents a detail chemical system with unity Lewis number assumption and equal species diffusivities. Unity Schmidt number and Prandtl number are also assumed in this solver. Therefore the species transport equation for this solver can be written as Eqn: 3.98,

$$\frac{\partial \bar{\rho} \tilde{Y}_k}{\partial t} + \frac{\partial}{\partial x_i} \left(\bar{\rho} \tilde{u}_i \tilde{Y}_k \right) = \frac{\partial}{\partial x_i} \left(\bar{\rho} \mu \frac{\partial \tilde{Y}_k}{\partial x_i} \right) + \tilde{\omega}_k \quad (3.98)$$

To calculate $\dot{\omega}_k$, the system of chemical reaction equations are solved using ordinary differential equation solver. This model can be used in both turbulent and in laminar flame conditions, but the turbulent flame calculations using this solver is not addressed in this thesis.

3.12.1 Favre Averaged Transport Equations

Species and enthalpy conservation equations presented above (Eqn: 3.85) are instantaneous conservation equations. However, to include the turbulent fluctuations of respective scalar quantities, the Reynolds decomposition is used in RANS context, and similarly, the filtered equations are used in LES context. In contrast to incompressible flow simulations, the reacting flow simulations give cross-correlations between scalar/vector fluctuations and density fluctuations. Therefore, in turbulent reacting flows, a density weighted time averaging process is performed to avoid additional closure terms. In turbulent flame solutions the Favre averaged continuity and momentum equations Eqn: 3.99, Eqn: 3.100 are resolved alongside Favre averaged enthalpy equation Eqn: 3.101 and other scalar transport equations. The Reynolds stress terms and scalar flux terms are closed similar to the incompressible turbulent flow approach using eddy viscosity and eddy diffusivity assumptions. In this thesis for the turbulent flames species, transport equations are not solved. Instead, combustion models

are used to incorporate the effects of the chemical reaction.

$$u = \tilde{u} + u'', \tilde{u} = \frac{\overline{\rho u}}{\bar{\rho}}$$

The term u'' represents the effects of velocity-density fluctuations. Using this decomposition method Favre averaged continuity (Eqn: 3.99) and momentum equations (Eqn: 3.100) and enthalpy equations are obtained as Eqn: 3.101.

$$\frac{\partial \bar{\rho}}{\partial t} + \frac{\partial \bar{\rho} \tilde{u}_i}{\partial x_i} \quad (3.99)$$

$$\frac{\partial (\bar{\rho} \tilde{u})}{\partial t} + \frac{\partial (\bar{\rho} \tilde{u}_i \tilde{u}_j)}{\partial x_j} = - \frac{\partial \bar{p}}{\partial x_i} + \frac{\partial (\overline{\tau_{ij}} - \overline{\rho u_i'' u_j''})}{\partial x_j} \quad (3.100)$$

Favre Averaged Enthalpy Equation

$$\frac{\partial \bar{\rho} \tilde{h}}{\partial t} + \frac{\partial \bar{\rho} \tilde{u}_j \tilde{h}}{\partial x_j} = \frac{\partial}{\partial x_j} \left(\Gamma_h \frac{\partial \tilde{h}}{\partial x_j} \right) + S_h \quad (3.101)$$

3.12.2 Steady Laminar Flamelet Method

Steady Laminar Flamelet Method (SLFM) is used for reacting flow simulations, and in this section, the governing equations are outlined. As it is discussed in the Section: 2.4.2, the counter-flow or separated air and oxidizer stream configuration is used in the theoretical derivation of non-premixed flame models. In the simulations of diffusion flames, some underlying assumptions were used,

- Thermodynamic pressure is constant and a Low Mach number flow
- D_k the diffusion coefficient for all chemical species are equal (D)
- Unity Lewis number is assumed $Le_i = \frac{\lambda}{\rho D_k c_p} = 1$

Mixture Fraction definition

Non-premixed combustion of a Fuel (F) and Oxidizer (Ox) to produce products (P) can be represented in a single step reaction as Eqn: 3.102.



If the reaction rate \mathcal{Q} (mol/s) is known then the fuel and oxidiser mass transport equations can be written as Eqn: 3.103 and Eqn: 3.104 respectively, where W_F and W_O are the molar

weights of fuel and oxidiser respectively. Then introducing the variable transformation to include mixture fraction (Z) as in Eqn: 3.105, the above two transport equations can be written as a transport equation of mixture fraction (Eqn: 3.106).

$$\frac{\partial \rho Y_F}{\partial t} + \frac{\partial}{\partial x_i}(\rho u_i Y_F) = \frac{\partial}{\partial x_i} \left(\rho D \frac{\partial Y_F}{\partial x_i} \right) - \nu_F W_F \mathcal{Q} \quad (3.103)$$

$$\frac{\partial \rho Y_O}{\partial t} + \frac{\partial}{\partial x_i}(\rho u_i Y_O) = \frac{\partial}{\partial x_i} \left(\rho D \frac{\partial Y_O}{\partial x_i} \right) - \nu_O W_O \mathcal{Q} \quad (3.104)$$

$$Z = \nu Y_F - Y_O, \nu = \frac{\nu_O W_O}{\nu_F W_F} \quad (3.105)$$

$$\frac{\partial \rho Z}{\partial t} + \frac{\partial}{\partial x_i}(\rho u_i Z) = \frac{\partial}{\partial x_i} \left(\rho D \frac{\partial Z}{\partial x_i} \right) \quad (3.106)$$

Mixture Fraction evaluation

There are different approaches to evaluate the mixture fraction from experimental measurements of species, or from numerical 1D chemistry analysis [230]. Simplest way of evaluating mixture fraction is from analysing a simple two-feed system with fuel side being 1 and oxidizer side 2. A normalized mixture fraction ($0 \leq Z \leq 1$) for two-feed system can be written as Eqn: 3.107 by assuming the fuel and oxidizer stream only carried their species only.

$$Z = \frac{\nu Y_F - Y_{Ox} + Y_{Ox,2}}{\nu Y_{F,1} + Y_{Ox,2}} \quad \nu = \frac{\nu_{Ox} W_{Ox}}{\nu_F W_F} \quad (3.107)$$

The mixture fraction definition based on the simple two-feed system (Eqn: 3.107) is based on assumptions of equal diffusivities of fuel mass fraction and oxidizer mass fraction. Combustion physics only conform to these assumptions in fast chemical reactions that occur in very thin layers (Methane like). In reactions with multiple steps (some slow reactions generate intermediate species) and broad reaction zones no longer conform with above assumptions. Bilger [231] derived a formula based on the local atom balance (Eqn: 3.108) by incorporating element mass fraction (Z_i) This definition is not solely based on the main fuel species and oxidizer species, but it requires all the intermediate species concentrations to be known. For numerical analysis, to incorporate differential diffusion effects, Pitsch [230] derived a transport equation for the mixture fraction Eqn 3.109 with an arbitrary diffusion coefficient. In one-dimensional detail chemistry flame calculations, the mixture fraction scalar transport can be calculated using a small amount of inert gas into the fuel mixture. The SLFM solver *flameletFoam*, the transport of a small amount of Argon is traced a passive scalar to calculate mixture fraction transport in 1D counter-flow flame solution.

$$Z = \frac{2Z_C/W_C + Z_H/2W_H - 2(Z_O - Z_{O,ox})/W_O}{2Z_{C,fu}/W_C + Z_{H,fu}/2W_H + 2Z_{O,ox}/W_O} \quad (3.108)$$

$$\rho \frac{\partial Z}{\partial t} + \frac{\partial}{\partial x_i}(\rho u_i Z) = \frac{\partial}{\partial x_i} \left(\rho D \frac{\partial Z}{\partial x_i} \right) \quad (3.109)$$

3.12.3 Presumed Probability Density Function Method

Steady Laminar Flamelet Method (SLFM)

As discussed in Section: 2.4.2, steady laminar flamelet models assume that the flame structure is a function of only mixture fraction and independent of time. These assumptions only conform to fast reacting simple hydrocarbon fuels. Therefore, to include the effect of finite chemistry (non-equilibrium) effects scalar dissipation rate (χ) is used to parameterise these laminar flamelets. The SLFM assumes any scalar of thermochemical composition field ($\phi = T, Y_k$) of the turbulent can be determined by laminar flamelets if mixture fraction and scalar dissipation rate are known. However, the mean quantities of these scalars are important in an engineering context. To evaluate any mean scalar quantities $\tilde{\phi}$ statistical distribution of mixture fraction and scalar dissipation rates are assumed, thus this method is known as a presumed probability density function method. Therefore flame structure can be calculated using a joint PDF of the mixture fraction and scalar dissipation rate as it is shown in Eqn: 3.110. It can be further assumed that mixture fraction and scalar dissipation rate are statistically independent, further simplifies mean flame composition calculation as Eqn: 3.111. Therefore in this approach pre-integrated laminar flamelet profiles with presumed probability functions can be used to calculate flame composition.

$$\tilde{\phi} = \int_0^\infty \int_0^1 Y_k(Z, \chi) \tilde{P}(Z, \chi) dZ d\chi \quad (3.110)$$

$$\tilde{\phi} = \int_0^\infty \int_0^1 Y_k(Z, \chi) \tilde{P}(Z) \tilde{P}(\chi) dZ d\chi \quad (3.111)$$

The mixture fraction transport equation can be Favre averaged similar to other transport equations to obtain turbulent mixture fraction equation Eqn: 3.112 in which the turbulent mixture fraction flux is approximated by gradient diffusion hypothesis and eddy diffusivity assumptions. This assumption usually causes discrepancies with experimental determination of mixture fraction, due to counter gradient transport of species. Further simplifying the mixture fraction diffusion term by introducing unity Schmidt numbers $Sc = Sc_t = 1$ an effective eddy viscosity μ_{eff} term can be introduced as the summation of molecular and

eddy viscosity (sub-grid viscosity in LES context) (Eqn: 3.113).

$$\frac{\partial}{\partial t}(\bar{\rho}\tilde{Z}) + \frac{\partial}{\partial x_i}(\bar{\rho}\tilde{u}_i\tilde{Z}) = \frac{\partial}{\partial x_i} \left[\left(\frac{\mu}{Sc} + \frac{\mu_t}{Sc_t} \right) \frac{\partial \tilde{Z}}{\partial x_i} \right] \quad (3.112)$$

$$\frac{\partial \bar{\rho}\tilde{Z}}{\partial t} + \frac{\partial \bar{\rho}\tilde{u}_i\tilde{Z}}{\partial x_i} = \frac{\partial}{\partial x_i} \left(\mu_{eff} \frac{\partial \tilde{Z}}{\partial x_i} \right) \mu_{eff} = \mu + \mu_t \quad (3.113)$$

Extensive discussion on suitable probability density function for mixture fraction has been discussed in the literature [232].

In this work the scalars were assumed to be distributed in a $\beta - PDF$ of mixture fraction as in Eqn: 3.114, which shows that to calculate the PDF the mixture fraction variance is required \tilde{Z}''^2 . Therefore, in addition to the mixture fraction, the mixture fraction variance is also added as a lookup variable to the integrated table. Similar to mixture fraction transport equation another transport equation is solved for the mixture fraction variance in RANS approach Eqn: 3.115. In LES context, by assuming the local homogeneous and local sub-grid scale equilibrium the algebraic relationship Eqn: 3.116 can be used to estimate the variance of mixture fraction [168]. Although there have been previous attempts of dynamically calculating the model coefficient C_Z [142], the flameletFoam solver uses a constant model coefficient $C_Z = 1$.

$$\begin{aligned} \tilde{P}(Z) &= Z^{\alpha-1}(1-Z)^{\beta-1} \frac{\Gamma(\alpha+\beta)}{\Gamma(\alpha)\Gamma(\beta)} \\ \alpha &= \tilde{Z} \left(\frac{\tilde{Z}(1-\tilde{Z})}{\tilde{Z}''^2} - 1 \right) \\ \beta &= (1-\tilde{Z}) \left(\frac{\tilde{Z}(1-\tilde{Z})}{\tilde{Z}''^2} - 1 \right) \end{aligned} \quad (3.114)$$

$$\frac{\partial \bar{\rho}\tilde{Z}''^2}{\partial t} + \frac{\partial \bar{\rho}\tilde{u}_i\tilde{Z}''^2}{\partial x_i} = \frac{\partial}{\partial x_i} \left(\mu_{eff} \frac{\partial \tilde{Z}''^2}{\partial x_i} \right) + 2\mu_{eff} \left(\frac{\partial \tilde{Z}}{\partial x_i} \right)^2 - \bar{\rho}\tilde{\chi} \quad (3.115)$$

$$\tilde{Z}''^2 = C_Z \Delta^2 \left| \frac{\partial \tilde{Z}}{\partial x_i} \right|^2, C_Z = 1.0 \quad (3.116)$$

A Dirac- δ function is assumed for the scalar dissipation rate PDF in which the stoichiometric scalar dissipation is used for characterization $\tilde{P}(\chi_{st}) = \delta(\chi - \tilde{\chi}_{st})$ [233]. The scalar dissipation which appears as a sink term in the mixture fraction variance transport equation provides a measure of the decay of scalar fluctuations, where smaller χ represents a

well-mixed scalar field, and larger χ indicates larger mixture fraction gradients and hence unmixedness. Although it is intuitive to model the scalar fluctuation decay based on the fluctuations of scalar variance \widetilde{Z}''^2 by assuming that scalar gradients are sharp in smaller scales which is acceptable at high Reynolds numbers, the χ is modelled as Eqn: 3.117 in RANS context. In LES the filtered scalar dissipation rate $\widetilde{\chi}$ is modelled as Eqn: 3.118.

$$\widetilde{\chi} = C_\chi \frac{\epsilon}{k} \widetilde{Z}''^2, C_\chi \simeq 2.0. \quad (3.117)$$

$$\widetilde{\chi} = C_\chi \frac{\mu_{eff}}{\bar{\rho}} \left| \frac{\partial \widetilde{Z}}{\partial x_i} \right|^2, C_\chi = 2.0 \quad (3.118)$$

3.13 Flamelet Generated Manifold

In this thesis work, the FGM model implemented in OpenFOAM platform by Kröger [234] is used and tested, and in this section, the governing equations are introduced. To calculate 1D laminar flamelets Cantera packages is used and to calculate the mean properties using the instantaneous laminar flame quantities, numerical integration is used by assuming a PDF (\tilde{P}) of progress variable and mixture fraction. In the transport equation of filtered combustion progress variable \tilde{c} (Eqn: 3.119), the Sub-grid progress variable flux term is closed using the gradient diffusion hypothesis.

$$\begin{aligned} \frac{\partial \bar{\rho} \tilde{c}}{\partial t} + \frac{\partial}{\partial x_i} (\bar{\rho} \tilde{c} \tilde{u}_i) &= \bar{\omega}_c + \frac{\partial}{\partial x_j} \left(\bar{\rho} \frac{\mu}{Sc} \frac{\partial \tilde{c}}{\partial x_j} \right) - \frac{\partial}{\partial x_i} \left(\bar{\rho} (\tilde{c} \tilde{u}_i - \tilde{c} \tilde{u}_i) \right) \\ \bar{\rho} (\tilde{c} \tilde{u}_i - \tilde{c} \tilde{u}_i) &= - \frac{\mu_{sgs}}{Sc_t} \left(\frac{\partial \tilde{c}}{\partial x_i} \right) \end{aligned} \quad (3.119)$$

In turbulent partial premixed non-adiabatic flames modelling, laminar flamelets are parametrized by using mixture fraction and enthalpy respectively, in addition to the progress variable. Therefore in description of non-adiabatic partially premixed turbulent flame, two more filtered transport equations are solved as Eqn: 3.120 and Eqn: 3.121.

$$\frac{\partial \bar{\rho} \tilde{Z}}{\partial t} + \frac{\partial}{\partial x_i} (\bar{\rho} \tilde{Z} \tilde{u}_i) = \frac{\partial}{\partial x_i} \left(\left(\frac{\mu}{Sc} + \frac{\mu_{sgs}}{Sc_{sgs}} \right) \frac{\partial \tilde{Z}}{\partial x_i} \right) \quad (3.120)$$

$$\frac{\partial \bar{\rho} \tilde{h}}{\partial t} + \frac{\partial}{\partial x_i} (\bar{\rho} \tilde{h} \tilde{u}_i) = \frac{\partial}{\partial x_i} \left(\bar{\rho} (\alpha + \alpha_{sgs}) \frac{\partial \tilde{h}}{\partial x_i} \right) \quad (3.121)$$

Similar to the SLFM method, in FGM the mean filtered progress variable reaction rates are determined using the assumed PDF profiles of control variables mixture fraction $\tilde{P}(Z)$ and progress variable $\tilde{P}(c)$. It is assumed laminar flamelets are distributed in $\beta - PDF$ variation for all control variables, and an integrated lookup table is created and stored before the solving the flow equations to lookup the mean reaction rate. Eqn: 3.122 and Eqn: 3.123 show relationships used to evaluate the mean reaction progress rate using the PDFs of single control variable for pure premixed situations and, two control variables for partially-premixed case respectively. For multidimensional control variables the presumed joint-PDF is integrated by assuming statistical independence between each control variable. Throughout this work, CO_2 mass fraction is used to calculate the progress variable ($c = Y_{CO_2}$).

$$\overline{\dot{\omega}_c} = \int \dot{\omega}_c \tilde{P}(c) dC \quad (3.122)$$

$$\overline{\dot{\omega}_c} = \int \int \dot{\omega}_c \tilde{P}(c) \tilde{P}(Z) dcdZ \quad (3.123)$$

Scalar variance is required for the $\beta - PDF$ integration and there are many ways to estimate the reacting scalar modelling in the LES context. Instead of calculating the scalar variance using algebraic relationships a transport equation is used in this implementation. Mixture fraction variance and progress variable variance are calculated using the transport equations Eqn: 3.124, Eqn: 3.125 respectively. The source term of the progress variable variance equation ($\widetilde{\dot{\omega}_c c}$) is also preintegrated and stored in the look-up table.

$$\frac{\partial \overline{\rho} \widetilde{Z''^2}}{\partial t} + \frac{\partial}{\partial x_i} (\overline{\rho} \tilde{u}_i \widetilde{Z''^2}) = \frac{\partial}{\partial x_i} \left[\overline{\rho} \left(\frac{\mu}{Sc} + \frac{\mu_{sgs}}{Sc_t} \right) \frac{\partial \widetilde{Z''^2}}{\partial x_i} \right] - 2\overline{\rho} \tilde{\chi}_z \quad (3.124)$$

$$\frac{\partial \overline{\rho} \widetilde{c''^2}}{\partial t} + \frac{\partial}{\partial x_i} (\overline{\rho} \tilde{u}_i \widetilde{c''^2}) = \frac{\partial}{\partial x_i} \left[\overline{\rho} \left(\frac{\mu}{Sc} + \frac{\mu_{sgs}}{Sc_t} \right) \frac{\partial \widetilde{c''^2}}{\partial x_i} \right] - 2\overline{\rho} \tilde{\chi}_c + 2\overline{\rho} \widetilde{\dot{\omega}_c c} \quad (3.125)$$

Scalar dissipation rate for a scalar ϕ ($\phi = c, Z$) is modelled by linear relaxation hypothesis in this implementation,

$$\overline{\rho} \tilde{\chi}_\phi = \overline{\rho D \left| \frac{\partial \phi}{\partial x_i} \right|^2} = \overline{\rho} D \left| \frac{\partial \tilde{\phi}}{\partial x_i} \right|^2 + C_D \frac{\mu_{sgs}}{Sc_t} \frac{\widetilde{\phi''^2} - \tilde{\phi} \tilde{\phi}}{\Delta^2} \quad (3.126)$$

For other thermophysical properties a lookup procedure with four dimensional lookup table is created according to Eqn: 3.127.

$$\begin{aligned}
 \tilde{\rho} &= \int \int \rho(c, Z) \tilde{P}_c \tilde{P}_Z dcdZ \\
 \tilde{\lambda} &= \int \int \lambda \tilde{P}_c \tilde{P}_Z dcdZ \\
 \tilde{\mu} &= \int \int \mu(c, Z) \tilde{P}_c \tilde{P}_Z dcdZ \\
 \tilde{C}_p &= \int \int C_p(c, Z) \tilde{P}_c \tilde{P}_Z dcdZ \\
 \tilde{T} &= \int \int T(c, Z) \tilde{P}_c \tilde{P}_Z dcdZ
 \end{aligned} \tag{3.127}$$

3.14 Artificially Thickened Flame Model

Artificially Thickened Flame model is an alternative approach to the computationally expensive method of resolving the very thin reaction zone of about 0.1 mm in a refined computational domain. In Section: 2.4.1 previous literature on the ATF modelling were discussed and in this Section mathematical formulations of the model are described. Eqn: 3.128 shows the Laminar flame properties (flame thickness and flame speed) relationship with thermochemical properties of the reacting mixture. Laminar flame speed (S_l) is proportional to square root of molecular diffusivity (D) and mean reaction rate ($\bar{\omega}$). Laminar flame thickness (δ_l) is proportional to molecular diffusivity and inversely proportional to the laminar flame speed and

$$\begin{aligned}
 S_l &\propto \sqrt{D \bar{\omega}} \\
 \delta_l &\propto \frac{D}{S_l}
 \end{aligned} \tag{3.128}$$

The reaction rate is usually expressed as an Arrhenius like an exponential function of temperature, which is difficult to be solved even on a LES grid resolution, therefore by multiplying the diffusivity by a factor F results in a flame thickened by a factor F . However, the laminar flame speed can be kept unaltered by dividing the mean reaction rate by a factor F , and this is shown in Eqn: 3.129. This is the principle concept behind the artificially thickened flame modelling.

$$\begin{aligned}
 D &\rightarrow FD \\
 \delta_l &\propto \frac{FD}{S_l} \rightarrow F \delta_l \\
 S_l &\propto \sqrt{(FD) \frac{\bar{\omega}}{F}} \rightarrow S_l
 \end{aligned} \tag{3.129}$$

3.14 Artificially Thickened Flame Model

However, thickening the flame results in a reduction of turbulence-chemistry interaction because the ability for vortices to wrinkle the flame front is reduced. It can be shown that the Damköhler number (Eqn: 2.12) is reduced by a factor F as a result of flame thickening, as shown in Eqn:3.130. Therefore, to compensate for the reduction of turbulent chemistry interaction caused by flame thickening, an efficiency function (E) which is a function of laminar flame characteristics (thickness and speed), sub-grid turbulence characteristics and the thickening factor is introduced.

$$Da = \frac{\tau_t}{\tau_c} = \frac{l_t/u'}{(F\delta_l)/S_l} \rightarrow \frac{Da}{F} \quad (3.130)$$

To account for the effect of smaller eddies compared to the flame thickness (δ_l) an efficiency function was used to estimate the flame surface strain rate induced by the flow field. The concept of efficiency correction was first introduced by Meneveau and Poinot [235], by conducting a direct numerical simulation of a flame front stretching by a vortex pair. In this thesis work the efficiency function derived by Colin et al. [132] is used Eqn:3.131. In LES context a flame wrinkling factor Ξ estimates the amount of flame front wrinkling, and the flame wrinkling function Γ takes combustion filter size Δ_e , laminar flame thickness δ_l and sub-grid turbulent velocity u'_{Δ_e} . Initial flame thickness is δ_l , and thickened flame thickness is $\delta_l^1 = F \times \delta_l$ where F is the thickening factor. The efficiency function magnitude is limited as $1 \leq E \leq F^{2/3}$.

$$\begin{aligned} \Xi(\delta_l^1) &= 1 + \alpha \Gamma\left(\frac{\Delta_e}{\delta_l^1}, \frac{u'_{\Delta_e}}{\Delta_e}\right) \frac{u'_{\Delta_e}}{S_l} \\ \Gamma\left(\frac{\Delta_e}{\delta_l^1}, \frac{u'_{\Delta_e}}{S_l}\right) &= 0.75 \exp\left[-\frac{1.2}{(u'_{\Delta_e}/S_l)^{0.3}}\right] \left(\frac{\Delta_e}{\delta_l^1}\right) \\ \alpha &= \beta \frac{2 \ln(2)}{3C(Re^{1/2}-1)}, C \approx 0.28, \beta \approx 1, Re = l_t u' / \nu \approx 4(l_t/\delta_l^o)(u'/S_l) \end{aligned} \quad (3.131)$$

The efficiency function E is the ratio of flame wrinkling factors of unthickened flame to thickened flame (Eqn: 3.132) (δ_l^o and δ_l^1 are the unthickened and thickened laminar flame thickness respectively).

$$E = \frac{\Xi(\delta_l^o)}{\Xi(\delta_l^1)} = \frac{1 + \alpha \Gamma\left(\frac{\Delta_e}{\delta_l^o}, \frac{u'_{\Delta_e}}{\Delta_e}\right) \frac{u'_{\Delta_e}}{S_l}}{1 + \alpha \Gamma\left(\frac{\Delta_e}{\delta_l^1}, \frac{u'_{\Delta_e}}{\Delta_e}\right) \frac{u'_{\Delta_e}}{S_l}} \quad (3.132)$$

3.14 Artificially Thickened Flame Model

Flame thickening transforms the instantaneous fuel mass fraction equation (Eqn: 3.133) to Eqn: 3.134, where the diffusion coefficient and the source term are changed according to the aforementioned flame thickening principal. Similarly, the energy equation is also modified to correspond with the same flame speed.

$$\frac{\partial \rho Y_F}{\partial t} + \frac{\partial}{\partial x_i} (\rho u_i Y_F) = \frac{\partial}{\partial x_i} \left(\rho D \frac{\partial Y_F}{\partial x_i} \right) + \dot{\omega}_F \quad (3.133)$$

$$\frac{\partial \rho Y_F}{\partial t} + \frac{\partial}{\partial x_i} (\rho u_i Y_F) = \frac{\partial}{\partial x_i} \left(\rho (DE)_F \frac{\partial Y_F}{\partial x_i} \right) + \frac{\dot{\omega}_F E}{F} \quad (3.134)$$

By introducing a reaction regress variable b (1-c), the fuel mass fraction is translated into a regress variable equation as Eqn: 3.135. The diffusivity multiplied by efficiency factor $ED = D + (1 - E)D$ is considered like effective diffusivity similar to turbulence scalar flux closure method using eddy diffusivity concept. The filtered regress variable transport equation (Eqn: 3.136) contains a source term (\tilde{S}_T) that can be calculated using an Arrhenius reaction rate. The reaction rate is for a single step reaction written in the form Eqn: 3.137, where F, O, P represents fuel, oxidizer and products respectively, Y_F, Y_O are the fuel and oxidizer mass fractions, $\nu_F \nu_O$ are the reaction order coefficients, and W_F is the fuel molar mass.

$$b = \frac{Y_F - Y_F^b}{Y_F^u - Y_F^b} \quad (3.135)$$

$$\frac{\partial \rho b}{\partial t} + \frac{\partial}{\partial x_i} (\rho u_i b) = \frac{\partial}{\partial x_i} \left(\rho (DE)_F \frac{\partial b}{\partial x_i} \right) + \frac{E \dot{\omega}_b}{F}$$

$$\frac{\partial \rho \tilde{b}}{\partial t} + \frac{\partial}{\partial x_i} (\rho \tilde{u}_i \tilde{b}) = \frac{\partial}{\partial x_i} \left(\rho (DE)_F \frac{\partial \tilde{b}}{\partial x_i} \right) + \tilde{S}_T \quad (3.136)$$

$$\tilde{S}_T = A \nu_F W_F Y_F^{\nu_F} Y_O^{\nu_O} \exp \left(\frac{-T_a}{\tilde{T}} \right) \left(\frac{E}{F} \right)$$



Legier et al. [134] used an Arrhenius like expression to identify the reacting zone and thicken only the reaction zone with a non-uniform thickening factor across the thickness. However during this work that approach produced numerical instabilities. Therefore flame is identified using the reaction progress variable, and the thickening factor (F) is defined as

a function of the regress variable (b),

$$F(b) = \begin{cases} F > 1, & \text{if } b \leq 0.005 \quad \text{and} \quad b \geq 0.995 \\ F = 1, & \text{otherwise} \end{cases} \quad (3.138)$$

The efficiency function requires the sub-grid scale velocity u'_{Δ_e} , and the sub-grid length scale Δ_e . It was recommended [132] that the Δ_e should be $\Delta_e \approx 10\Delta_x$, in which Δ_x is the LES filter width. Although there are many methods suggested in the literature to estimate the sub-grid turbulent velocity, during this thesis the formulation Eqn: 3.139 is used.

$$u'_{\Delta_e} = 2\Delta_x^3 \frac{\partial^2}{\partial x_i^2} |curl \bar{u}| \quad (3.139)$$

3.15 Chapter Summary

In this chapter, the governing equations for numerical modelling of both non-reacting and reacting flow using FVM were introduced. Governing equations for RANS models used in this thesis namely realizable $k - \varepsilon$, $k - \omega$ -Shear Stress Transport, and Reynolds stress transport models were introduced. Then, LES modelling method was introduced with the three dynamic Sub-Grid-Scale stress models; namely, dynamic Smaogrinsky model, dynamic mixed model, dynamic one-equation model, are introduced. Inlet boundary condition generation, outlet and wall boundary treatments used in this thesis work were also discussed. Error sources affecting LES results were discussed, and subsequently, the LES resolution estimation methods were reviewed. Coherent structure identification methods used to realise the vortex structures in JICF have been presented. Lastly, the governing equations for the combustion models used in all three combustion regimes were outlined. Governing equations for the steady laminar flamelet method based model was introduced in non-premixed combustion modelling context. In premixed combustion, the equations solved in the artificially thickened flame model and the flamelet generated manifold method were described.

Chapter 4

RANS modelling of Jet in Cross-Flow

4.1 RANS modelling of Jet In Cross-Flow

In this chapter results of the numerical simulations of scalar mixing in Jet In Cross-Flow (JICF) problem using RANS turbulence models are presented. Numerical simulations were performed using the commercial CFD code STAR-CCM+ and the open-source C++ code OpenFOAM, and one objective was to compare the performance and abilities of the two codes. These numerical simulations were validated using the experimental study reported by Cárdenas et.al [61, 39] and Galeazzo et.al [37, 38].

The primary objective of this experiment was to investigate the scalar mixing in JICF in contrast to many previous numerical studies which were conducted to understand the complex vortex formation. Since most previous research attempts focused on vortex formation, research on scalar mixing receded and this is explicitly emphasised by Smith and Mungal [236] in their statement "*Despite the abundance of engineering applications involving molecular mixing, the body of work devoted to mixing in the cross-flowing turbulent jet is relatively small*". Simultaneous measurements of the 2-D velocity field and concentration field on high turbulent flow conditions was an important improvement over many previous JICF experimental data where only velocity measurements were available, and most of the previous studies were conducted on low turbulent flows. In addition, high turbulent numbers of the order of $Re \sim 10^4$ and a velocity ratio of approximately $R = 4$ are prominent reasons behind the selection of this experimental data for this study.

4.1.1 Experimental Setup

The experimental work in the study used for validation was performed at the division of Combustion Technology Karlsruhe, Institute of Technology - Germany, where a series of

4.1 RANS modelling of Jet In Cross-Flow

experiments with different velocity ratios varying from 4.15 to 6.62 were conducted. A wind channel with $108 \times 108 \text{mm}^2$ and a circular nozzle with a diameter of $D = 8 \text{mm}$, was used to supply the cross flow and the jet flow into the system. The jet nozzle was flush mounted to the channel, and sufficient distance was provided, so a fully developed velocity profile was obtained. The jet centre was placed 328 mm downstream of the channel inlet to allow a fully developed flow, and the jet pipe was also reported to be sufficient to ensure a fully developed flow. Figure: 4.1 shows the computational geometry which resembles the physical system. Both cross-flow and jet flow were fed air, and di-ethyl-hexyl-sebacate particles were added for PIV measurements while maintaining the particle diameter less than $2 \mu\text{m}$ so the effects of particle size was negligible. Jet-flow was fed with a NO_2 5000 ppm concentration for LIF measurements. Measurement uncertainties are listed in Table: 4.1, where velocity components u, v, w , are velocity components in x, y, z directions respectively, and passive scalar is denoted by C . Boundary conditions are listed in Table: 4.2.

Table 4.1 Measurement uncertainties of the JICF test case [61]

Variable	Uncertainty [$\pm\%$]
w	1.0
u	7.0
C	5.0
w'	1.0
u'	9.0
C'	7.0
u'u'	2.0
w'w'	13.0
u'w'	13.0
u'C'	13.0
w'C'	7.0

Table 4.2 Boundary Conditions [37]

Crossflow inlet	Bulk velocity	9.08 m s^{-1}
	U_{cross}	9.43 m s^{-1}
	Turbulence intensity	1.5%
	Re	6.24×10^4
Jet inlet	Bulk velocity	37.72 m s^{-1}
	Turbulence intensity	7.0%
	Re	1.92×10^4

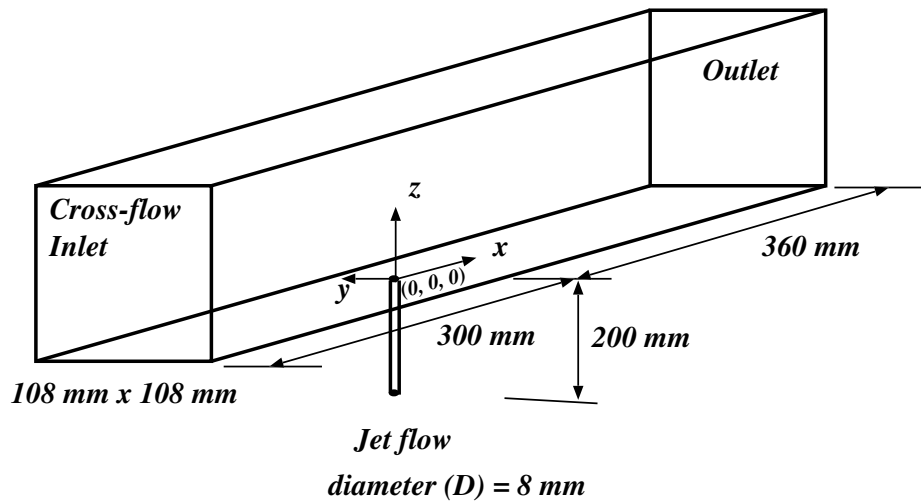


Figure: 4.1 Jet in Cross-Flow test case geometry

4.2 RANS Simulations - STAR-CCM+

STAR-CCM+ CFD software provides turbulence modelling capabilities with many RANS models and second-order accuracy numerical schemes for temporal and convection scheme discretisation. In this section, the modelling of JICF problem was investigated using STAR-CCM+ adaptive mesh solution technique and compared steady-RANS models. In some simulations initially, unsteady RANS simulations were conducted until the velocity field developed into a mean flow structure, and then continued on the steady model to circumvent numerical difficulties arose from the initial transient flow. One of the main objectives of this study was to understand the computational feasibility of industrial-scale problems. Therefore Unsteady RANS (URANS) simulations were avoided because trial simulations revealed that for the computational cost associated with URANS simulations the improvements in results were not appreciable. All model coefficients were unchanged from the default values. In designing the computational grid, the origin of the Cartesian coordinate system was aligned with the centre of the jet orifice at the cross-flow channel surface (Figure: 4.1). The x direction was aligned with cross-flow direction, the y direction was aligned with spanwise direction, and z direction was aligned with the jet flow direction.

4.2.1 Simulation setup

STAR-CCM+ provides automatic unstructured mesh generation facility with adaptive mesh refinement feature. This adaptive mesh refinement facility allows the user to increase mesh resolution locally in critical regions where the flow undergoes a sudden change, or in a region with highly non-linear flow dynamics. In this work, the passive scalar concentration

was used to recursively refine the mesh along the path of jet flow until no appreciable change in the solution was obtained. In order to resolve the boundary layer flow, a layer of prism cells was used close to all solid wall boundaries. A computational grid with 3.7×10^6 hexahedral cells was used for all simulations. Towards the outlet, the mesh size was increased to avoid unnecessary flow recirculation at the outlet boundary. Initial boundary conditions for RANS two-equation models were estimated using the boundary measurements from Table: 4.2 and the relationships given by Eqn: 4.1. Turbulent length scale (l) was estimated using the hydraulic diameter (D_h) and the relationship $l = 0.038 \times D_h$.

$$\begin{aligned}
 k &= \frac{3}{2}(UI)^2 \\
 \varepsilon &= C_\mu \frac{k^{3/2}}{l} (C_\mu = 0.09) \\
 \omega &= \frac{k^{1/2}}{l}
 \end{aligned} \tag{4.1}$$

A passive scalar transport equation was used to model the scalar mixing in jet flow, and the turbulent scalar flux term was modelled with a turbulent Schmidt number Sc_t of 0.9. Passive scalar boundary condition was set to unity at the jet flow inlet and zero at the cross-flow. Hence the passive scalar value indicates the volume fraction of the jet flow. At walls, Neumann boundary condition was specified with zero gradient in the wall normal direction for the passive scalar. In RANS modelling the effect of turbulent Schmidt number on scalar mixing cannot be neglected due to the relative significance of turbulence scalar diffusivity compared to molecular scalar diffusivity, that is numerically enhanced from the introduction of eddy viscosity. Therefore, a sensitivity analysis was performed on the effect of turbulent Schmidt number and results are shown in Appendix (Figure: A.2), and it can be seen that only the $Sc_t = 0.3$ case and $Sc_t = 1.3$ case showed a noticeable deviation in passive scalar distribution when compared to experimental data. Further, it showed that the passive scalar distribution for the case $Sc_t = 0.7$ and 0.9 showed good agreement with experimental measurements in both streamwise and cross-stream directions. Hence, in the subsequent RANS simulations a turbulent Schmidt number of 0.9 was used.

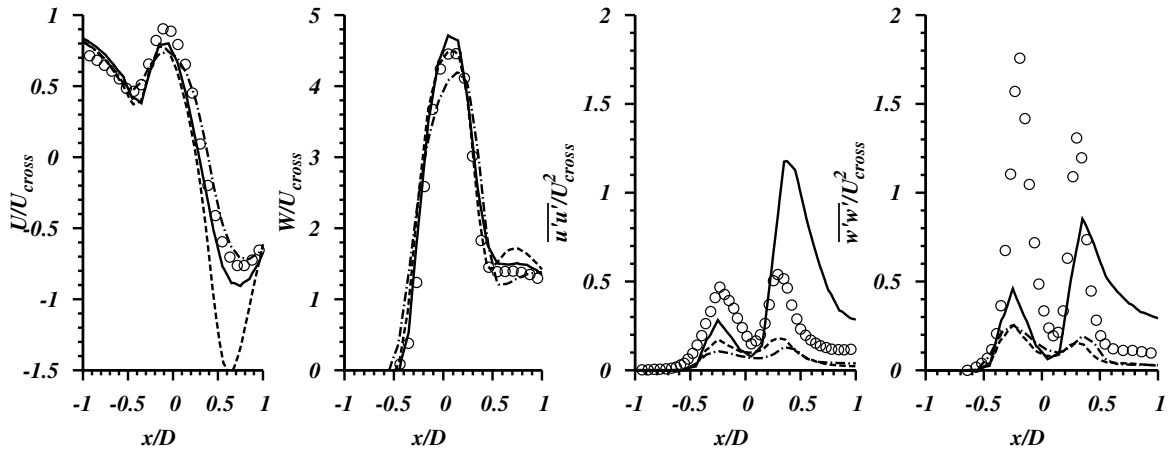
4.2.2 RANS Results - STAR-CCM+

Results of RANS simulations are presented in this section, firstly the effects of inlet boundary conditions are investigated, and then mean velocity field statistics and Reynolds stress components (second-order moments of velocity) are presented in subsequent subsections

followed by passive scalar field results. Results are shown in non-dimensionalized format where spatial dimensions are represented as $x/D, y/D, z/D$ and velocity measurements are represented as U/U_{cross} where U_{cross} is defined as the maximum stream wise velocity at upstream distance $X = -1.5D$.

Because inlet boundary conditions for velocity and other scalars were imposed sufficiently away from the jet nozzle, it is essential to ensure that the flow field in the inspection is independent of imposed boundary conditions. Figure: 4.2 shows non-dimensionalized velocity components in cross-flow direction and in jet flow direction ($U/U_{cross}, W/U_{cross}$) at a jet height close to the jet exit nozzle ($z = 1D$), therefore it can be considered as an approximate estimation of the boundary condition at the nozzle outlet. In Figure: 4.2 the U/U_{cross} variation across the jet nozzle diameter on the centre-plane ($y = 0$) shows an initial deceleration as the cross-flow approaches the jet ($x/D < 0.5$), and then with the jet inflection a flow acceleration can be seen before the flow retardation caused by flow reversal after reaching the lee side edge of the jet ($x/D > 0.5$). All three RANS turbulence models show very good agreement with the upstream flow mean velocity measurements, which is a testimony that the specified inlet boundary conditions agreed sufficiently with experimental conditions. $k - \omega$ -SST model result showed a stronger negative mean velocity component in the lee side of the jet compared to experimental data than other RANS models. In addition, two normalized Reynolds stress components ($\overline{u'u'}/U_{cross}^2, \overline{w'w'}/U_{cross}^2$) predictions agreed qualitatively with experimental data, and both Stress components exhibits local maxima near the edges of the circular jet nozzle ($x/D \simeq -0.5, 0.5$) caused by jet deflection and flow reversal. $k - \omega - SST$ and RST model underpredicted both Reynolds Stress components, whereas realizable $k - \epsilon$ model over-predicts the lee side Reynolds stress $\overline{u'u'}$ which is an indication of stronger prediction of the recirculation zone. Therefore Figure: 4.2 shows that imposition of bulk velocity profiles away from the jet nozzle results in a reasonable agreement of the velocity field and Reynolds stress field, with experimental conditions near the jet outlet.

Numerically predicted mean velocity components in cross-flow and jet flow directions are compared against experimental data in Figure: 4.3. Considering U velocity component, the Realizable $k - \epsilon$ model predictions agree well with experimental measurements at both near field and far field locations. RST model predictions agree well with experimental data only at near field locations $x < 2D$, and it can be seen that at far field locations the U component is underpredicted. $k - \omega$ -SST model consistently overpredicts the negative velocity component resulting in a stronger reverse flow zone near the jet flow, and at far field locations, the positive U velocity is underpredicted. This overprediction of the negative velocity component by the $k - \omega$ -SST model is consistent with the observations on Figure: 4.2. At the lee side edge of the jet nozzle $x = 0.5D$ due to the strong jet deflection experimental



○ Experimental Data , — Realizable $k-\epsilon$, - - - $k-\omega$ SST , - · - · RST

Figure: 4.2 Mean Velocity and Reynolds Stress component variation along x direction at $z = 1D$ height ($y = 0$ plane - STAR-CCM+, Experimental data : [37])

data show a negative non-dimensionalized velocity of $U/U_{cross} \approx -0.8$, whereas $k-\omega$ -SST model over predicted the value $U/U_{cross} \approx -1.25$. Therefore, according to these observations realizable $k-\epsilon$ model show good agreement with experimental measurements in the prediction of the mean velocity component in cross-flow direction. Similarly, the W velocity component prediction also shows that Realizable $k-\epsilon$ model predictions agreed well with experimental data both at near field and far field, and RST model agrees well with experimental data at near field locations and shows a disparity at far field locations. However, at far field distances, all three model results show an overestimation of the velocity component. Whereas, $k-\omega$ -SST model exhibits a deviation from experimental measurements especially in downstream locations indicating that the model result shows an over penetration of the jet compared to experimental data. Therefore, by inspection of both velocity components, $k-\epsilon$ model stands out as the best model to predict velocity field at both near field and far field locations, and RST model predicts the velocity field to be in good agreement at near field locations.

Figure: 4.4 shows non-dimensionalized Reynolds stress components $\overline{u'u'}$ and $\overline{w'w'}$ compared against experimental data for different locations on the $y = 0$ plane. Apart from the realizable $k-\epsilon$ model, other two models show a severe underprediction of both Reynolds stress components. The Reynolds stress component $\overline{u'u'}$ prediction also show that realizable $k-\epsilon$ model results agree with experimental results than other two model results where stress component is severely underpredicted. Along the line plot at $x = 0.5D$ which is at the lee side edge of jet nozzle, shows a strong overprediction of stress component $\overline{u'u'}$ near the noz-

zle edge. This can be understood as a result of strong turbulent kinetic energy source caused by the jet flow deflection and by the reverse flow generation. Similarly, the Reynolds stress component $\overline{w'w'}$ prediction shows that realizable $k - \varepsilon$ model predictions agreed quantitatively with experimental results whereas other two model results are under-predicted. It can be seen that Reynolds stress components maxima occurred at increasing z heights with increasing downstream distance as the jet profile evolves, and the realizable $k - \varepsilon$ predictions of Reynolds stress components agree well with the peak of experimental stress variation. Therefore, it shows that the realizable $k - \varepsilon$ model can predict the jet penetration to agree with experimental observations. Figure: 4.5 compares mean velocity field and the normal Reynolds stress component in the cross-flow direction, at three different jet heights. It shows that the realizable $k - \varepsilon$ model results agree with velocity predictions at all three jet heights, and also Reynolds stress component is predicted both quantitatively and qualitatively better than other two RANS models.

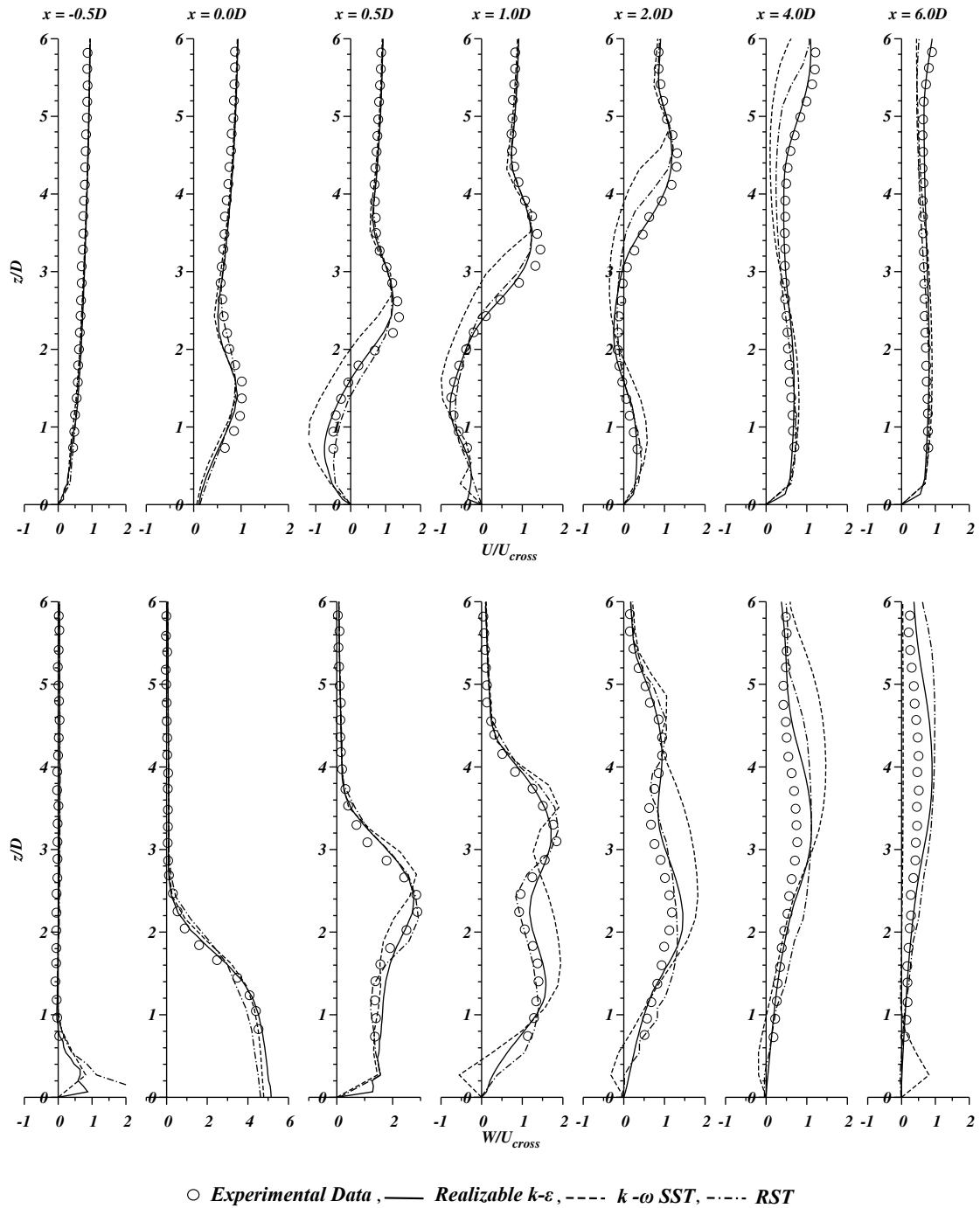


Figure: 4.3 Mean Velocity components in flow direction at $y = 0$ (Experimental data : [38]).

4.2 RANS Simulations - STAR-CCM+

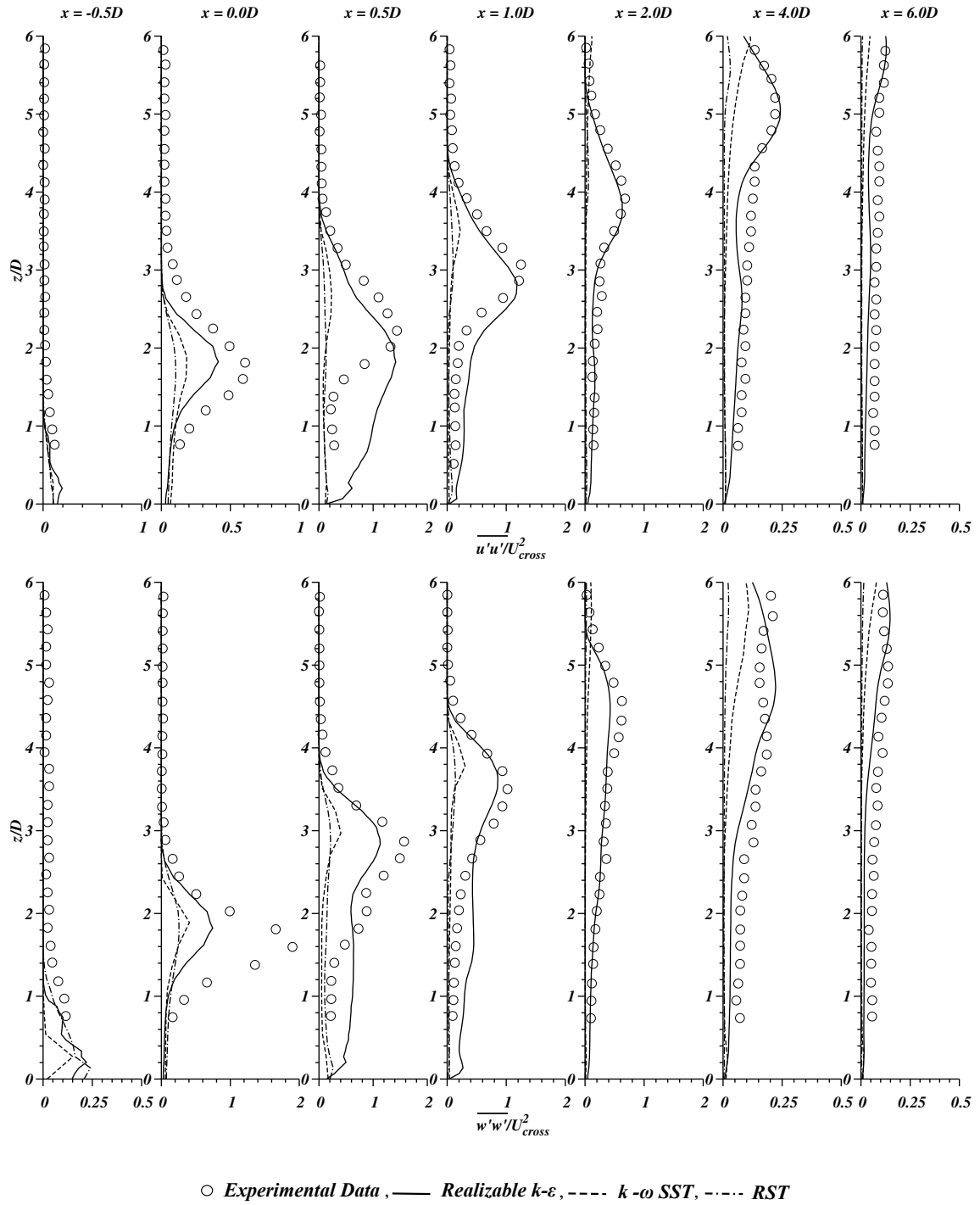


Figure: 4.4 Reynolds Stress components variation in flow direction $y = 0$ (Experimental data : [38]).

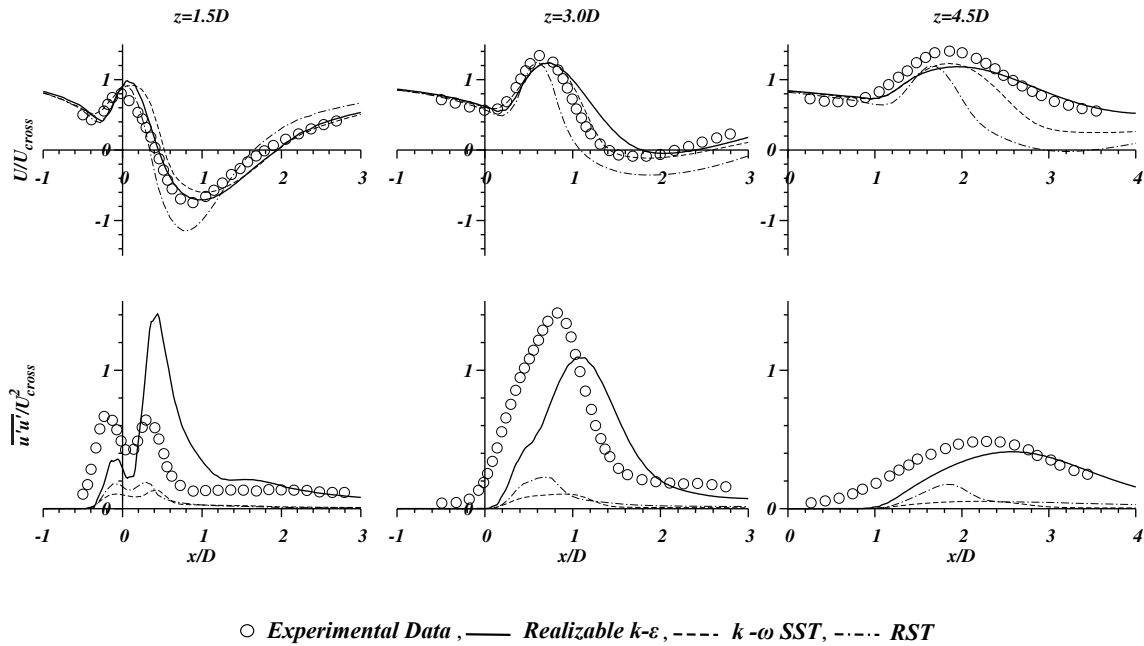


Figure: 4.5 Mean Velocity and Reynolds Stress component at different at three different heights on the plane $y = 0$ (Experimental data : [37]).

Reynolds stress components were modelled using Boussinesq approximation in two equation models as $\overline{\rho u'_i u'_j} = [2/3 \rho k I - 2 \mu_t S_{ij}]$, thus over estimation of turbulent kinetic energy (k) reflects into an increase of Reynolds stress component, while over estimation of eddy viscosity ν_t results in a decrease of Reynolds stress magnitude. Effects of overprediction of turbulent kinetic energy therefore directly translate into overprediction of Reynolds stress. As Figure: 4.6 shows realizable $k - \epsilon$ model results produce excessive amount of turbulent kinetic energy in the initial jet deflection zone (upwind side) as much as $100 m^2/s^2$, while $k - \omega$ -SST model predicted turbulent kinetic energy is limited to $5 m^2/s^2$ near this region, and RST model predictions are even smaller. In addition, realizable $k - \epsilon$ model results show a larger downstream region with very high turbulent kinetic energy than $k - \omega$ -SST model. Figure: 4.7 shows realizable $k - \epsilon$ model predicts nearly five times eddy viscosity μ_t as $k - \omega$ -SST model. Therefore, even if realizable $k - \epsilon$ model produced an excessive amount of eddy viscosity, due to its significantly higher turbulent kinetic energy production the Reynolds stress components magnitude are comparatively more significant than other two RANS models and agree well with experimental data. Nevertheless, the amount of eddy viscosity produced by the realizable $k - \epsilon$ model is unphysical, because it is known that near the jet flow ejection inviscid flow dynamics are more dominant than viscous flow dynamics.

The excess eddy viscosity produced near the jet deflection zone is an attribute of the $k - \varepsilon$ models and known as *stagnation point anomaly* [237], that produces an excess amount of turbulent kinetic energy and eddy viscosity in regions of greater strain. This anomaly is seen in impinging jets, aerofoils and flows around blunt objects [238, 239]. Similarly, the jet-flow and cross-flow interaction also create a highly strained jet flow stream, and cross-flow is obstructed causing a stagnation like a path along the jet flow bend. Additionally at the lee side nozzle edge cross-flow is highly strained, and as a result, a zone with high turbulent kinetic energy and turbulent viscosity can be observed from the realizable $k - \varepsilon$ results as shown in Figure: 4.6 and Figure: 4.7. Therefore, the overprediction of Reynolds stress along the line $x = 0.5D$ on Figure: 4.4 can be explained by the overprediction of turbulent kinetic energy. Although the $k - \omega$ -SST model implementation uses a limiter on turbulence production term P_k (Eqn: 3.11) to avoid overprediction of turbulent kinetic energy, the model results of Reynolds stress components show severe underprediction in the downstream region. This indicates that the turbulence statistics field predicted by $k - \omega$ -SST model in the high strain region is not satisfactory.

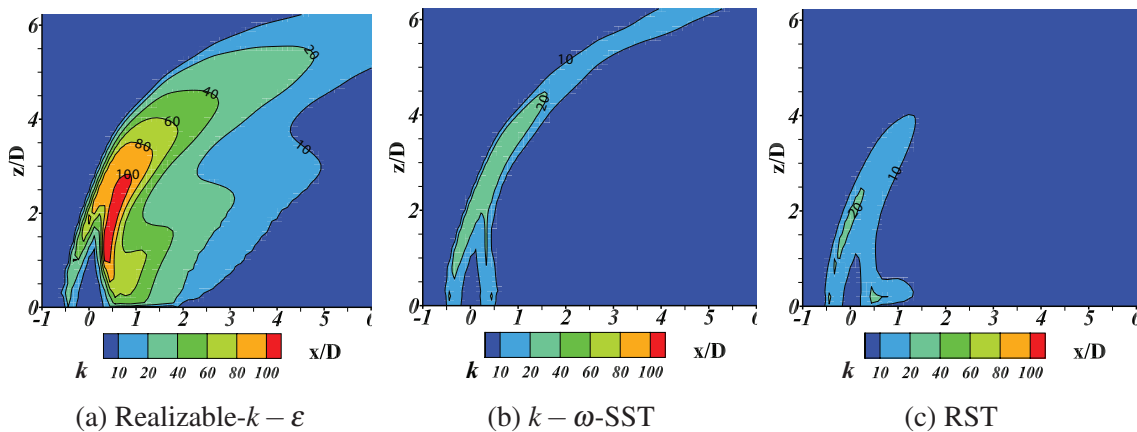


Figure: 4.6 Turbulent Kinetic Energy ($\text{k/m}^2\text{s}^{-2}$) Prediction by three RANS models

Figure: 4.8 shows two-dimensional contours of mean velocity in the streamwise direction at $z = 1.5D$ height. The zone with large negative streamwise velocity shown at the centre of contour map indicates the flow reversal and the small low-velocity zone in the upstream of the jet nozzle ($x < 0$) shows the flow stagnation caused by the jet stream interaction. All three RANS models, in general, predict the negative streamwise velocity at the centre, but the $k - \omega$ -SST model prediction of this flow reversal zone is shown to be shorter in the downstream distance, whereas other two models results show good quantitative and qualitative agreement with experimental results. Besides of the core jet flow, two positive streamwise velocity locations indicates the cross-flow acceleration around the

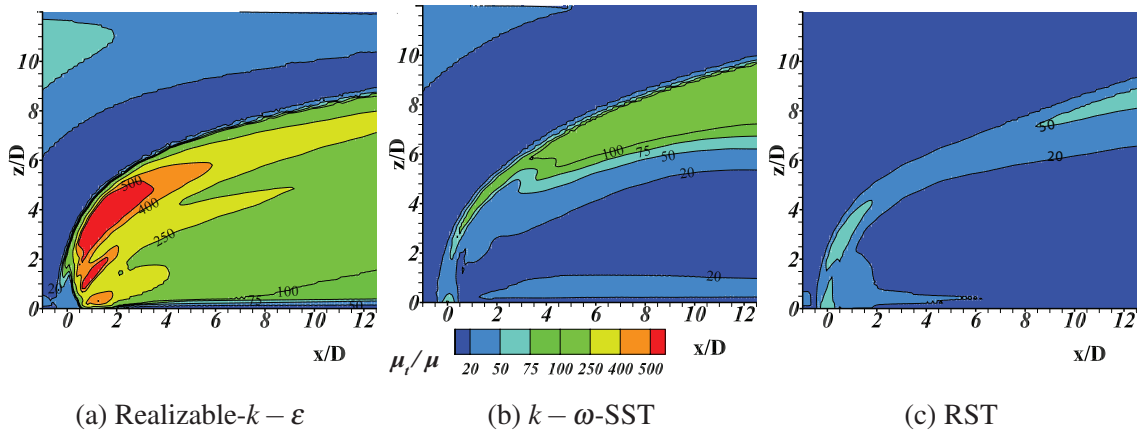
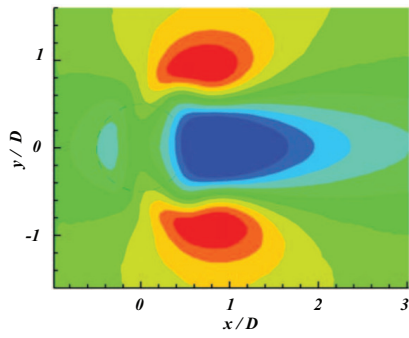


Figure: 4.7 Turbulent viscosity ratio (μ_t/μ) prediction by three RANS models

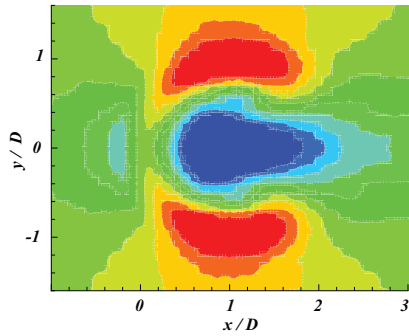
central jet. Both realizable $k - \varepsilon$ and $k - \omega$ -SST models show extended regions of flow acceleration compared to experimental measurements, while RST model results show a smaller cross-flow acceleration zone and thus exhibit similar agreement with experimental results at this height. Figure: 4.9 shows the two-dimensional contours of spanwise direction velocity at $z = 1.5D$ height. Positive and negative spanwise velocity zones indicate flow direction change of the cross-flow due to jet interaction with cross-flow. As shown, both two equation RANS models predictions are similar, yet stronger flow direction change is seen in numerical predictions than experimental results, while RST model prediction shows a more diffused zone of peak velocity. Therefore even though RST model predicted mean velocity field along line plots in the symmetric plane ($y = 0$) agree with experimental measurements, considering the total velocity field prediction the RST model prediction does not show adequate similarity with experimental data.

Figure: 4.10, Figure: 4.11 and Figure: 4.12 show non-dimensionalized Reynolds stress components $\overline{u'u'}$, $\overline{v'v'}$, $\overline{u'v'}$ predictions by realizable $k - \varepsilon$ and $k - \omega$ -SST models compared with experimental data at $z = 1.5D$ as two dimensional contours. Reynolds Stress Transport model results are excluded in this comparison because predicted Reynolds stress components were small in magnitude. As Figure: 4.10 shows the normal Reynolds stress component ($\overline{u'u'}$) in streamwise direction show two zones besides the jet with higher stress in experimental measurements. These higher stress regions are consistent with the physical observation of downstream velocity increase around the jet plume as it is shown in Figure: 4.8. Contrarily realizable $k - \varepsilon$ model shows a zone with higher stress component $\overline{u'u'}$ in the zone where jet penetration occurs. $k - \omega$ -SST model predictions show numerical under-prediction of Reynolds stress components compared to both experimental results and $k - \varepsilon$ model results.

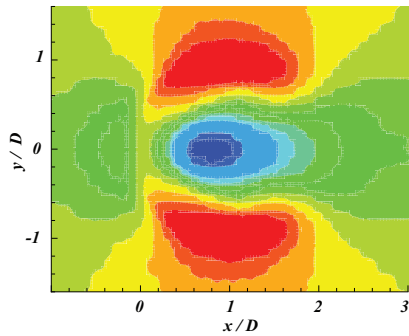
Figure: 4.11 shows the Reynolds stress component contour comparison in cross stream direction $\overline{v'v'}$. The experimental data show two zones with higher Reynolds stress above the two lateral edges of the jet nozzle, which corresponds to the jet flow deformation in cross-stream direction. However, neither of two-equation models exhibit such two distinct locations with similar magnitudes as experimental data for Reynolds stress component $\overline{v'v'}$. The realizable $k - \varepsilon$ model results show nearly 30% numerical underprediction compared to experimental results, and $k - \omega$ -SST under predicts by approximately 60%. As Figure: 4.12 shows, Reynolds stress component $\overline{u'v'}$ predicted by the realizable $k - \varepsilon$ model not only show quantitative agreement with experimental data but a qualitative agreement also can be seen. Comparatively the $k - \omega$ -SST model predictions significantly underpredicted the Reynolds shear stress component.



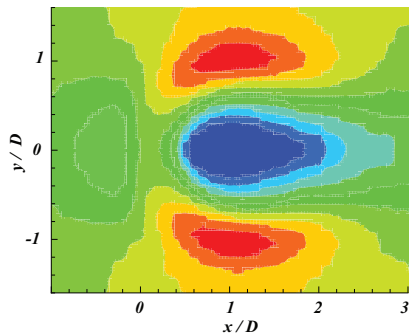
(a) Experimental data



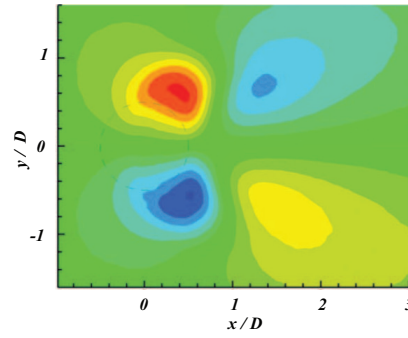
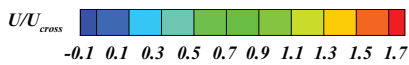
(b) Re $k - \epsilon$



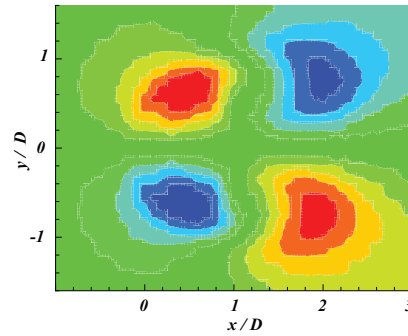
(c) $k - \omega$ -SST



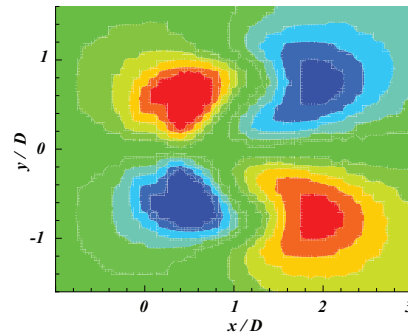
(d) RSM



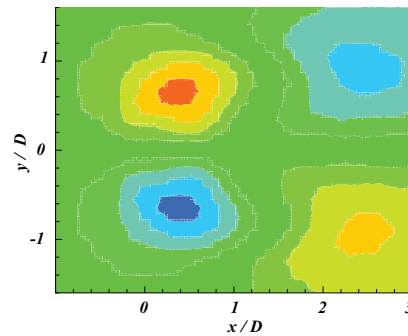
(a) Experimental data



(b) Re $k - \epsilon$



(c) $k - \omega$ -SST



(d) RSM

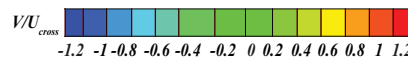


Figure: 4.8 U/U_{cross} at $z = 1.5D$ plane, RANS (STAR-CCM+), experimental data from [37].

Figure: 4.9 V/U_{cross} at $z = 1.5D$ plane, RANS (STAR-CCM+), experimental data from [37].

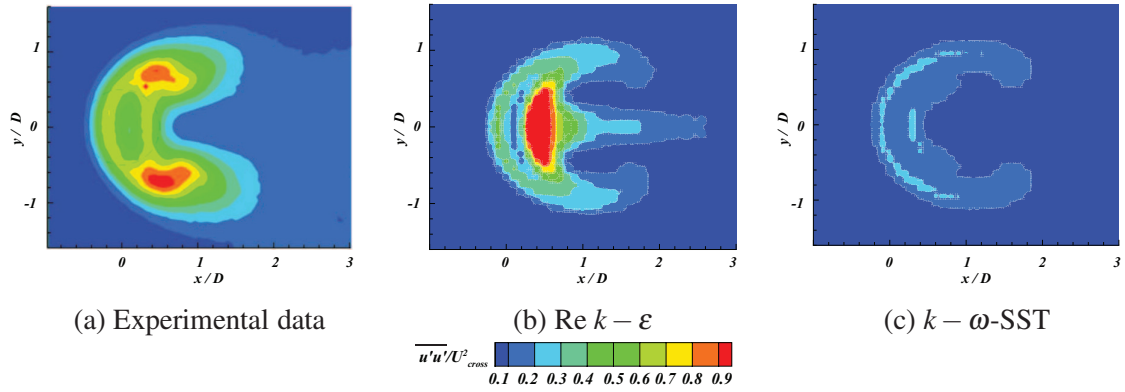


Figure: 4.10 $\overline{u'u'}/U_{cross}^2$ at $z = 1.5D$ plane - RANS(STAR-CCM+), experimental data from [37] taken under permission.

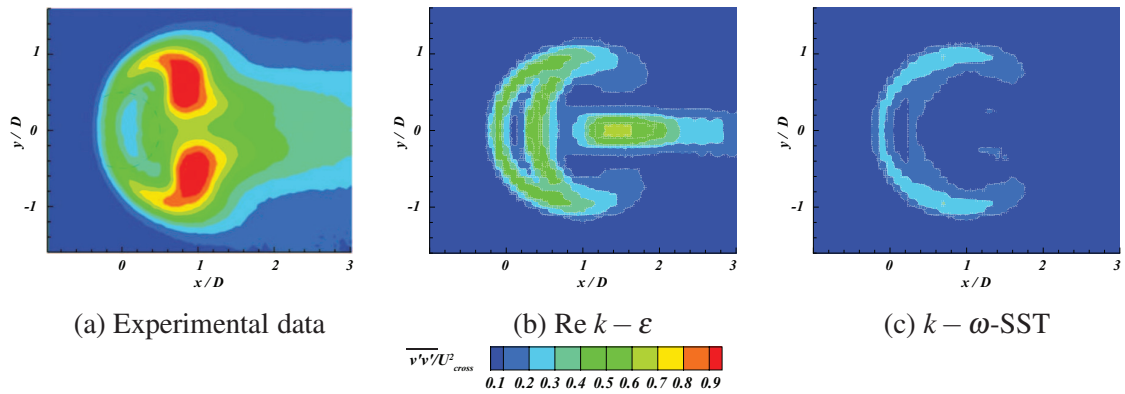


Figure: 4.11 $\overline{v'v'}/U_{cross}^2$ at $z = 1.5D$ plane - RANS(STAR-CCM+), experimental data from [37] taken under permission.

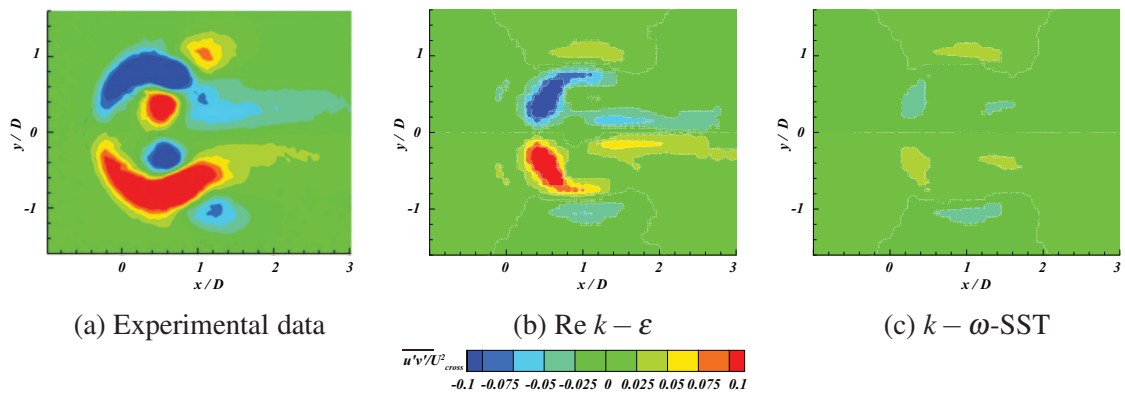


Figure: 4.12 $\overline{u'v'}/U_{cross}^2$ at $z = 1.5D$ plane - RANS(STAR-CCM+), experimental data from [37] taken under permission.

Passive scalar distribution from JIC is an essential investigation of this numerical study. Figure: 4.13 shows the comparison between numerical prediction and experimental measurements of passive scalar distribution along z direction lines on the symmetric plane ($y = 0$). Realizable $k - \varepsilon$ model shows better agreement with experimental data than other two RANS models at both near field and far field locations, while other two RANS model predicted scalar concentration shows an over penetrated jet profile by about $1D$ in the z direction. Along the line of $x = 2D$, $k - \varepsilon$ model results show a deviation from experimental data at heights below $z \leq 3.5D$, yet the peak concentration values coincide with experimental data, further suggesting that the jet penetration height is predicted better than the other two models. At downstream distances beyond $5D$, the discrepancy between numerical results and experimental data show an attenuation, but the one-dimensional variation of passive scalar concentration along the symmetric plane is insufficient to verify the overall accuracy of scalar mixing field.

Figure: 4.14 shows passive scalar concentration and time averaged non-dimensionlized turbulent scalar flux component ($\overline{u'c'}/U_{cross}$) variation along stream wise direction lines, at three different heights. At the height of $z = 1.5D$ passive scalar concentration predicted by the realizable $k - \varepsilon$, and RST models agree well with experimental data, while $k - \omega$ -SST model shows a steeper concentration spread rate than experimental data in the lee side of the jet. However, on the upstream side ($x < 0$) all three model predictions coincide with experimental data.

At the height of $z = 3.0D$ realizable $k - \varepsilon$ model underpredicts the peak passive scalar concentration by about 15%, but qualitatively the scalar spreading rate in the downstream direction is predicted to be in good agreement with experimental data. However, the $k - \omega$ -SST model and the RST model predict the peak concentration of $C = 0.6$, but the scalar decay rate in the downstream direction is overpredicted, hence beyond $x = 1.5D$ downstream distance, the realizable $k - \varepsilon$ model prediction agree better with experimental data. Similarly, at the height of $z = 4.5D$ also, with increasing downstream distance the $k - \omega$ -SST model and the RST model predictions produce a sharper decay rate in the x direction than experimental data pattern. However, the maximum concentration level at $z = 4.5D$ height is predicted to be within 10% accuracy by all these models. Therefore, considering all three passive scalar distributions at $z = 1.5D, 3.0D, 4.5D$ heights, the realizable $k - \varepsilon$ model predictions agree better with experimental results than other two models especially in downstream distances. However, notably the maximum concentration level from realizable $k - \varepsilon$ model shows an underprediction indicating an increased scalar diffusion at near field distances. The increase in scalar diffusion in near-field predicted by realizable $k - \varepsilon$ model

can be explained by the increased eddy viscosity, hence causing the increase in effective scalar diffusivity.

Non-dimensional turbulent scalar flux component ($\overline{u'c'}/U_{cross}$) variation as shown in Figure: 4.14 illustrates that the realizable $k - \epsilon$ model agree better with the experimental results in both magnitude and direction compared to other two RANS models. Turbulent scalar flux is calculated by post-processing the mean scalar field gradient and using eddy diffusivity. Since the gradient diffusion hypothesis (Eqn: 2.3) is used in the calculation of turbulent scalar flux, the scalar flux gradient takes the opposite sign of scalar gradient. At $z = 1.5D$ height all three models show the turbulent scalar flux pattern as same as the experimental variation. Numerically only the realizable $k - \epsilon$ model results are in the order of magnitude as experimental values, while other two model predictions were severely underpredicted. Similarly at $z = 3.0D, 4.0D$ heights also the realizable $k - \epsilon$ model results only match with the magnitude of experimental data of turbulent scalar flux. As discussed earlier and showed in Figure: 4.7 the realizable $k - \epsilon$ model produce a significantly larger amount of eddy viscosity compared to other two RANS models and therefore increases the calculated eddy diffusivity (μ_t/Sc_t) causing the magnitude of turbulent scalar flux to be greater than other two RANS models. Therefore, the better agreement observed between the turbulent scalar flux values by the realizable $k - \epsilon$ and experimental data can be attributed to the increased eddy viscosity generated by realizable $k - \epsilon$ model.

Since the one-dimensional variation of passive scalar distribution is insufficient to conclude the accuracy of scalar field predictions, in Figure: 4.15 experimental and RANS predictions of passive scalar distribution contours on a 2D plane at $z = 1.5D$ height are compared. The passive scalar distribution shows a kidney-shaped variation because the cross flow bends around the core jet flow. Therefore the core of the kidney shape shows higher scalar concentration than the outer region. All three RANS models reproduced the kidney-shaped passive scalar structure well, however, increased scalar diffusion compared to experimental data were observed, especially in the direction of cross-flow. RST model shows more scalar diffusion in downstream direction than other two RANS models, and this is understood to be caused by the numerical relaxation introduced to reduce the stiffness of six Reynolds stress transport equations.

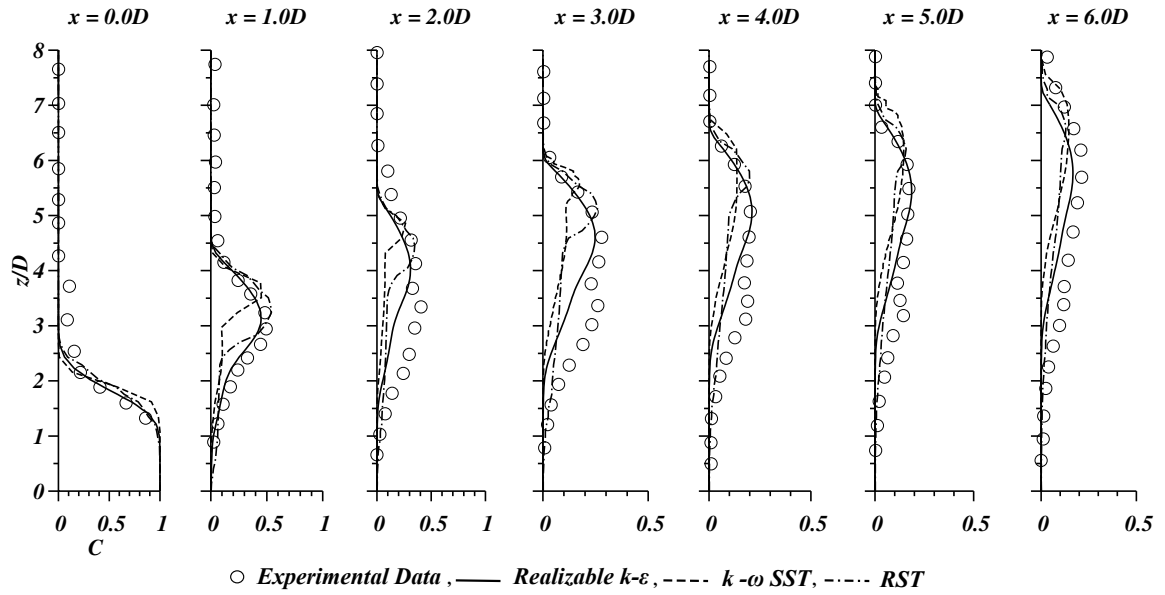


Figure: 4.13 Passive Scalar prediction comparison in z direction on the $y = 0$ plane (Experimental data : [39]).

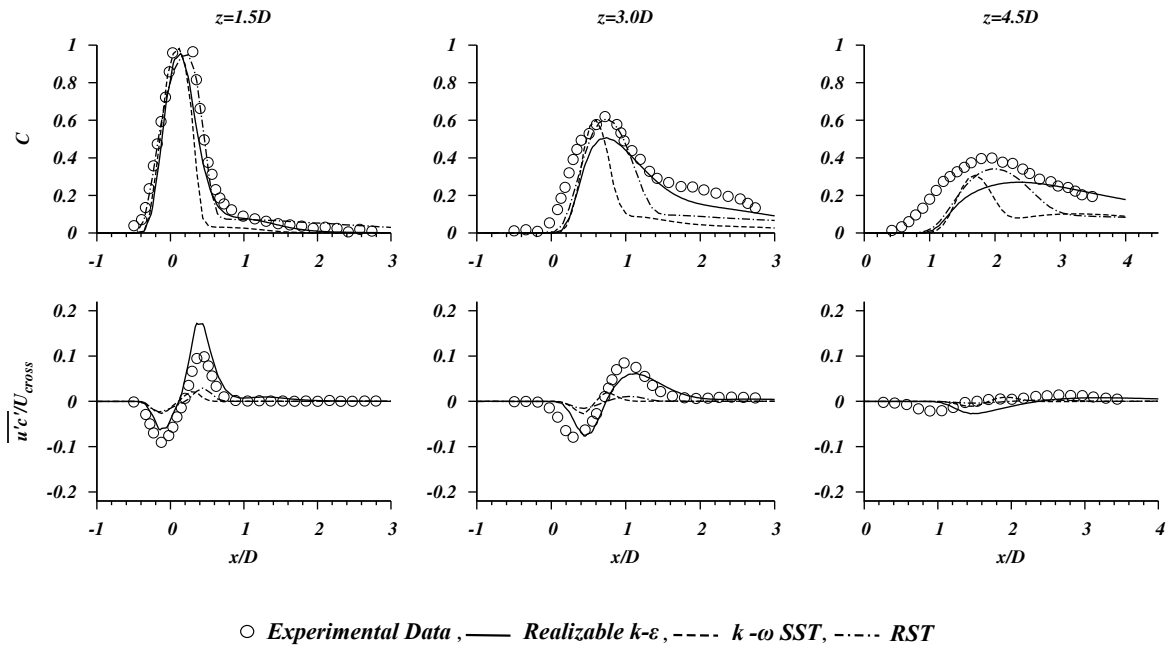
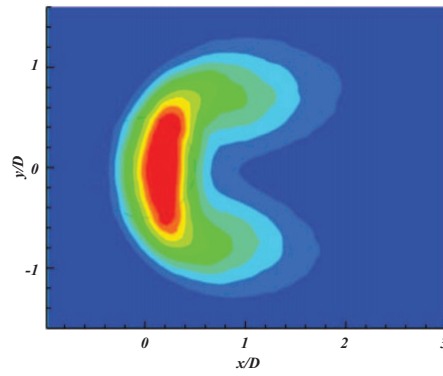
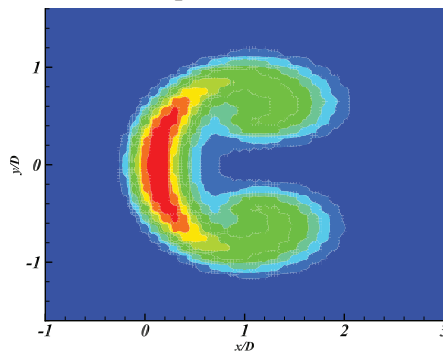


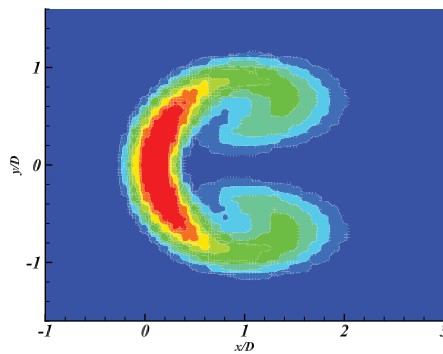
Figure: 4.14 Passive Scalar prediction compared in x direction on the $y = 0$ plane (Experimental data : [37]).



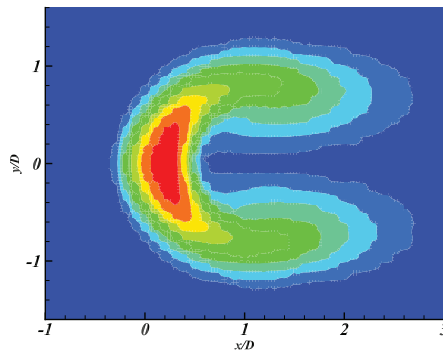
(a) Experimental data



(b) Re $k - \epsilon$



(c) $k - \omega$ -SST



(d) RSM

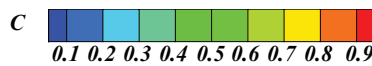


Figure: 4.15 Mean passive scalar concentration C at $z = 1.5D$ plane, experimental data from [37] taken under permission.

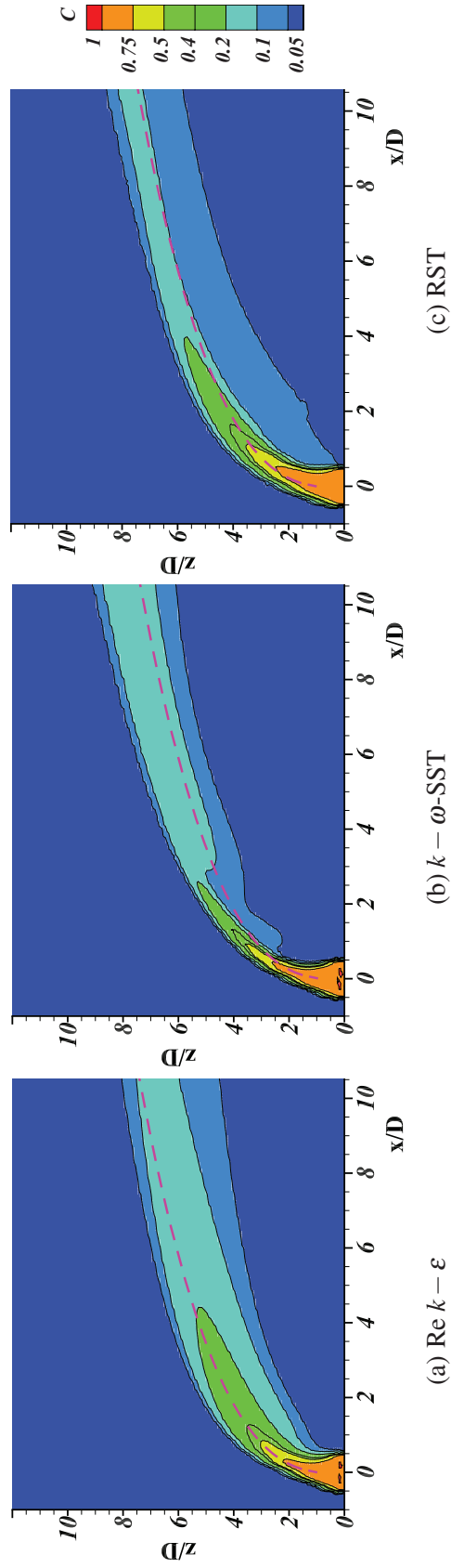


Figure: 4.16 Passive Scalar concentration predictions by three RANS models - STAR-CCM+, dashed line indicates the jet path predicted by empirical relationship Eqn: 4.2

Empirical relationships for jet flow profiles have been developed by many authors, and they can be used as a preliminary test to validate numerical simulations [17]. Jet trajectory defined as the locus of maximum velocity for a circular jet in cross-flow can be approximated by Eqn: 4.2 [240].

$$\frac{y}{D} = a J^b \left(\frac{x}{D} \right)^c \quad (4.2)$$

J is the momentum ratio between cross-flow and jet flow, and empirical constants vary as $0.7 \leq a \leq 1.3$, $0.36 \leq b \leq 0.52$ and $0.28 \leq c \leq 0.40$. However in this case constants were fixed at $a = 0.85$, $b = 0.47$, $c = 0.38$ which were considered to give reasonable estimation for intermediate momentum ratios. Even though the maximum scalar concentration does not directly correlate with the locus of maximum velocity, penetration of the passive scalar can be considered as a measurable quantity of the maximum velocity especially near the jet exit.

Figure: 4.16 shows the passive scalar distribution on the central ($y = 0D$) plane compared against the jet trajectory predicted by the empirical relationship Eqn: 4.2, and it can be seen that realizable $k - \varepsilon$ model agrees with the empirical jet trajectory better than other two RANS models. The maximum penetration levels of each scalar concentration contour levels from realizable $k - \varepsilon$ model results coincided with jet trajectory path until $x \approx 4.0D$. It implies that the jet penetration predicted by this model is in good agreement with the empirical model as well as experimental data as previously shown in Figure: 4.13 and Figure: 4.14. Further, it can be seen that both $k - \omega$ -SST model and RST model results show an over penetration of jet path compared to realizable $k - \varepsilon$ model.

4.3 RANS simulation - OpenFOAM

4.3.1 Simulation set-up

In this section results of the RANS modelling of the same JICF configuration using the open-source CFD code OpenFOAM are presented. A pure hexahedral cell block-structured computational grid was used with a total of 2.4×10^6 cells, and 25 cells were placed across the jet nozzle diameter. Figure: 4.17 illustrates a cross-sectional view of the grid structure near the jet flow and cross flow interface and a quartile of the grid structure inside the jet nozzle and surrounding. No local mesh adaptation was used, yet reasonably good mesh-independent results were obtained for this cell count. The same three RANS models namely the realizable $k - \varepsilon$ model, $k - \omega$ -SST model and Reynolds Stress Transport (RST) model by Launder and Gibson were used for the computation with default model coefficients for

OpenFOAM-2.2.x. In these simulations also, the inlet boundary conditions were imposed far away from the jet and cross-flow interaction zone, and turbulence levels and inlet boundary conditions are same as shown in Table: 4.2. Across all OpenFOAM RANS simulations, the y^+ value was maintained such that jet flow conducting pipe was modelled with an average y^+ value of 30 and the cross-flow conducting channel was modelled with an average y^+ value of 35.

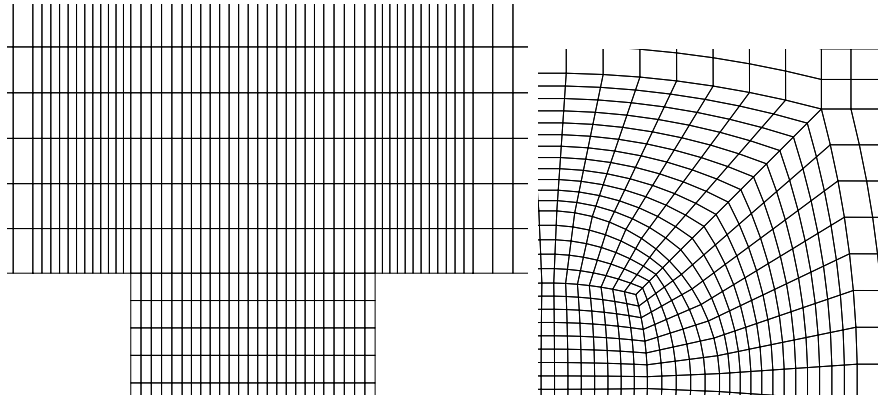


Figure: 4.17 OpenFOAM RANS mesh structure

4.3.2 RANS Results - OpenFOAM

Figure: 4.18 shows the both mean velocity components U, W agree reasonably well with experimental data for all three RANS models, only $k - \omega$ -SST model showed an excess cross-flow deceleration. Similar to STAR-CCM+ simulation results (Fig: 4.2), realizable $k - \epsilon$ model and the RST model produce mean velocity components that agree very well with experimental data, while $k - \omega$ -SST model result overpredicts the negative velocity in cross-flow velocity resulting from the reverse flow. The Reynolds stress component $\overline{u'u'}$ predicted by both two-equation turbulence models nearly coincide with experimental measurements, whereas the RST model prediction significantly underpredicts the stress magnitude. The Reynolds stress component in the jet flow direction ($\overline{w'w'}$) prediction show that all RANS models severely underpredict the peak stress magnitude value, and similar to $\overline{u'u'}$ stress prediction, RST model produced a significant underprediction in magnitude compared to other two RANS models. When compared with the results of STAR-CCM+ (Fig: 4.2) results from OpenFOAM $k - \omega$ -SST model performance show a significant improvement in prediction of the magnitude of Reynolds stress components. In addition, OpenFOAM results showed more consistent behaviour between the two two-equation RANS models compared to STAR-CCM+ results.

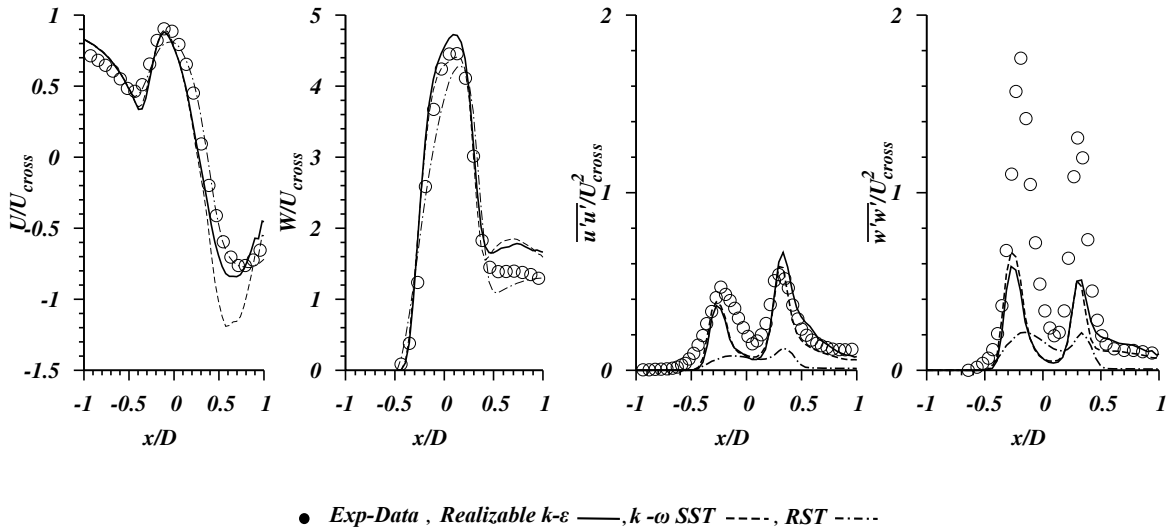


Figure: 4.18 Mean Velocity and Reynolds Stress component variation along x direction at $z = 1D$ height ($y = 0$ plane - OpenFOAM, Experimental data : [37]).

Figure: 4.19 illustrates the comparison of predicted mean velocity components U, V and experimental measurements along vertical lines on $y = 0D$ plane. Mean velocity in cross-flow direction U shows virtually indistinguishable predictions from all three RANS models and beyond $x = 2D$ downstream distances at elevated jet heights velocity magnitude is underpredicted. Mean velocity component W shows good agreement with experimental results in the near field, however with increasing downstream distance all three RANS models show overprediction of the velocity magnitude. From the mean velocity field predictions all three RANS models show similar predictions for both mean velocity components, therefore it is safe to declare all three RANS models perform similarly in predicting the mean velocity field statistics. Therefore, when compared with the results from STAR-CCM+ results (Figure: 4.3) again, a similarity between the two-equation model results can be seen in OpenFOAM results as well. In conclusion, when both mean velocity components shown here are considered, at near-field distances and far-field distances, it can be seen that the realizable $k - \epsilon$ model predictions show better agreement with experimental data than other two RANS models.

Figure: 4.20 illustrates the Reynolds stress components predictions comparison against experimental measurements. Reynolds stress component $\overline{u'u'}$ results show that the realizable $k - \epsilon$ model predictions agree the best with experimental results. Numerical predictions by the $k - \omega$ -SST model show a decrease in magnitude than the realizable $k - \epsilon$ predictions in near field region ($0.5D < x < 4.D$), however at far field distances both model predictions nearly coincide. Both two-equation model predictions show more similarity with each

other than the RST model. More importantly, it can be seen that the magnitude of RST model stress predictions is severely underpredicted, but a close inspection reveals that predicted stress variation coincide with the pattern in other two models. Similarly the Reynolds stress component $\overline{w'w'}$ predictions also show that realizable $k - \varepsilon$ model result agreed better with experimental results than other two RANS models both quantitatively and qualitatively. However, even the realizable $k - \varepsilon$ model predicted values of Reynolds stress component near the highly strained areas are significantly underpredicted when compared with experimental measurements. As downstream distance increases the flow strain diminishes, hence all three model results show to have a similar magnitude of Reynolds stresses. The general observation from Figure: 4.20 is that near the jet flow deflection zone where the flow is dominated by inviscid flow dynamics the realizable $k - \varepsilon$ stress prediction shows superior agreement with experimental data then $k - \omega$ -SST model, yet further upstream where the dominant effects inviscid flow dynamics fade away both models predict Reynolds stress components. When compared with STAR-CCM+ results (Figure: 4.4), the OpenFOAM results show a significant improvement of the Reynolds stress component predictions by $k - \omega$ -SST model and, RST model performance is similar in both cases where the Reynolds stress is severely underpredicted by order of magnitudes.

Figure: 4.21 shows the variation of mean velocity component and Reynolds stress component $\overline{u'u'}$ in the cross-flow direction at three different heights. As it was shown earlier in Figure: 4.19, generally the mean velocity predictions by all three RANS models are in good agreement with experimental results at all three heights. At the $z = 4.5D$ height all model predictions show smaller underprediction of mean cross-flow direction velocity by approximately 20% at the peak. In addition at $z = 1.5D$ height and in the region $0D \leq x \leq 0.4D$ which is above and adjacent to the jet, the mean velocity component U shows an overprediction in all simulations, indicating an acceleration due to jet flow bending. Reynolds stress variations again show that RST model values are significantly underpredicted, and realizable $k - \varepsilon$ model predictions are higher in magnitude than $k - \omega$ -SST predicted values. When compared with the predictions of STAR-CCM+ simulations as shown in Figure: 4.5, OpenFOAM predictions show a noticeable improvement in the Reynolds stress component predictions by $k - \omega$ -SST model.

Figure: 4.22 shows the eddy viscosity to molecular viscosity ratio produced by three RANS models in OpenFOAM simulations, and illustrates that realizable $k - \varepsilon$ model produced more eddy viscosity in the regions where the flow is highly strained (jet and cross-flow interaction zone). As previously observed in STAR-CCM+ results (Figure: 4.7), the realizable $k - \varepsilon$ model result exhibit excessive amounts of turbulent kinetic energy and eddy viscosity near the stagnation zone. All theoretical explanations of this excessive turbulent

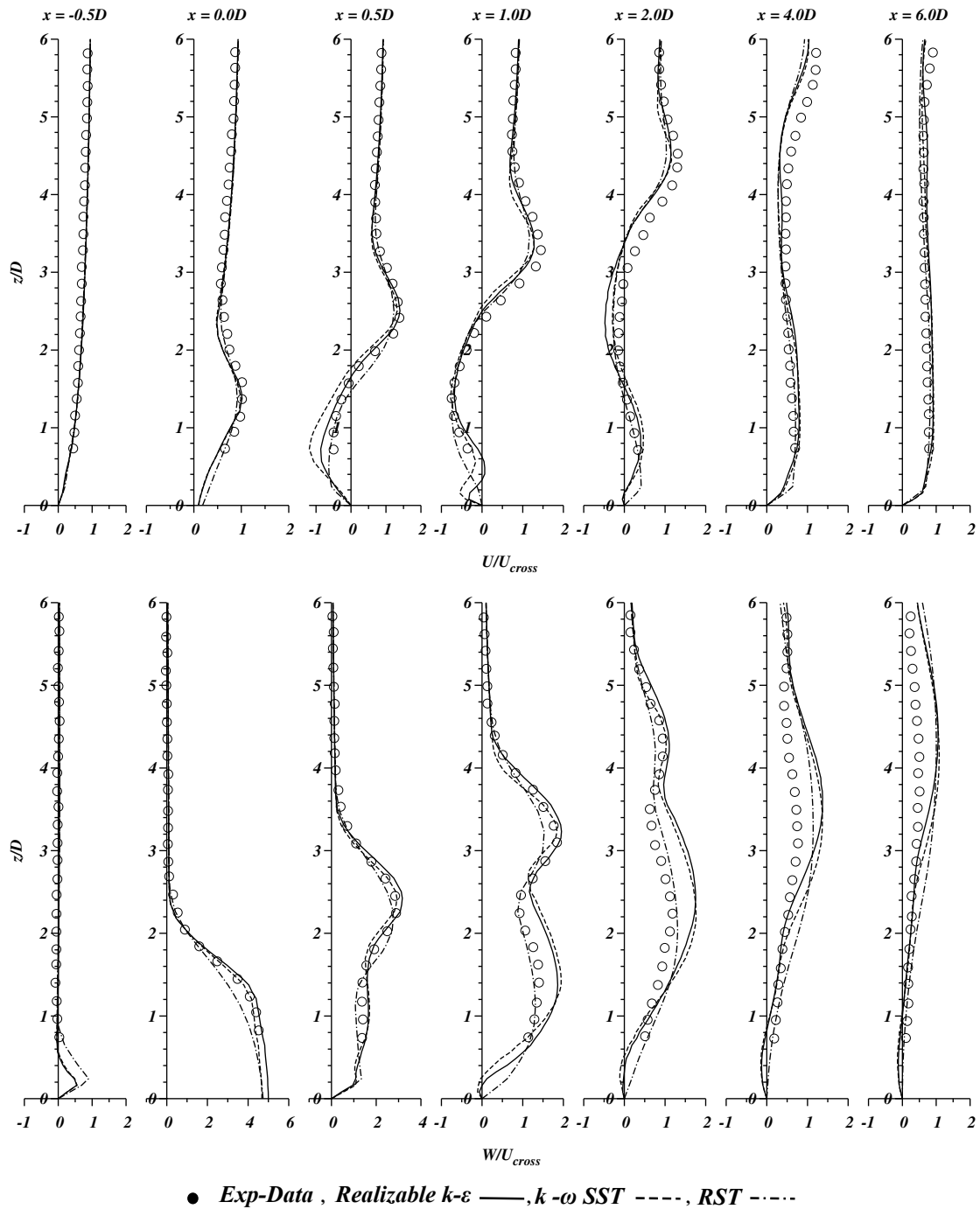


Figure: 4.19 Mean Velocity components in flow direction at $y = 0$, RANS simulations using OpenFOAM (Experimental data : [38]).

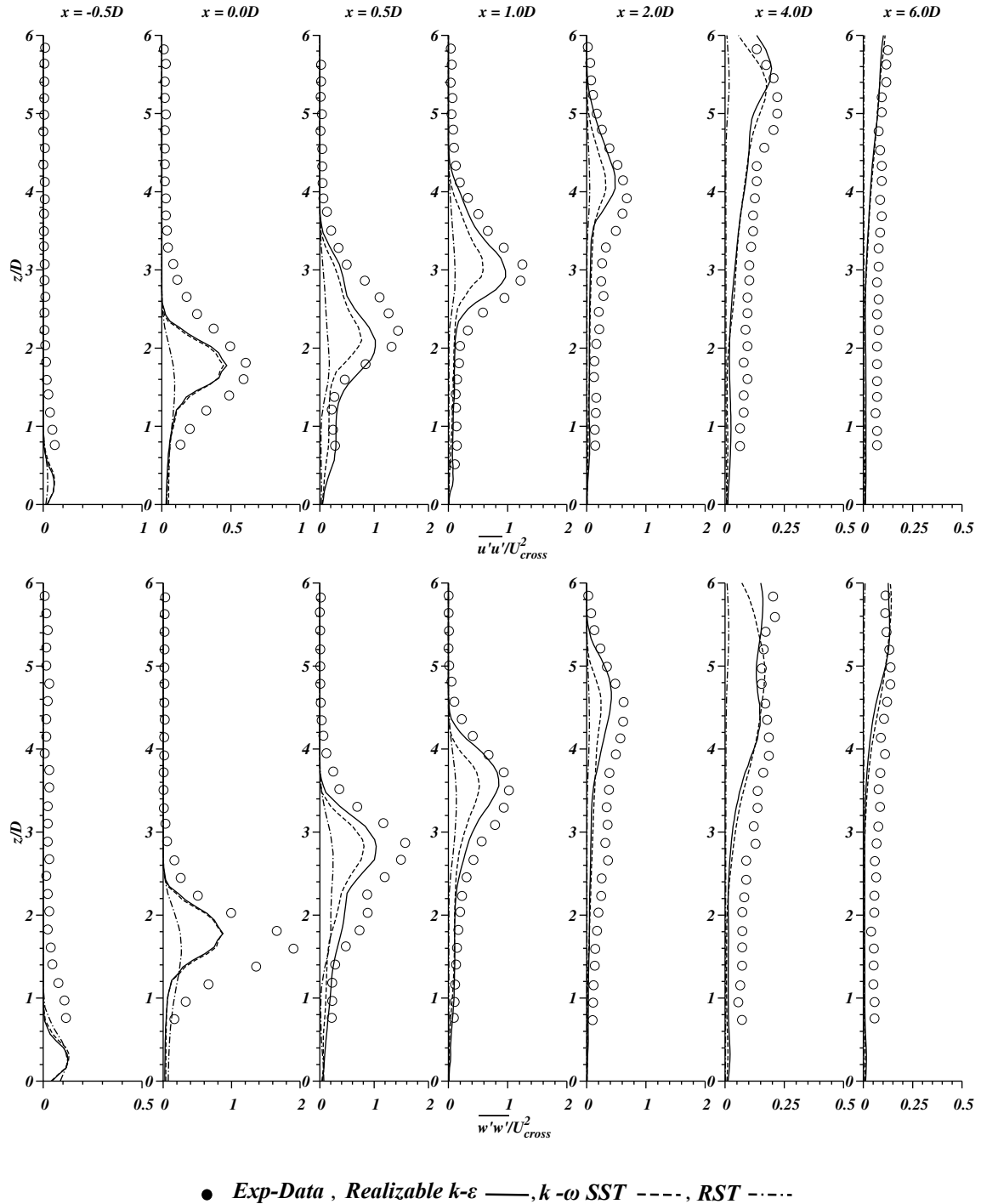
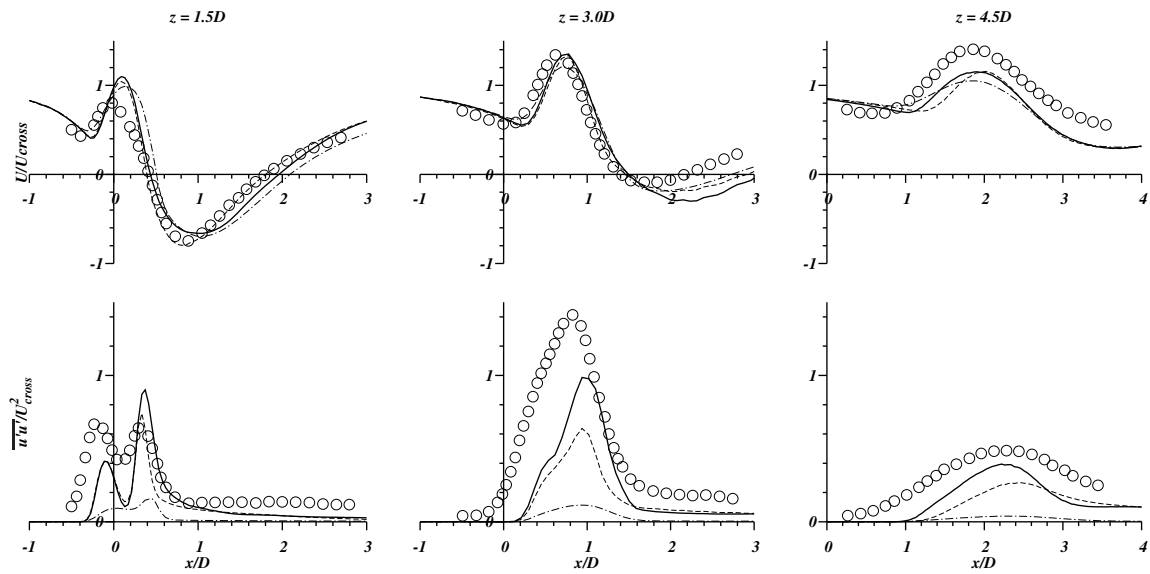


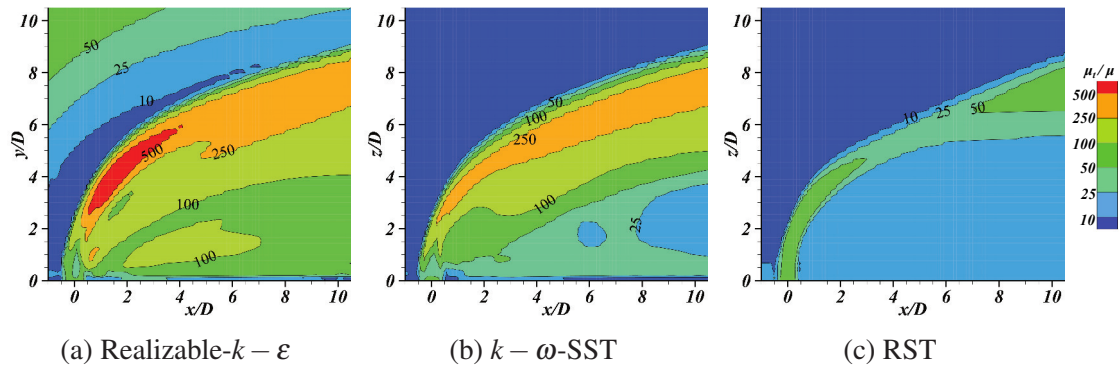
Figure: 4.20 Reynolds stress components on $y = 0$, RANS simulations using OpenFOAM (Experimental data : [38]).

kinetic energy are attributed to the overprediction of turbulence production term P_k , or to the insufficient increase of turbulence dissipation term [241]. Since the jet flow impedes the cross-flow and the cross-flow bending around the jet flow creates a stagnation point locus along the initial development of jet trajectory line. Therefore, the excess turbulent viscosity and turbulent kinetic energy observed near the jet ejection and initial jet development zone, as a stagnation point anomaly. However, unlike STAR-CCM+ results, Reynolds stress components predicted by $k - \omega$ -SST model were significantly higher in magnitude and qualitatively similar to experimental observations.



● *Exp-Data* , *Realizable $k-\epsilon$* ———, *$k-\omega$ SST* - - - - , *RST* -

Figure: 4.21 Mean Velocity and Reynolds Stress component at different at three different heights on the plane $y = 0$ (Experimental data : [37]).



(a) Realizable- $k - \epsilon$

(b) $k - \omega$ -SST

(c) RST

Figure: 4.22 Turbulent viscosity ratio (μ_t/μ) prediction by three RANS models

Passive scalar variation in the z direction is compared against experimental data in Figure: 4.23. Noticeable observation is that passive scalar prediction by the RST model is severely underpredicted and shows a very sharp spatial gradient compared to other RANS models and experimental data. All three RANS models show nearly similar scalar field prediction up to $x = 3D$, and the maximum scalar concentration location is seen to be slightly displaced in the z direction, indicating that jet penetration level is slightly overpredicted. Only the realizable $k - \epsilon$ model results are seen to have reproduced the double-peaked passive scalar variation caused by recirculation zone at $x = 3.0D$ line. However, at all distances all three RANS models have failed to predict the passive scalar at lower z heights when compared with experimental measurements. Taking STAR-CCM+ simulations also into consideration (Figure: 4.13) it can be inferred that realizable $k - \epsilon$ model predictions are superior in both software platforms.

Figure: 4.24 shows jet concentration comparison of RANS results and experimental data along the streamwise direction, and shows that all three model results are similar and do not show significant differences that were observed in z direction variation. However, apart from $z = 1.5D$ height, other line plots show that all RANS results show steeper mean scalar gradients compared with experimental data. Mean turbulent scalar flux predictions also show that realizable $k - \epsilon$ model results agree better with experimental data, however when compared with STAR-CCM+ results (Figure: 4.14) OpenFOAM results show a noticeable improvement in $k - \omega$ -SST results.

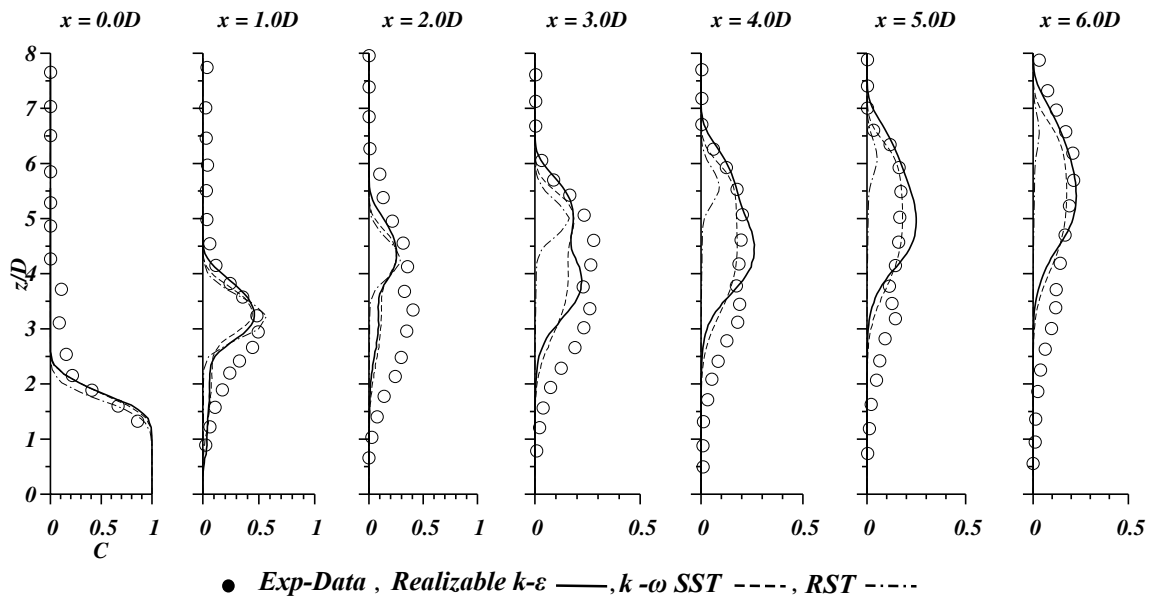


Figure: 4.23 Passive scalar prediction comparison along z direction on the $y = 0$ plane (Experimental data : [39]).

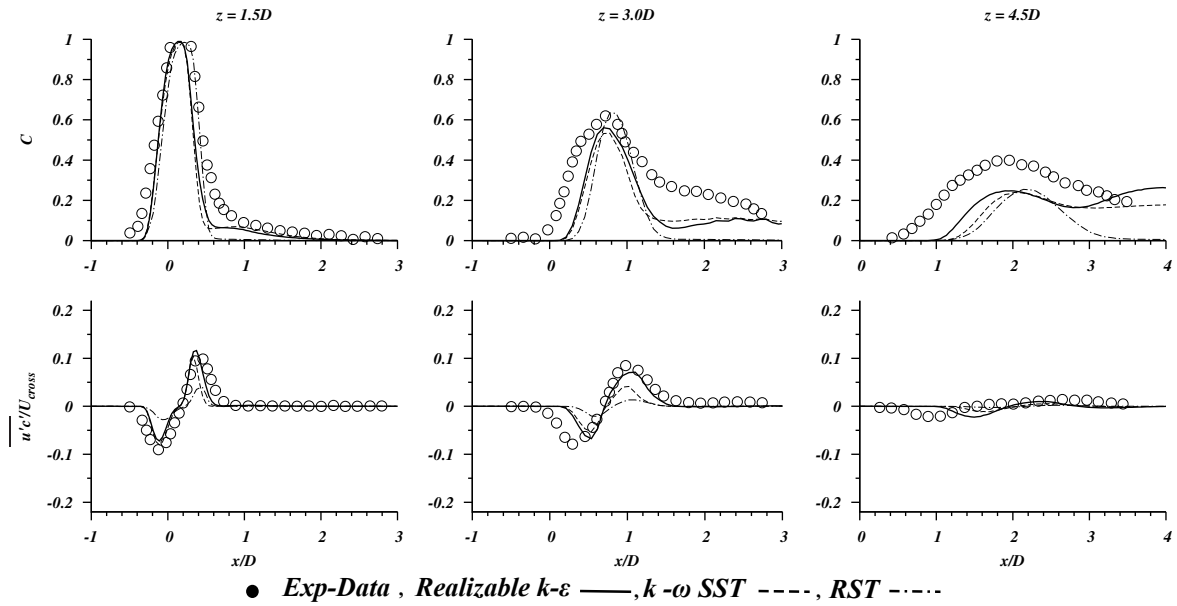
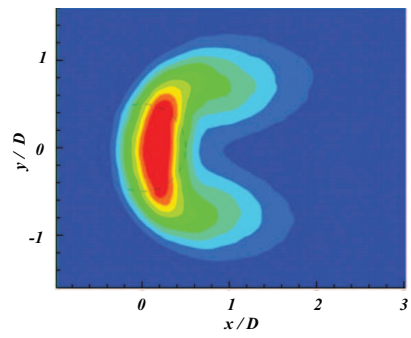
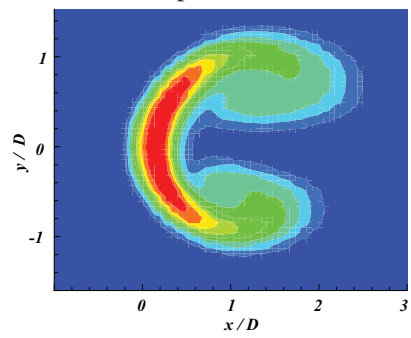


Figure: 4.24 Passive scalar prediction compared along x direction on $y = 0$ plane (Experimental data : [37]).

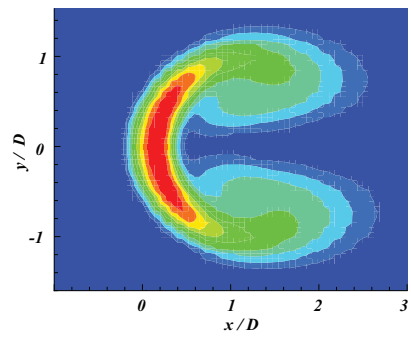
Figure: 4.25 shows the passive scalar concentration modelled by OpenFOAM RANS models compared against experimental data, and it again shows that all three RANS model results captured the dominant shape of the scalar distribution. However, it can be seen that the two two-equation model predictions are more similar to each other and the contour from experimental measurements than the RST model predictions. Therefore, considering the all passive scalar predictions comparisons, it can be said that realizable $k - \varepsilon$ and $k - \omega$ -SST model results show similar trends, but realizable $k - \varepsilon$ model results agreed better with experimental data.



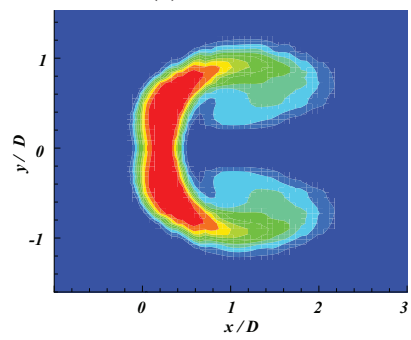
(a) Experimental data



(b) Re $k - \epsilon$



(c) $k - \omega$ -SST



(d) RSM

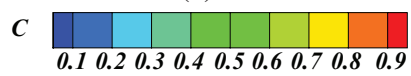


Figure: 4.25 Mean passive scalar concentration C at $z = 1.5D$ plane, experimental data from [37] taken under permission.

4.4 Chapter Summary

Two Finite Volume CFD codes STAR-CCM+ and OpenFOAM performances were tested with similar cell count and similar numerical schemes using RANS turbulence models namely, realizable $k - \epsilon$, $k - \omega$ -SST and Launder-Gibson Reynolds Stress Transport model for a three-dimensional flow problem of Jet in Cross-Flow. The realizable $k - \epsilon$ model performance was found to stand out as to provide the best agreement with experimental data, when mean velocity field and passive scalar concentration results are considered. In contrast to STAR-CCM+ simulations where $k - \omega$ -SST model results showed under predictions of Reynolds stress component magnitudes and showed over penetration of jet flow, the OpenFOAM simulations showed that $k - \omega$ -SST model performance was comparable to realizable $k - \epsilon$ model results, however still underpredicted the Reynolds stress components. Reynolds Stress Transport model performance in both software packages revealed that only mean velocity fields were predicted with acceptable accuracy by this model, and Reynolds stress components were very seriously underpredicted. Therefore, in summary, it can be stated that both software packages showed comparable results using realizable $k - \epsilon$ model that can be compared against experimental data for both mean velocity field and scalar mixing results, but Reynolds stress components were not modelled sufficiently by the RANS modelling technique. Further studies should be done to investigate the difference of results $k - \omega$ -SST model between two software platforms.

Chapter 5

LES modelling of Jet in Cross-Flow

In this Chapter Jet In Cross Flow problem is numerically simulated using LES method, modelling strategy and results are discussed. Both velocity field statistics and scalar mixing statistics are compared against available experimental data. Further simulations of of twin Jets In Cross-Flow are presented, and the physics of the twin-jet interaction is discussed using numerical results.

5.1 Simulation set up

In this endeavour, LES simulations were performed with three different dynamic SGS models to understand their performance under high Reynolds number and highly strained flow problem of Jet in Cross-Flow. The same experimental configuration that was discussed in Chapter 4 is simulated using the LES method with different dynamic SGS stress models. Dynamic Smagorinsky Model (DSM), Dynamic Mixed Model (DMM), Dynamic One Equation (k-Equation) Model (DOEM) models as introduced in Section:3.3.1 were used in this study. Compared to RANS results LES results showed significantly improved agreement with experimental results, especially in Reynolds stress components prediction. Furthermore, coherent structure identification methods were used to look into turbulence structures resolved by the LES results. Simulations were conducted in a similar grid structure mentioned in Section:4.3 but with a higher mesh resolution with 11×10^6 total cells and 48 cells across the jet nozzle diameter. Two different inlet turbulence generation methods were used for two inlet streams. The cross-flow turbulence was generated using the mapping method (Section:3.5) by mapping the flow solution from an interior plane back to the inlet. The jet flow the inlet section was extended sufficient distance ($l > 80D$) to generate fully developed flow and at the inlet surface random number based fluctuations were imposed.

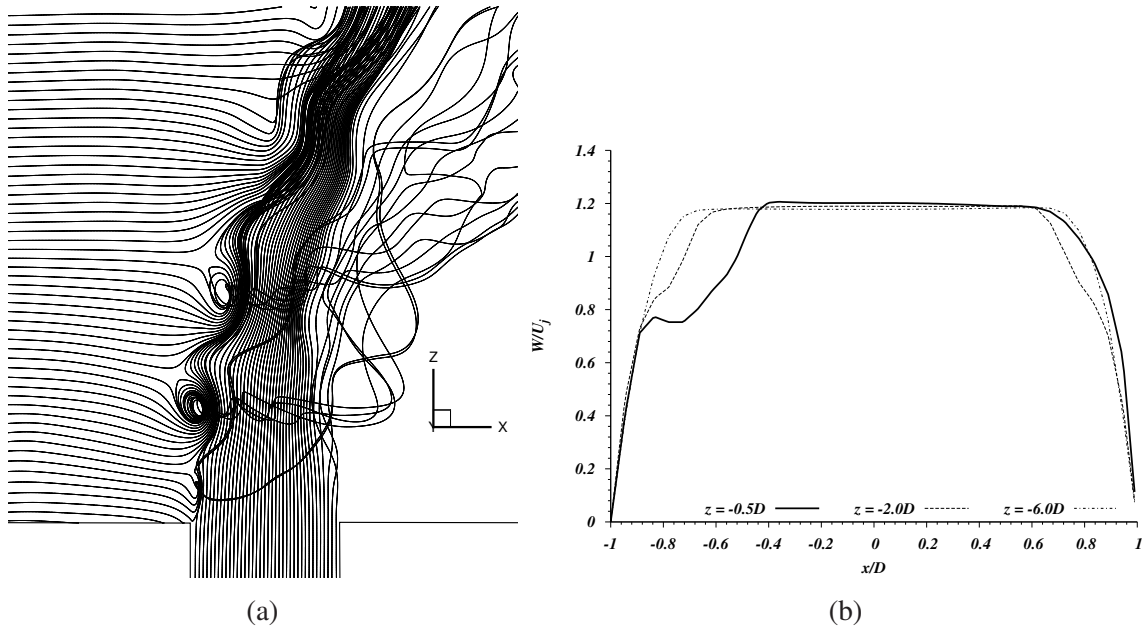


Figure: 5.1 (a) Streamlines generated from upstream sides of cross-flow and jet inlet, (b) Effect of jet and cross-flow interaction on upstream flow pattern

Second order backward implicit time discretisation scheme was used in time derivative discretisation, and vanLeer TVD Scheme was used for the discretisation of convection term. For diffusion terms discretisation second order central differencing scheme was used, and a non-orthogonal correction loop was performed to compensate for the mesh non-orthogonality surrounding the radially expanding grid [227]. Courant number was maintained at $Co < 0.4$ ($\Delta t \sim 1 \times 10^{-6}$) for solver stability. For time averaging purposes results were collected over a period of 0.750s after five flow passes through the system domain. The time for a single particle to enter from the cross flow inlet and exit from the outlet is estimated to be $T_{cyl} \approx 40ms$. The OpenFOAM flow solver *pisoFOAM* that uses PISO algorithm was used with modifications to include passive scalar transport equation and to output modelled Reynolds Reynolds stress component and other turbulence quantities.

Figure 5.1a shows streamlines generated using LES from upstream locations of the jet stream and cross-flow stream, in which cross-flow streamline pattern shows that the jet deflection acts as an impediment. Figure 5.1b compares velocity profile inside the pipe that carries jet flow, and it can be seen that near the jet exit, mean velocity profile inside the jet flow is influenced by the jet and cross-flow interaction. Therefore it can be seen that close to the jet ejection the pipe flow shows, elliptic behaviour and even the cross-flow is also affected by the upstream recirculation caused by jet and cross-flow shear.

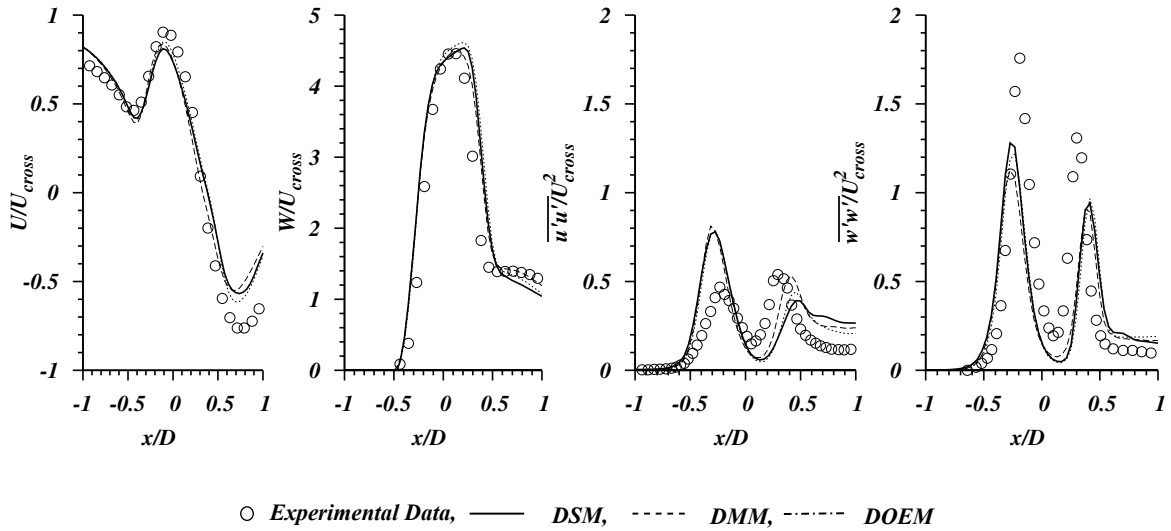


Figure: 5.2 Mean Velocity and Reynolds Stress component at different on $y = 0$ plane, at $z = 1D$ (Experimental data : [37]).

The importance of correct inlet boundary conditions on LES simulations is emphasized on Section:3.5, therefore before proceeding into the discussion of LES results the effect of boundary conditions are compared closer to the jet and cross-flow interaction zone. Figure: 5.2 shows the non-dimensionalized time averaged velocity components U and W and two principal Reynolds stress components along the $z = 1D$ line on the $y = 0$ symmetric plane. It (Figure: 5.2) shows that all LES results agree very well with the experimental data near the jet outlet region, hence it can be inferred that effects of inlet boundary conditions are in good agreement with the flow physics closer to the critical region and do not introduce any undesirable effects. The mean velocity component U variation illustrates that closer to the jet penetration the mean velocity reduces indicating that jet flow acts as an impediment to the cross-flow and an effect similar to stagnation point effect. On the leeward side, U velocity component increases after $x = 0.5D$ which is indicative of a recirculation zone, and LES results also have reproduced the same variation and agree with experimental observations. As it can be seen LES results have underpredicted the negative velocity magnitude, that is indicative of the underpredicted strength of the recirculation zone. The mean velocity component W distribution shows that above the jet diameter the velocity in jet penetration direction is very well predicted by numerical results, further confirming that jet inlet effects are sufficiently defined by the boundary conditions.

Both principal Reynolds stress components in cross-flow direction ($\overline{u'u'}$) and in jet-flow direction ($\overline{w'w'}$) shows bimodal distributions corresponding to windward side ($x < 0$) and lee side ($x > 0$). The principal Reynolds stress component $\overline{u'u'}$ shows a slight increase in

magnitude in the lee side compared to the windward side, in contrast, $\overline{w'w'}$ shows a greater increase in windward side compared to the leeward side. While LES results agree reasonably well with the experimental data, the Reynolds stress component $\overline{u'u'}$ prediction in the windward side peak is overpredicted by nearly 50% indicating a strong shear flow on the windward side due to stagnation effect and flow bending. The Reynolds stress component $\overline{w'w'}$ measurements show that windward side peak is approximately 1.4 times the leeward side peak, and the LES results even though underpredict the peak values, maintains a ratio between two peaks around 1.3. When compared to RANS predictions as it is shown in Figure: 4.18, Reynolds stress components especially the $\overline{w'w'}$ component is predicted with much-improved accuracy. Therefore, in the vicinity of the jet exit, LES results show good agreement with experimental measurements considering the highly strained flow and measurements and numerical errors at the location. Further, all three SGS stress models exhibit similar performance for first order statistics and second order statistics of the velocity field closer to the jet cross-flow interaction zone.

5.1.1 Velocity field results

Figure: 5.3 shows the mean normalized velocity components in the cross-flow direction and jet-flow direction respectively on the symmetric plane $y = 0D$. It can be seen that all three SGS stress models have resulted in virtually identical velocity field prediction for both velocity components. While overall velocity field is in good agreement with experimental data, the minor disparity in U velocity prediction appears with increasing downstream distance $x \leq 4D$ suggests that LES results have produced a minor underprediction of jet penetration about $0.2D$. Along the line $x = -0.5D$, which is the imaginary line over the windward edge of the circular jet nozzle, the velocity profiles U and W are in very good agreement with experimental data and shows weak influence from the jet flow.

The $x = 0.0D$ line is the virtual centreline of the jet flow nozzle, and the velocity variation along that line shows that up to $z \leq 3.0D$ the velocity component in x direction increases due to the jet flow deflection. Beyond that height, the downstream velocity component reduces to coincide with cross-flow velocity. Along the $x = 0.5D$ line which is the virtual line drawn on the lee side edge of the circular jet nozzle, U velocity component shows a negative magnitude indicating a reverse flow below the height of $z \approx 1.6D$. Beyond that height along the jet deflection, U component magnitude increases until the end of jet flow envelope. On the same line with increasing z height, the velocity component W initially shows a very small increase until the height reaches $x \approx 1.6D$. Thereafter, inside the jet flow envelope, the W magnitude increases to reach a maximum near $z = 2.6D$ height, then reduces to free stream value. Similarly, along the line plots of $x = 1.0D, 2.0D$ effect of re-

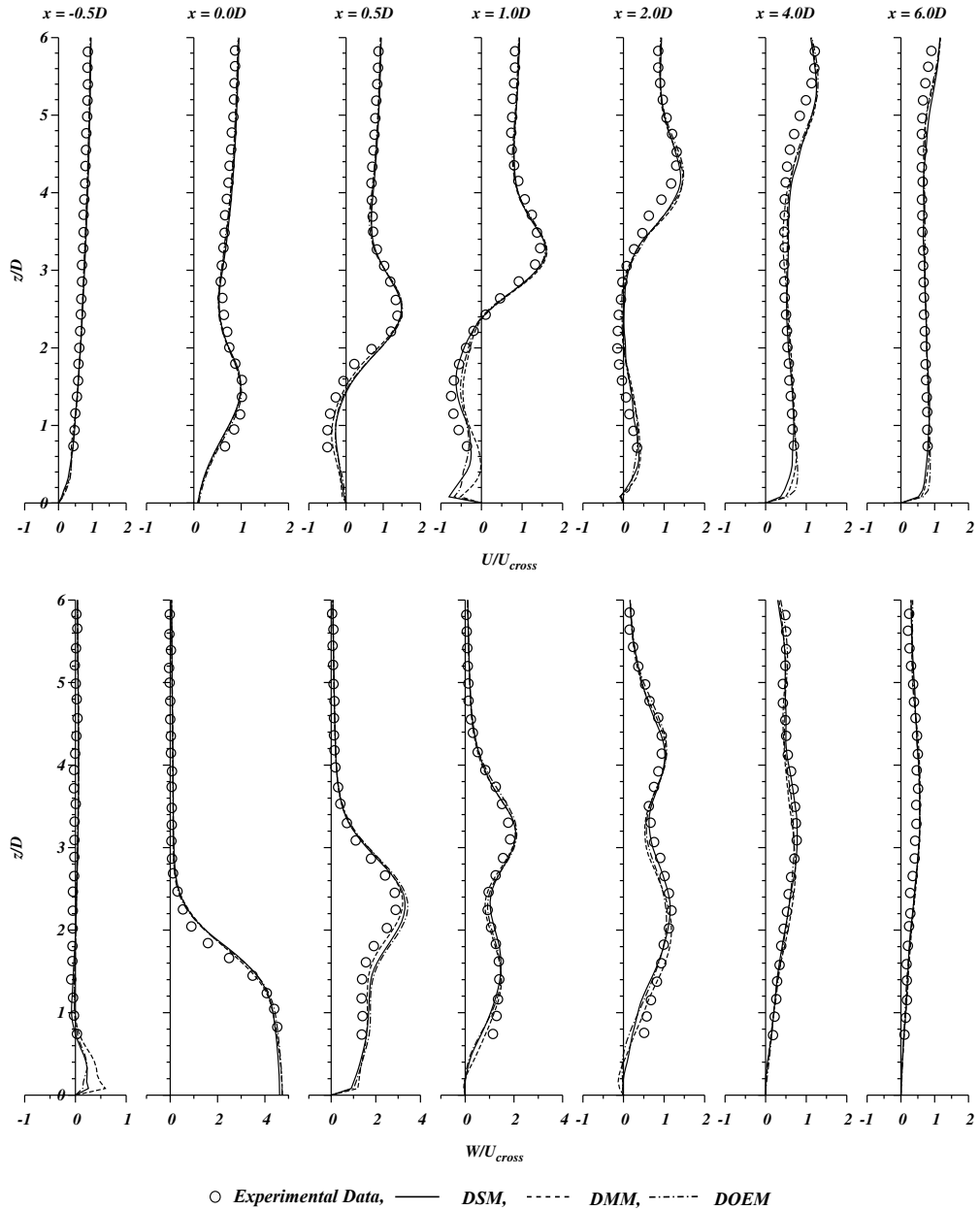


Figure: 5.3 Normalized LES mean velocity components variation on the symmetric plane $y = OD$ (Experimental data : [38]).

verse flow is manifested as a negative U velocity component and beyond $x = 2D$ the reverse flow can be seen to have diminished. Compared to RANS results as shown in Figure: 4.19 and Figure: 4.3, LES model results show significantly improved results for mean velocity field at both near field and far field, and most importantly the SGS models shows negligible effects on the mean velocity field results. (Figure: A.3, Figure: A.4 shows a comparison of LES and RANS results of mean velocity and Reynolds stress) As a consequence of the better velocity prediction of the LES method, the passive scalar distribution also showed better agreement with experimental data than RANS modelling approach.

Figure: 5.4 illustrates the velocity field alongside streamlines injected at upstream locations to the cross-flow on a plane at $z = 1.5D$ height. According to the mean velocity component contours, the negative velocity zone indicates the reverse flow region, and streamlines also show that towards the lee side edge, flow reversal occurs causing the negative velocity. Furthermore, towards the lateral edges of the jet nozzle cross-flow accelerates causing high-velocity zones.

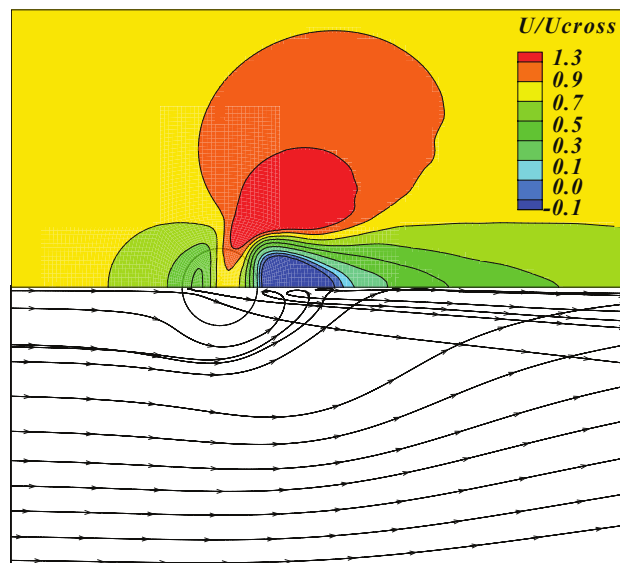


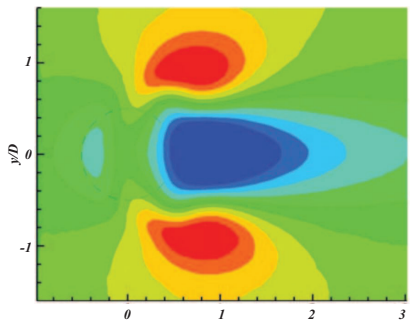
Figure: 5.4 Mean velocity field U on $z = 1.5D$ plane, and comparable streamlines

Figure: 5.5, and Figure: 5.6 show 2D contours of non-dimensional velocity components in cross-flow direction and span wise direction compared against 2D PIV data. It can be seen that all three SGS models reproduce very similar prominent features of the jet and cross-flow interaction and agree with experimental data. However, a noticeable difference between LES and experimental data can be seen in the region upstream of the jet nozzle ($-0.5D \leq x \leq 0.5D$), where the numerical results show increased cross-flow direction velocity component compared to experimental data. Furthermore, careful inspection of Figure: 5.5 shows that the recirculation zone in the middle of the velocity field is slightly underpredicted by dynamic Smagorinsky model (approximately by $0.2D$) compared to experimental data and the other two SGS stress models. The spanwise velocity (V) contour shows the effect of jet stream acting as an obstruction to the cross-flow stream. Therefore cross-flow travels around the jet flow stream causing two symmetric velocity peaks closer to windward and leeward side respectively. However, these contour maps are subjected to interpolation schemes used in visualisation, and experimental data were extracted from published literature; consequently, a rigorous comparison cannot be performed.

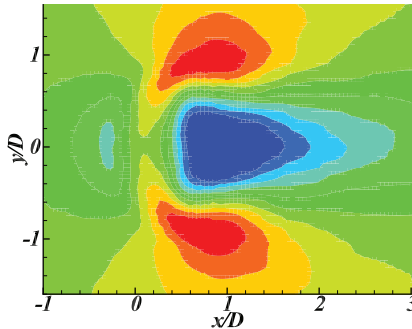
5.1.2 Reynolds stress field results

Large eddy simulations resolve the filtered velocity field. Therefore the resolved Reynolds stress tensor (second-order velocity moments T_{ij}) can be calculated. However, to include the effects of the SGS stress tensor the total Reynolds stress tensor ($T_{ij} + \tau_{ij}$) must be calculated explicitly. Figure: 5.7 shows the difference between total Reynolds stress and the resolved Reynolds stress along a virtual line at $x = 0.5D$, and it can be seen that the difference between total Reynolds stress and resolved Reynolds stress is not significant even at this highly strained flow area. Throughout subsequent discussions in this chapter total Reynolds stress is used without explicit mention.

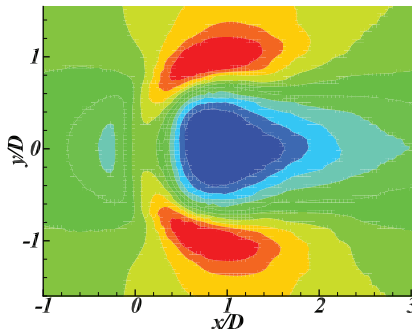
As discussed in the previous chapter, RANS results showed moderate agreement with experimental results for Reynolds stress component predictions (Figure: 4.20), where numerical results showed under prediction of stress magnitude. However, as shown in Figure: 5.8 experimental data and LES results are in good agreement for both principal Reynolds stress components in cross-flow direction and jet-flow direction. At $x = 0D$, the virtual line plot over the jet nozzle centre shows the greatest disparity between experimental and numerical predictions, where the peak magnitude of the Reynolds stress component in the cross-flow direction ($\overline{u'u'}$) is overpredicted by all SGS models approximately 30%. Further, it can be seen that the peak magnitude of the principal Reynolds stress component in the jet-flow direction ($\overline{w'w'}$) is underpredicted by a similar percentage. At this particular point where the initial jet flow deflection occurs, a physical observation can be made to argue that the jet



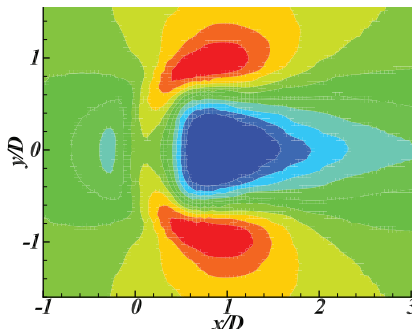
(a) Experimental data



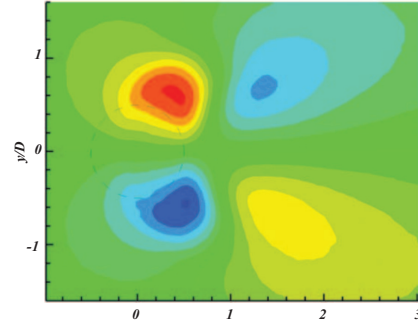
(b) DSM



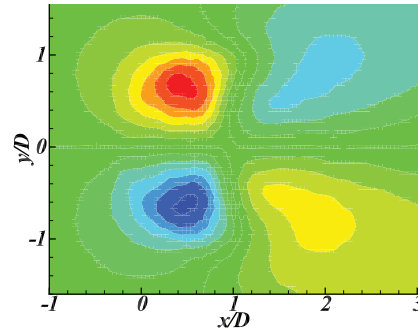
(c) DMM



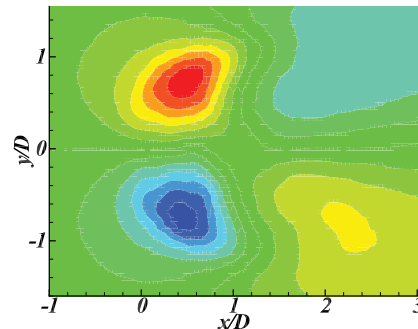
(d) DOEM



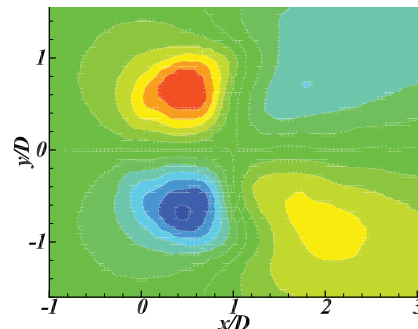
(a) Experimental data



(b) DSM



(c) DMM



(d) DOEM

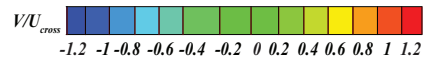


Figure: 5.5 Normalized velocity contour U on $z = 1.5D$ plane (Experimental data : [37]). Figure: 5.6 Normalized velocity contour V on $z = 1.5D$ plane (Experimental data : [37]).

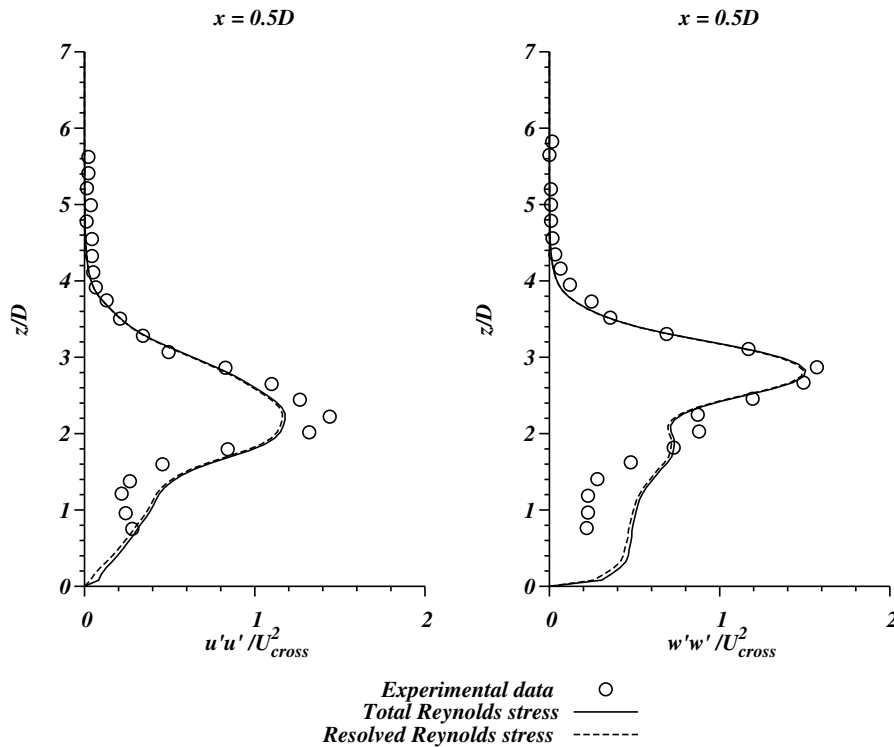


Figure: 5.7 Total Reynolds stress and Resolved Reynolds stress terms comparison for dynamic Smagorinsky model

deflection in the cross-flow is more dominant, thus causing a larger strain in the cross-flow direction (x) compared to other strain tensor components. However, to resolve such a highly anisotropically strained flow using SGS models that assumed isotropy of the scales below sub-grid eddies a substantially finer mesh resolution is required. Wall boundary layer measurements were not available for this experiment because it was out of the scope of their study, and measurements were available approximately from $1D$ distance from the wall. It can be seen that from above two figures the Dynamic Mixed Model (DMM) show an increased Reynolds stress component at the edges of the circular jet nozzle ($x = -0.5D, 0.5D$). The flow strain perpendicular to the original flow direction at these nozzle edges shows very high flow strain gradients. Therefore requires very high mesh resolution to resolve these velocity gradients accurately. In the vicinity of the wall boundary, the Reynolds stress components exhibit a peak compared to the region beyond the wall boundary layer, indicating that turbulence levels are much higher than the nearest grid cell adjusted viscosity could dissipate. Furthermore, it can be seen that when compared to Reynolds stress component predictions by RANS models (Figure: 4.4, Figure: 4.20) LES results show remarkable improvement in accuracy.

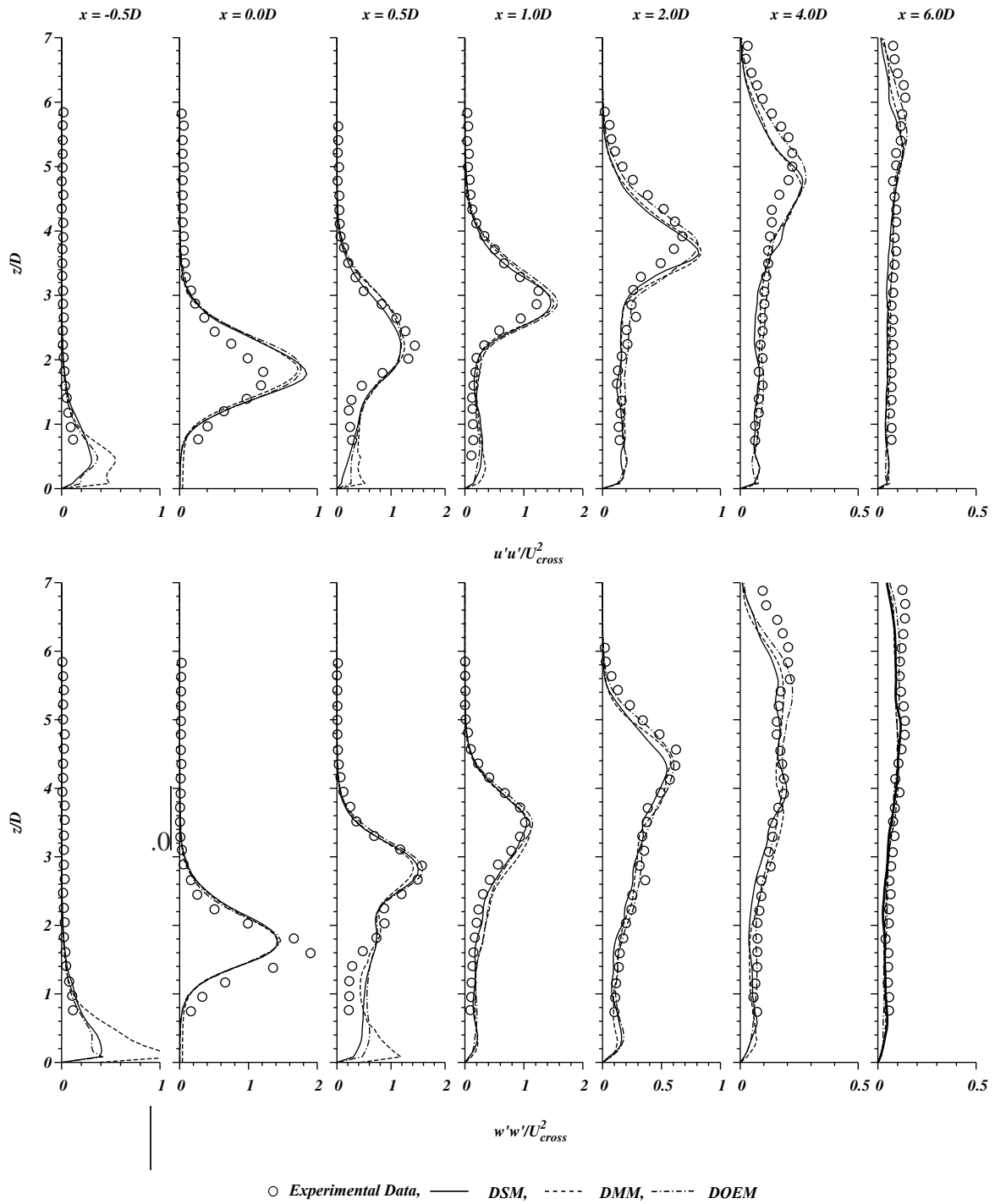
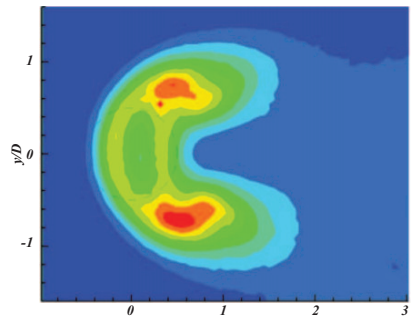


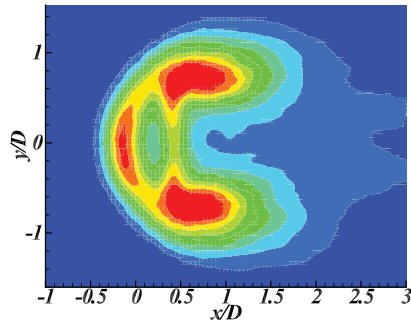
Figure: 5.8 Normalized LES mean Reynolds stress components variation on the symmetric plane $y = 0D$ (Experimental data : [37]).

Two-dimensional contour maps of non-dimensionalized principal Reynolds stress components $\overline{u'u'}$, $\overline{v'v'}$ and shear stress component $\overline{u'v'}$ are compared against experimental data at the height $z = 1.5D$ in Figure 5.9, Figure 5.10 and Figure 5.11 respectively. The normal Reynolds stress component $\overline{u'u'}$ predictions by dynamic Smagorinsky model (DSM) and dynamic one equation model (DOEM) model predictions show better agreement with experimental data than the dynamic Mixed Model (DMM) results. Dynamic Smagorinsky model results show that the stresses generated at windward side edge over the jet nozzle are overpredicted compared to experimental data. The effects of cross-flow acceleration around the jet plume are represented well by all three SGS models, but DMM predictions show minor underprediction of flow strain.

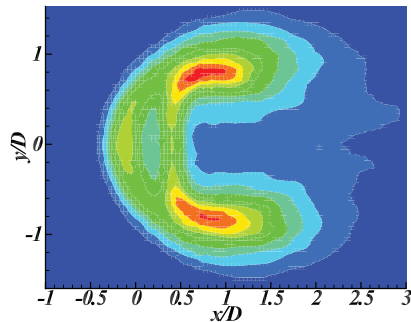
Nevertheless, all three SGS models reproduced the kidney-shaped Reynolds stress variation in cross-flow direction adequately. It can be seen from Figure: 5.10, the normal Reynolds stress component in span wise direction $\overline{v'v'}$ shows two symmetric peak stress zones towards the lee side of the jet ($0.5D < x < 1.4D$). Results from LES fails to reproduce these two zones with the same magnitudes, but dynamic Smagorinsky model results showed a better agreement with experimental data when compared with other two SGS model results in predicting the strain caused by flow direction changing in cross-stream direction. The shear stress component $\overline{u'v'}$ shows (Figure: 5.11) two distinct higher stress zones in opposing directions. The shear stresses the zone closer to the centre of jet flow is caused by the emanating jet flow, and the surrounding high-stress zone is caused by the cross-flow travelling around the jet flow. While dynamic Smagorinsky model predicts (DSM) these two higher stress locations, other two SGS stress models fail to reproduce the circular zone with higher shear stress. Therefore, investigating all three dynamic SGS stress models, results reveal that dynamic Smagorinsky model shows better agreement with experimental data for the second-order momentum of velocity.



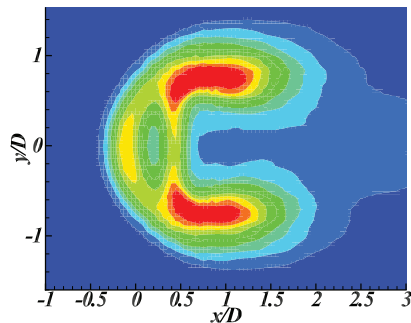
(a) Experimental data



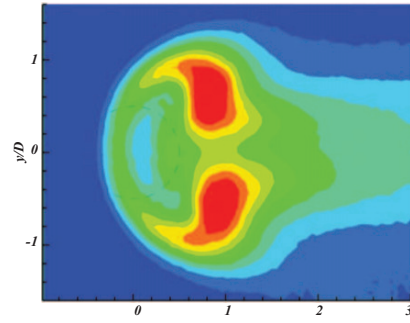
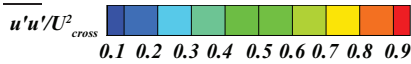
(b) DSM



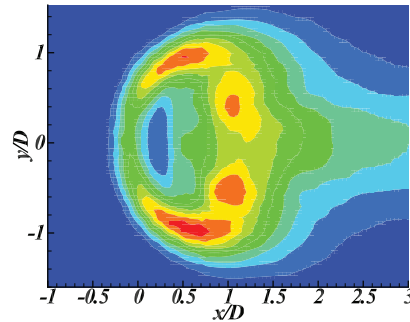
(c) DMM



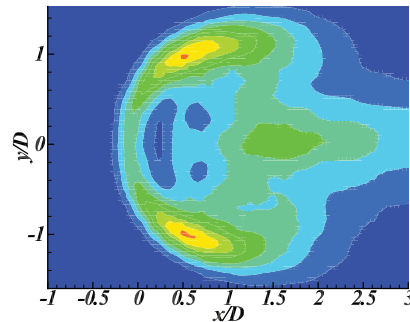
(d) DOEM



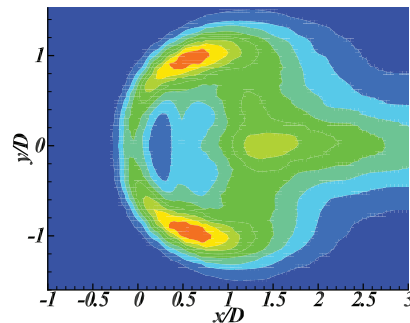
(a) Experimental data



(b) DSM



(c) DMM



(d) DOEM

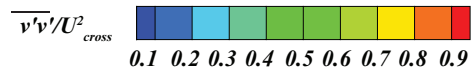
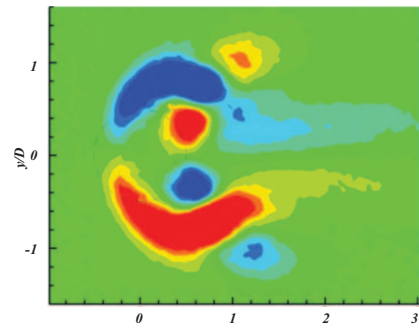
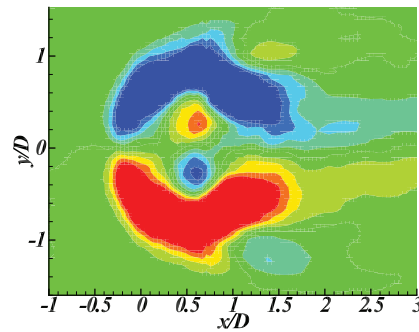


Figure: 5.9 Reynolds stress component $\overline{u'u'}$ distribution on $z = 1.5D$ plane (Experimental data : [37]).

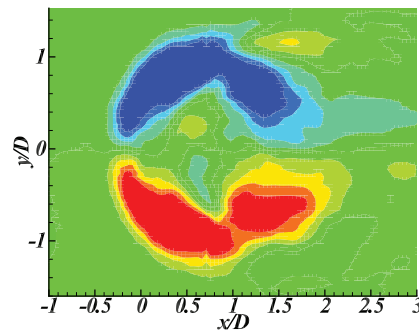
Figure: 5.10 Reynolds stress component $\overline{v'v'}$ distribution on $z = 1.5D$ plane (Experimental data : [37]).



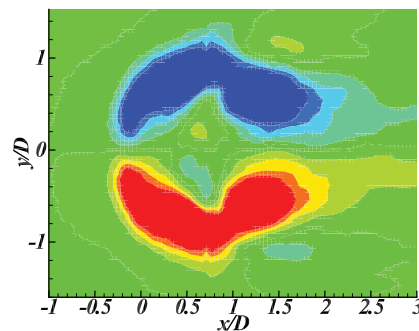
(a) Experimental data



(b) DSM



(c) DMM



(d) DOEM

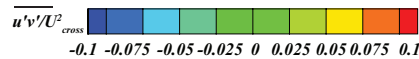


Figure: 5.11 Non dimensionalized Reynolds stress component $\overline{u'v'}$ distribution on $z = 1.5D$ plane (Experimental data : [37]).

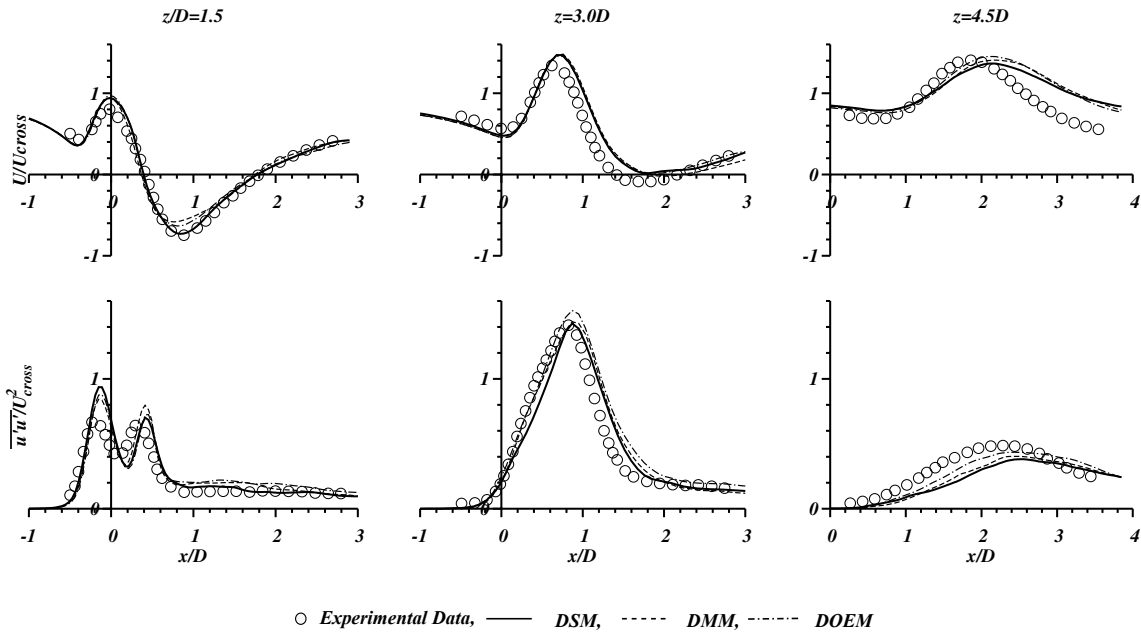


Figure: 5.12 Mean velocity and Reynolds stress variation in downstream direction (Experimental data : [37]).

Figure: 5.12 shows mean velocity component in cross-flow direction (U) prediction and principal Reynolds stress component $\overline{u'u'}$ at three different heights $z = 1.5D, 3.0D, 4.5D$. In general, all three SGS stress models show similar performance and at heights $z = 1.5D, 3.0D$. The mean velocity profile agreed very well with experimental data, but at $z = 4.5D$ the predicted velocity gradient in streamwise direction shows a slower decline. The principal Reynolds stress component predicted by all three SGS stress models also show similar response except at $z = 4.5D$ height where DOEM predicted values show slightly better agreement with experimental data. When these results are compared against RANS results, a remarkable improvement of Reynolds stress component prediction can be seen from LES results.

Therefore, after comparing all the results of mean velocity components and Reynolds stress components with available data, it can be said that all three SGS stress models provide very close agreement with each other. However comparisons with 2D Reynolds stress components show that dynamic Smagorinsky model shows marginal improvement over other two models.

5.1.3 Passive Scalar Mixing

One of the major objectives of this study is to investigate the scalar mixing using computational modelling techniques, and LES provides an improved insight into the scalar field

through instantaneous scalar field results compared to steady RANS results. Figure: 5.13 shows time mean passive scalar (C) predictions compared against experimental data and as expected three different SGS models produce virtually indistinguishable results. Passive scalar distribution by LES results show good agreement with experimental data, but at far field distance, $x = 6D$ the difference between numerical predictions and experimental data is found to be less than 5%. When compared with RANS simulations as shown in Figure: 4.13 and Figure: 4.23, numerical predictions by LES modelling show significant improvement in accuracy of passive scalar concentration. The eddy viscosity produced by LES are of the same order as molecular viscosity. Therefore the influence of turbulent Schmidt number on sub-grid scalar flux closure is also reduced, which can be considered as an additional advantage of LES over RANS modelling.

Figure: 5.14 shows mean passive scalar concentrations are predicted very well by all three SGS model simulations and compared to RANS simulations (Figure: 4.14, Figure: 4.24) show a significant improvement in accuracy. Further, both dynamic Smagorinsky and dynamic one equation model show very similar scalar field predictions, while dynamic mixed model showed a minor underprediction of scalar concentration compared to other SGS stress model results. At $z = 4.5D$ height, the passive scalar concentration shows slower spread rate compared to experimental data, and the velocity component U at this particular height also showed similar decaying as it is shown in Figure: 4.21. Therefore the disparity in scalar field result is understood to have caused by the discrepancies in velocity field results. Standard deviation (RMS) values of passive scalar concentration predictions show good agreement with experimental measurements both quantitatively and qualitatively at distances closer to the jet ejection, however with increasing jet heights LES show under predicted RMS values. Therefore, after investigating both velocity field statistics and scalar field statistics it is safe to conclude that jet penetration shows a slightly underpredicted. Figure: 5.15 shows passive scalar concentration distribution on a plane at $z = 1.5D$ compared against experimental measurements, and all three SGS stress models predict very similar results as expected. When compared with results from RANS predictions (Figure: 4.15, Figure: 4.25) LES results showed that passive scalar distribution was virtually independent of the turbulence model while RANS results showed dependence on RANS models.

Figure 5.16 shows instantaneous passive scalar field and the scalar concentration standard variation obtained from dynamic Smagorinsky model. The passive scalar distribution shows the effects of jet shear layer vortices generated by the shear between cross-flow and jet flow. It can be seen that beyond $x = 6.0D$, the effect of near-field turbulence attenuates causing a more uniform passive scalar distribution. However, to complete the picture of passive scalar distribution scalar field on another orthogonal plane is shown in Figure: 5.17.

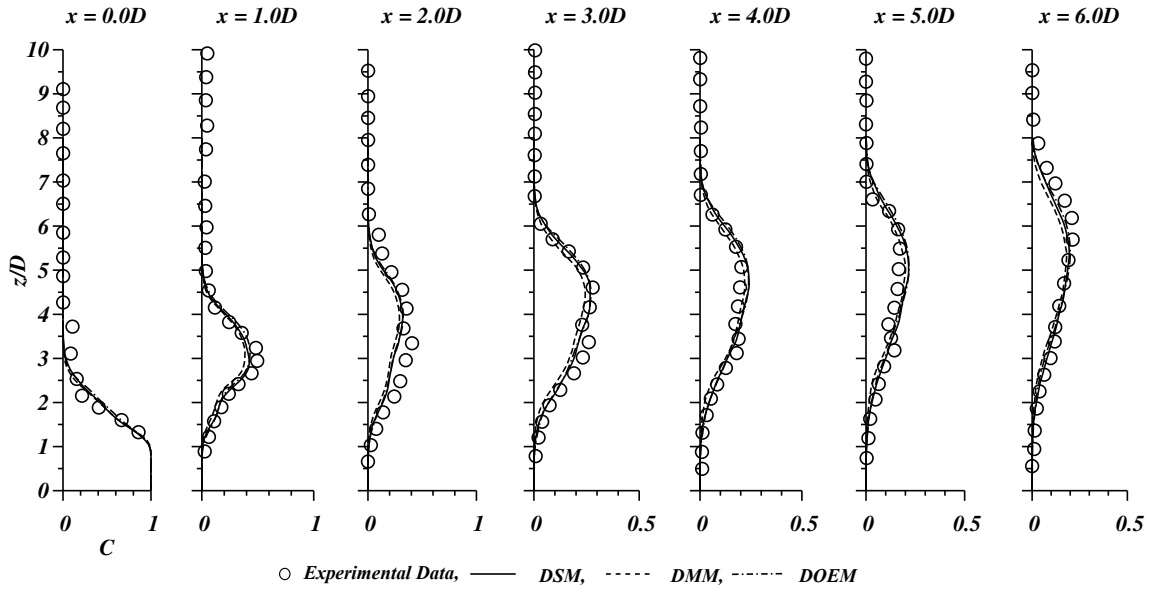


Figure: 5.13 Passive scalar concentration variation in z direction with increasing downstream distance (Experimental data : [39]).

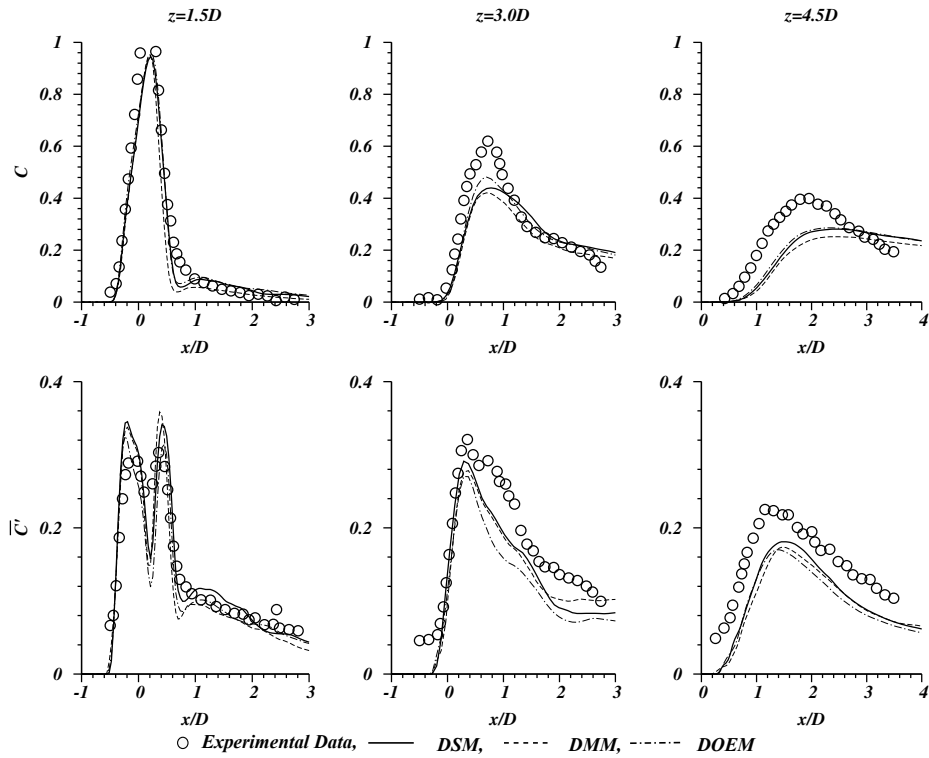
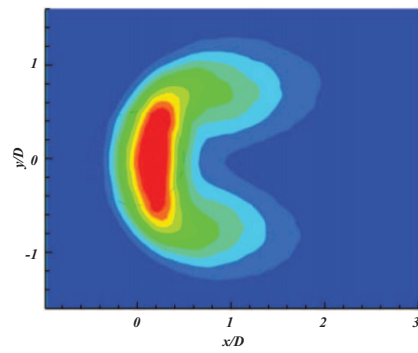
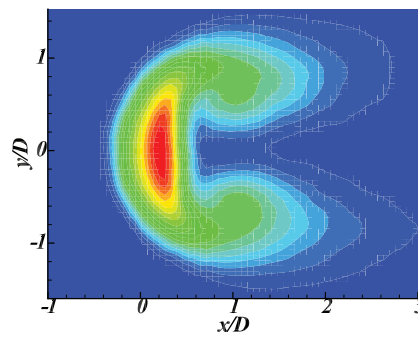


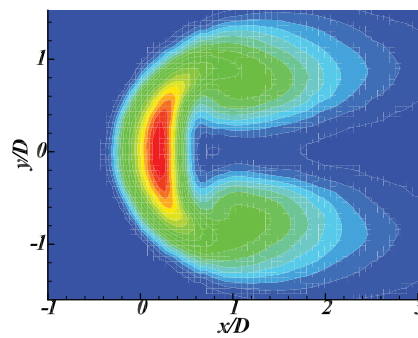
Figure: 5.14 Passive scalar concentration variation in x direction with increasing jet direction distance (Experimental data : [37]).



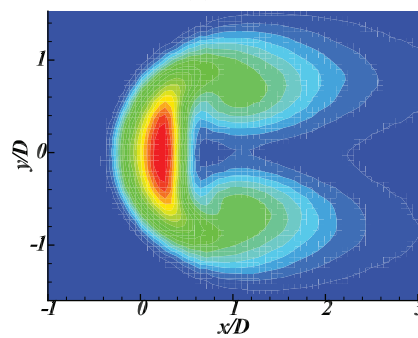
(a) Experimental data



(b) DSM



(c) DMM



(d) DOEM



Figure: 5.15 Mean passive scalar contours on $z = 1.5D$ plane (Experimental data : [37]).

The mean passive scalar concentration on the plane at $x = 3.0D$ shows that the influence of counter-rotating vortex pair on the shape of the scalar distribution, and importantly it shows that inside of the jet core the scalar variance shows to be lesser than the outer edges of the jet envelope. This phenomenon can be understood by the structure of counter-rotating vortex pair, where inside the vortex core the scalar concentration is conserved. At $x = 6.0D$ distance the passive scalar concentration can be seen as diluted and more uniform in space when the strength of counter-rotating vortex pair is diminished.

Since LES results produce very good agreement with experimental measurements of scalar concentration, LES data can be used to quantify the scalar mixing quality. To compare different scalar mixing arrangements quantitative mixing indices can be used [64]. Temporal Mixing Deficiency (TMD) index defined using time mean scalar concentration (C) and standard deviation values ($\overline{C'}$) as Eqn: 5.1 is used in this study to quantify the scalar mixing quality.

$$TMD = Avg \left[\frac{C'}{C_{mean}} \right] \quad (5.1)$$

The averaging operation (Avg) is performed over a cross-sectional plane normal to the cross-flow direction. To avoid the issue of numerical singularity, TMD is calculated using a threshold concentration value C_t , and the averaging area is calculated using the cross-section of the scalar field above this threshold value. Figure: 5.18 shows the TMD index calculated using three different C_t values, indicating that with increasing downstream distance TMD monotonically decrease as a result of more uniform mixing field.

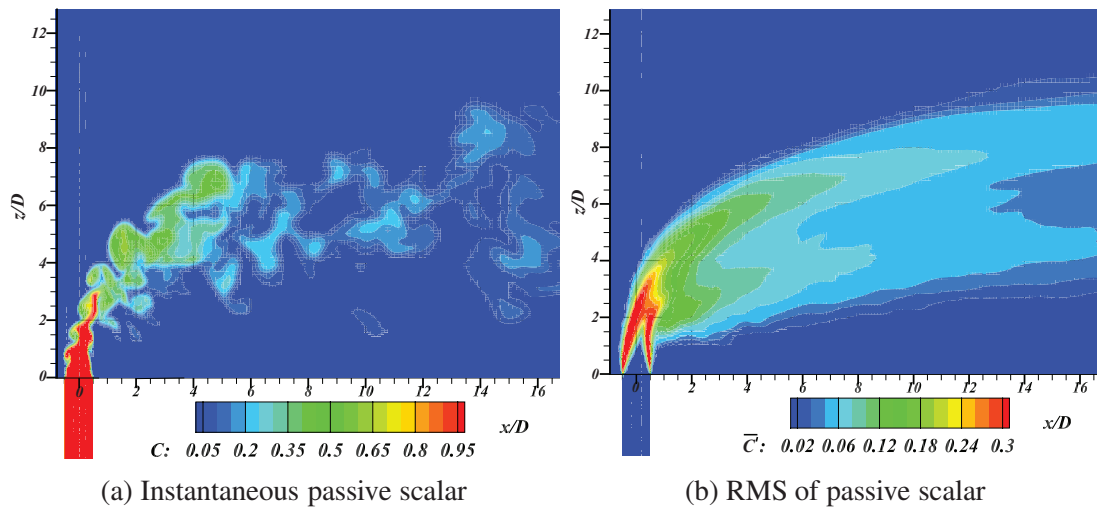


Figure: 5.16 Passive scalar field on symmetric plane $y = 0D$

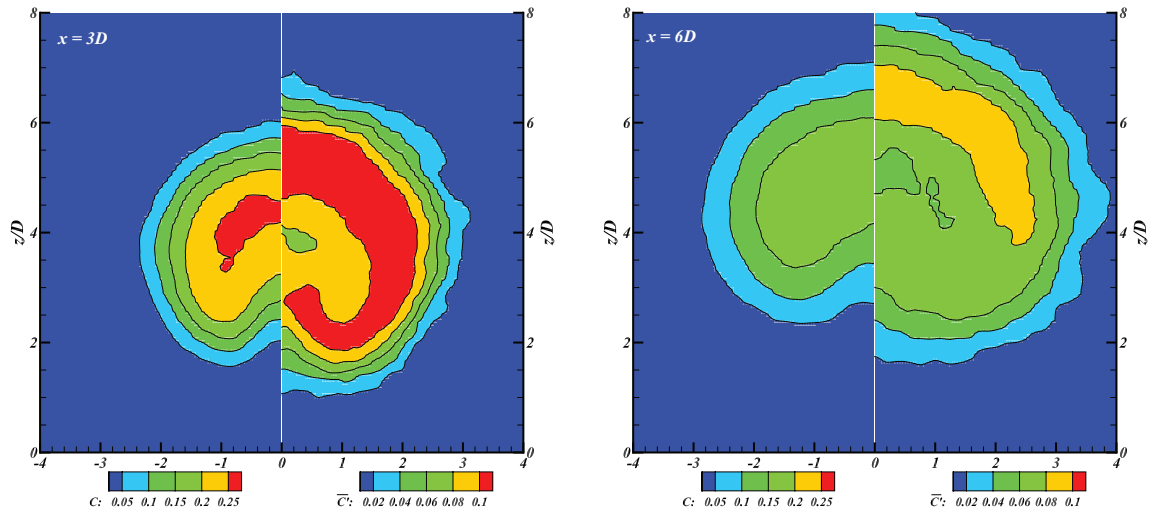


Figure: 5.17 Mean passive scalar concentration and standard deviation on $x = 3.0D$ and $x = 6.0D$

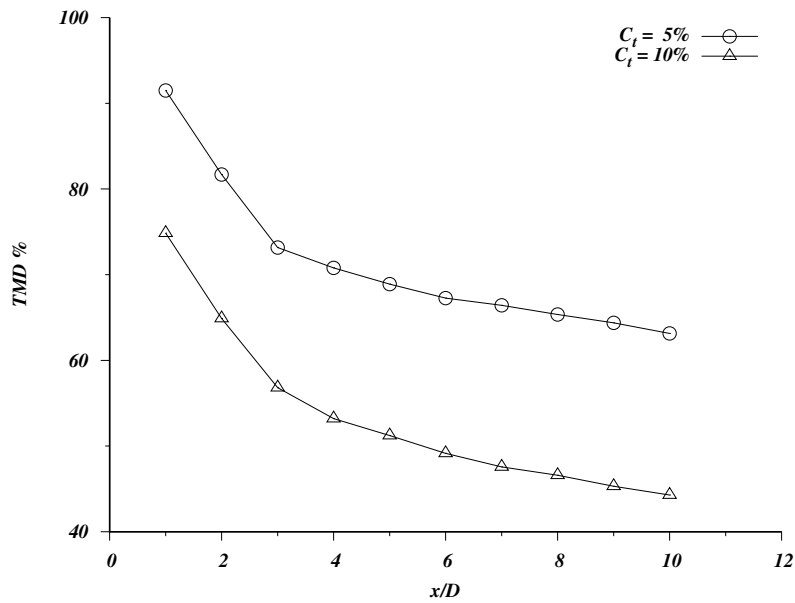


Figure: 5.18 Temporal Mixing Deficiency index

5.1.4 Coherent Structures

In Chapter 2 the Figure: 2.3 illustrated the four prominent vortex structures present in a JICF arrangement. A successful numerical simulation should realize these vortex structures to completely understand the problem. However, for scalar mixing the Counter-Rotating Vortex Pair (CVP) is the most dominant vortex structure in the determination of scalar mixing quality. Since LES resolves the turbulent eddies larger than grid scale, LES results can be

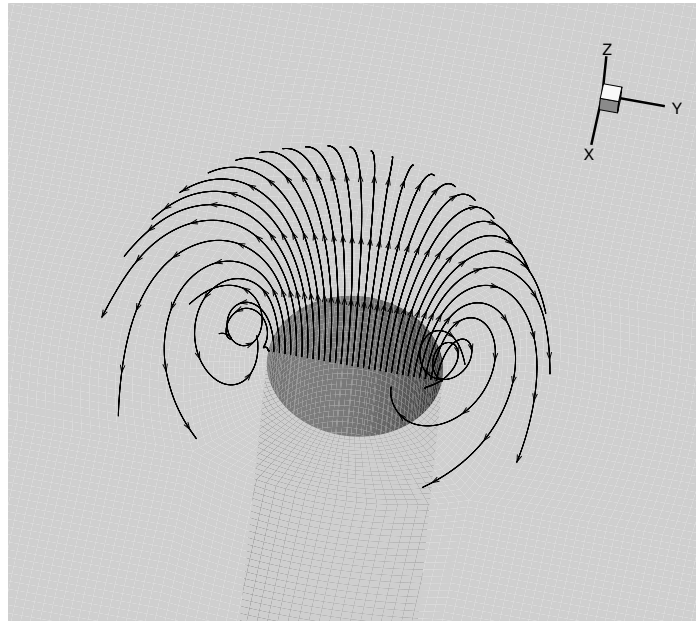


Figure: 5.19 Mean stream lines starting from nozzle orifice

used to capture vortex structures formed in this problem, and in this section vortex structures resolved using LES are discussed. Figure: 5.19 shows streamlines generated using mean velocity components, and it shows the counter-rotating vortex pair developing from the streamlines placed across jet nozzle diameter.

Figure: 5.20 illustrates a comparison between two vortex identification criteria namely λ_2 and Q , where both methods successfully realized vortex structures surrounding the jet and cross-flow interaction region. Importantly both methods capture vertically aligned vortical structures that can be categorized as wake vortices. On the upwind side of the jet flow, jet shear layer vortices can be seen that are formed because of the shear between cross-flow and jet flow. However, clear identification of horseshoe vortex structures is not possible from these vortex identification methods. Figure: 5.21 shows passive scalar concentration mapped onto λ_2 iso-contours, and it can be seen that along evolving vortical structures the passive scalar concentration dilutes. Further careful inspection indicates that along the vertical vortical structures (wake vortices) the passive scalar is transported towards the wall in the downstream direction.

Wake vortex structures

Similar to the well known Karman vortices formed in flow past solid bodies, jet in cross-flow interaction also generates oscillating vortices at the lee side of the jet flow, and these vortical structures were studied by Fric and Roshko [242]. Fric and Roshko's experimental

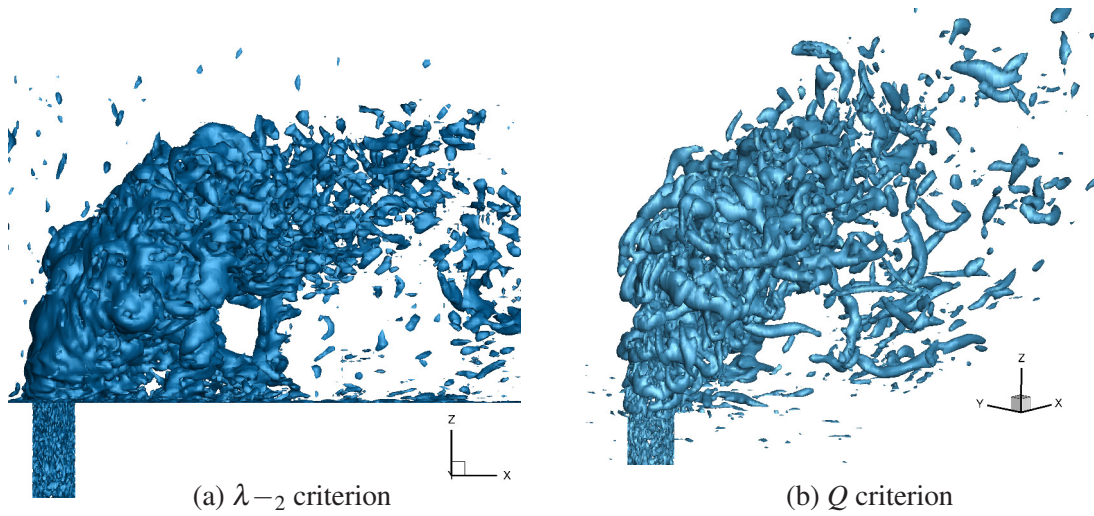


Figure: 5.20 Vortex identification method comparison between Q and λ_2 criteria

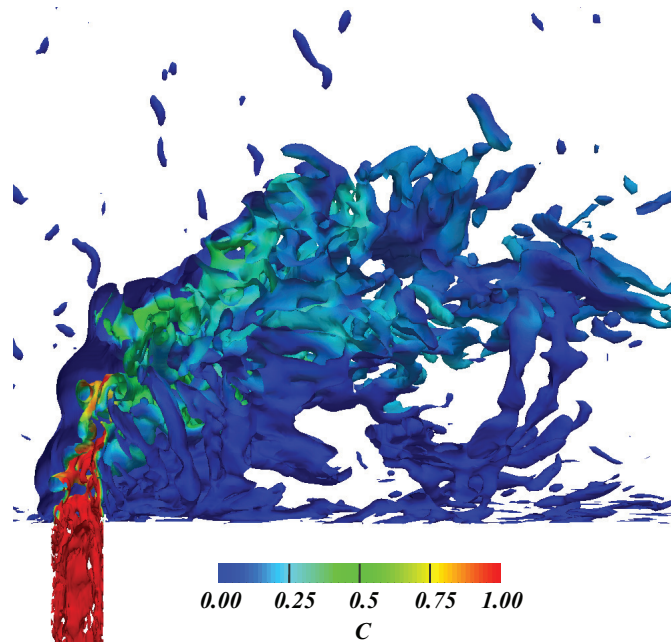


Figure: 5.21 Passive scalar concentration mapped on λ_2 iso-contours

study revealed that the vortex structures in the wake are formed from cross-flow boundary layer wall contrary to the previous understanding of that these vortices are shed from the jet flow. Their study was conducted over several velocity ratios and concluded that velocity ratio of 4 ($R = 4$) showed the most ordered vortex structure, and used wake vortex Strouhal number (St_w , defined in Eqn: 5.2) to define and characterise the wake vortex structures. f is the vortex shedding frequency.

$$St_w = \frac{fD_j}{U_{cross}} \quad (5.2)$$

They investigated the existence of a constant Strouhal number similar to the characteristic Strouhal number of Karman vortex behind solid bodies and showed that for the range of similar Reynolds numbers ($Re_{cf} = U_{cross}D_j/\nu$) corresponding Strouhal number for the vortex shedding behind solid bodies is around 0.2. For the range of Reynolds numbers investigated by Fric and Roshko between $Re_{cf} = 3.8 \times 10^3$ to 11.4×10^3 , JICF wake Strouhal number was measured to vary between 0.12 and 0.16 as shown by points in Figure 5.22. To ensure the LES results have reproduced the wake vortex shedding which is an unsteady flow phenomenon, the Strouhal number can be used. Velocity sampling points were located in the computational domain, and the point at $x = 3.5D, y = 1.5D, z = 1D$, and the wake vortex shedding frequency was calculated from the velocity signal. The dominant frequency at this location recorded to be approximately 250 Hz, which translates to a wake Strouhal number of 0.22. For the experimental configuration studied in this thesis which has a $Re_{cf} = 4.9 \times 10^3$, it can be seen from the Figure: 5.22 the wake Strouhal number calculated from LES results on average is 0.22 is comparable with experimental measurements of Fric and Roshko. Even though the wake Strouhal number from LES result is slightly over-predicted compared to experimental measurements, accounting for the boundary conditions ambiguity and numerical errors, this result indicates that LES results have resolved the turbulence field sufficiently to represent the unsteady flow dynamics of wake vortex shedding.

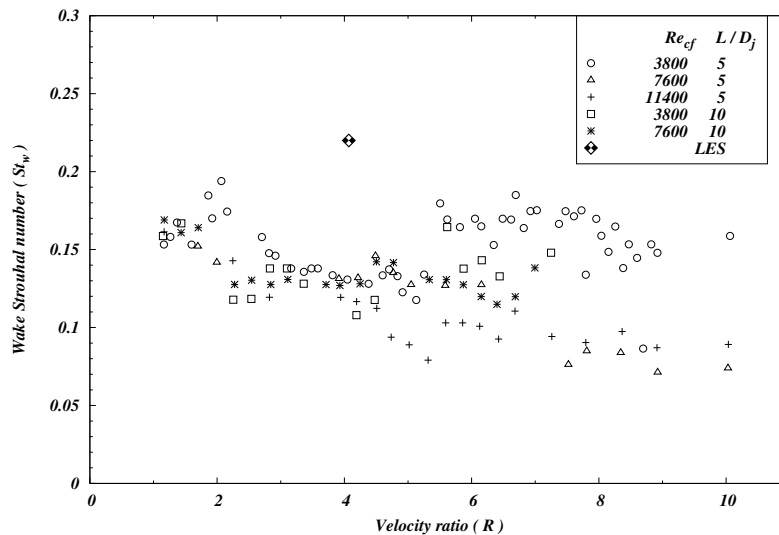


Figure: 5.22 Wake Strouhal number calculated from the experimental measurements by Fric and Roshko, reproduced from [242]

5.1.5 LES Resolution

The turbulence energy spectra can be used as an indication of the LES resolution. Figure: 5.23 shows turbulence energy spectra calculated from velocity probes recordings extracted from three locations, and it shows that turbulent energy spectrum captures the inertial range (slope $f^{-5/3}$) indicating that the grid resolution is sufficient in these locations to satisfy the assumption, that the cut off filter width is in the isotropic dissipative scale range.

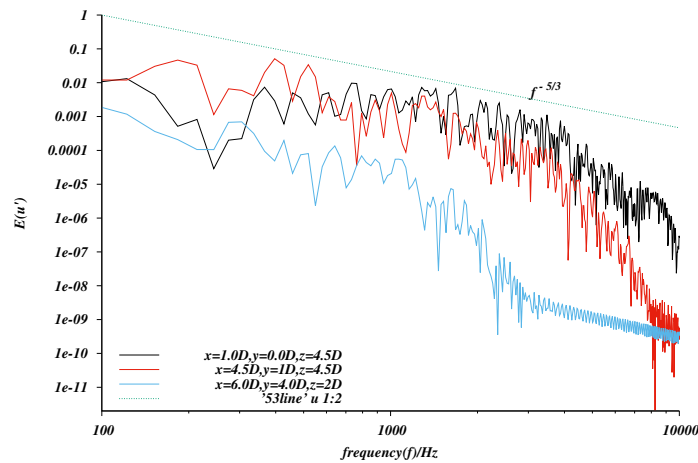


Figure: 5.23 Power spectrum of u'

However, the inspection of turbulent energy spectrum at selected sampling points only provides a local estimation. In a more global estimation of the LES resolution, Figure: 5.24 shows the resolved turbulent kinetic energy percentage (γ) and the computational grid resolution. It shows that the very small mesh size gradient in the downstream direction shows a negligible influence on the resolved kinetic energy percentage. However, the first mesh size change occurred near $x = 2D$, and coincidentally γ value shows a decrease from approximately 95% to 92%. Furthermore, it can be seen that closer to solid wall boundaries the γ value is smaller than the core of the flow, and this is due to the eddy viscosity generated from wall function method near wall boundaries. In addition, a coarse grid resolution was maintained at the top wall boundary as a compromise, because the top wall boundary layer can be assumed to have negligible influence on the overall flow dynamics. As a result, it can be seen that near the top wall also the resolved turbulent kinetic energy percentage is smaller than the core of the computational domain. All three SGS stress models showed a similar variation of the γ variation, and the volume average of γ is calculated to be above 85% for all simulations. Therefore, it can be concluded that even if the spatial variation of grid size showed an influence over the resolved turbulence energy percentage, the grid resolution is sufficient to resolve the turbulence field.

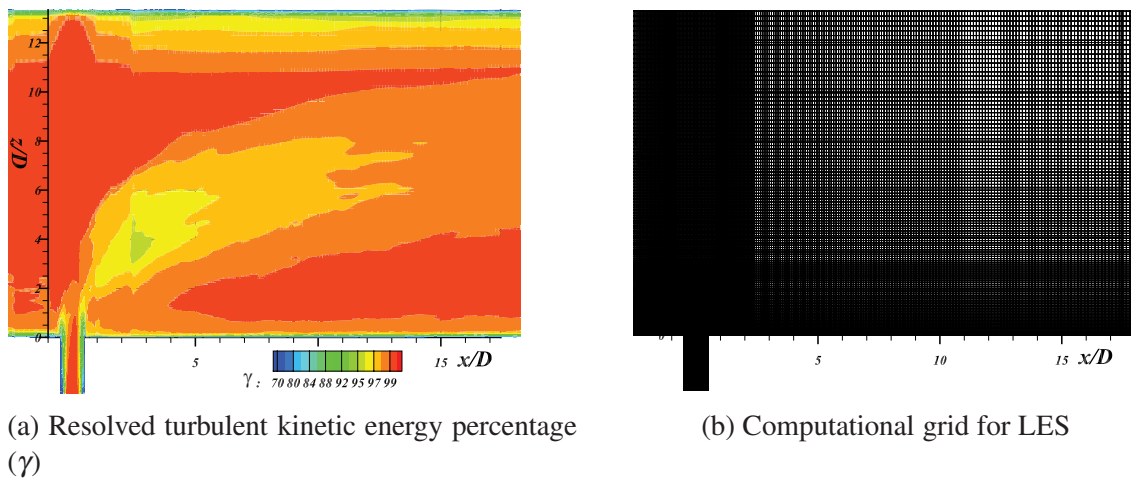


Figure: 5.24 Resolved turbulent kinetic energy percentage

Figure: 5.25 shows an instantaneous view of the eddy viscosity ratio on two orthogonal planes, and they show similar magnitudes by all three SGS stress models. However, a careful inspection of these figures shows that the dynamic one equation model has produced the least amount of eddy viscosity compared to other two models, and the eddy viscosity produced by dynamic k-equation is more localized to the jet trajectory. This observation can be attributed to the fact that one equation model was developed without the assumption of local equilibrium of turbulence generation and dissipation via eddy viscosity; hence local turbulence dissipation is balanced out by transportation. In a similar study by Jones and Wille [47] compared Smagorinsky model, k-equation model for turbulent kinetic energy, and a dynamic Smagorinsky model by using eddy viscosity ratio, and reported that dynamic model produced the least amount of eddy viscosity and k-equation model produced the greatest amount of eddy viscosity throughout the computational domain. However, their study was conducted on a relatively coarse mesh and showed more disparity between numerical predictions and experimental data. Therefore, this result further confirms that with sufficiently resolved LES solution, the effect of SGS model is negligible in producing eddy viscosity compared to RANS models as shown in Chapter 4 where different eddy viscosity models produced substantially different levels of eddy viscosity.

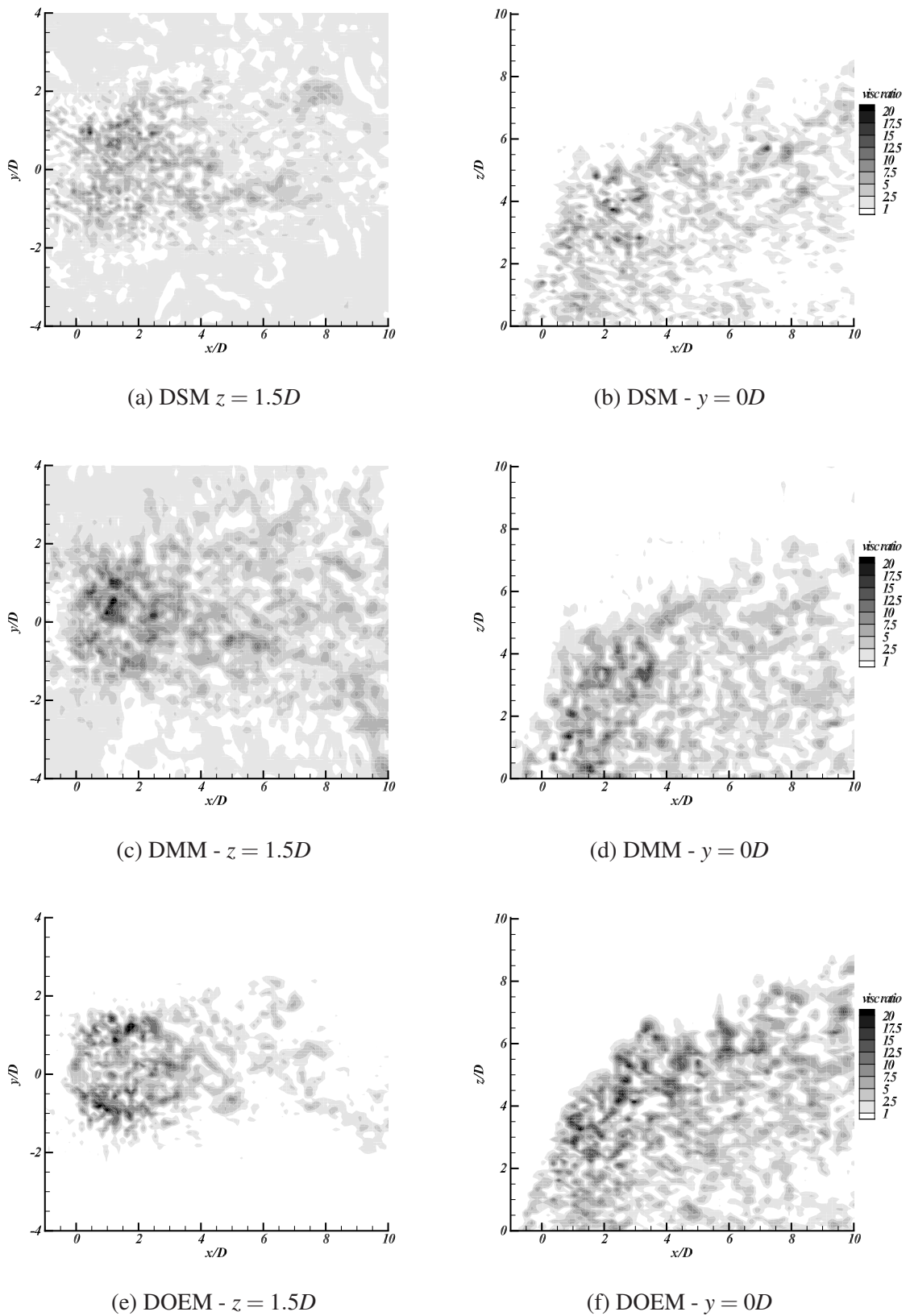


Figure: 5.25 Sub-grid viscosity ratio (v_{sgs}/ν) of SGS models on $z = 1.5D$ and $y = 0D$ plane.

5.2 Twin Jet in Cross Flow

In complex air-fuel mixing applications multiple fuel jets are injected into swirling/non-swirling cross-flows, therefore the understanding of the interaction of multiple jets in cross-flow is critical in design and optimization of air-fuel mixers. Toy et al. [34] conducted experiments on the interaction zone between twin jets by using smoke seeded jets of different velocity ratios. From their experimental work Toy et al. observed a twin jet interactions produce a single counter-rotating vortex pair instead of two vortex pairs for each jet. Schlüter and Schönfeld [19] carried out LES on this problem and obtained good agreement with very limited experimental data available for mean velocity field. In this section, the LES method which was tested in the previous section is used to numerically model the twin jet interaction in cross-flow, and in addition to previous work by Schlüter and Schönfeld, here simulations are carried out by introducing hypothetical passive scalar to investigate the scalar mixing field.

5.2.1 Experimental details

The experimental work by Toy et al. [34] was conducted using real-time quantitative video image analysis of two circular smoke jets entering into a cross flow. An open circuit smoke tunnel was used in this experiment was of 0.75m in height, 0.62m in width and 3.6m in length, the cross-flow reported a turbulence intensity of 0.2%. Smoke generated particles were less than $5\mu\text{m}$ in diameter with 90% less than $1\mu\text{m}$. Jet nozzle diameters (D) were 13.5 mm, and two nozzles were spaced $5D$ apart, and a velocity ratio of $R = 6$ was used. Cross-flow velocity (U_c) was set to be 1m/s resulting in a Reynolds number of 9.3×10^2 based on the nozzle diameter, and a measured boundary layer thickness of 60 mm. Jet velocity was set to 6m/s and measurements were taken at $x = 2.5D, 5D, 10D, 20D$ distances on the symmetric plane between two side by side jets. For comparison in the present study, experimental data were carefully extracted from the original article. Figure: 5.26 shows the problem geometry.

5.2.2 LES modelling of twin jet in cross-flow

Numerical simulations with dynamic Smagorinsky SGS stress model were carried out on a with 6×10^6 hexahedral cells. Inlet velocity condition for cross-flow was generated using a power law profile for channel flow and mapping from an internal plane. Jet-flow boundary conditions were generated using pipe-flow profile and using the Random spot method (Section:3.5). Data were time averaged over a period of 2.5s, after the simulation reached

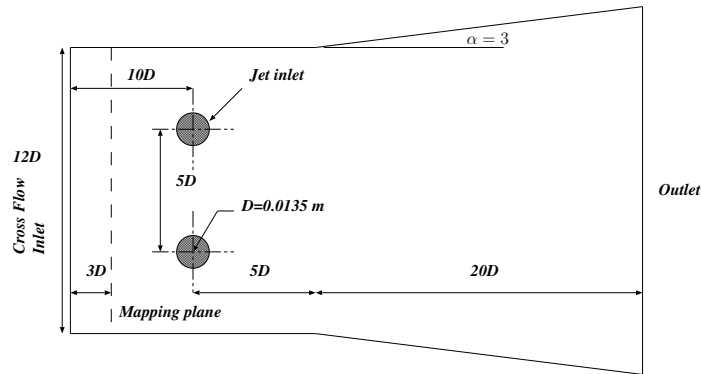


Figure: 5.26 Twin Jet in Cross-Flow computational domain (Experimental data : [34]).

numerical stability. Similar numerical schemes and wall treatment methods were used as in Section:5.1. Due to flow instabilities caused by large vortex interactions time step was kept to maintain a Courant number less than 0.3.

5.2.3 Results

Figure: 5.27 shows numerically simulated mean velocity component in cross-flow direction compared with experimental measurements. It can be seen that overall LES results agreed well with experimental data. These velocity measurements were taken from a plane along the symmetric plane between the two jets. At $x = 2.5D$, the U velocity reduction near $z = 3D$ is not reproduced by LES results, but with increasing downstream distance LES results shows better agreement with experimental data. Further, at $x = 2.5D$ downstream distance from the jet nozzle, the two jet interaction is weaker especially closer to the wall boundary layer. Therefore, it shows that as the flow develops LES results tend to agree with experimental measurements.

Figure: 5.28 shows passive scalar concentration iso-contours at ($C = 0.1$) and provides an insightful view of the flow structure. It shows that till $x \approx 10D$, the passive scalar contour remains coherent and, further downstream the passive scalar contours breaks into separate bubble-like structures indicating that the influence of jet diminishes. Furthermore, the effects of jet shear layer vortices can be seen on the windward side of the iso-contours in the form of ring-like structures. More importantly this view illustrates that these two jets interaction with each other is very weak.

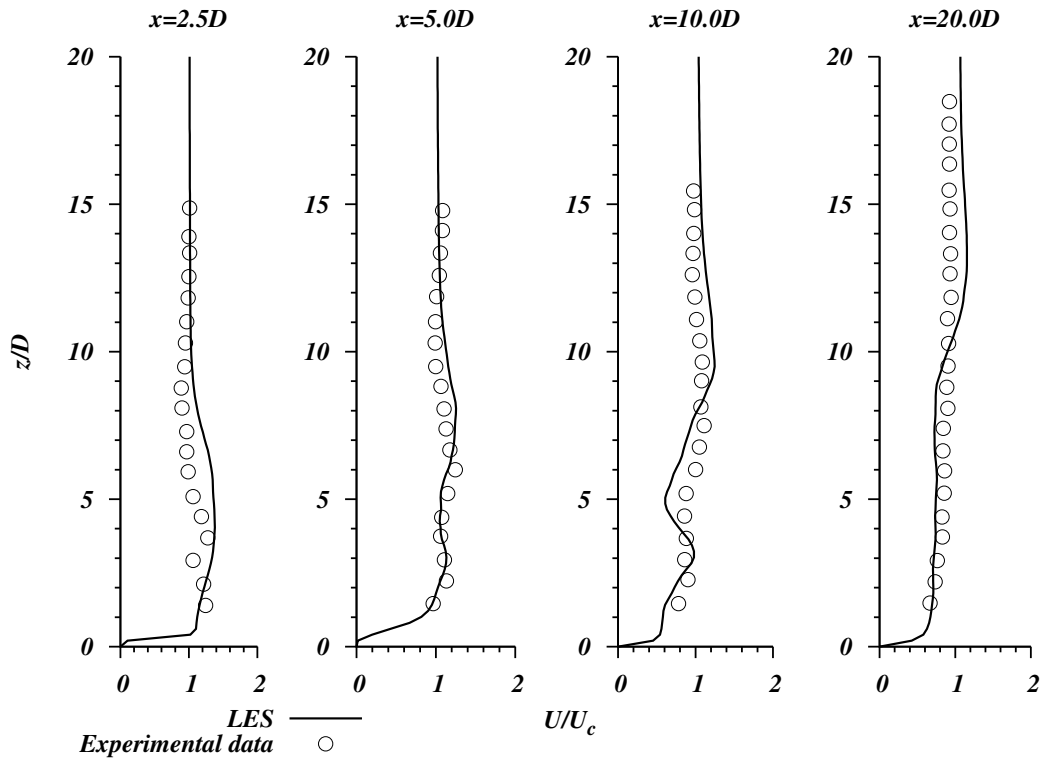


Figure: 5.27 Mean velocity component U/U_c along z direction on $y = 0$ plane

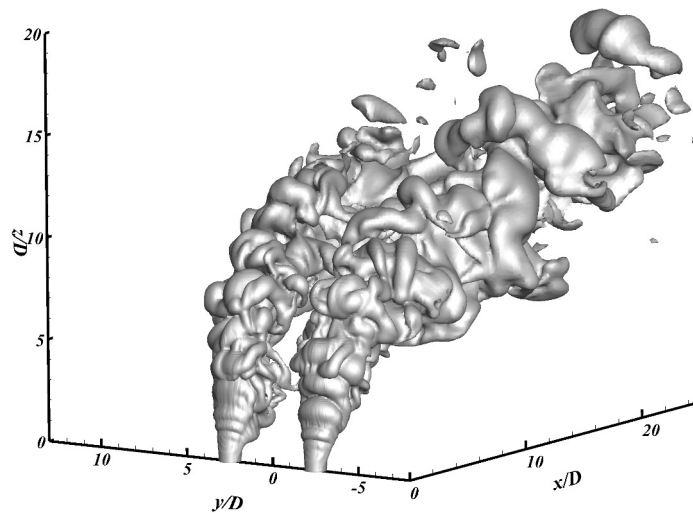


Figure: 5.28 Passive scalar iso-contours for $C = 0.1$

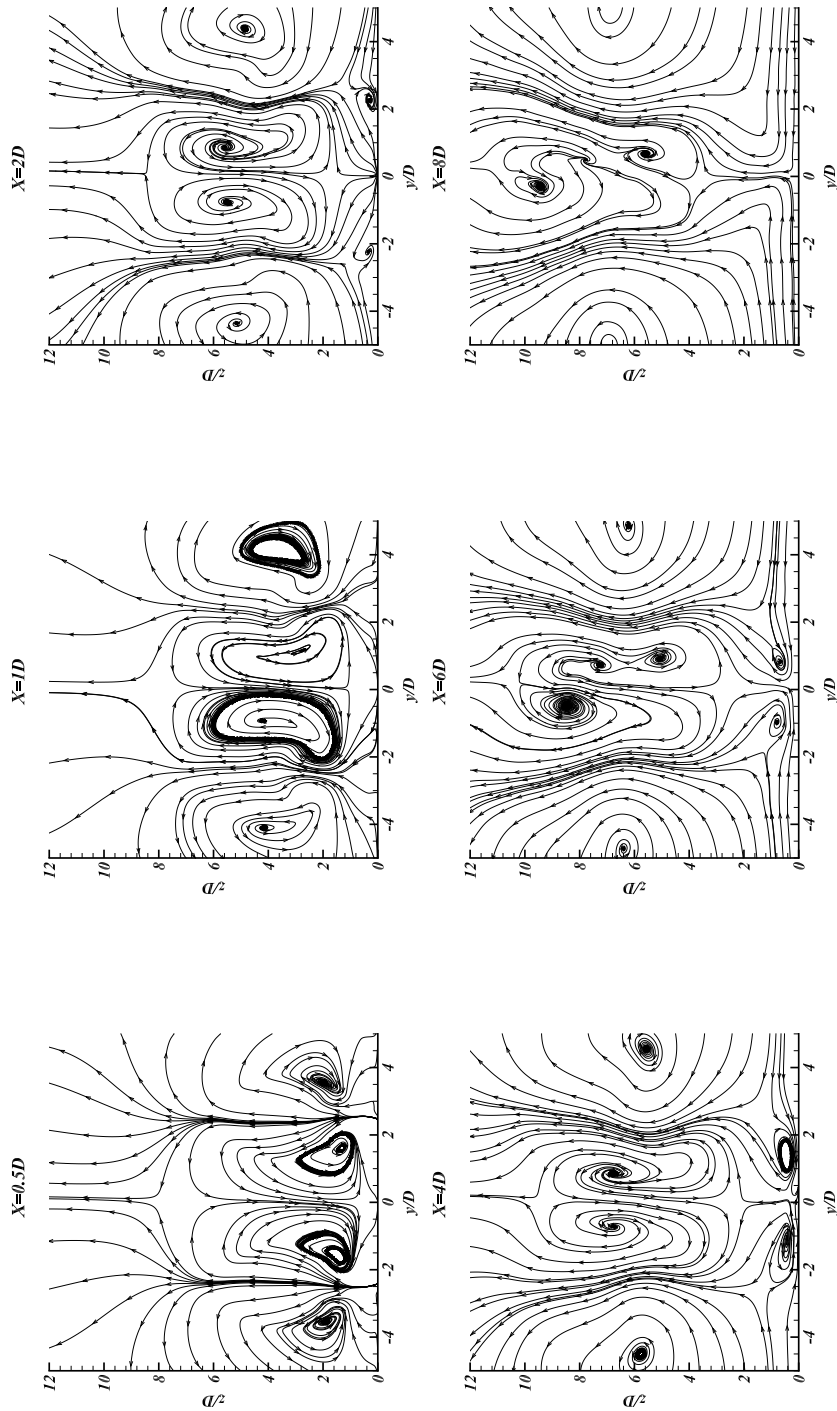


Figure: 5.29 Mean streamline structures of twin jet in cross-flow

Figure: 5.29 shows 2-D streamline contours drawn from mean velocity components (V, W) and the vortex formation and destruction is illustrated. At the lee-side edge of the nozzle ($x = 0.5D$) two distinct CVPs for each jet can be observed forming symmetrically. It can be seen that with increasing downstream distance, each vortex from two jets that are closer to the symmetric axis get attracted to each other, while the other vortex separate and move away from the symmetric plane. By $x = 4D$ it can be seen that at the middle of the domain two vortex cores are separated yet rotating towards each other, and at $x = 6D$ these vortices interact with each other and breakaway vortex is formed. In addition at $x = 2D$ distance, closer to the wall boundary a roll-up vortex can be seen to form near the middle of each original CVP, and with increasing downstream distance these roll up vortices gets closer to each other as well. Streamlines map at $x = 8D$ shows two vortices have interacted with each other, thus have dissipated the vortical energy by breaking into smaller vortical structures. The two opposing vortex attraction is explained by Schlüter and Schönfeld [19] using the *Coanda* effect, which is the phenomenon of a straight fluid flow continues to attached to the wall even if wall curves away from the original flow direction. Their explanation hypothesised that the distance between these two eddies is separated by a thin fluid layer and that fluid layer acts like a wall that keep these two eddies attracted to the wall. Figure 5.30 sheds more light to this problem when two distinct passive scalars are introduced to each jet stream. It can be seen that at $x = 4D$ two flow streams have not mixed with each other, but at $x = 8D$ as expected from the stream lines interaction, the two streams have interacted and mixed into each other. Therefore in multiple jet in cross-flow injection applications scalar concentration is influenced by the interaction of two jets as shown in Figure: 5.31 It can be seen that passive scalar concentration at far field is influenced by the entrainment of two vortices closer to the symmetric plane, and as a result a region in between the original two vortices are formed with conserved scalar concentration.

5.3 Chapter Summary

In this Chapter, the JICF problem that was analysed using RANS models were simulated using LES technique, and as an extension, a twin jet in cross-flow was modelled using LES. LES using dynamic Sub-Grid SGS models showed very good improvement in the accuracy of velocity fluctuating statistics of the JICF problem when compared with RANS results. LES of all three SGS models were sufficiently resolved, and as a result, the SGS model showed negligible influence on velocity field predictions. However, two-dimensional Reynolds stress contours showed that dynamic Smagorinsky model (DSM) produced marginally better agreement with experimental data compared to dynamic mixed model (DMM) and,

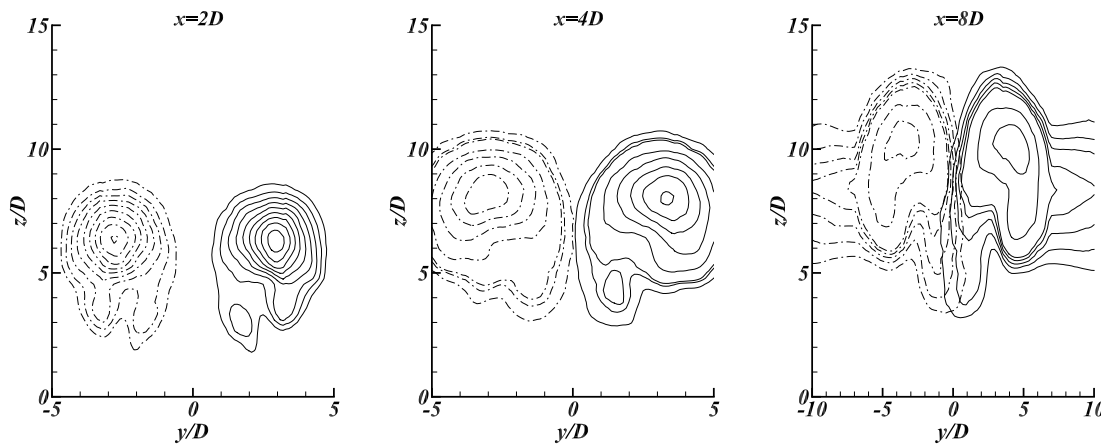


Figure: 5.30 Passive scalar profile interaction from two jet streams (contours are drawn from $C=0.05$ to $C=0.65$ at 0.05 interval)

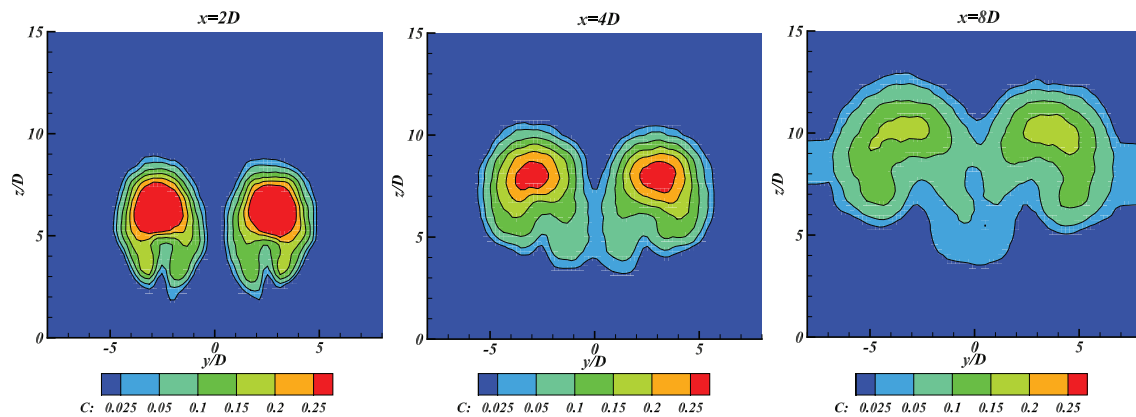


Figure: 5.31 Passive scalar contours of twin jet in cross-flow mixing

dynamic one equation (k-equation) model (DOEM). Reynolds stress predictions at highly strained locations at the jet nozzle revealed stress overprediction by dynamic mixed model. To further investigate these effects based on SGS models, further experimental data or DNS data are required on Jet in cross-flow problems on higher velocity momentums. The study showed that LES technique provides accurate velocity field and scalar field results. Further most importantly when compared with RANS simulations, LES results showed negligible sensitivity to the turbulent Schmidt number on scalar mixing in the range $Sc_t = 0.3 - 1.3$. Coherent structures were realized using LES velocity field statistics, and the scalar mixing is seen mostly dominated by the counter-rotating vortex pair. However, the wake vortical structures also contribute toward the convecting scalar field from the jet towards the wall boundary. LES of single JICF simulations was easily extended to investigate twin JICF problem, and good agreement between numerical results and available meagre experimen-

tal data were obtained. Numerical simulations of twin JICF revealed important observations of pairs of counter-rotating vortex interaction between each other. Therefore, these results suggested that LES technique can be successfully applied to understand the complex flow dynamics of multi-nozzle air fuel injection into cross-flowing air streams, However, these simulations revealed that to comprehensively validate models for twin jets or multiple jets in cross-flow problems more comprehensive experimental data on multiple planes are required because this flow problem is inherently three dimensional compared to many other canonical flow problems.

Chapter 6

Non-Premixed flames

The primary objective of this thesis is to numerically simulate the gas turbine combustion process. In previous chapters the air-fuel mixing arrangement was modelled using LES and RANS methods. In this chapter, strategy and results of the computational modelling of a swirl-stabilized flame are discussed. In this work, a non-premixed swirl burner was computationally modelled using the adiabatic Steady Laminar Flamelet Method in OpenFOAM platform. Since there is a growing tendency to use Hydrogen blends with hydrocarbon fuels, in this thesis efforts were taken to model a Hydrogen-Methane fuel mixture. Hydrogen has been identified as a potential energy storage medium for fluctuating renewable energy sources such as wind power. However, hydrogen combustion in existing burners is challenging and raises safety concerns and design considerations because of increased diffusivity, lower ignition temperatures and increased flammability limits of hydrogen when compared to hydrocarbon fuels. Due to these difficulties in syn-gas operated plants $CO - H_2$ mixtures have been used with H_2 content less than 40% in diffusion flame mode [4]. Given the inherent nature of diffusion flames that NO_x emission production is directly related to the adiabatic flame temperature and hydrogen increases the flame temperature hence NO_x emissions. However, recent research and development have been focused on the use of hydrogen in premixed gas turbine burners, by addressing additional issues of the potential of flame flashback caused by higher flame speeds of hydrogen, and higher pressure drops [243]. Therefore, to understand the working and optimization of such novel burners computational modelling tools are indispensable.

The Sydney swirl burner provides comprehensive experimental data for velocity and scalar for both reacting and non-reacting flows. In this study, the test case with Methane-Hydrogen (1:1) fuel blend was used as a test case (SMH1) to be investigated using the established non-premixed combustion modelling techniques [244], [245]. The burner configuration operates at low to high swirl numbers and therefore, the presence of vortex break-

down structures and the recirculation flow above the bluff body, Numerical simulations of such turbulent reacting flow fields are computationally challenging, and LES modelling can be used due to its inherent ability to resolve turbulent flow structures. In reacting flows, recirculation zones and instabilities caused by Vortex Breakdown structures are decisive physical phenomena that require accurate modelling to comprehensive understanding of the flow field. Therefore, a successful computational modelling approach for gas turbine combustion process should reproduce these flow structures and their effects on reacting flow. The Sydney swirl burner experiments have been performed under different swirl strengths at high velocities which produce flow fields similar to gas turbine burners (high Re numbers). This experimental data has been previously used by researchers to validate different computational codes [172].

6.1 Non-reacting swirl flow simulations

Modelling of Swirl flows presents challenges due to the presence of recirculation zones, vortex breakdown regions and vortex precession. The flow field is predominantly three dimensional even though the far downstream flow can be approximated as axisymmetric. Reacting flows introduce combustion induced instabilities and vortex breakdown structures. Therefore, first non-reacting simulations were carried out to capture the flow dynamics of the swirl burner and to validate solver settings. Two Non-reacting test cases namely, low swirl number case $S = 0.54$ (*N29S054*) and high swirl number case $S = 1.59$ (*N16S159*), were modelled in iso-thermal simulations (In these experiments swirl number S is defined as $S = \text{Tangential velocity}/\text{Axial velocity} = W_s/U_s$).

6.1.1 Experimental setup

The experiments on Sydney swirl burner were performed at the Sydney University in collaboration with the Sandia National laboratory [244]. Figure: 6.1 shows the burner geometry, which primarily consists of a central jet nozzle, a bluff body, an annular swirl flow inlet, and an outer chamber that contains the burner. Outside of swirl flow, a co-flow of air with 2% free stream turbulence was provided with $U_e = 20\text{m/s}$ to avoid local entrainment near the bluff body face. In iso-thermal test cases air was supplied through both, swirl inlet and central jet at 293 K, and in reacting test cases swirl flow only provided air and the central jet provided fuel into the burner. Laser Doppler Velocimetry measurements were carried out to measure three velocity components (U : axial velocity, V : radial velocity, W : tangential velocity) and scalar measurements were performed with a Raman-Rayleigh-LIF measuring

6.1 Non Reacting Swirl Flows

system. Three tangential swirl intakes with an angle of 15° to the horizontal were used to generate swirl air flow, and main central fuel jet is sent through a honeycomb mesh to straighten the flow. Boundary conditions for the test cases used in this thesis work are shown in Table: 6.1. Swirl flow Reynolds number is based on the outer radius swirl annular (r_s) $Re_s = U_s r_s / \nu$. Hereafter in this Chapter the test cases N29S054 and N16S159 are referred as Low Swirl and High Swirl test cases respectively.

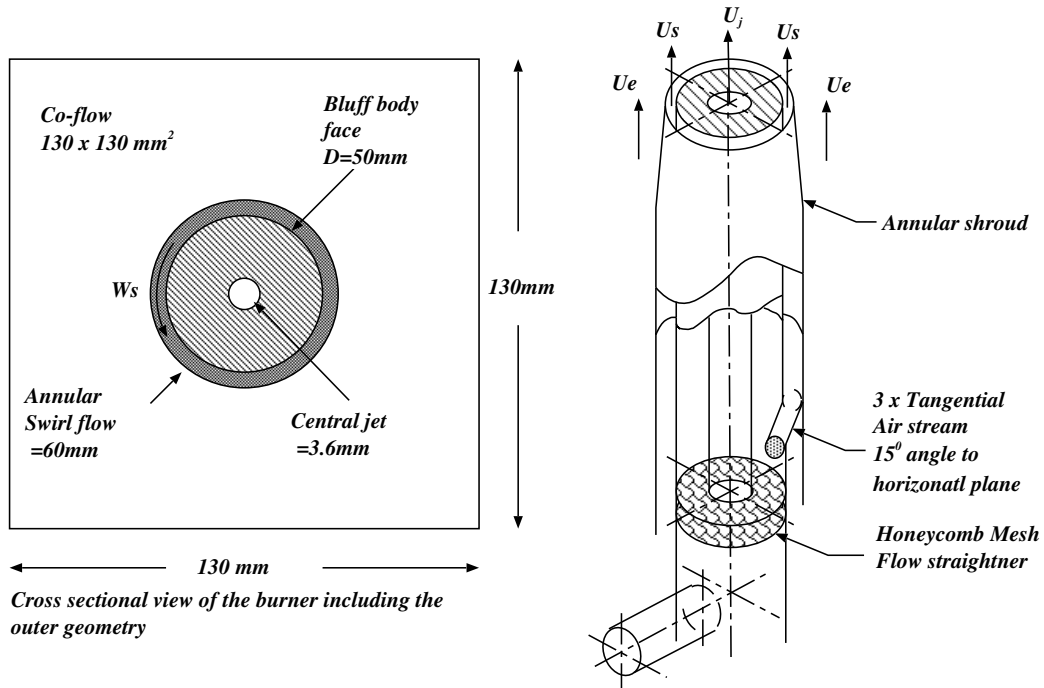


Figure: 6.1 Sydney swirl burner geometry.

Table 6.1 Boundary conditions for Sydney swirl burner test cases.

Boundary condition	Low Swirl (N29S054)	High Swirl (N16S159)	Reacting (SMH1)
$U_j / (ms^{-1})$	66.0	66.0	140.8
$U_s / (ms^{-1})$	29.74	16.26	42.8
$U_e / (ms^{-1})$	20.0	20.0	20.0
$W_s / (ms^{-1})$	16.06	25.85	13.70
S	0.54	1.59	0.32
Re_s	59000	32400	85900

6.1.2 Simulation set up

The computational domain was approximated using block structured grid with 1.7×10^6 cells for the non-reacting flow simulation. A very fine grid with 7×10^6 cells was used for the reacting flow simulation. Figure: 6.2 shows the computational grid structure used to simulate the Sydney swirl burner flows, the mesh was gradually increased radially and axially to avoid commutative errors caused by sudden grid size gradients. Mean inlet velocity profiles were calculated using a priori simulation, and inlet turbulence structures were artificially generated using the random spot method [213], and imposed on the swirl boundary and central jet boundaries. For the co-flowing air flow, a white noise was introduced with assumed turbulence intensities of 0.01, 0.01, 0.05 in radial, tangential and axial directions respectively.

The outlet boundary was placed $200 \times r_{fuel,jet}$ distance away from the inlet and mesh was gradually extruded towards the outlet to avoid reverse flow so that zero-gradient boundary condition could be used at the outlet boundary. Non-reflective boundary condition was imposed on the outlet pressure, and zero-gradient boundary condition was imposed on other scalars. For the outlet velocity boundary condition, a convective boundary condition was imposed to avoid reverse flow caused by larger eddies generated as a result of flow evolution towards the outlet of the domain. Spalding's continuous wall function was imposed on the wall boundary of the bluff body surface and side walls. Locally dynamic Smagorinsky model was used for SGS stress closure. Second order implicit temporal discretization was used alongside *vanLeer* TVD scheme for scalar convection term discretization. Low dissipative discretization scheme (*filteredLinear2V*) was used for momentum equations ensuring second order accuracy. Time step was maintained to keep a Courant number less than 0.4. LES results were accumulated after several flow-passes and time-averaged for about 60ms temporarily and across four perpendicular planes to compare against experimental data.

6.1.3 Non-Reacting flow : Velocity Field

From Figure: 6.3, to Figure: 6.5 mean velocity field statistics are compared for the high swirl test case (Left,N16S159) and low swirl test case (Right,N29S054). Figure: 6.3 compares the non-dimensionalized mean axial velocity flow component for the two test cases using LES simulations and experimental data at different axial distances from the inlet. The plot $z = 0.136D$ is the distance nearest to the inlet of the computational geometry, and it can be seen that LES results agree very well with experimental data. Therefore, it confirms that the imposition of inlet boundary values closer to the computational domain did not cause an appreciable error in the solution, and the velocity field showed excellent agreement closer

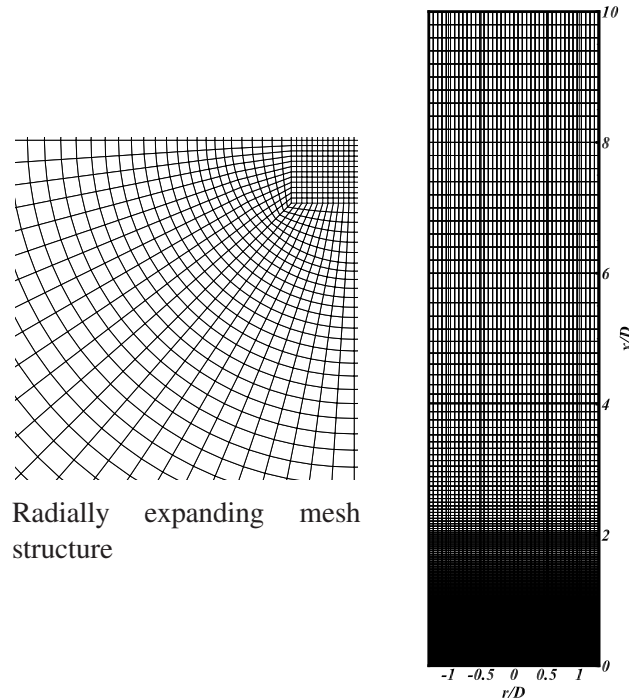


Figure: 6.2 Computational grid used to model the Sydney swirl burner.

to the inlet. However, in subsequent distances at $x = 0.2D, 0.4D, 0.6D$ the high swirl test case showed a small discrepancy of the maximum axial velocity that occurred on the symmetric axis, yet maintaining ample agreement with the velocity decay variation in radial direction. It is inconclusive the source of this error which caused this discrepancy. However, it should be noted that the bulk central-jet velocity was $66m/s$ that corresponds to a Mach number of 0.2 which borders the applicability of incompressible flow assumption (density is not changed by the flow velocity) [174]. Irrespective of this local discrepancy, the overall axial velocity variation prediction was in good agreement with experimental data. Further, it shows that as the axial distance increases, the strength of axial velocity of the central jet decreases, but noticeably in the low swirl flow case the axial velocity decays faster than high swirl flow test case, and LES results captured the velocity decaying to be in good agreement with experimental data. In the case of high swirl test case, the axial flow velocity on the central axis reached stagnation in the region of axial distance $x = 1.4D(70mm) - 2.0D(100mm)$. The low swirl flow velocity faster decay, and stagnation was reached by $x \approx 0.8D(40mm)$ and showed negative axial velocity on the central axis at $x \approx 1.4D(70mm)$. To understand the negative axial velocity components resulted from the recirculation zones the streamlines plot (Figure: 6.11) and velocity contour plot (Figure: 6.12) can be used. From the streamlines contour it can be seen that in the high swirl test case a stronger and longer recir-

culating zone exists behind the bluff body that extended close to $x \approx 2D(100mm)$. Whereas in the low swirl test case the recirculation zone behind the bluff body only extends close to $x \approx 0.5D(25mm)$. However, most importantly in the low swirl test case a vortex break-down structure formed as a bubble break-down present and can be seen as a recirculation zone in the region of $x \approx 1D(50mm)$. That can be considered as a significant finding of this experiment because, in contrast to the common understanding that high swirl flows exhibit vortex breakdowns, this evidence shows that even in low swirl number flows combined with a strong axial jet, vortex breakdown structures could exist. Therefore, the small negative velocity seen in the axial velocity plot for the high swirl test case (Figure: 6.3) is caused as a result of the extended bluff-body recirculating zone (as seen from Figure: 6.12). Therefore, it can be said that LES results show good agreement in axial flow velocity prediction and captured essential vortex structures of the swirl flow burner for both test cases, and the downstream discrepancies are probably caused by the gradual increase of grid resolution.

In Figure: 6.4, the mean tangential velocity component (W) results from LES are compared against experimental data. It shows that for both cases LES results show excellent agreement with experimental data. It can be seen that over the annular inlet ($r \sim 1R_b$) the high swirl number test case shows greater rotating velocity (tangential velocity) than the low swirl test case, as it is expected. However, it shows that in the low swirl test case the rotational momentum gradually transfers closer to the central axis, whereas in the high swirl test case the rotational momentum only decays with the increase of axial distance. More importantly, it shows that in the low swirl test case, in the region between $x \approx 0.6D - 0.8D$, the maximum rotational velocity magnitude is greater than the inlet specified rotational velocity. Hence, it can be inferred that in the high swirl test case the rotational momentum is restricted to the annular inlet zone when compared with the low swirl test case where the rotational momentum transferred closer to the central axis. To explain this paradox the rotational velocity contours Figure: 6.13 can be used, in which it shows that in both cases a central non-rotating (or weakly rotating) fluid mass is surrounded by a rotating fluid mass. However, it shows that in the low swirl test case the central non-rotating fluid body is narrower. Whereas in the high swirl test case the rotating fluid mass is localized inside the annular radial distance, as a result, broadens the non-rotating fluid body. Also it is shown in the axial velocity contour (Figure: 6.12) that in the low swirl test case existence of a shorter recirculation zone behind the bluff body that ends closer to $x = 25mm(0.5D)$ paves the way to rotating fluid body to get closer to the central axis (induced by the flow stagnation as a result of the recirculating axial flow). Thus, it can be said that due to the recirculation zone behind the bluff body and tangential flow interactions, in the low swirl test case the rotational fluid mass becomes closer to the central axis and therefore increases its velocity

to conserve the rotational momentum. Therefore, the existence of this strong local rotating fluid mass explains the greater tangential velocity in the region $x \approx 0.6D - 0.8D$ than at the swirl-inlet. As a result of this accelerated rotational velocity in the low swirl flow test case, a vortex breakdown bubble can be seen just above this high rotational velocity zone at $x 1D - 1.2D(50 - 70mm)$. Effects of this vortex breakdown bubble can also be seen as a separated recirculation structure in the axial velocity contour (Figure: 6.12). According to this evidence, the presence of vortex breakdown structures cannot be solely characterized by Swirl number, but the relationship between jet velocity and swirl velocity should be taken into consideration. Further downstream the rotational velocity is reduced in magnitude as the angular momentum is dissipated, and LES results showed excellent agreement with experimental data in predicting rotational velocity.

In contrast to axial and rotational velocity components, the radial velocity component was not specified with a numerically significant value at the swirl boundary. Therefore, the strength of the radial velocity component is dictated by the strength of recirculating eddies behind the bluff body surface and the expansion of swirl flow. Therefore the size and strength of recirculation zone dominate the radial velocity component. This can be seen in Figure: 6.5 in which the radial velocity component distribution by LES and experimental data are compared. LES results exhibit the general pattern of radial velocity variation in the radial direction when compared against experimental data, and similar results have been shown by previous studies [246]. The radial velocity component direction changes across the recirculation zone, and this feature is captured by LES results. In the high swirl test case, the LES results have captured these essential features of radial velocity at both near field and far field distances. However, in the low swirl test case, LES results show only qualitative agreement with experimental results close to the bluff body $x < 0.8D$. However, in the low swirl test case, LES results show the radial velocity variation pattern similar to experimental measurements close to the bluff body, but with the increase of axial distance, strong discrepancies appear. At $x = 1.4D, 2.0D, 2.5D$ distances the radial velocity measurements show a negative velocity at the symmetric axis, which is controversial considering that a sufficiently time-averaged velocity field for a swirl flow should resemble axis-symmetry, hence radial velocity at the axisymmetric axis must be zero. Therefore, this discrepancy is attributed to an experimental anomaly and the LES results showed consistency by maintaining axisymmetric radial velocity field.

Figure: 6.14 and Figure: 6.15 shows the axial and rotational velocity contours compared against experimentally calculated velocity contours for high swirl test case and low swirl test case respectively. The high swirl axial flow velocity contour shows that the recirculation zone that stagnates closer to $70mm$ axial distance and in LES results also the recirculation

zone stagnate closer to $65mm$. The low swirl axial flow velocity contours show that the central axial jet strength decays much quicker than high swirl test case and the recirculation zone stagnation occurs close to $30mm$ in experimental contour plot, and the LES results also shows that the recirculation zone stagnates closer to $30mm$. The rotational momentum contour for the high swirl test case (Figure: 6.14) shows that the radial momentum spreads radially outward, according to both experimental and LES data, however in the low swirl test case a negligible radial spread of rotational momentum can be seen. Therefore these evidence shows that the LES results have reproduced the momentum field in both test cases successfully.

6.1 Non Reacting Swirl Flows

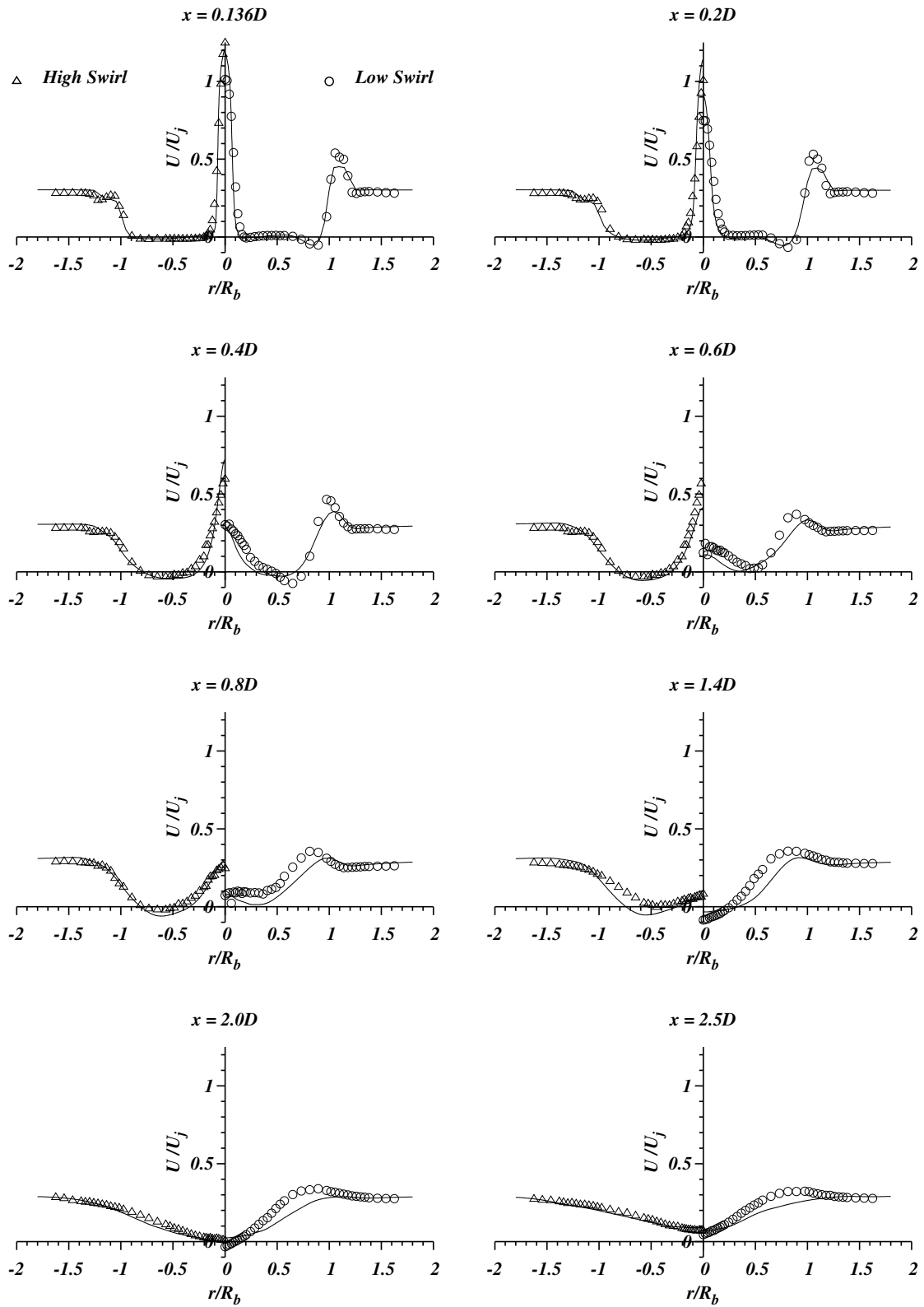


Figure: 6.3 Mean axial velocity comparison for Low Swirl (Right) and High Swirl (Left) test cases, Lines : LES, Points : Experimental data[247].

6.1 Non Reacting Swirl Flows

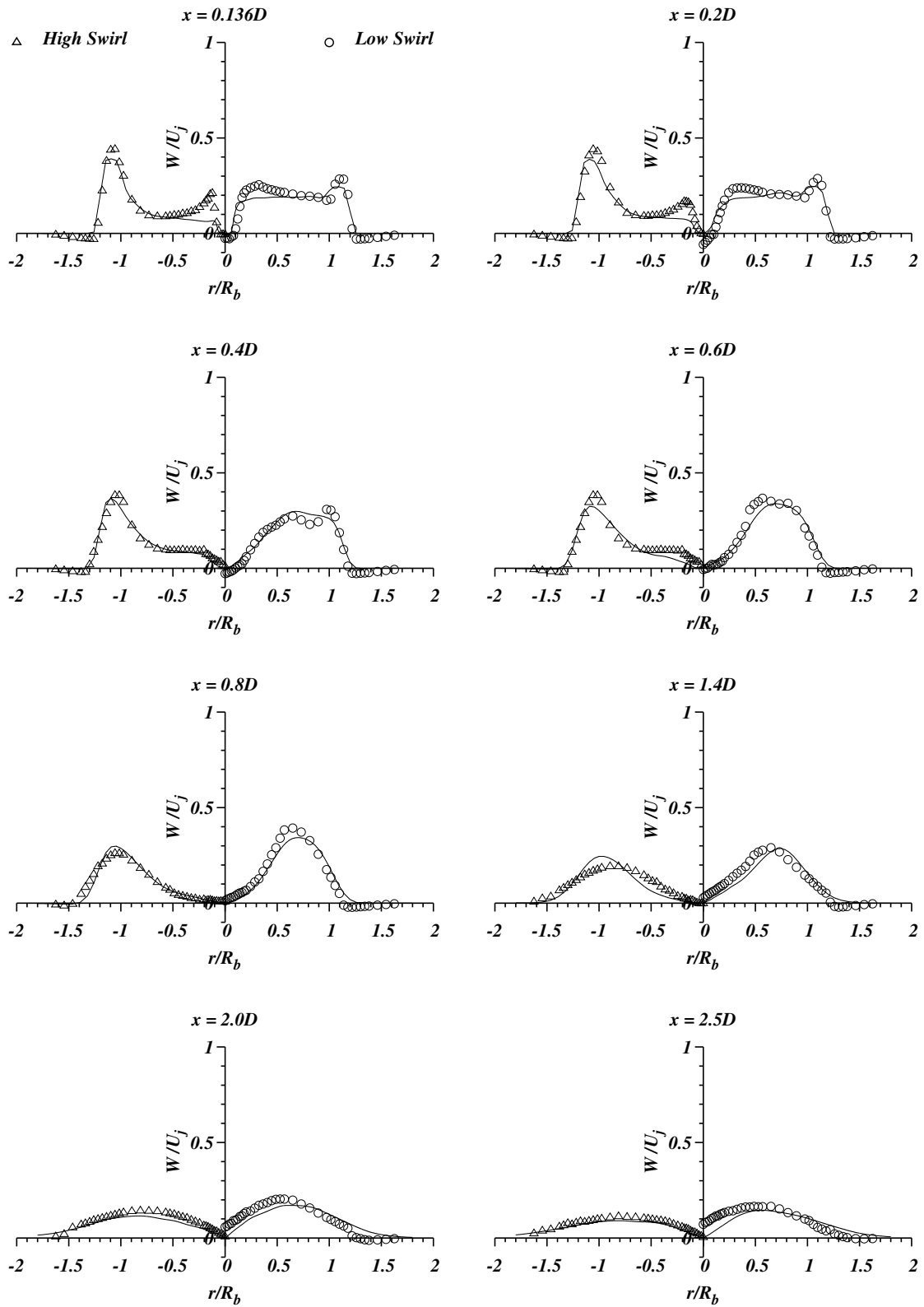


Figure: 6.4 Mean tangential velocity comparison for Low Swirl (Right) and High Swirl (Left) test cases, Lines : LES, Points : Experimental data[247].

6.1 Non Reacting Swirl Flows

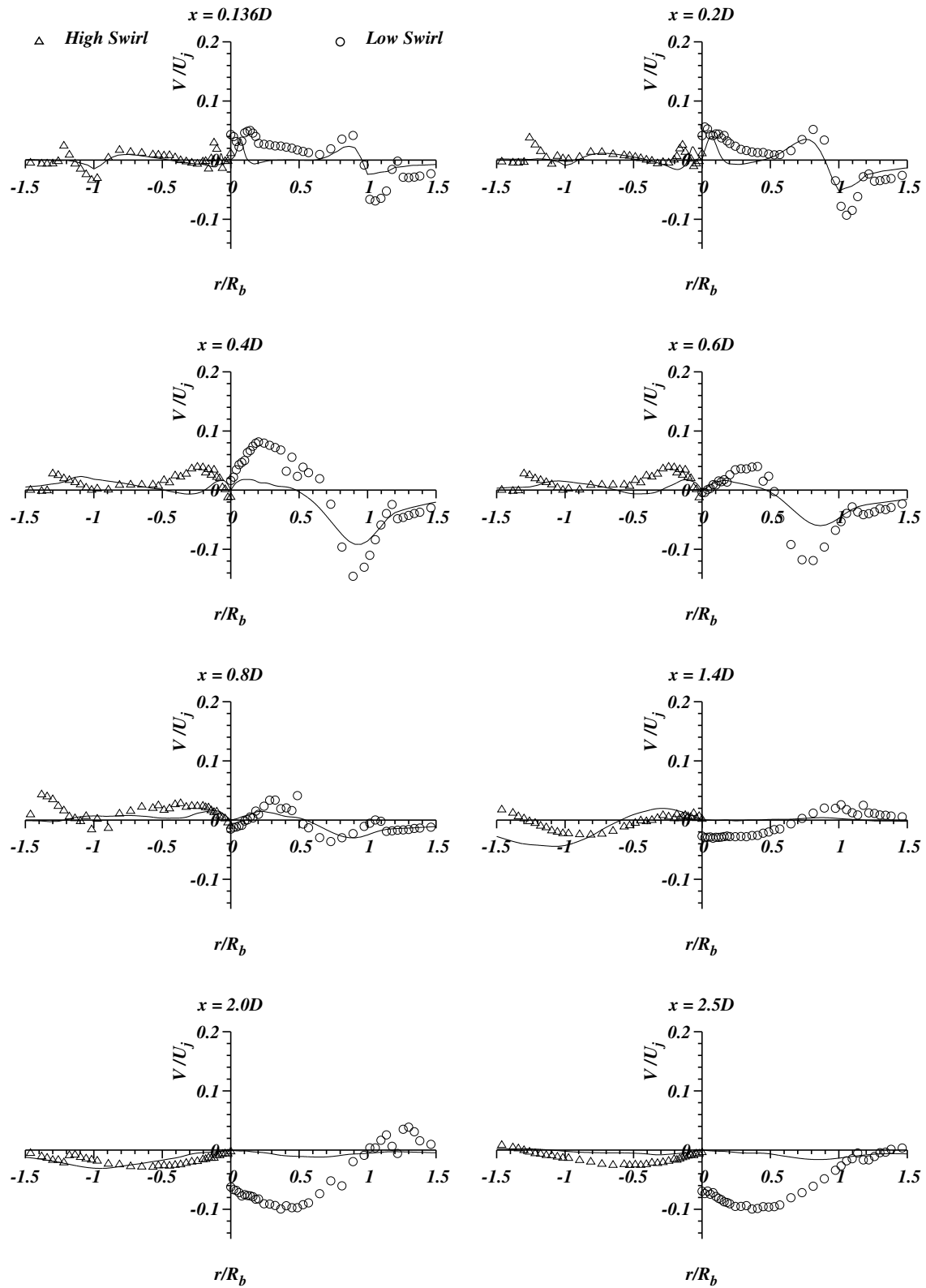


Figure: 6.5 Mean radial velocity comparison for Low Swirl (Right) and High Swirl (Left) test cases, Lines : LES, Points : Experimental data[247].

6.1 Non Reacting Swirl Flows

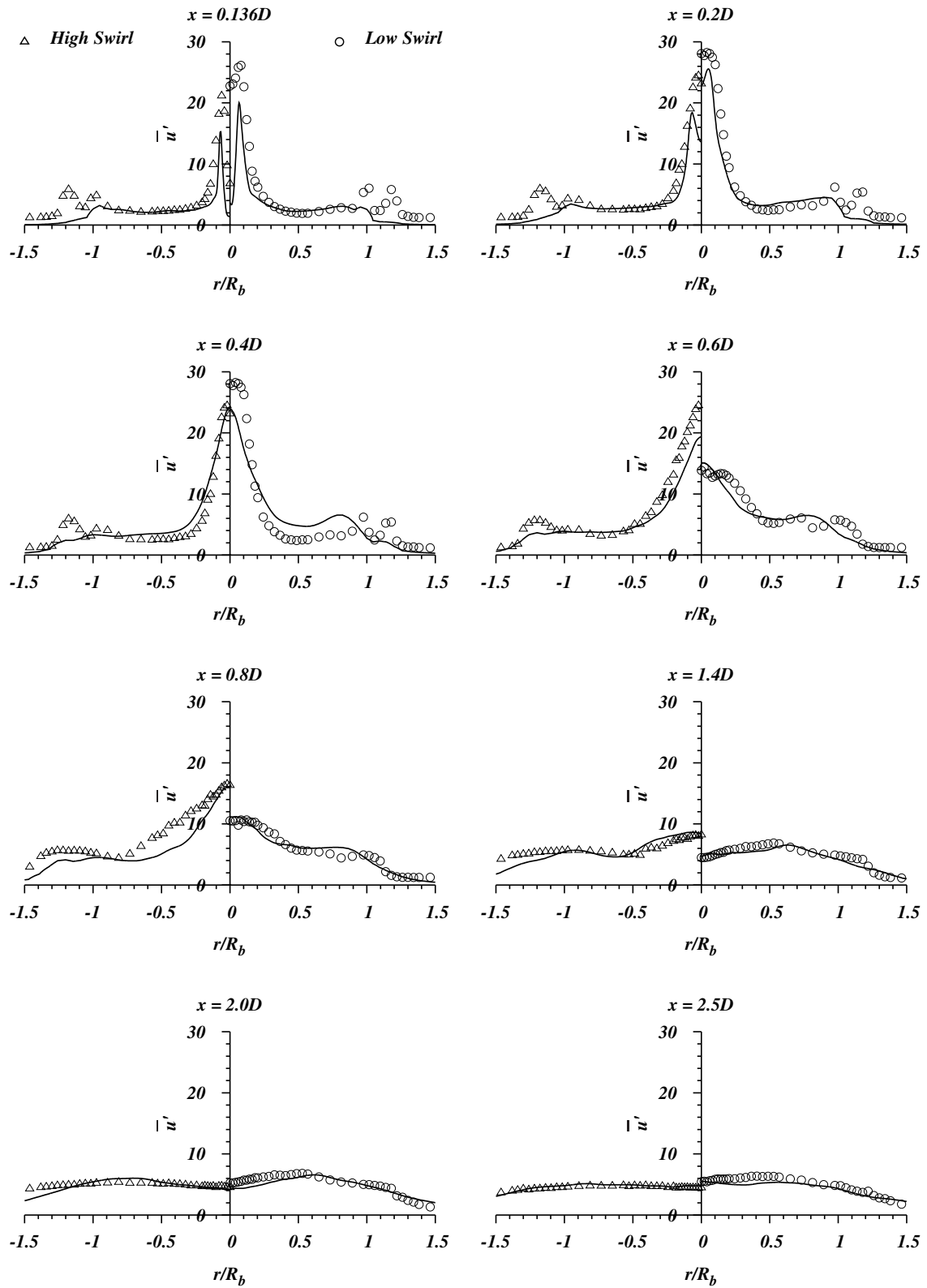


Figure: 6.6 Axial velocity RMS ($\overline{u'}/(ms^{-1})$) comparison for Low Swirl (Right) and High Swirl (Left) test cases, Lines : LES, Points : Experimental data[247].

6.1 Non Reacting Swirl Flows

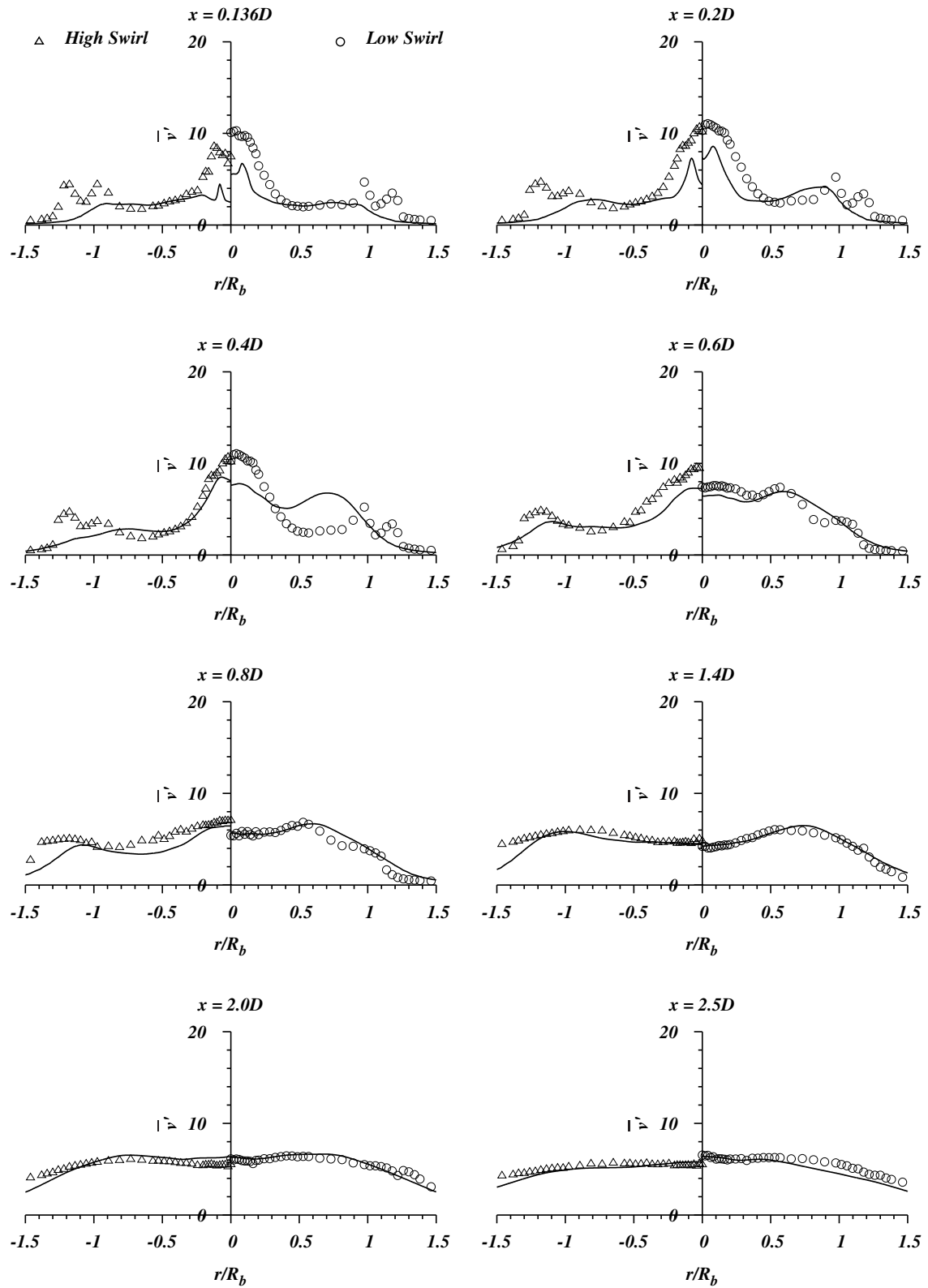


Figure: 6.7 Radial velocity RMS ($\overline{v'}/(ms^{-1})$) comparison for Low Swirl (Right) and High Swirl (Left) test cases, Lines : LES, Points : Experimental data[247].

6.1 Non Reacting Swirl Flows

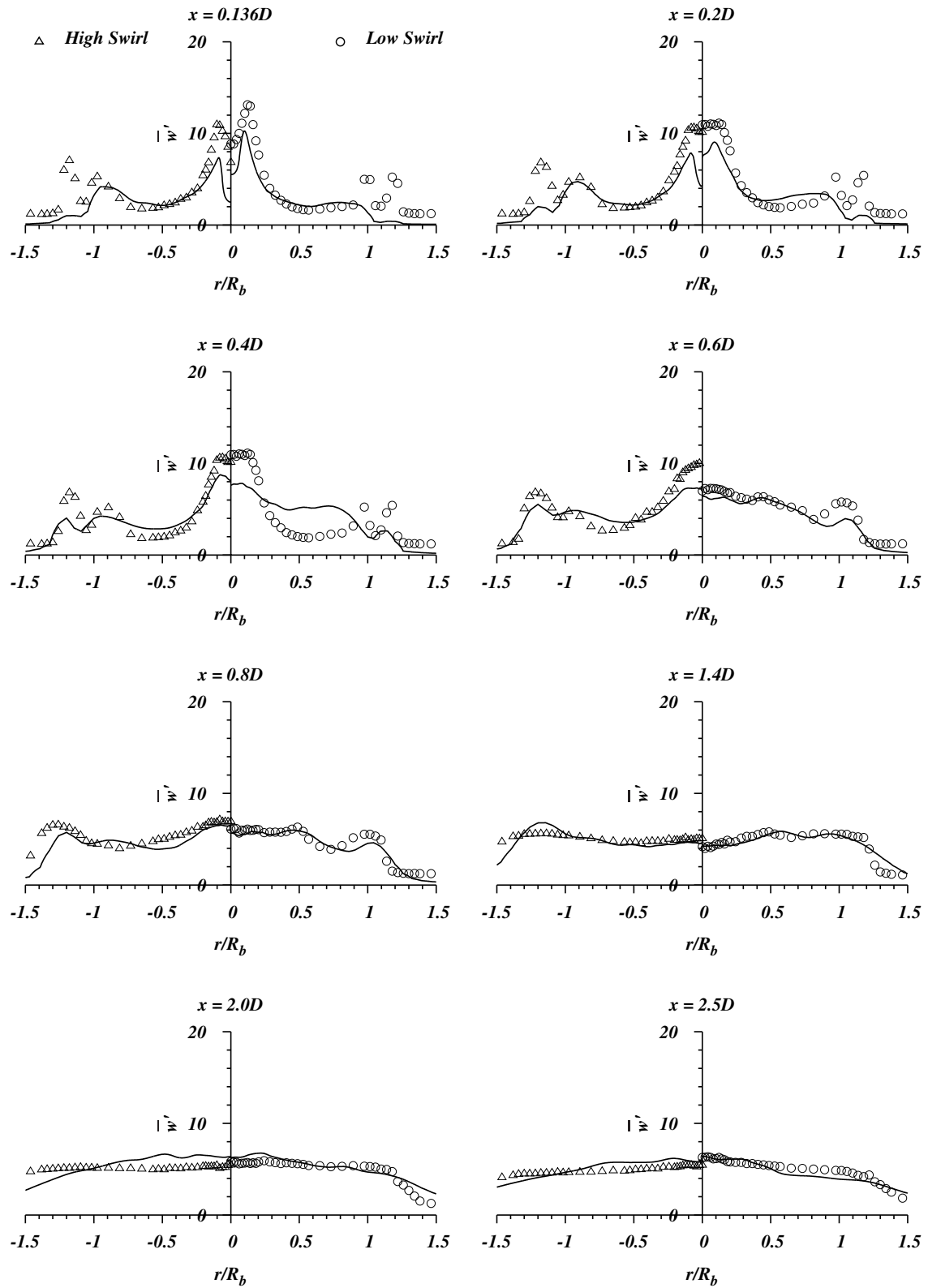


Figure: 6.8 Rotational velocity RMS ($\overline{w'}$)/(ms^{-1}) comparison for Low Swirl (Right) and High Swirl (Left) test cases, Lines : LES, Points : Experimental data[247].

6.1 Non Reacting Swirl Flows

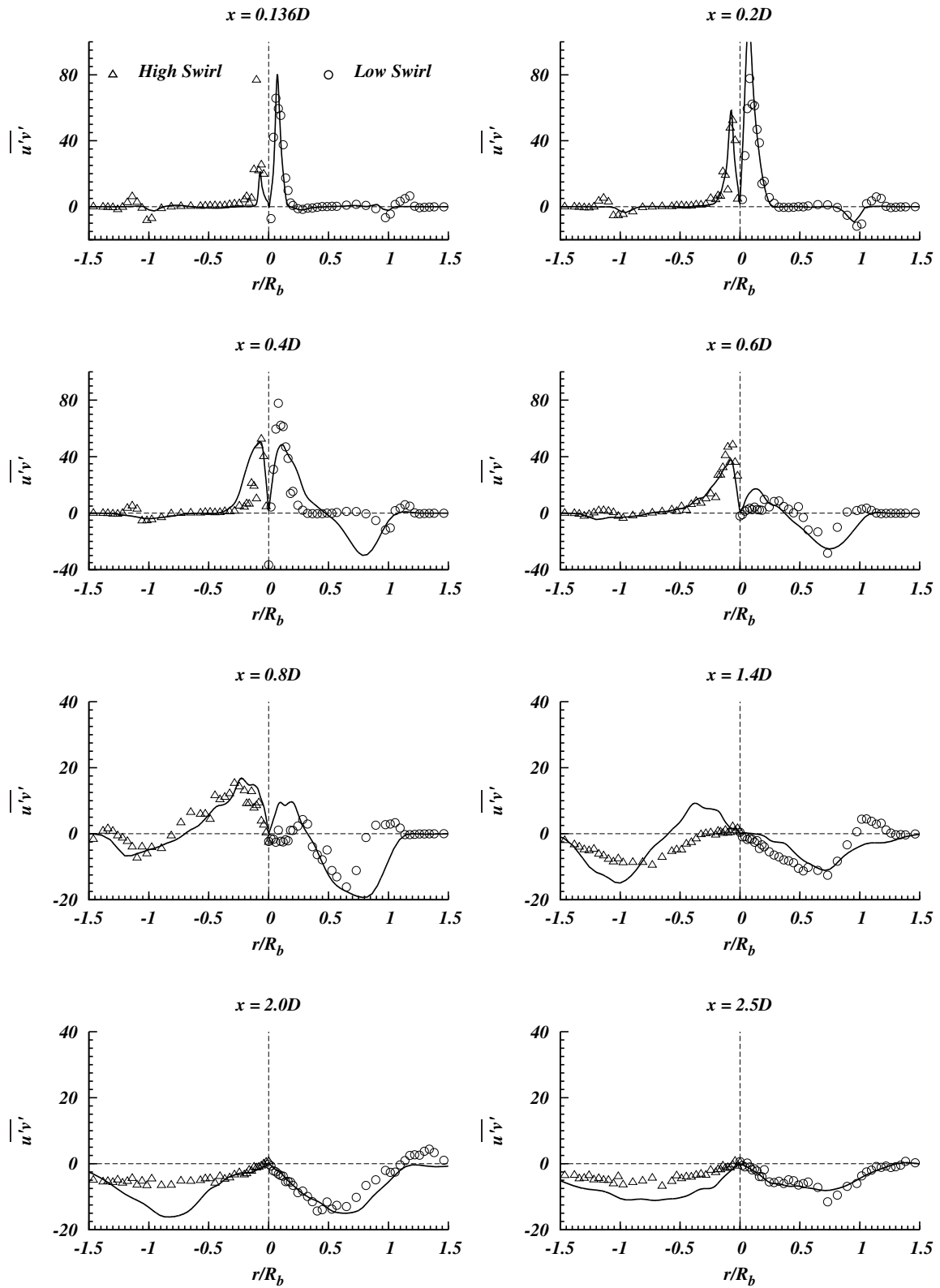


Figure: 6.9 Reynolds stress component $\overline{u'v'}/m^2s^{-2}$ comparison for Low Swirl (Right) and High Swirl (Left) test cases, Lines : LES, Points : Experimental data[247].

6.1 Non Reacting Swirl Flows

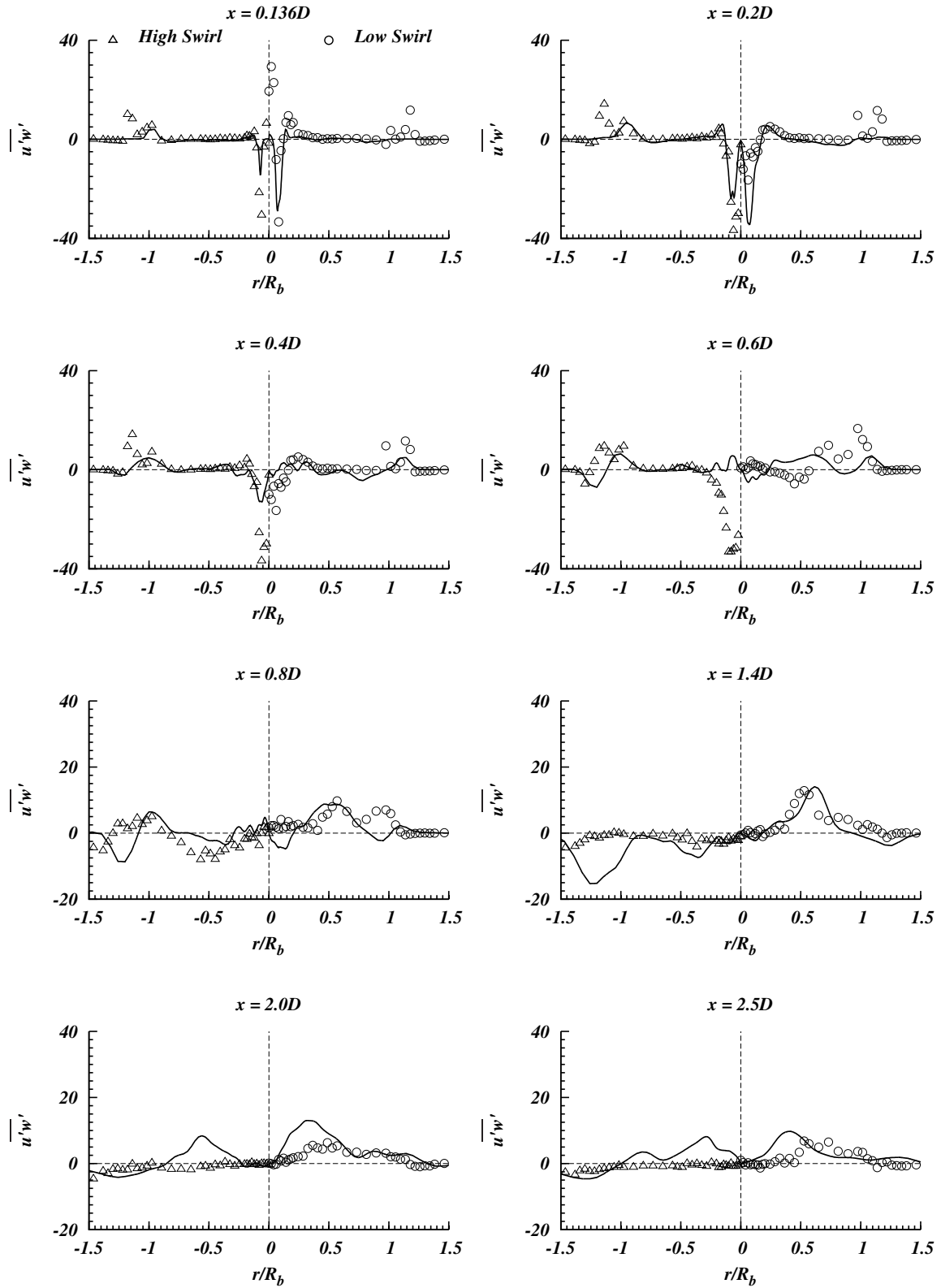


Figure: 6.10 Reynolds stress component $\overline{u'w'}/m^2s^{-2}$ comparison for Low Swirl (Right) and High Swirl (Left) test cases, Lines : LES, Points : Experimental data[247].

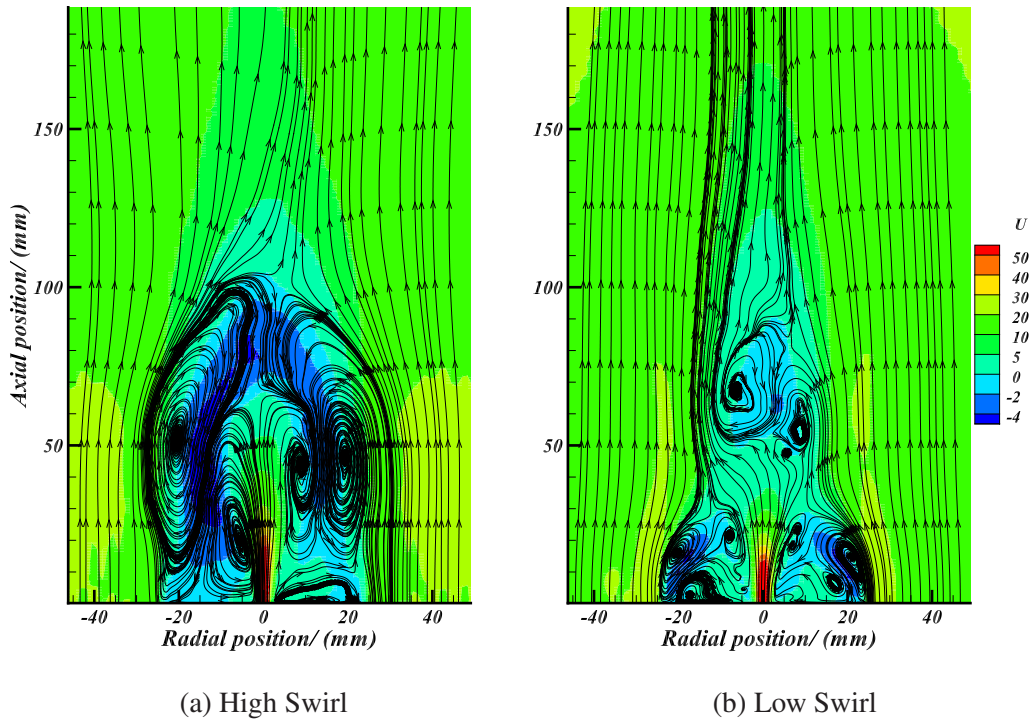


Figure: 6.11 Axial velocity field and 2D streamlines for the non-reacting swirl flow test cases U (m/s).

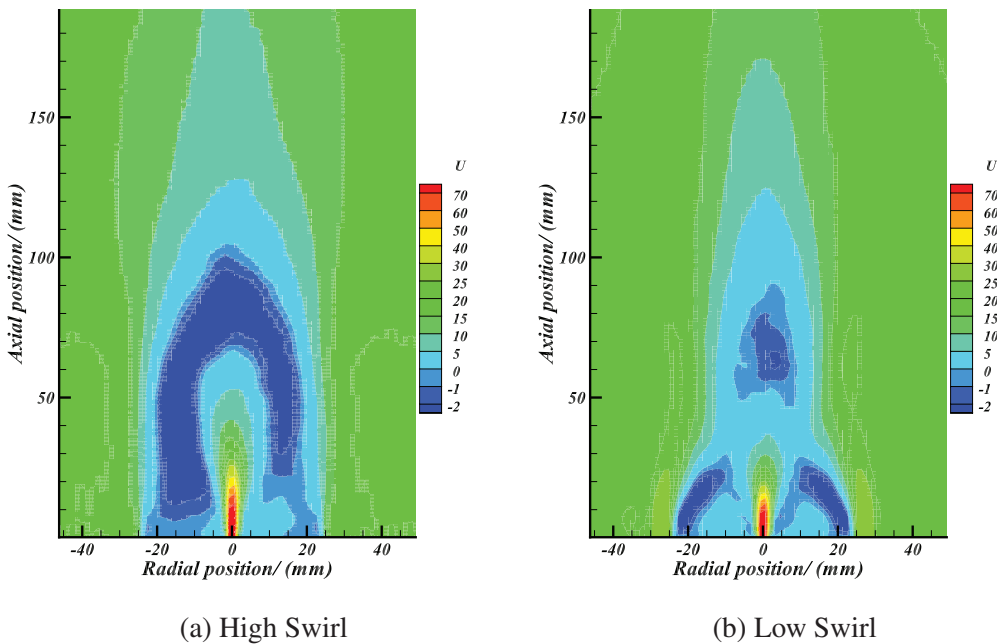


Figure: 6.12 Axial velocity field of the non-reacting swirl flow test cases U (m/s).

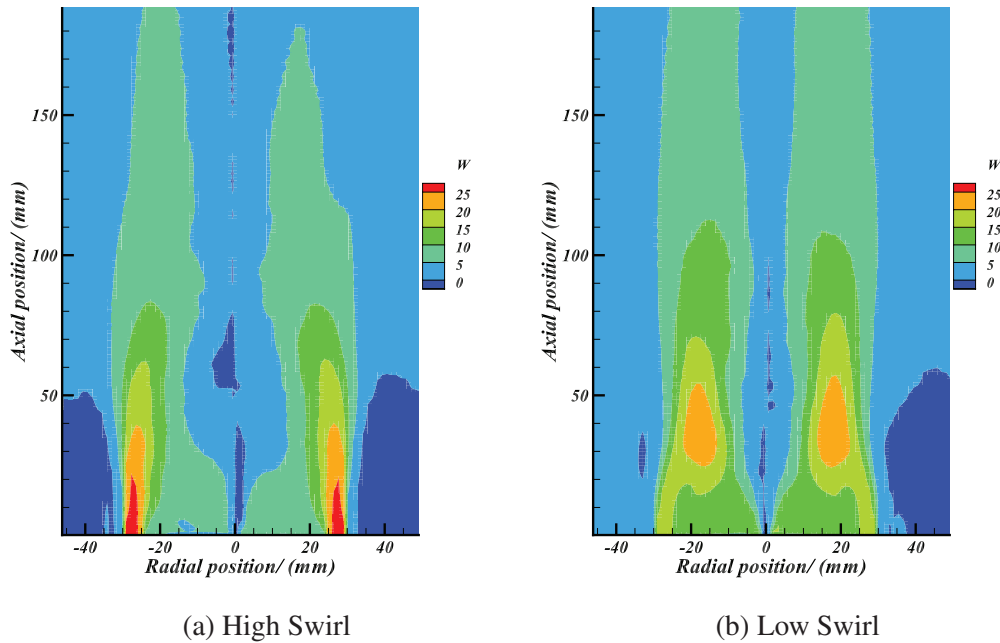
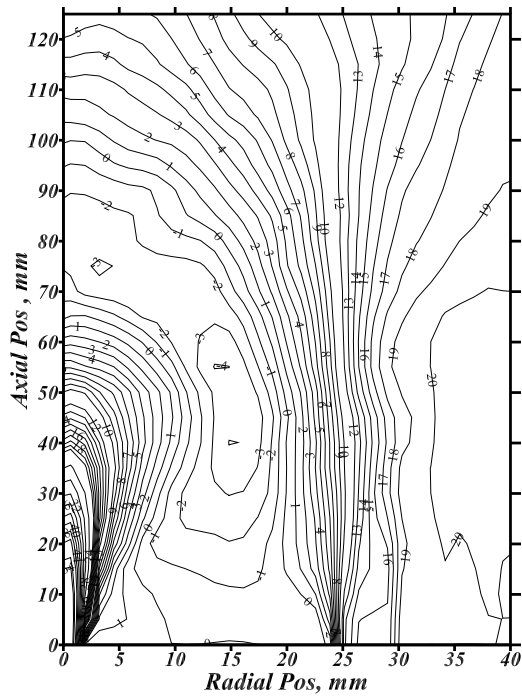


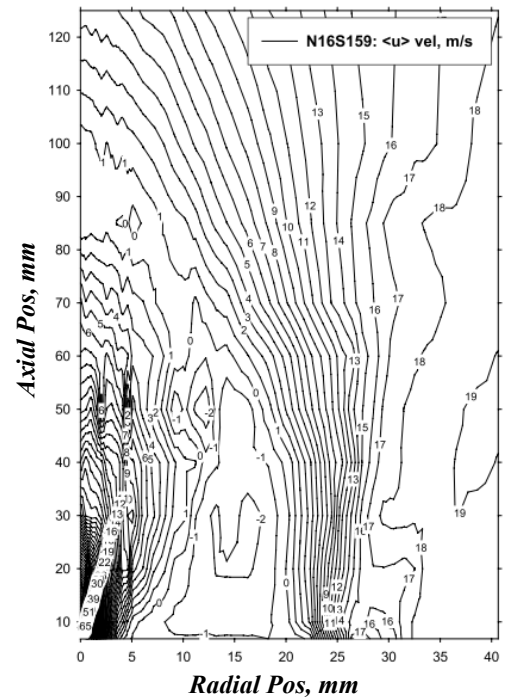
Figure: 6.13 Rotating velocity field of the non-reacting swirl flow test cases W (m/s).

Figure: 6.3 shows in both cases similar axial momentum is introduced from the central jet but in low swirl test case more axial momentum is introduced from the annular inlet than the high swirl test case. Further, the mean axial flow velocity distribution showed that overall axial momentum decay was faster in low swirl test case. Therefore the RMS of axial velocity component also shows a similar pattern, that in the low swirl test case the axial flow variance shows a greater magnitude than the high swirl case. Following the mean axial flow velocity distribution, the RMS of axial velocity component also shows very good agreement between LES and experimental data in Figure: 6.6. In contrast to the presumptive variation of velocity fluctuations, the lower swirl test case shows greater axial velocity RMS closer to the inlet. With increasing axial distance from $x = 0.136D(6.8mm)$ to $x = 0.4D(20mm)$ along the central axis \bar{u}' peak values for the low swirl test case varies between $20 - 30m/s$ whereas in the high swirl test case showed values in the range of $20 - 25m/s$. This seemingly contradicting velocity fluctuations can be explained by using the rotational velocity component contours shown in Figure: 6.13, in which it shows that surrounding the central jet closer to the bluff body, the rotational velocity component is greater in the low swirl test case than in the high swirl test. Therefore, more interaction of rotational momentum and axial momentum raises the fluctuations of both velocity components. Furthermore, another important feature can be seen from the axial velocity RMS distribution of the low swirl test case, in which from $0.4D(20mm)$ to $0.6D(30mm)$ the axial velocity fluctuations shows a sharp decrease in magnitude. This is also can be explained by the existence of bluff body

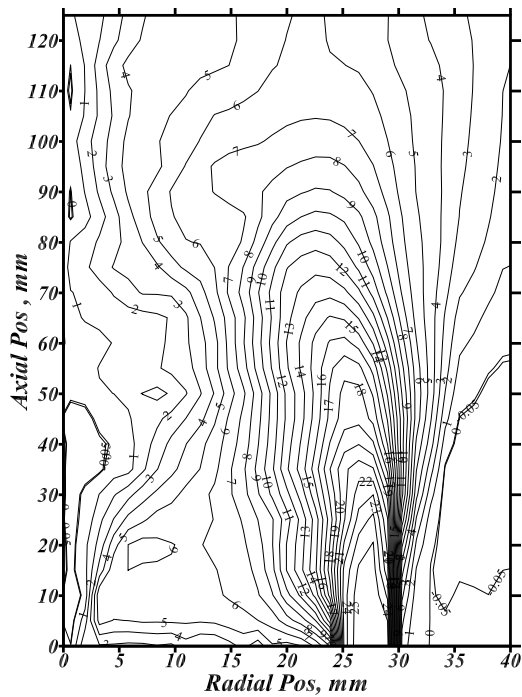
6.1 Non Reacting Swirl Flows



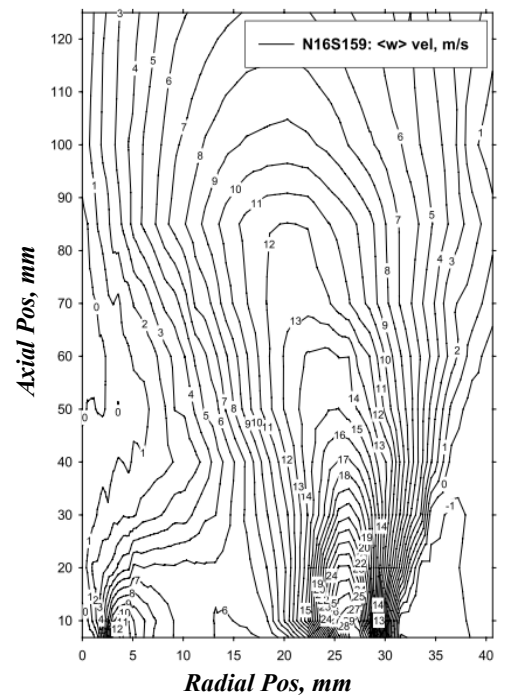
(a) LES



(b) Experiment - Axial velocity



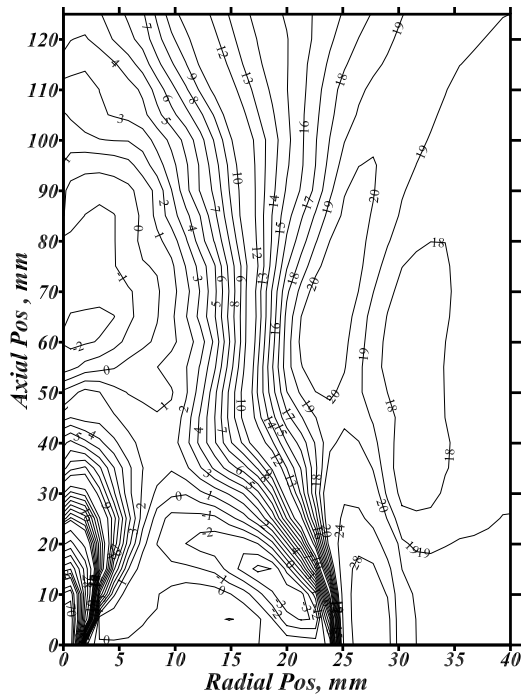
(c) LES - Rotating velocity



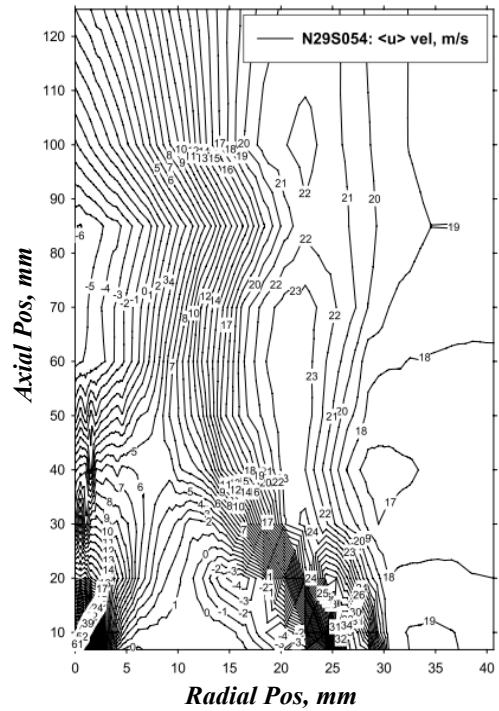
(d) Experiment - Rotating velocity

Figure: 6.14 Mean axial and tangential velocity contours for High swirl test case (N16S159) compared against experimental data from [245].

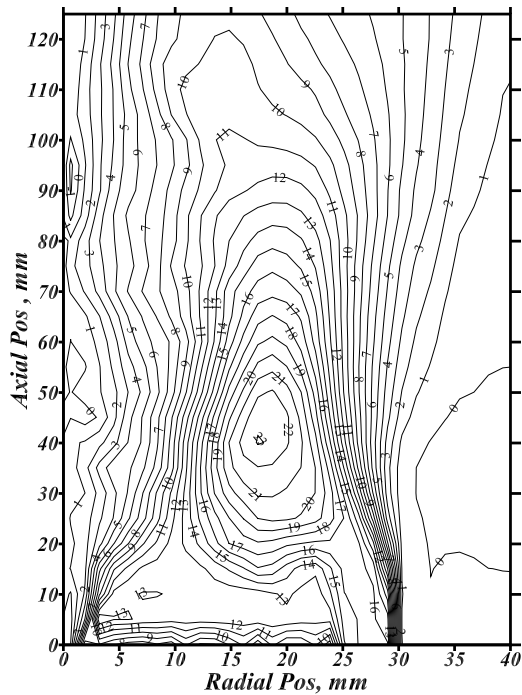
6.1 Non Reacting Swirl Flows



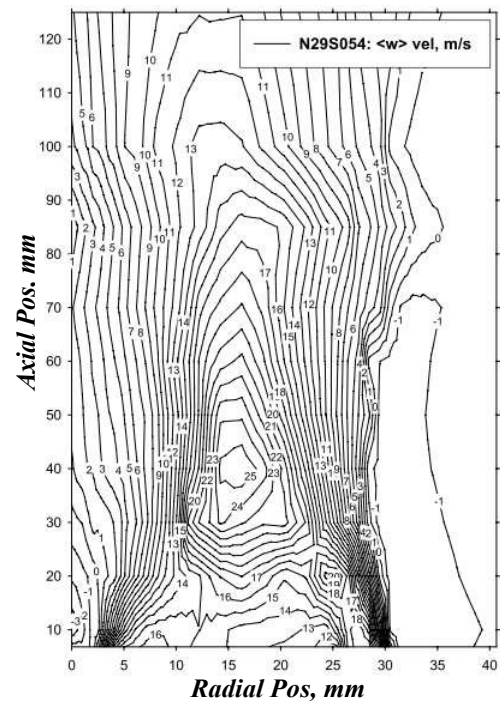
(a) LES - Axial velocity



(b) Experiment - Axial velocity



(c) LES - Rotating velocity



(d) Experiment - Rotating velocity

Figure: 6.15 Mean axial and tangential velocity contours for Low swirl test case (N29S054) compared against experimental data from [245].

recirculation zone which is highly turbulent. As Figure: 6.13 shows, by $0.6D(30mm)$ the strength of the central jet and bluff body recirculation, are diminished, therefore, the velocity fluctuations also shows an attenuation. Similarly, the high swirl test case also showed a gradual decrease of axial velocity fluctuations with the increase of axial distance.

Figure: 6.8 shows the RMS of radial velocity component ($\overline{v'}$) compared against experimental data. It illustrates that the low swirl test case shows the greater magnitude of radial velocity RMS than the high swirl test case because of the increased interaction of swirl flow and axial flow caused by the VB structure. Underpredicted velocity fluctuations at the centre of the jet for both test cases at $x = 0.136D, 0.2D$ are indicative of insufficient turbulence near flow inlets. It further shows that LES results are generally in good agreement with experimental data except at $x = 0.4D$ in the low swirl test. Beyond $x = 0.8D$ radial velocity fluctuation shows gradual decay to a co-flowing like fluctuations with a uniform profile over the flow domain as the influence of recirculation zone diminishes. Figure: 6.7 shows the RMS of tangential (rotational) velocity component ($\overline{w'}$), and similar to the radial velocity component LES results show good overall agreement with experimental data. However in low swirl test case, at $x = 0.4D$ discrepancies appear in both radial and tangential velocity fluctuations. A closer inspection of the velocity field of the low swirl test case (Figure: 6.12,6.13) shows that the bluff body recirculation zone ends near $x \approx 0.4D - 0.6D = 20 - 30mm$. Therefore the discrepancies in this region can be attributed to minor differences in prediction of the length of bluff body recirculation zone. Across the swirl inlet, velocity fluctuations from experimental data show double peaked variation but LES results have not accurately reproduced that pattern, yet the RMS values within the rotating fluid mass are unaffected by the numerically under-represented velocity fluctuations at the swirl inlet. Only five grid cells were placed across the swirl inlet boundary in these simulations, therefore it can be stated that the insufficient grid resolution in the radial direction could have introduced numerical errors in representing the velocity non-linearities at the swirl inlet accurately. However further increase of grid resolution across the annular inlet a fully unstructured grid structure would be required, and such methods were not pursued in this study.

Figure: 6.9 shows the shear stress component of the Reynolds stress tensor $\overline{u'v'}$ predictions, and shows that at distances closer to the inlet results from numerical and experimental methods agree very well. It can be seen in the downstream region $x \approx 0.4D - 1.4D$ distance discrepancies start to appear. However, numerical predictions have maintained the overall qualitative agreement with experimental data, and further downstream towards the outlet LES results show better agreement with experimental data. Both high swirl and low swirl test cases indicate similar patterns of shear stress component variations, but at near field distances it can be seen that the low swirl test case shows the greater magnitude of shear stress

component than high swirl test case. Figure: 6.10 shows LES results of the shear stress component of the Reynolds stress tensor $\overline{u'w'}$ for the two test cases compared against experimental data. Again closer to the inlet boundaries the experimental measurements and LES results show similar magnitudes and variation, however, between the range, $x = 0.4D - 0.8D$ discrepancies start to appear and further downstream the spatial variations diminish; hence LES and experimental results show closer agreement. However, it can be seen that near the inlet boundaries Reynolds stress component $\overline{u'w'}$ is underpredicted, suggesting the need of a comprehensive numerical modelling of the full inlet domain to obtain accurate inlet boundary conditions and, more grid resolution across the annular boundary is required.

Streamlines distribution in Figure: 6.11 shows that in low swirl test case around $x \approx 0.4D = 90mm$ the vortex breakdown bubble ends and the axial flow re-establishes after that, therefore in this region, it can be expected to have a change in radial flow direction. In Figure: 6.5 at the same axial distance strong alternating radial flow directions can be seen in both experimental and numerical findings. Therefore, it can be said that the disparity between experimental and LES results of radial velocity component RMS values near $x = 0.4D$ are caused by the presence of a strong vortex breakdown structure.

From mean velocity results and second moment of velocity results, it can be seen that LES results have shown very good agreement with experimental data. LES results also have captured the vortex breakdown structures that were evident from experimental measurements. The locally dynamic Smagorinsky model performance can be considered to be satisfactory in modelling the mean velocity field, and Reynolds stress components show good agreement with experimental data. Therefore, from these simulations, it is evident that the same simulation setup can be extended to swirling reacting flow simulations.

6.2 Reacting Flow Modelling

6.2.1 Validation Test : Sandia flames

In this section results of a validation study for the Steady Laminar Flamelet solver *flamelet-Foam* using the pilot burner Sandia Flame - D [248] is presented. The $k - \epsilon$ RANS turbulence model for the compressible flow (Section 3.11) is used in this validation study. In the experiments, Sandia flame D was operated at lean $\phi = 0.77$ and power of the flame was maintained at a 6% of the main flame power. Thus the pilot flame is neglected in the modelling. The main jet diameter was $D = 7.2mm$, and the annulus that contained pilot flames had 18.9 mm and 18.2 mm outer and inner diameters respectively. The main jet composition was maintained at 25% CH_4 and 75% air. Figure: 6.16 illustrates the Sandia burner

geometry. This pilot flame burner was contained inside a wind tunnel with a $30 \times 30 \text{ cm}^2$ cross-section that carried a small co-flow velocity to avoid entrainment near the jet exit. The boundary conditions are listed in Table: 6.2. Inlet velocity profile was obtained from the experimental data and imposed on the inlet boundary. Laminar flamelets were created using the Cantera Open source package for scalar dissipation ratios varying from 0.007 to 550, to include the flame extinction due to stretching as well. A computational domain of the size $0.1 \times 0.1 \times 0.65 \text{ m}$ and radially increasing grid with 0.3×10^6 cells were used in this study and grid was gradually expanded in the axial distance. Implicit second order time discretization and the TVD scheme *vanLeer* was used for convection term discretization.

Figure: 6.17 shows mixture fraction and mixture fraction variation compared alongside temperature at three different axial heights. Three different axial heights are selected so that closer to the jet nozzle ($x = 2D$), intermediate distance ($x = 15D$) and far field ($x = 60D$) distances are represented. It can be seen that at near field distances both mixture fraction and mixture fraction variance are very well predicted and with increasing axial distance, a slower mixture fraction decay rate in the radial direction was predicted. Similarly mixture fraction variance also shows a similar pattern, and as a result, it can be seen that the predicted temperature also shows the same trend as mixture fraction, that with increasing the axial distance a radial decay rate is increased. Therefore, the validation test showed that *flameletFoam* solver could be successfully used to numerically predict the flame structure of pilot burner Sandia Flame D, and in next sections, the *flameletFoam* solver is applied to model highly strained swirl stabilized burner flames.

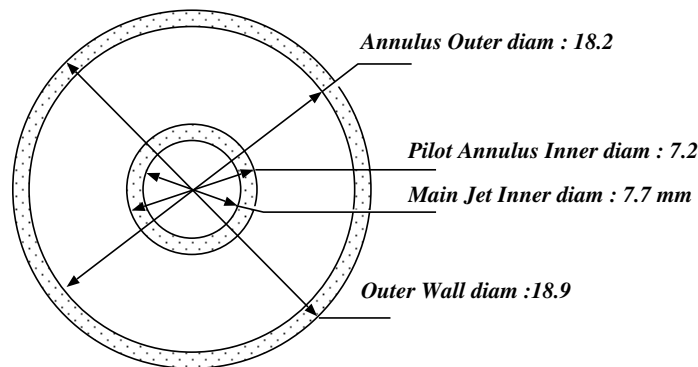


Figure: 6.16 Sandia pilot jet burner geometry

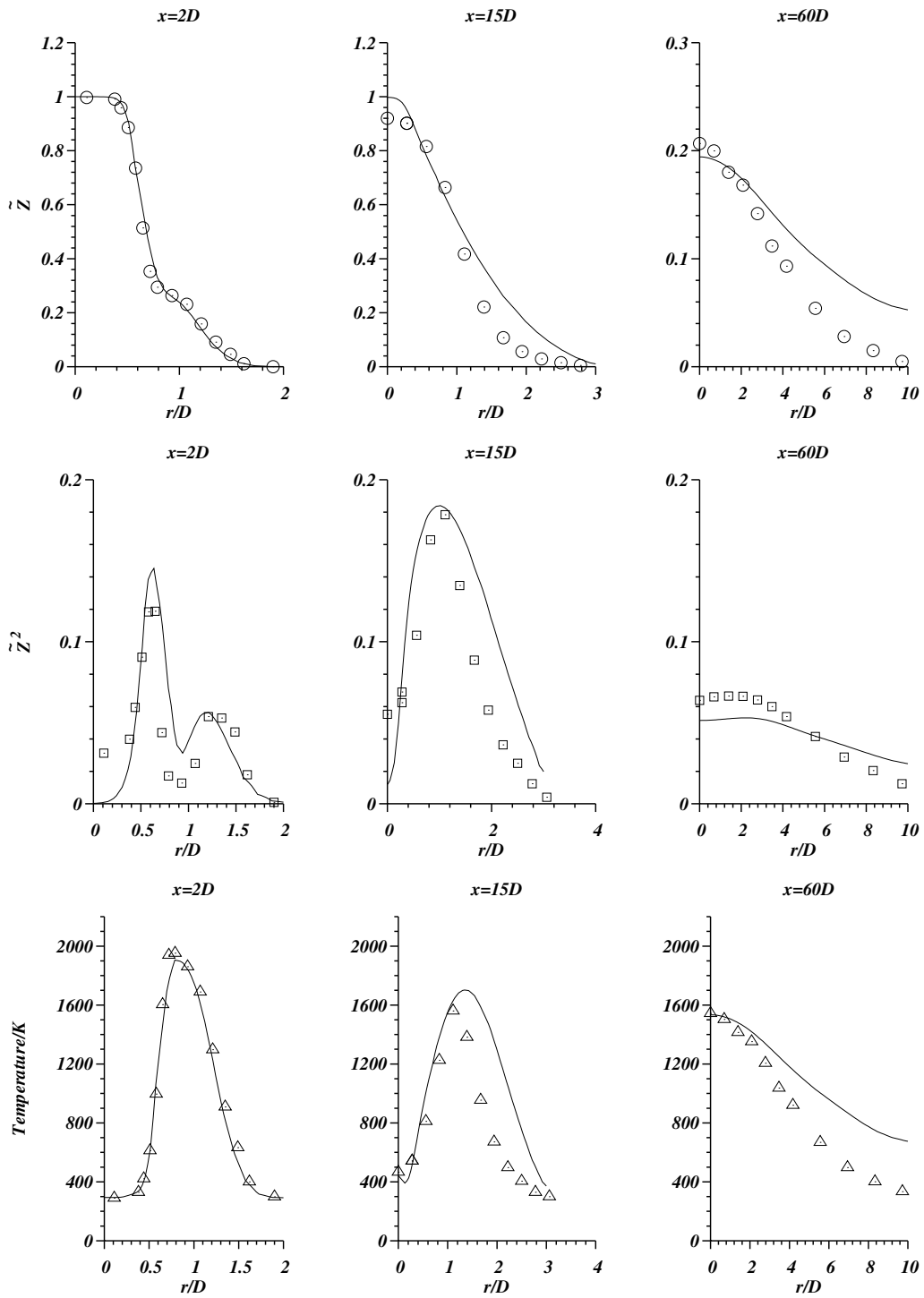


Figure: 6.17 Sandia Flame D - Favre Average Mixture fraction (\tilde{Z}), Favre Average Mixture Fraction Variance (\tilde{Z}'^2), Temperature variation in radial direction at different axial distances (x), points : Experimental measurements [249], lines : LES.

Table 6.2 Boundary conditions for Sandia flame D

Boundary Condition	Value	Units
Coflow velocity	0.9 (+/- 0.05)	m/s
Coflow temperature	291	K
Main jet velocity	49.6 (+/- 2)	m/s
Main jet kinematic viscosity	1.58e-05	m/s

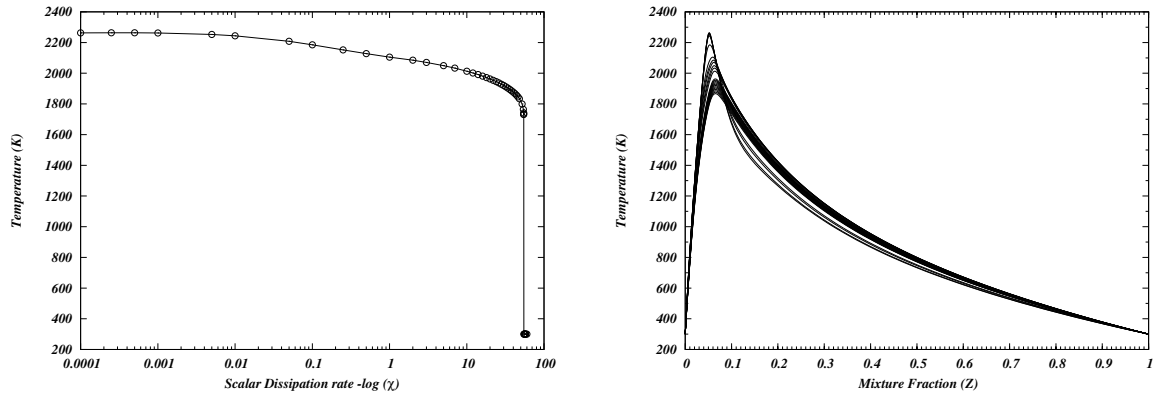
6.2.2 Sydney Swirl Flame HMS1

The SMH1 flame is a swirl flame with low swirl number of $S = 0.32$, which used a hybrid fuel mixture ($CH_4 : H_2 = 1 : 1$). For the reacting flow simulations, one-dimensional steady flamelets were generated for a counterflow flame arrangement using the 1D flame solver packages using both Cantera [80] and FlameMaster [81], and the GRI-3.0 mechanism [250]; both codes yielded similar results. In Figure: 6.18a, the flamelet solutions are shown against different scalar dissipation ratios, and it shows that the flame extinction occurs closer to $\chi = 56.1/s$. The gradual increase of scalar dissipation rate was used to calculate laminar flamelets near the flame extinction due to stretch. The laminar flamelets are integrated by using the *flameletFoam* solver, which assumed a $\beta - PDF$ distribution in the mixture fraction space, and *Dirac - δ* function in the scalar dissipation space [233]. The scalar dissipation rate space was divided into 60 divisions from ignition to extinction with more resolution towards extinction, and normalized mixture fraction space and normalized mixture fraction variance were uniformly divided into 50 divisions in preparations for the integrated flamelet lookup table. The integrated Favre averaged variables temperature and CO_2 mass fraction are shown in Figure: 6.19 at $\chi = 1.01/s$ in mixture fraction and normalized mixture fraction variance space (coarser integration resolution was used to generate the plot than the actual calculation). It shows that the higher flame temperatures occur near the stoichiometric mixture fraction ($Z \sim 0.05$), and at higher scalar variances temperature is reduced indicating the effects of insufficient air-fuel mixing effects.

Experimental scatter plots of the flame composition are compared against the calculated laminar flamelets in Figure: 6.20. It should be noted that the GRI-3.0 mechanism is a chemical kinetic mechanism dedicated to model natural gas combustion, therefore the applicability of this chemical mechanism to model combustion of $CH_4 : H_2(1 : 1)$ mixture requires detail analysis. The Figure: 6.20 further shows that the calculated laminar flamelets only encompassed the mean range of the temperature measurements, while the flamelet profiles capture the CH_4 and H_2 composition adequately. However, it can be seen that the O_2 composition is underpredicted from the majority of flamelet profile. Two major products of the

6.2 Reacting Flow Modelling

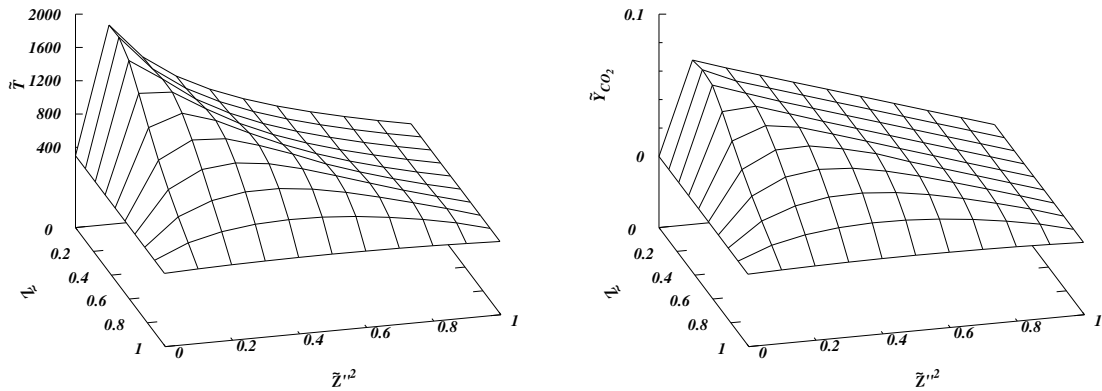
reaction CO_2 and H_2O also show that the flamelet profiles only captured the mean of the compositional space but turbulent flame composition shows more distributed variation that was not captured by the flamelet solutions. Nevertheless, it should be noted that the integrated mean composition table will capture more area of the scattered compositional space due to assumed PDF profiles.



(a) 1D laminar flamelet solutions generated for SMH1 flame for different scalar dissipation rates.

(b) 1D laminar flamelet relationship between temperature and mixture fraction.

Figure: 6.18 Steady laminar flamelet relationship for SMH1 fuel mixture.



(a) Flamelet relationship for favre averaged temperature for the SMH1 flame.

(b) Flamelet relationship for favre averaged temperature for the SMH1 flame.

Figure: 6.19 Integrated flamelet table relationship.

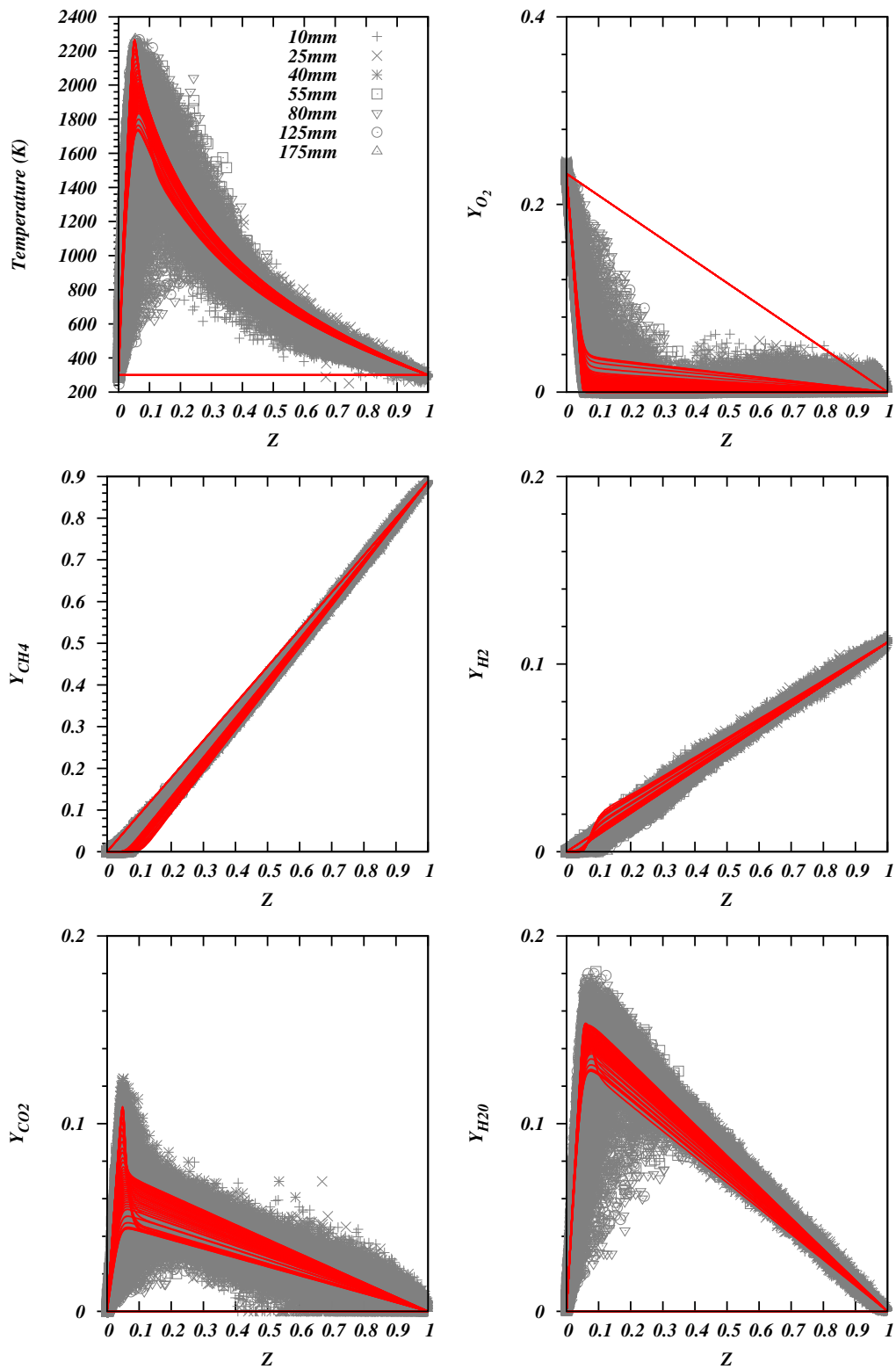


Figure: 6.20 SMH1 Flame scatter plots of flame composition comparison with 1D adiabatic steady flamelets (points: Experimental measurements [247], lines: 1D counter-flow flame solutions).

Results and Discussion

SMH1 Flame : Velocity Field

The numerically predicted mean axial velocity component variation in the radial distance are compared with experimental measurements at increasing axial distances in Figure: 6.21. From the axial velocity comparison, it can be seen that closer to inlet boundaries the LES results show excellent agreement with experimental measurements. LES very well realizes the negative axial flow velocity component which represents the recirculation zone results at the $x = 20mm$ line, but at $x = 40mm$ the negative velocity component is not reproduced sufficiently by LES results, even though the numerical result qualitatively represented the velocity distribution. Thus it is evident that the LES results have predicted a shorter recirculation zone behind the bluff body surface. At $x = 60, 80mm$ also, LES results show reasonable agreement with experimental results, especially that at the central axis the experimental velocity magnitude and LES results agree very well. Further downstream at $x = 125mm$ experimental results indicate a negative velocity on the central axis which is indicative of a secondary flow reversal zone, but LES results only produce a reduced axial velocity magnitude from $x = 80mm$ but not a negative velocity. Therefore, this shows that the effects of a secondary recirculation zone are underpredicted by LES results. However, at $x = 175mm$, LES results show excellent agreement with experimental results, and axial velocity increases radially indicating the effects of the secondary recirculation zone, that at the core of recirculation zone has lesser axial velocity. Figure: 6.32a shows the axial velocity contour map and shows the existence of two recirculation zones, one behind the bluff body ($0 \lesssim x \lesssim D(50mm)$). The first recirculation zone is a typical recirculation zone behind the bluff body, and a much longer extended recirculation zone is established away from the nozzle. This secondary recirculation zone extends from about $x = 2D$ to $7.0D(100mm - 300mm)$, and consistent with experimental velocity measurements. The secondary toroidal flow recirculation zone is visually different from the smaller vortex breakdown bubble structure in the non-reacting low swirl test case. In the reacting flow test case, a combustion induced recirculation zone with an axially elongated structure can be seen. Although the velocity measurements showed some discrepancies in the region of swirl stabilized recirculation zone, the LES results have successfully captured the effects of toroidal flow reversal and thus the flame stabilisation away from the bluff body surface.

Given that the bulk velocity of the central jet was $140.8m/s$ and when the power law velocity profile imposed on the central jet the peak velocity at the centre of the jet nozzle is closer to $176m/s$. Such high velocity of the central jet which is closer to $Ma = 0.6$ and imposes an error associated with the density calculated using the ideal gas state equation and

flow compressibility. Overall it shows that LES results agree well with experimental results at the especially at the central core of this radially expanding mesh. As it is discussed in Section: 3.7 LES grid expansion introduces commutative filtering errors in dynamic SGS models. Therefore discrepancies in velocity field can be attributed to turbulent combustion model inadequacies and filtering errors.

The tangential velocity component (rotational) variation is shown in Figure: 6.22 and LES results exhibit good overall agreement with experimental measurements. Near the central axis of the domain $r \sim 0$, the tangential velocity is underpredicted by LES results. Furthermore, it shows that similar to the low swirl non-reacting test case, and the rotational momentum is transferred closer to the central axis with the increase of axial distance, and in the region of $x \approx 60 - 80\text{mm}(1.2D - 1.6D)$ the radial velocity shows a local increase. Figure: 6.32b shows time mean tangential velocity contours, and shows this localized increase of rotational velocity increase closer to the end of bluff body recirculation zone. Moreover, it can be seen that above of this particular high rotational velocity zone lies the toroidal recirculation zone that is caused by vortex breakdown. However, as mentioned earlier the very high central stream axial velocity component introduces a dominant axial flow momentum weakening the swirl flow, and this can be considered as a reason behind the rotational velocity discrepancy near the central axis. Furthermore, because the block-structured grid used in this simulation was radially expanding, the tangential grid filter size increased radially. Therefore, insufficient tangential grid resolution and commutative filtering error might have contributed to the tangential velocity underprediction.

Velocity component fluctuations are represented by RMS velocity measurements. In Figure: 6.23 the axial velocity RMS component variation is plotted at different axial distances, and it shows very good agreement between LES results and experimental measurements. Closer to the central jet very high-velocity fluctuations are observed due to the magnitude of the central jet velocity and the flow shear. It can be further seen that in the region between the central jet and annular inlet ($0 \leq r \leq 25\text{mm}$), the axial velocity fluctuations remain fairly uniform closer to the bluff body. However, with the increase of axial distance, the axial velocity fluctuations in the region above bluff body increased as a result of the bluff body recirculation zone. Figure: 6.24 shows the tangential flow velocity RMS comparison with experimental measurements. Similar to axial velocity fluctuations, tangential velocity RMS component also shows good agreement with experimental measurements. Near the bluff body surface the rotational velocity fluctuations show minimal influence, but with increasing axial distance the magnitude of the fluctuations grow as the recirculation zone is developed. Further downstream LES results show some disparity near the secondary recirculation

zone, but the magnitude of the velocity fluctuations are maintained to acceptable levels with experimental results.

SMH1 Flame: Turbulent Flame Structure

The time-averaged mixture fraction results are compared against experimental measurements in Figure: 6.25. The experimental mixture fraction is determined by the Equation: 6.1 where Y_i is the element mass fraction of element i , W_i is the molar mass of element i , and superscript F , O denotes fuel stream and oxidizer stream. Therefore, the experimentally determined mixture fraction is influenced by the preferential diffusion of different species, but in the numerical modelling approach, preferential diffusion is neglected.

$$Z = \frac{2\frac{Y_C - Y_C^O}{W_C} + \frac{Y_H - Y_H^O}{2W_H} - \frac{Y_O - Y_O^O}{W_O}}{2\frac{Y_C^F - Y_C^O}{W_C} + \frac{Y_H^F - Y_H^O}{2W_H} - \frac{Y_O^F - Y_O^O}{W_O}} \quad (6.1)$$

However, as the Figure: 6.25 shows that LES results generally represent the overall mixture fraction distribution pattern, closer to the wall the mixture fraction is severely underpredicted. Especially in the region between $5\text{mm} < r < 20\text{mm}$, which is above the central bluff-body the numerical predictions show serious under prediction of mixture fraction. As the axial distance increases, the magnitude of mixture fraction diminishes and shows increased diffusion in the radial direction. Several main contributory factors can be identified to cause this discrepancy near the bluff body recirculation zone. Firstly, the effects of preferential diffusion of species that are not represented by LES modelling is severe in the presence of a recirculation zone where lighter and smaller atoms relatively move out of the recirculation zone, while heavier and larger atoms are retained inside the recirculation zone. Secondly, the inaccurate scalar dissipation prediction from CFD calculations caused by high flow strain lead to an erroneous feedback loop between (density-heat release coupling) mixture fraction and density distribution near the bluff-body recirculation. The scalar dissipation rate χ is independent of molecular diffusivity of the scalar but decreases with time, but steady laminar flamelet approach cannot accurately calculate this unsteady dynamics of scalar dissipation rate because scalar dissipation modelled using a simple algebraic relationship (Eqn: 3.118). Since LES simulations have not sufficiently represented the accumulation of fuel mass by the bluff-body recirculation zone, more simulation time to let the mixture fraction accumulate up in this region could reduce potentially reduce the mixture fraction underprediction. It can be shown that the eddy diffusivity based turbulent scalar mixing models are only valid after many Lagrangian integral timescales, which is an inherent weakness of that class of models ([68]: Chapter 3). Therefore, the mixture fraction discrepancies can be attributed to

the inherent shortcomings of scalar mixing modelling and with more time averaging results are expected to improve. Besides, accurate measuring of mixture fraction from these molar mass fractions is also difficult, therefore could contain measurement uncertainties.

Mixture fraction RMS measurements (Z_{rms}) are compared against the LES results ($\sqrt{Z''^2}$) in Figure: 6.26, and shows that in general throughout the computational domain the mixture fraction variance is predicted with acceptable accuracy. However, with increasing the axial distance, the predicted mixture fraction variance magnitude is reduced as the air-fuel streams become well mixed with the distance travelled is increased. In Figure: 6.27 the mean temperature measurements are compared against LES results, and it shows that LES results agree sufficiently with experimental data. Closer to the bluff body, the experimental measurements show that maximum flame temperature occurs above the swirl inlet. However, LES results show that the maximum flame temperature occurs closer to the central fuel jet. The disparity in the prediction of mixture fraction closer to the bluff body as discussed earlier can be identified as the leading cause of the disparity in temperature predictions. It can be seen that with the increase of axial distance the temperature prediction improves but the mean temperature remains under predicted near the toroidal flow reversal zone. This disparity can be attributed to the disparity of mixture fraction field prediction. In addition, as the presence of recirculation zones worsen the effect of preferential diffusion, to accurately model the turbulent flame structure especially with a fuel mixture that contains Hydrogen which has different transport properties from other hydrocarbon species, the effect of Lewis number must be taken into consideration. Furthermore, the Figure: 6.31 compares unity Lewis number assumed flamelets and non-unity Lewis number flamelets for a 1D counter-flow flame arrangement for the fuel mixture of SMH1 flame. It can be seen that the non-unity Lewis number flamelets show increased temperature for the fuel-rich end of the mixture fraction space, illustrating that preferential diffusion of species contributes to the disparity of temperature prediction.

Figure: 6.28 shows the CO_2 mass fraction predictions compared against experimental data, and it can be seen that the numerical predictions are in general agreement with experimental measurements even though the CO_2 mass fraction is overpredicted along the axial distance. Commutative filtering error that is caused by the radial grid expansion and the numerical diffusion caused by TVD schemes are understood to be two contributory factors towards the qualitative discrepancy of CO_2 predictions. CO mass fraction predictions are compared in Figure: 6.29 and similar to CO_2 predictions, closer to the bluff body the LES results show an under predicted CO presence but as axial distance increases CO mass fraction is overpredicted. However, the general magnitude and the distribution of two most important oxides of carbon are predicted to be in with good agreement with experimental results.

In the Figure: 6.30 also show LES results underpredict the H_2O concentration closer to the bluff body while over predict at downstream locations, which is comparable with mixture fraction predictions.

In Figure: 6.33 the temperature field and other scalar field contours are shown. They show that two high-temperature zones are present in the two recirculation zones. In the near bluff-body recirculation zone and the secondary bluff-body stabilized recirculation zone in the region $x \approx 2D - 6D$ two high-temperature zones are present, which attributed to the recirculation of hot combustion products. The OH radical distribution can be used to visualize the oxidation of hydrocarbon fuels [251], and as it can be seen from the scalar contours of OH radical concentration that primary oxidation zones at the bluff body recirculation zone and the secondary stabilized recirculation zone closer to $x \approx 5D$. The O_2 mass fraction contours also illustrate that since the central jet only contained a $CH_4 - H_2$ mixture the effect of the O_2 diffusion occurs from the periphery of the rotating central fluid mass. The CO_2 mass fraction contour shows that the CO_2 presence is greater in the region where O_2 is scarce and the CO mass fraction shows that CO production preceded the CO_2 production. Similarly, the H_2O production also showed that similar to the temperature contours, H_2O molecules were recirculated in the secondary bluff-body stabilized recirculation zone. Therefore, it can be seen that even though there were minor numerical discrepancies between LES results and experimental measurement, the temperature and other major species fields showed good agreement with the physics of the swirl flow and recirculating reacting flows.

Figure: 6.34 shows non-premixed flame regimes of this Swirl burner on a non-premixed Borghi diagram. To identify flame regimes, LES data are sampled on the centre line, and lines across the domain at axial distances $x = 0.01, 0.02m$. As it shows, most of the sample locations fall into separated flamelets regime and only the sample points along the centre line fall into connected flamelets region while a significant number of sample points can be seen in the flame extinction region due to very high flame stretch (high $\tilde{\chi}_{st}$ values). From these observations, the applicability of laminar flamelet model for such highly strained flame is questioned because most of the flames are in discontinued flamelets because of very high mixture fraction variances caused by intense turbulence. Since the model implementation is validated for the Sandia-D pilot flame using RANS model, the accuracy of the model implementation can be assured as well. Therefore, the discrepancies found between experimental and numerical results primarily stem from the modelling inadequacies that are unable to capture the complex flow physics in a highly strained, high velocity and swirling reacting flow with a blended fuel.

In conclusion, the LES results show reasonably good agreement in velocity field and the second moment of velocity field with experimental measurements. Due to the radial

grid expansion and the coarser tangential grid resolution, the anisotropic turbulence is not resolved equally in all three dimensions. The mixture fraction field and the mixture fraction variance show under prediction near the central jet and this result in further discrepancies in the prediction of temperature and other scalars. Due to the very high-velocity field of the central fuel jet, scalar dissipation modelled by the simple algebraic assumption [252] resulted in local zones with extremely high scalar dissipation along the edges of the central fuel jet, this caused local flame quenching. These reasons cause numerical discrepancies in LES results, yet maintained a reasonable agreement with experimental data and the physical process of the problem. However, LES results successfully captured the effect of two recirculation zones and the flame stabilization via recycling of combustion products.

6.3 Chapter Summary

In this chapter non-reacting swirl flows are successfully simulated using LES modelling, and obtained good agreement with experimental data with realizing vortex breakdown structures and recirculation zones behind the bluff body. The low swirl test case produced vortex breakdown structures when compared to high swirl test case, which from the outlook seems as contradictory, but a close inspection of the actual rotational velocity field shows that a local acceleration of rotational flow caused the formation vortex breakdown bubble structure. Then, SLFM was used with reasonable success to model the reacting flow test case (HMS1) with $CH_4 : H_2(1 : 1)$ fuel mixture. Considering the test case involved multiple modelling challenges such as preferential diffusion and very high-velocity scales and flow swirl that induces highly strained flame, the SLFM model predictions agreed well in predicting velocity field statistics very well. The discrepancies of mixture fraction field are reflected as errors in other scalar fields as well. Therefore, further attention is required to improve the numerical results by incorporating unsteady flamelet effects and preferential diffusion of chemical species. The flow compressibility caused by the very high velocities at the central jet inlet also needs to be addressed to improve the numerical predictions.

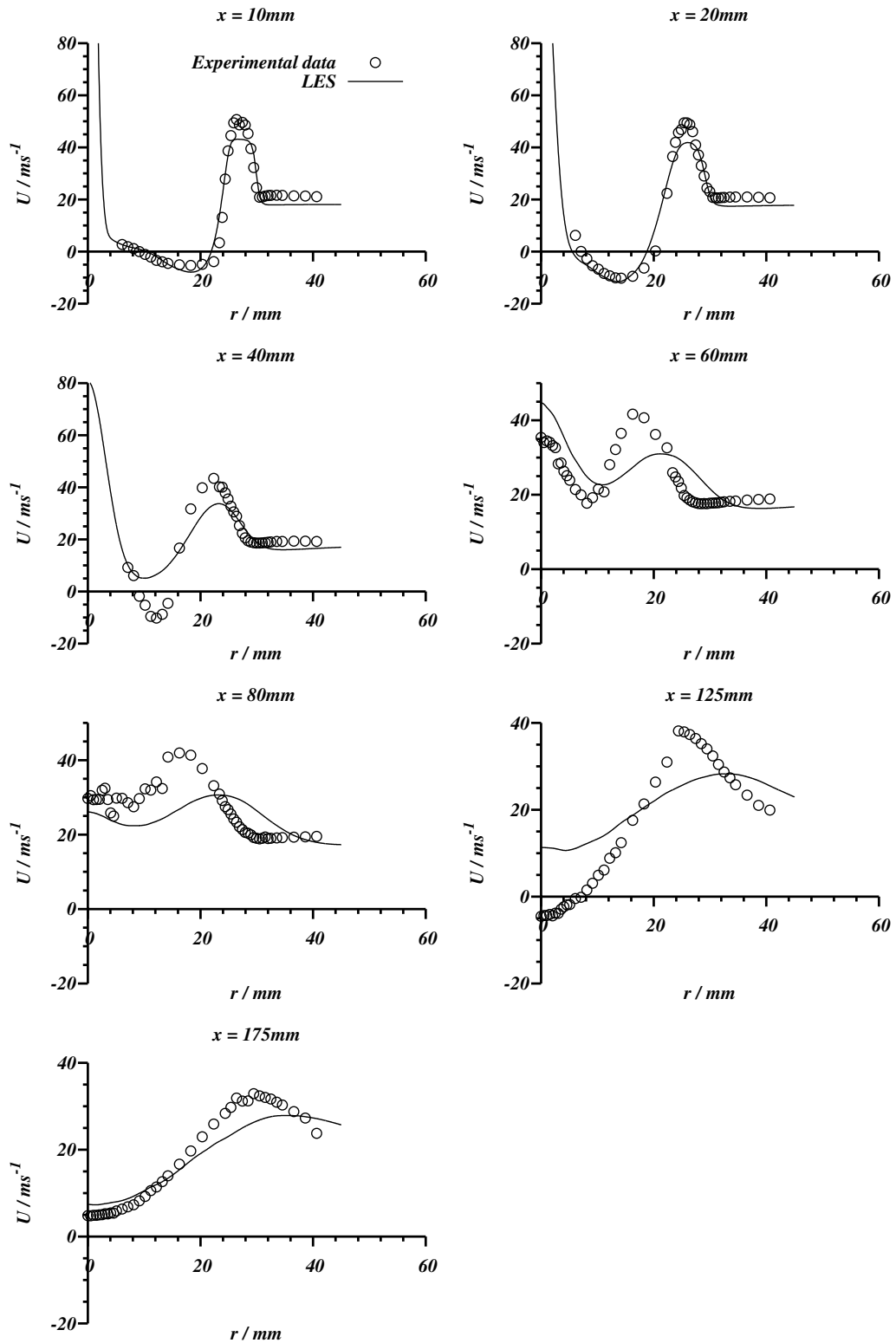


Figure: 6.21 SMH1 Flame axial velocity comparison, Lines:LES, Points:Experimental data[247].

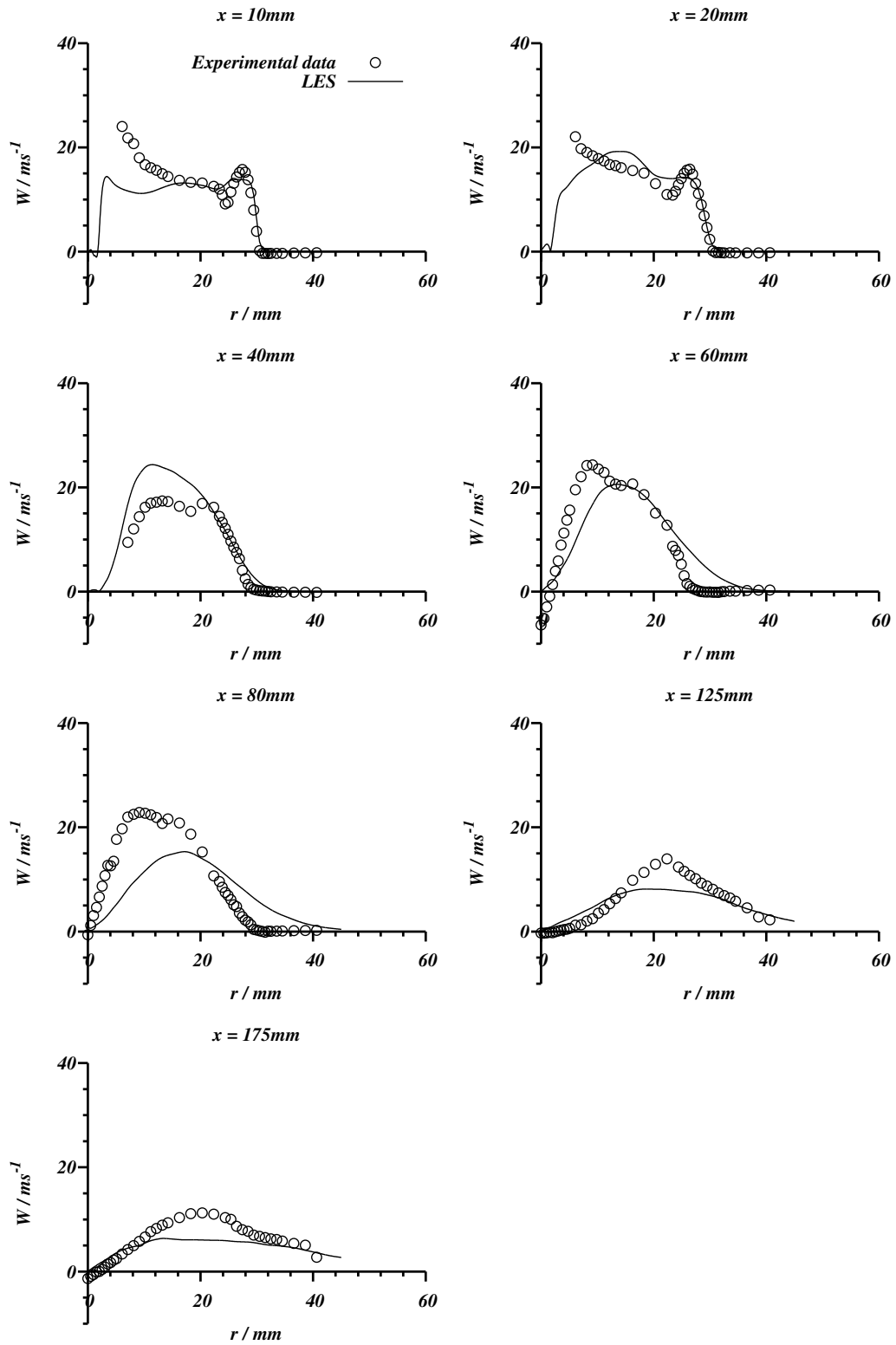


Figure: 6.22 SMH1 Flame tangential velocity comparison, Lines:LES, Points:Experimental data[247].

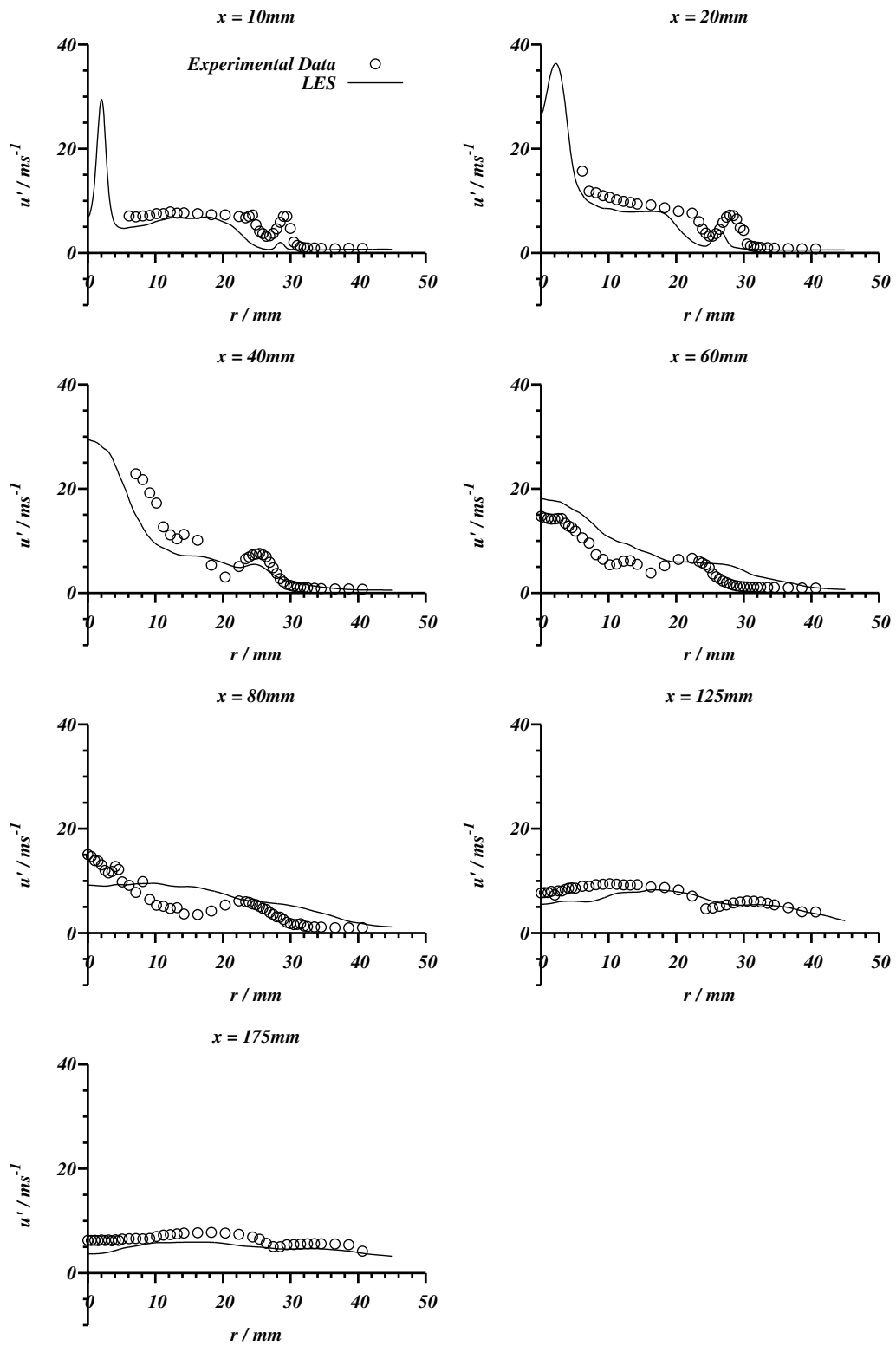


Figure: 6.23 SMH1 Flame axial velocity RMS comparison.

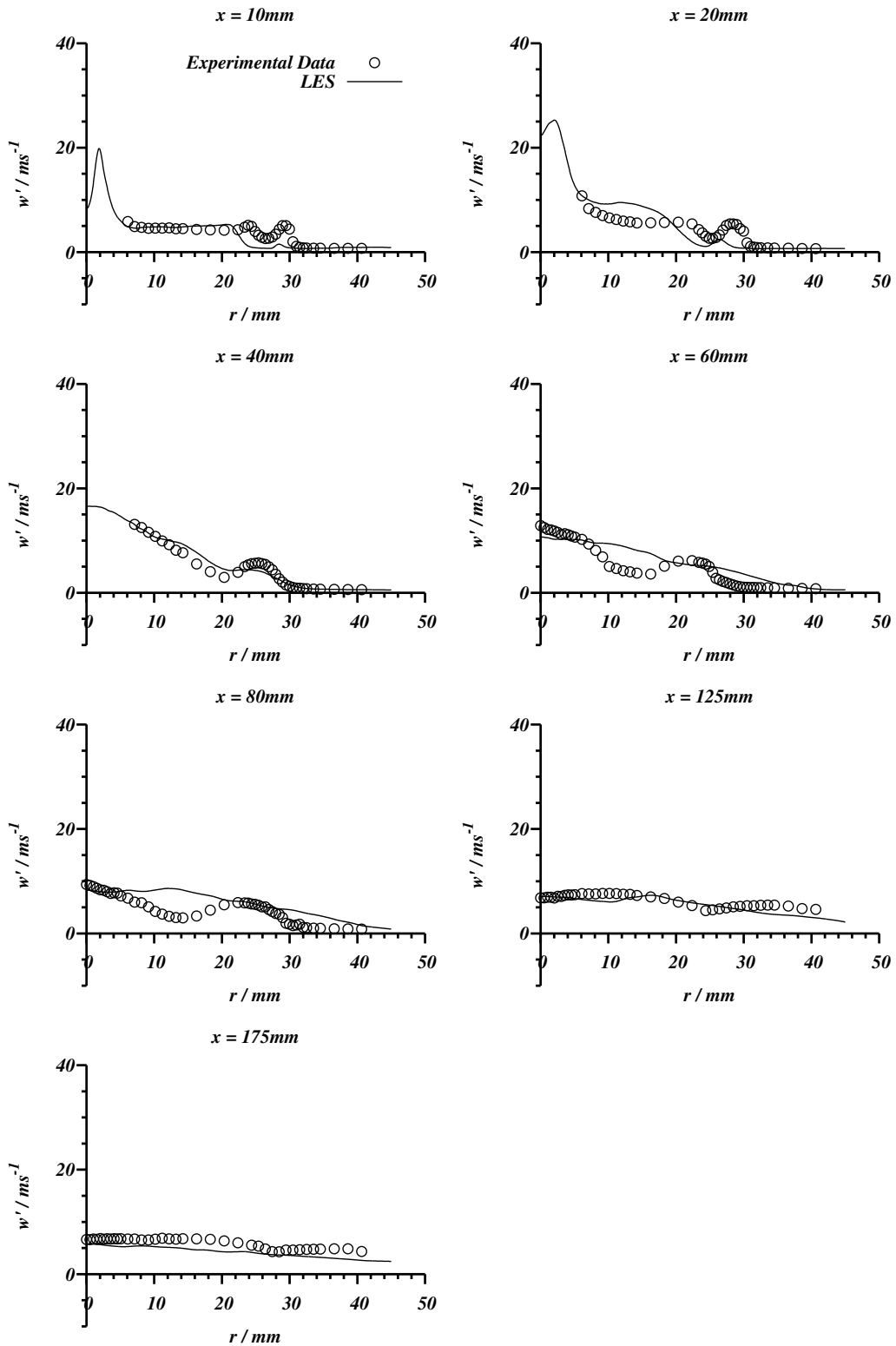


Figure: 6.24 SMH1 Flame axial velocity RMS comparison, Lines:LES, Points:Experimental data[247].

HMS1 - Mean Mixture Fraction (\bar{x}_i) 0.145059280359

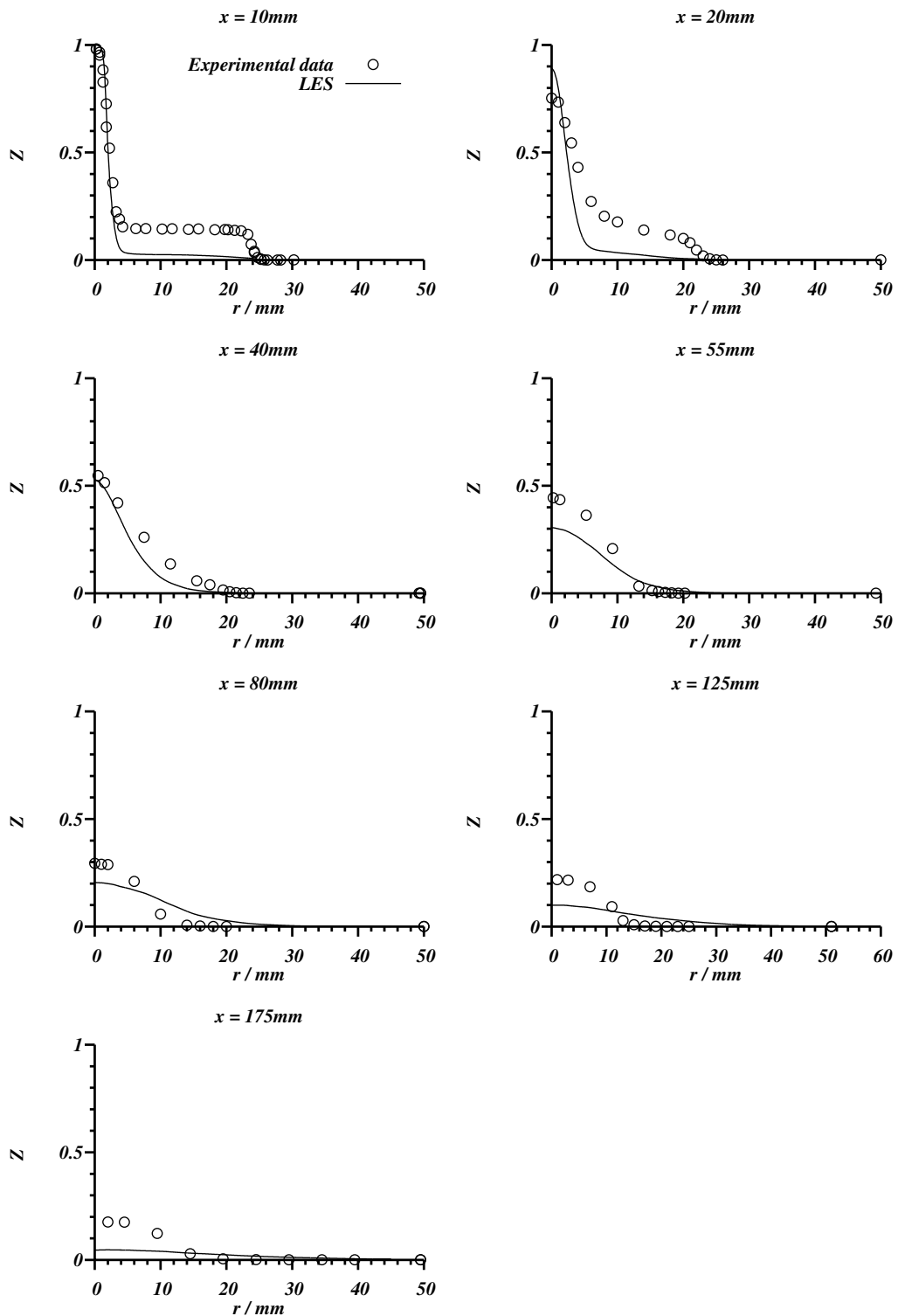


Figure: 6.25 SMH1 Flame : Mixture fraction comparison, Lines:LES, Points:Experimental data[247].

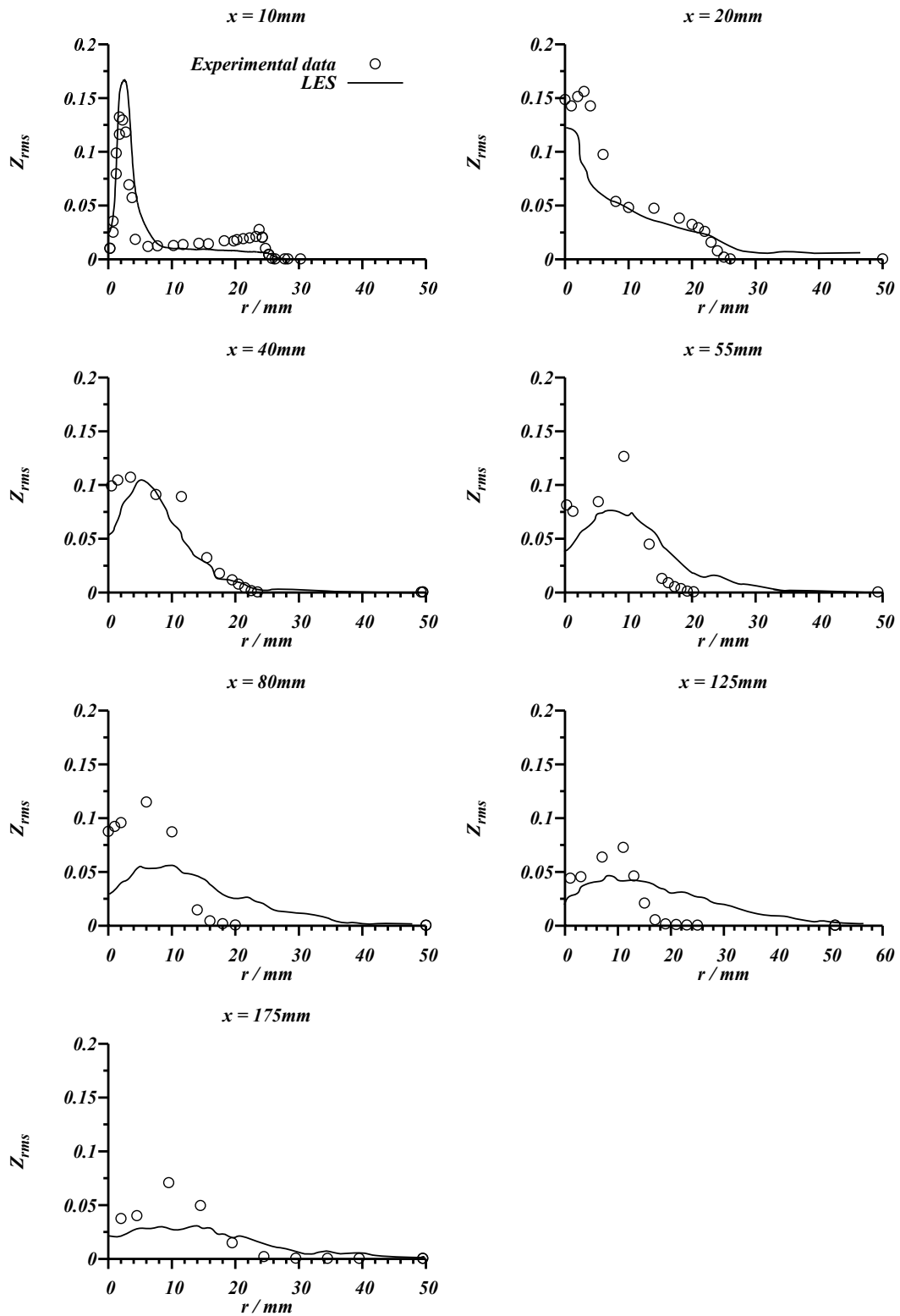


Figure: 6.26 SMH1 Flame : Mixture fraction RMS comparison, Lines:LES, Points:Experimental data[247].

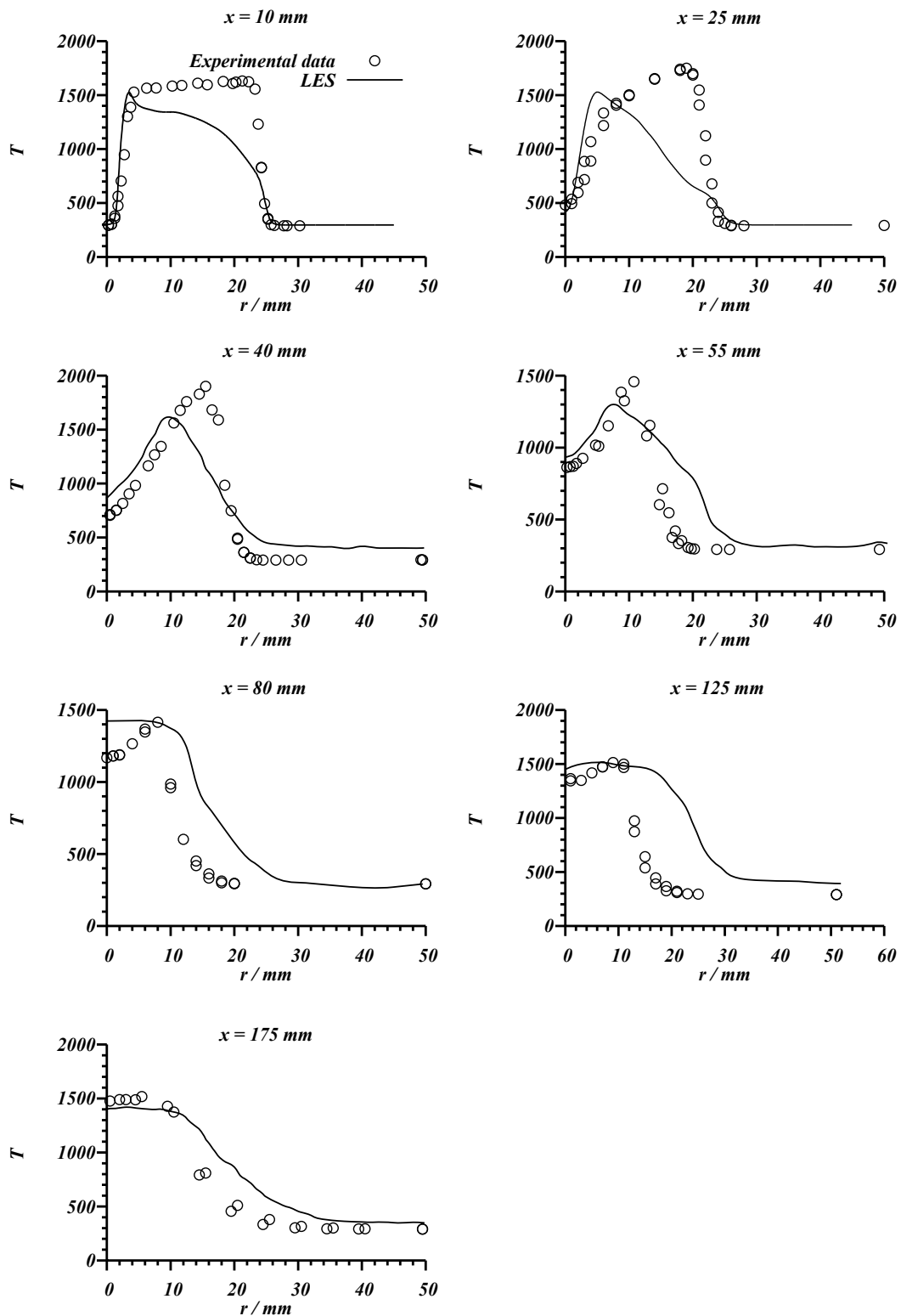


Figure: 6.27 SMH1 Flame : Mean temperature comparison, Lines:LES, Points:Experimental data[247].

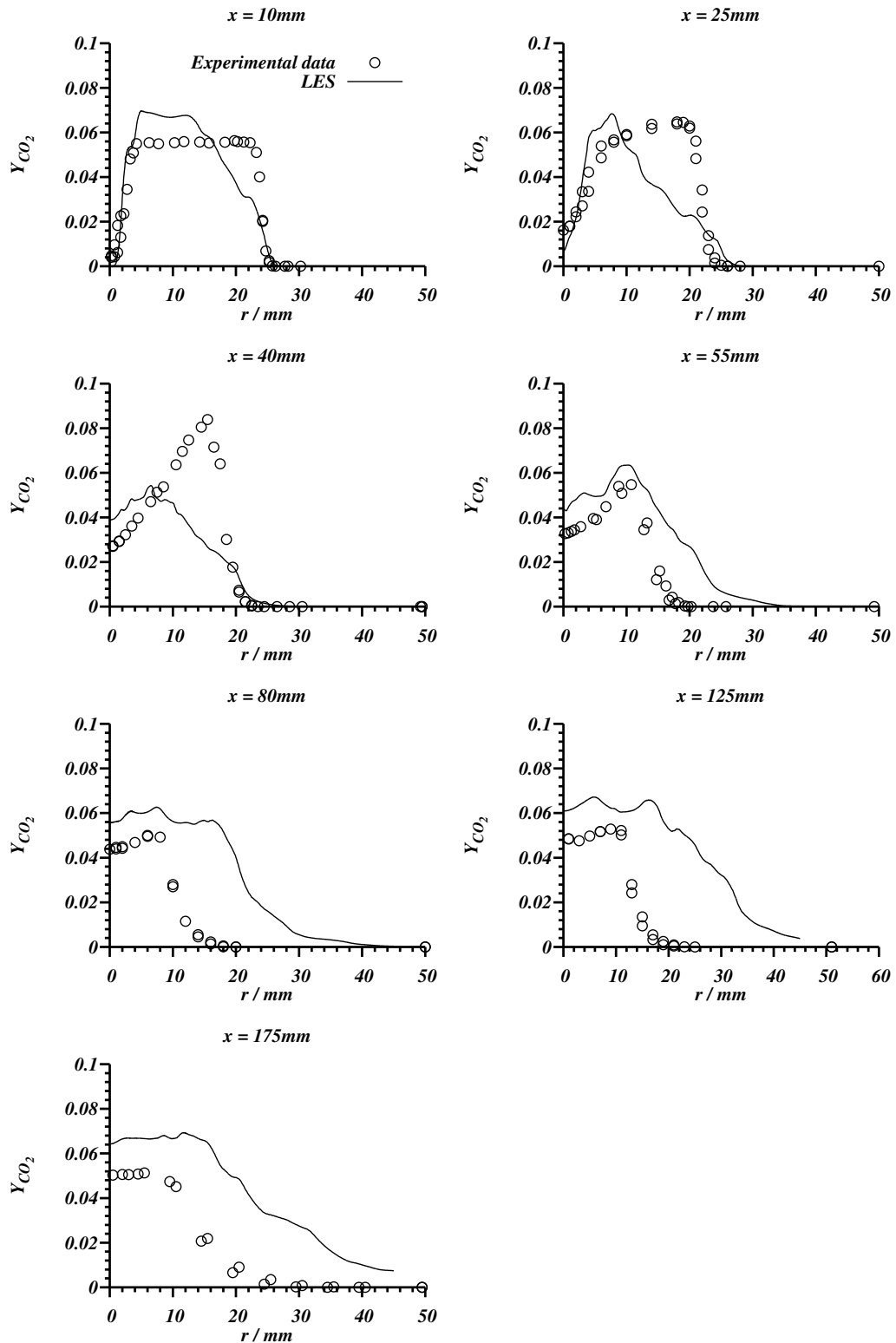


Figure: 6.28 SMH1 Flame : CO_2 Mass fraction comparison, Lines:LES, Points:Experimental data[247].

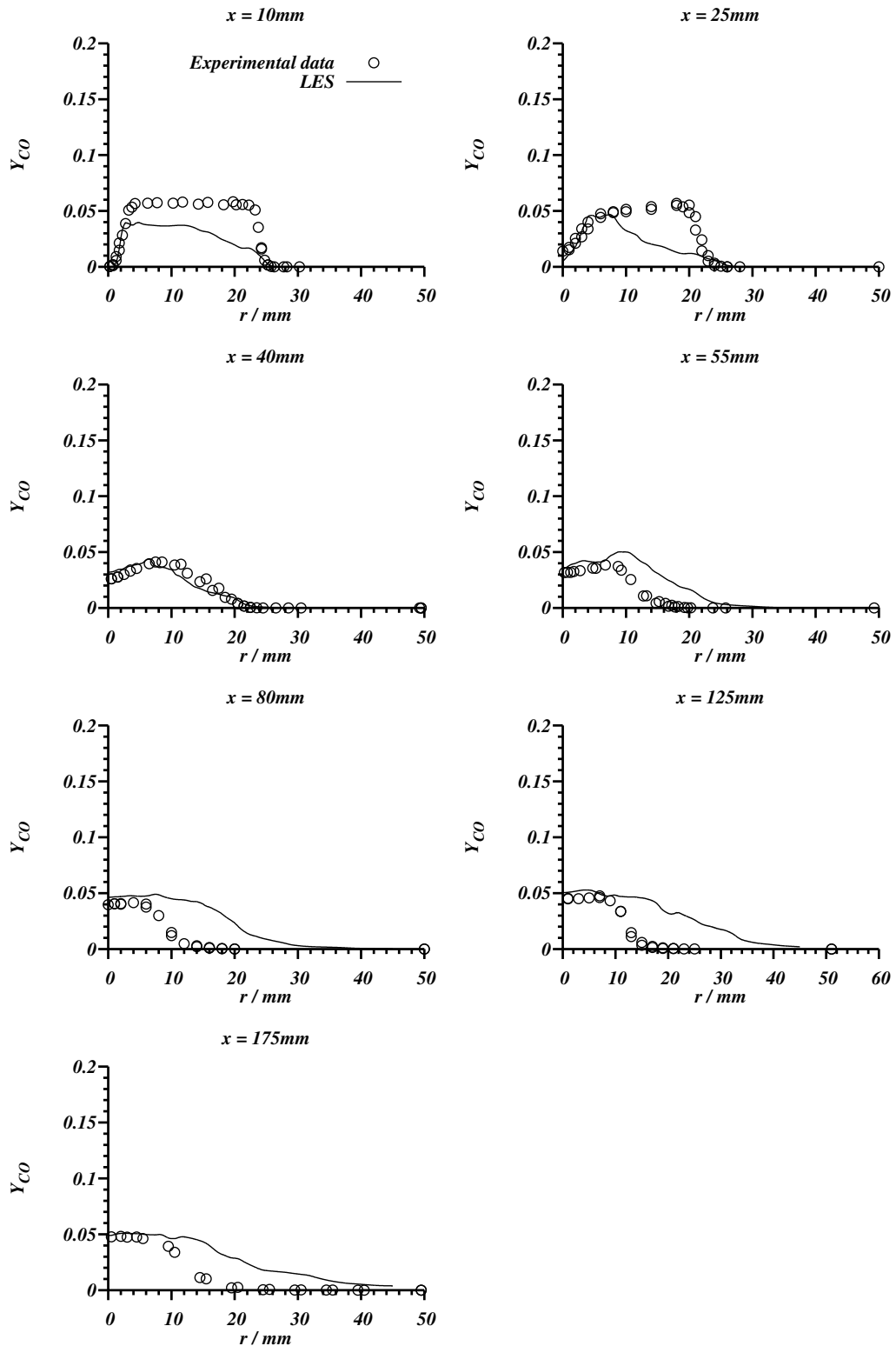


Figure: 6.29 SMH1 Flame : CO Mass fraction comparison, Lines:LES, Points:Experimental data[247].

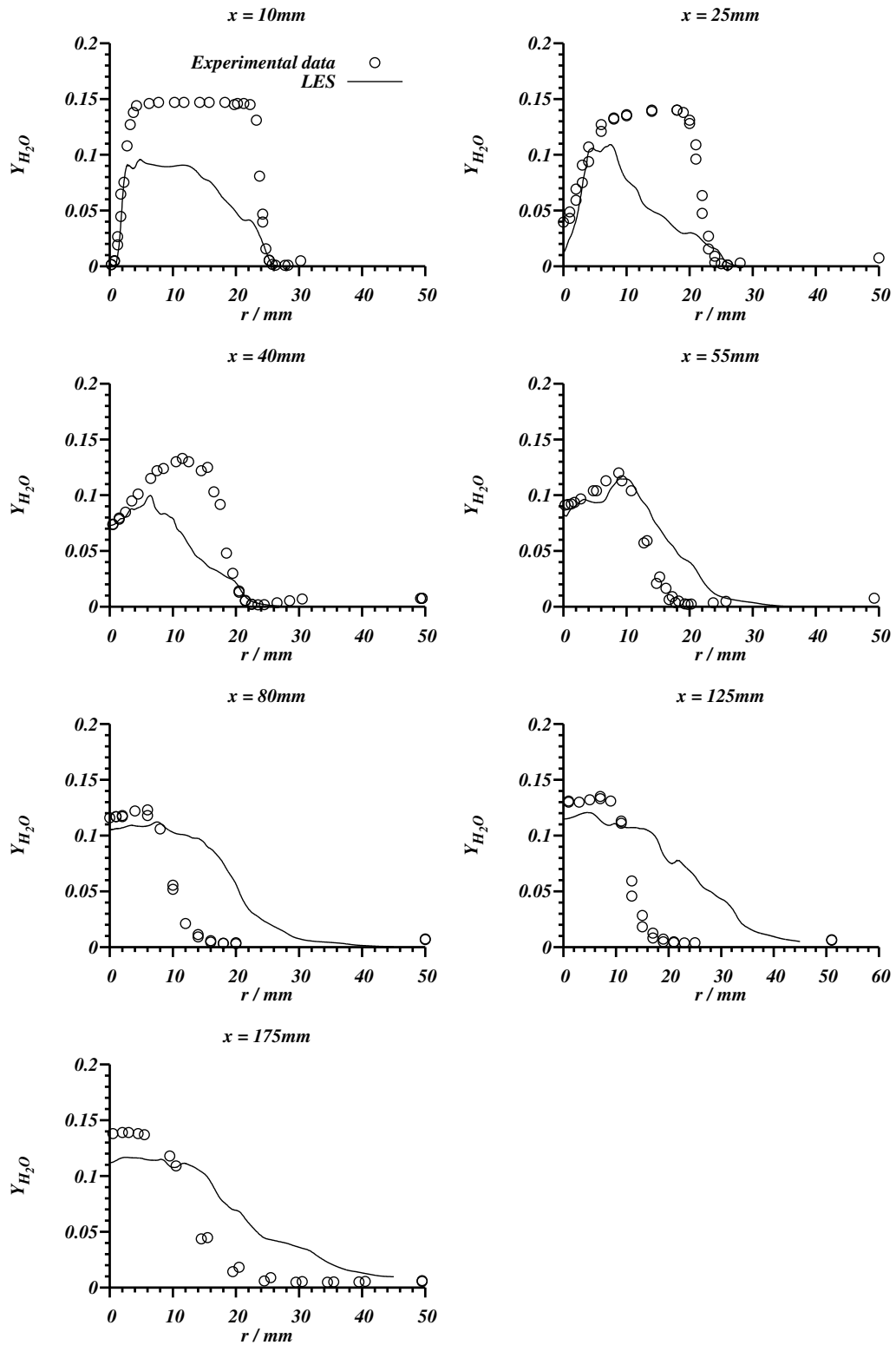


Figure: 6.30 SMH1 Flame : H_2O Mass fraction comparison, Lines:LES, Points:Experimental data[247].

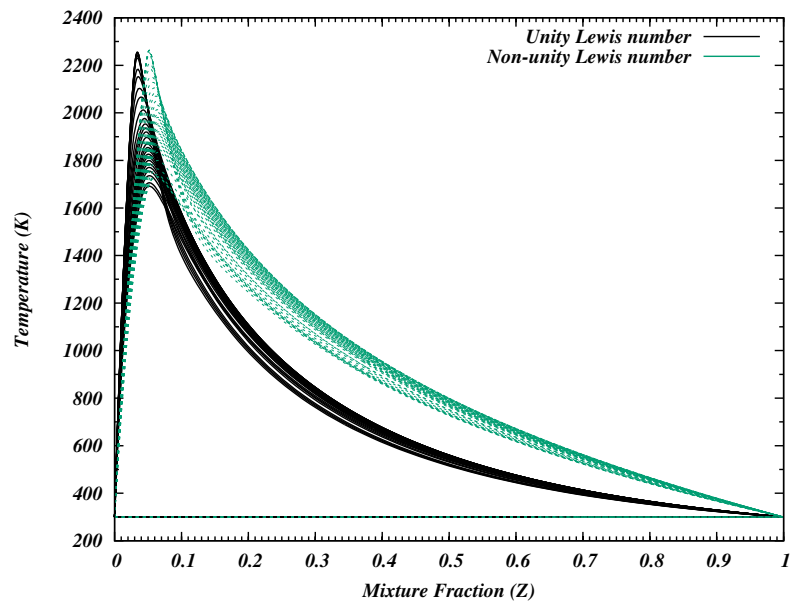
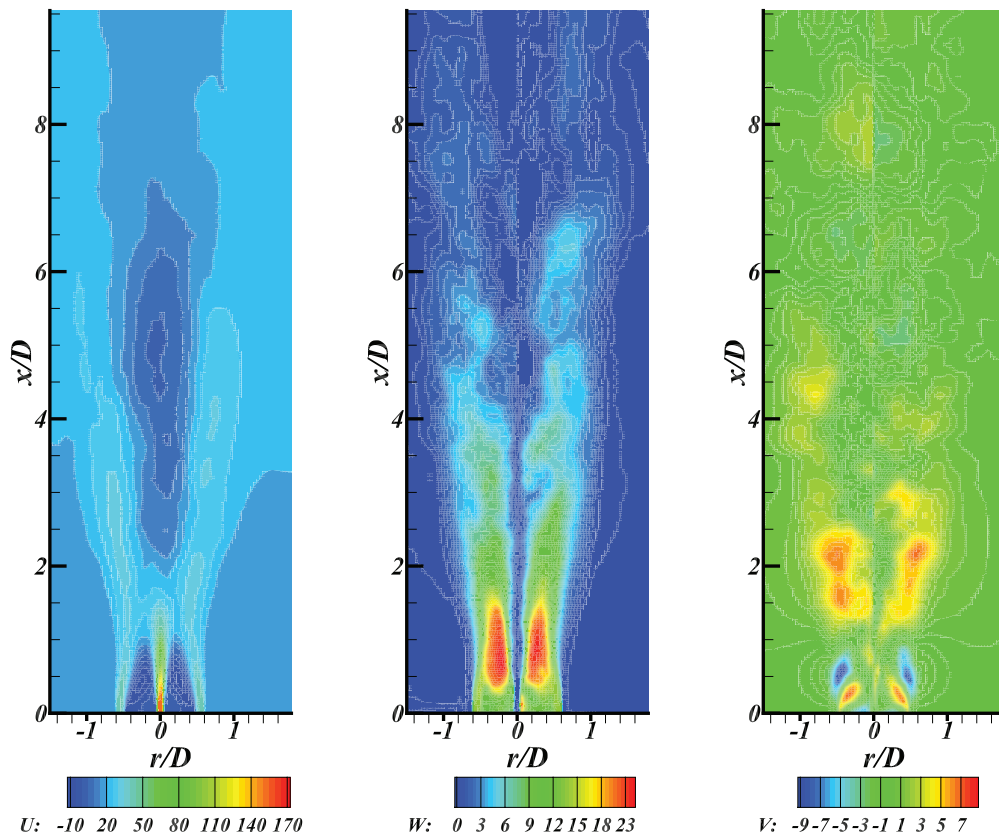


Figure: 6.31 Non-unity Lewis number based laminar flamelet comparison versus unity Lewis number based flamelets.



(a) Axial velocity component. (b) Tangential velocity component. (c) Radial velocity component.

Figure: 6.32 Velocity contours for SMH1 flame.

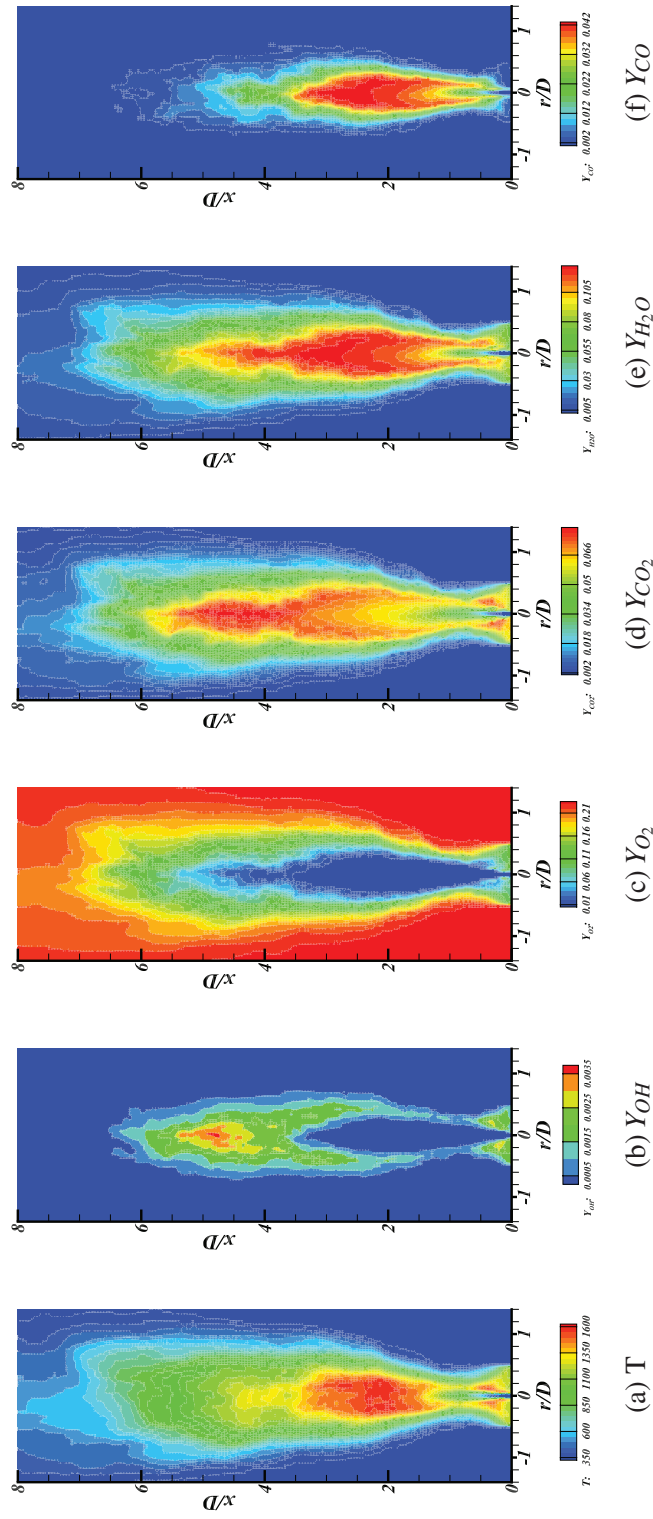


Figure: 6.33 SMH1 Flame : Scalar contours.

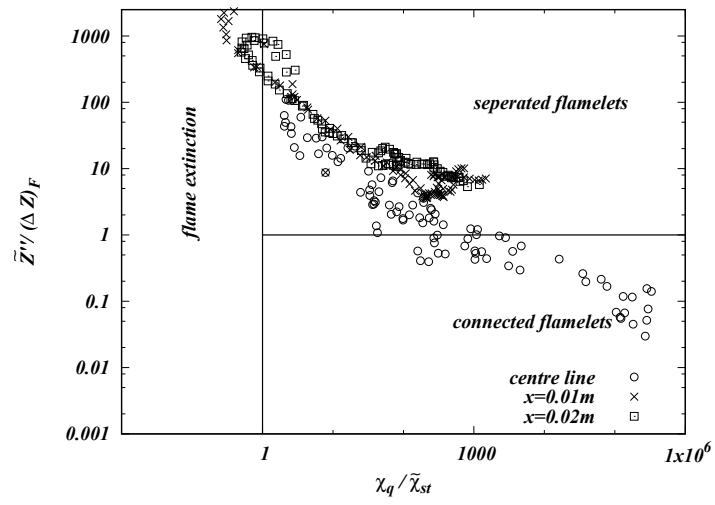


Figure: 6.34 Flame regimes of Sydney swirl burner on a Borghi diagram for non-premixed combustion.

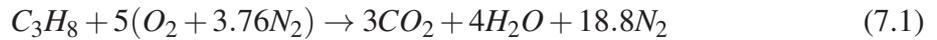
Chapter 7

Premixed/Partially Premixed Flames

In this chapter numerical simulations of Premixed/Partially-Premixed flames are presented and discussed. Flamelet Generated Manifold (FGM) and dynamic Artificially Thickened Flame model (ATF) models are used, and model performances are evaluated using experimental data and detail chemistry analysis of a 2D laminar flame test case. This work was performed with the view to develop a combined model of FGM and ATF.

7.1 Thickened Flame Model Performance

In this section results of test cases using the dynamically thickened flame modelling are presented and discussed. Two purely premixed flame test cases were used to verify the model implementation and accuracy in predicting turbulent premixed flames. In both these test cases, Propane-Air mixtures were used, and the chemical kinetics were approximated using a single step reaction as,



The fuel consumption rate is calculated using Arrhenius type equation (Eqn: 7.2 and following constants [253]).

$$\dot{\omega} = Av_F W_F \left(\frac{\rho_F Y_F}{W_F} \right)^{v_F} \left(\frac{\rho_O Y_O}{W_O} \right)^{v_O} \exp \left(- \frac{T_{act}}{T} \right) \quad (7.2)$$

$v_F = 0.5, v_O = 1, T_{act} = 15080K, A = 1.65 \times 10^{11} (cgsunits), W_F = 44g/mol, W_O = 32g/mol, \rho_O = 0.001429g/cm^3, \rho_F = 0.00201g/cm^3$

7.1.1 Turbulent Flame kernel

In this test case, development of a turbulent Propane flame kernel is numerically simulated using the dynamically thickened flame model. The experiments performed by Nwagwe et al. [254] on turbulent Propane flame kernel growth provides turbulence flame kernel growth rate data that can be compared against numerical simulations. In this experiment, a combustion chamber with 380 mm diameter was used with optical access and isotropic homogeneous turbulence structures were created using a stirring fan. A well stirred stoichiometric propane-air mixture was ignited to obtain a turbulent flame kernel that grows with time. The mean flame radius has been estimated using high-speed Schlieren images obtained via optical access windows of the combustion chamber. RMS velocities of 2.36 m/s and 4.72 m/s were recorded using LDV measurements, and integral length scale of 20 mm was found using spatial correlations. According to the operating conditions of the flame and laminar flame speeds the two cases Flame kernel 1 ($u' = 2.36$ m/s) and 2 ($u' = 4.72$ m/s) are located in the thin flame region of the modified Borghi diagram as shown in Figure: 7.1. Furthermore, it suggests that the fast chemistry reaction assumption can be applied to this problem. Initial conditions of the two test cases are shown in Table: 7.1.

For numerical computations a cubic computational domain with side $L = 0.2$ m, divided into 128 cells per side resulting in a filter size $\Delta = 0.0015$ m, and a ratio $\Delta/\delta_l = 2.60$ was used. Non-reflecting pressure boundary condition was imposed on all sides of the domain, and zero gradients boundary condition was imposed for all other variables. The simulation was conducted using dynamic Smagorinsky turbulence model and second order implicit time discretization schemes were used with van Leer TVD schemes to discretize other convection terms. The initial turbulence of the computational domain was created using the synthetic divergence free turbulence generation tool (*boxTurb*) provided with the OpenFOAM platform. Integral length scale and time scales were calculated using velocity data of a non-reacting decaying turbulence simulation for a given initial turbulence field and repeated this process to obtain correct integral length scale and RMS velocity. It was observed that the initial growth of the flame kernel was highly sensitive to the grid resolution; thus a time steps with $Co < 0.05$ were required to generate a stable initial flame kernel. Initial flame variables (thermophysical properties) were mapped from a precomputed simulation on a 128^3 grid to a computational grid with 64^3 to reduce computational demand. The artificial thickening factor was set at $F = 6$ and results showed negligible sensitivity to the thickening factor beyond $F > 4$.

Figure: 7.2 shows the numerically simulated rate of turbulent flame radius growth is compared against experimental measurements. In the case with low turbulence intensity (Figure: 7.2a, $u' = 2.36$ m/s), the flame radius growth is very well modelled by LES results.

7.1 Thickened Flame Model Performance

Table 7.1 Initial conditions of turbulent flame kernel growth measurements test [254]

Fuel	ϕ	P/(bar)	T/(K)	$u'/(ms^{-1})$	$S_l/(ms^{-1})$	$\delta_l/(mm)$
Propane	1.0	1	300	2.36, 4.72	0.383	0.3

The initial flame kernel imposed had nearly 10 mm flame radius and gradually increased the flame radius accelerating the growth with time. The high turbulent intensity configuration (Figure: 7.2b, $u' = 4.72 m/s$) simulation shows good agreement with the rate of flame radius growth initially but as the flame grows beyond 30 mm in radius the numerical flame growth indicates a slower turbulent flame speed. However, during this simulation flame surface breakaway was observed due to flame surface stretching. Therefore, it can be seen that the combustion model can reproduce turbulent flame speeds that conform with experimental observations. Figure 7.3 shows temperature mapped onto progress variable isosurface of $c = 0.5$ at three different instances of the kernel growth, and in all three instances, the flame volume can be considered as spherical although flame surface wrinkling can be observed. In addition, this view shows that at the particular progress variable iso-contour the temperature of the flame remained uniform, which is an indication that the calculation of thermophysical properties (enthalpy) using progress variable has been consistent throughout the simulation.

The instantaneous model variables for the low turbulent intensity test case are shown in the Figure: 7.4 and these scalar values can be used to verify the model implementation. Figure: 7.4a shows the temperature prediction which shows that the burned mixture temperature is close to the adiabatic flame temperature for stoichiometric Propane air-fuel mixture ($T_a = 2260 K$) and the moderately wrinkled reaction zone that separates burned gases from unburned gases. The velocity of the reaction zone is much higher compared to the unburned gases as shown in Figure: 7.4b due to the expansion of gases, and the burned gases also showed comparatively smaller velocity magnitude because of the increase of viscosity. Therefore, it can be seen that the model has predicted the effects caused by the changes in thermophysical properties of burned and unburned gases, and providing further evidence the Figure: 7.4c shows that density of the burned gas is also magnitudes of order smaller than unburned gases as expected. In Figure: 7.4d the artificially thickened reaction zone can be recognized because the progress variable source term represents the reaction zone. Efficiency function which is used to compensate the flame area reduction caused by flame thickening is shown in Figure: 7.4e and it shows that the efficiency function conform with the model assumption that $E_{max} < F^{2/3}, E_{min} = 1$. As the discussion on evaluation of sub-grid scale velocity u'_{Δ_e} (Section: 3.14), one of the important requirement is to estimate the energy of scales larger than the grid-filter. In Figure: 7.4f the sub-grid scale velocity is

7.1 Thickened Flame Model Performance

shown. The sub-grid velocity can be seen to be significantly larger in the thickened zone suggesting and has captured the effects of larger velocities of the expanding flame front. The test case of turbulent flame kernel growth reveals that the dynamic thickened flame model implementation can accurately predict the turbulent flame speed by solving the reaction progress variable equation with a chemical source term that is resolved. Furthermore, vital thermophysical variables and model parameters exhibit agreement with each other and conform with the physics of the spherical turbulent flame kernel growth. Therefore it confirms that the model implementation and the reduced chemical reaction can predict the premixed turbulent flame propagation.

The mean flame kernel radius can be calculated by assuming a spherical burned gas volume (Eqn: 7.3), by using burnt gas density (ρ_b) and regress variable (b),

$$R = \left(\frac{3}{4\pi\rho_b} \int \int \int \rho(1-b) dx dy dz \right)^{1/3} \quad (7.3)$$

7.1 Thickened Flame Model Performance

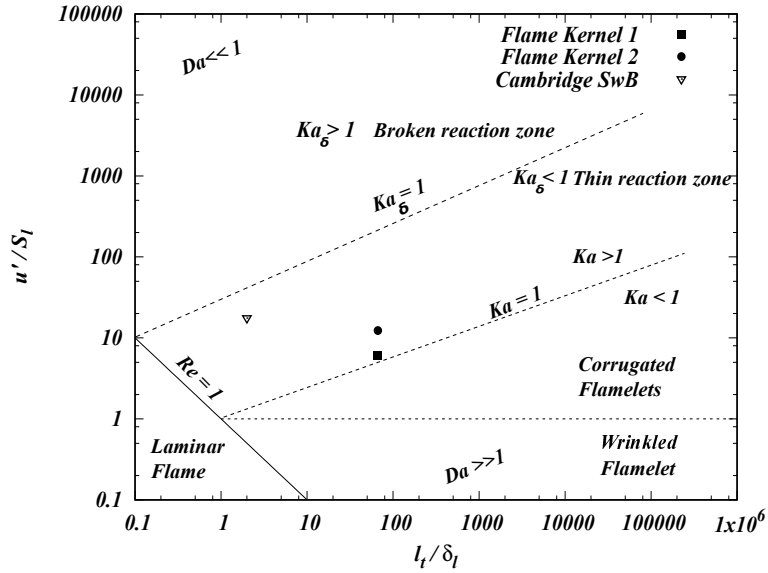


Figure: 7.1 Modified Borghi diagram : turbulent premixed flame regimes

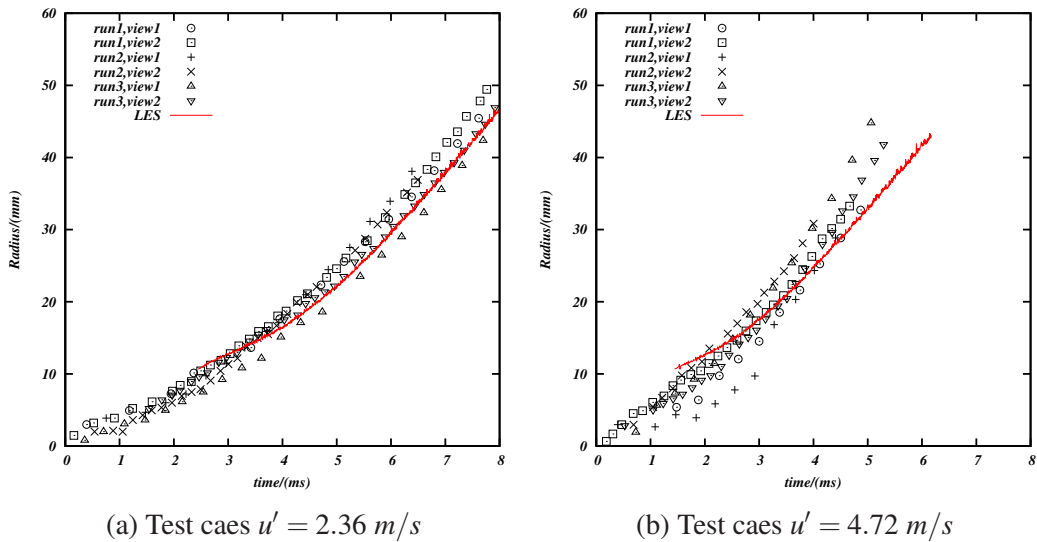


Figure: 7.2 Turbulent flame kernel radius growth rate, (Experimental data from [254]).

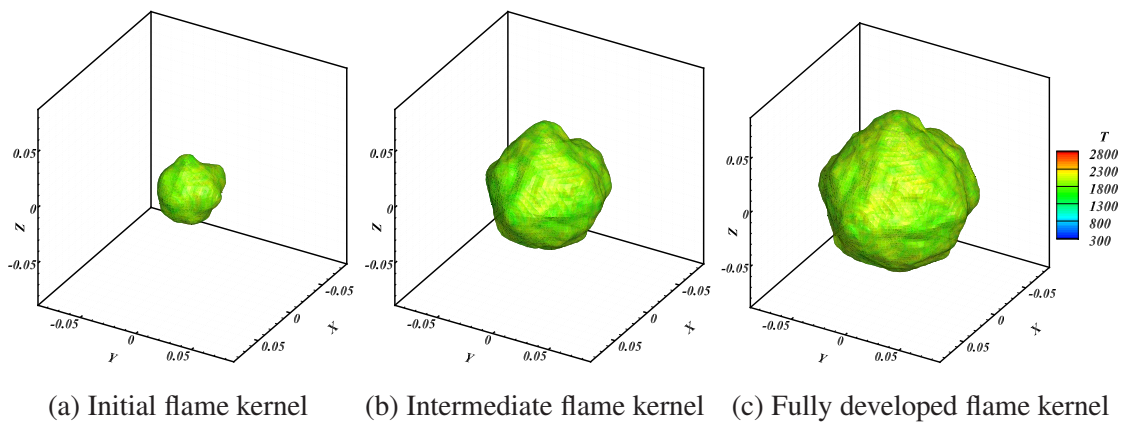


Figure: 7.3 Development of turbulent flame kernel

7.1 Thickened Flame Model Performance

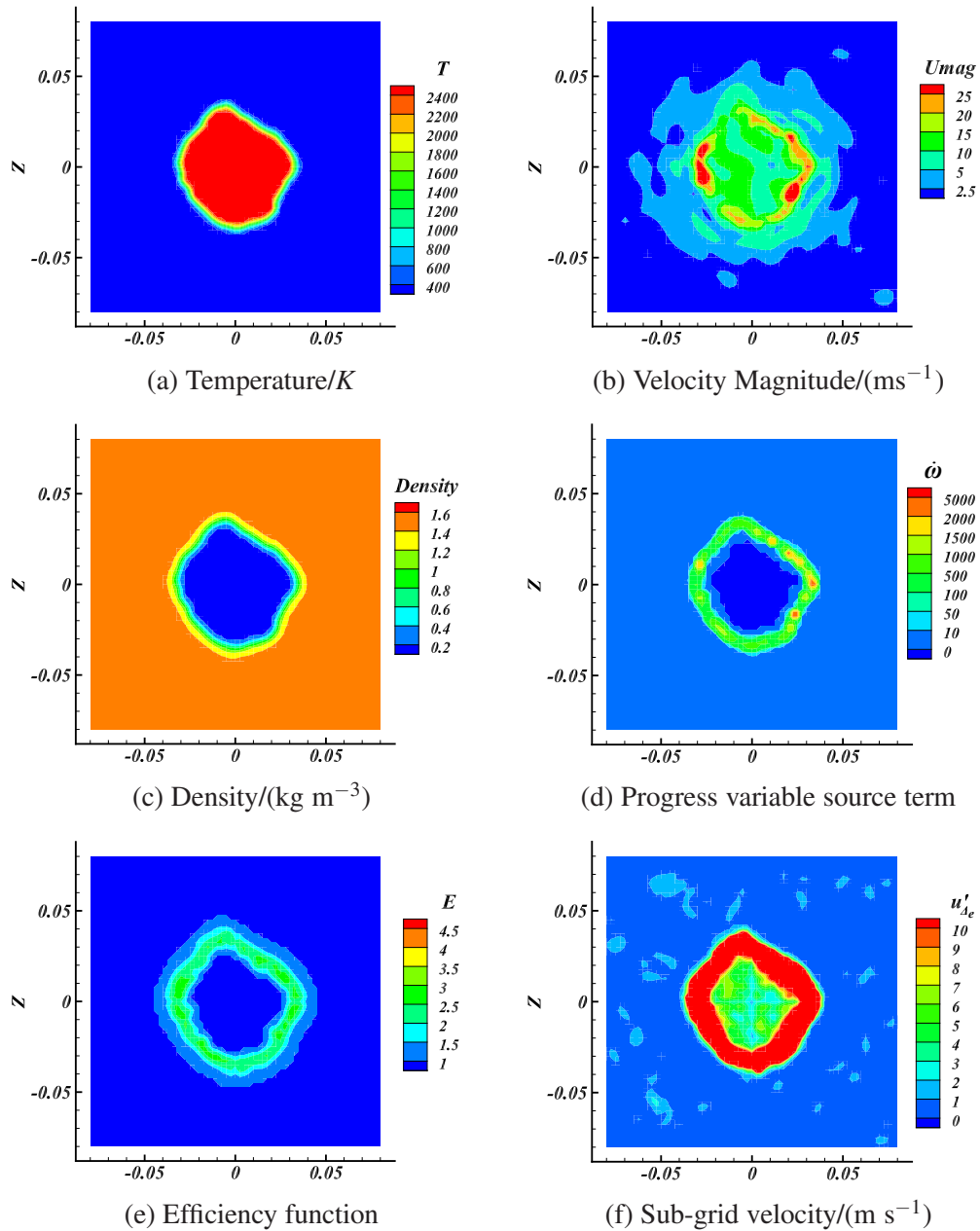


Figure: 7.4 Turbulent Flame Kernel: Flow variables and Model variables

7.1.2 Turbulent Premixed Flame in Backward Facing Step

Experimental setup

Previous test case showed that the turbulent flame progression was accurately captured by the dynamically thickened flame model. However the test case was inadequate to fully validate the model implementation because the temperature fields and chemical reaction progress were not quantified. Therefore, in this section results of a numerically simulated turbulent premixed flame in a backward facing step mixing layer are presented and compared with velocity data and temperature data from an experimental combustor [255],[256]. The geometry of the experimental combustor is shown in Figure: 7.5, in which the step height $H = 25\text{mm}$ is designed to be the same as the height of the inlet section, the width of the combustion chamber was $6.5H$. In this experimental analysis, propane air mixture was used as the reacting mixture, and 1m long inlet section was provided to enhance the mixing, that section is excluded in this modelling effort.

In this validation study, the $\phi = 0.57$ test case was simulated which operated at a Reynolds number based on step height $Re_H = 22 \times 10^4$. Free stream turbulence was estimated as $U_{rms} = 0.03\text{m/s}$ and the mean axial flow velocity at the inlet section was measured to be $U_0 = 13.3\text{m/s}$ for both reacting and non-reacting cases. In the experiments, cooling water was sprayed into the converging section, however, in the numerical simulation the effect of cooling water was neglected, and the outflow boundary was set at the end of the converging section. Laser Doppler Anemometry was used with alumina particles that gave an error of 3% and silica-coated thermocouples were used to measure temperature. Measurements of equivalence ratio and inlet flow velocity were within 6% and 1.3% uncertainty respectively. This experimental set up has been used by many numerical validation efforts [83],[234],[257] due to the simple geometry and predominantly two-dimensional flow structure.

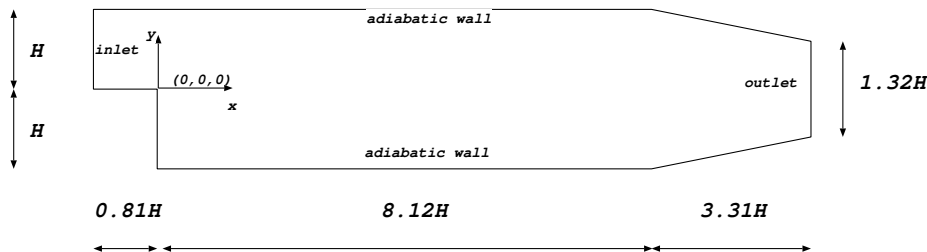


Figure: 7.5 Backward facing step geometry.

Numerical setup

Large eddy simulations were performed, and locally dynamic Smagorinsky model was used for both non-reacting and reacting flow simulations. For non-reacting simulations, a computational grid with 0.6×10^6 hexagonal cells was used, and for reacting flow, the grid number was increased to 0.86×10^6 . The computational grid was designed with the consideration that the flow in this combustor is predominantly two-dimensional; therefore periodic boundary conditions were used in transverse directions, and transverse width was set to be $2H$. Inlet boundary conditions for velocity profile was generated from the experimental measurements and re-mapping from an internal plane was used to generate and sustain velocity fluctuations. Second order implicit time integration and TVD schemes were used for all scalar convection term discretization. In thickened flame modelling a constant artificial thickening factor of $F = 10$ was applied across the reaction zone, and other model coefficients are calculated as in Section: 7.1.1. Ignition was set up by a sphere of progress variable set to 1 closer to the step, and it was maintained sufficiently ($50ms$) to establish a sustainable reaction zone. It was observed that the ignition phase was required to stay until the recirculation zone established a reaction inside, otherwise, the weak reaction zone extinguished due to strain induced by shear layer fluctuations. LES results were time averaged $140ms$ and $80ms$ for non-reacting and reacting flow simulations respectively.

Results - Non-Reacting simulation

Non-reacting simulations were conducted ($\phi = 0$) to validate the numerical setup and the mesh resolution. It was assumed that dominant shear flow structures would remain in the reacting flow as well when the non-reacting simulation was extended to reacting flow simulations. Initially, at the backwards-step, the flow generates a shear flow due to the velocity differential, and this shear flow generates Kelvin-Helmholtz instabilities which grow with downstream distance. Closer to the step the flow can be seen as a mixing layer, that is similar to flow past a split plate where two fluid streams entrain. However, unlike the flow past a plate problem, with increasing downstream distance the flow below the mixing layer forms a recirculation zone causing the shear layer to curve downward and grow. As the shear layer grows the shear layer curves further and mixing layer analogy is no longer valid, then the flow impinges on the bottom wall at the reattachment point. Beyond the reattachment point, the flow starts to establish a flow similar to the flow between two plates hence forming a relaxation zone.

Figure: 7.6a illustrates the mean streamlines generated from LES simulations that show a recirculation zone formed in the bottom fluid of the mixing layer and the flow reattach-

7.1 Thickened Flame Model Performance

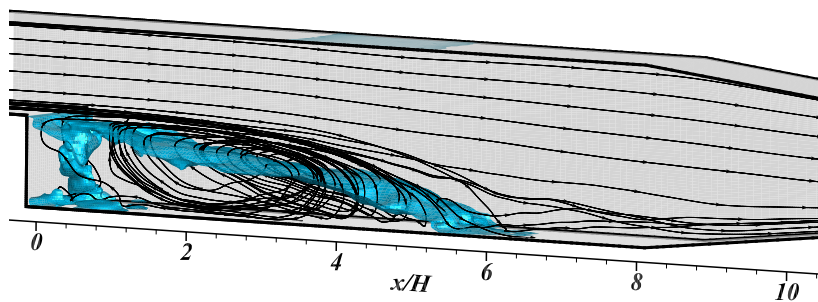
ment. The sharpness of the velocity change diminishes as shear layer flow develops, and the mean flow curves down and reattaches the bottom wall at $x = 7H$. Figure: 7.7 shows the mean streamwise velocity profiles and RMS velocity compared against experimental data. The sharp change in magnitude of velocity at the interface of step height indicates the higher positive velocity of the incoming stream and the negative velocity of the recirculating velocity field. Although LES results slightly underpredict the magnitude of the negative velocity component, the variation of negative velocity component is well predicted by LES results. Similarly, closer to the step the RMS velocity component shows a sharp peak at $y = 0$ because of the formation of a shear layer. With increasing downstream distance the RMS component increases in magnitude because of the recirculation flow and the growing shear layer that spreads into the upper flow. Therefore, the mean velocity field prediction shows that LES results agree sufficiently with experimental data to capture the effects of the shear layer, recirculation and reattachment. In Figure: 7.6a, the mean iso-contour of zero streamwise velocity is shown, this iso-contour can be considered as a surface that separates the shear layer and recirculation zone, and shows the reattachment point. The reattachment point depends on the development of large-scale structures generated from Kelvin-Helmholtz instabilities. Experimental measurements have recorded a reattachment distance of $x = 7H$ for the non reacting flow it can be seen that for the non-reacting simulation the reattachment location located closer to $x = 7H$.

In the reacting flow case also a shear layer flow is developed and closer to the step due to very high flow strain the reaction is delayed allowing Kelvin-Helmholtz instabilities to occur. In Figure: 7.8 the mean velocity field and RMS component of the streamwise velocity component for the reacting flow test case is shown, and when compared with the non-reacting velocity field it can be seen that the recirculation zone length has shortened. LES results have reproduced the velocity field to agree with experimental measurements, however closer to the wall the sharp velocity difference across the mixing layer is diffused by LES results indicating insufficient grid resolution. The RMS velocity component shows that the velocity fluctuations in the recirculation zone are larger when compared to non-reacting flow case and LES predictions are in reasonable agreement with experimental measurements. From Figure: 7.6b the zero velocity iso-contour shows that the curved shear layer re-attaches around $x = 5H$, and experimental measurements also had recorded a reattachment point at $x = 5H$. Therefore it can be said that the simulated reacting flow field also agrees well with experimental observations.

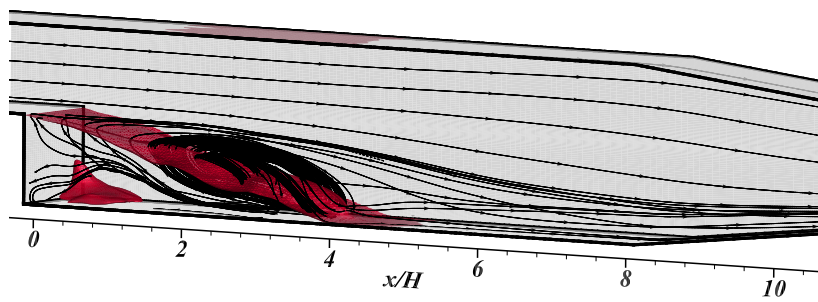
Schlieren photographs were used in the experimental investigation to identify the reaction zone. Schlieren shadow is a result of density differential of the flow, hence can be used to visualize the reaction zone, and it can be seen that the reaction zone is attached to

the step and grows with streamwise distance while entraining recirculating flow and fresh gases. As this entrainment facilitates the sustainable reaction, the width of the reaction zone grows with distance. However, the termination of reaction cannot be determined clearly by Schlieren images because it is not a measurement of the reaction zone but rather a manifestation of density differential. A shadowgraph using the density differential can be generated from postprocessing the LES results Figure: 7.10b, and compared with Schlieren photograph in Figure: 7.10a, and it can be seen that LES results show similar initial flow topological features as experimental images. Initially, the shear layer structure is formed and then as the reaction occurs, and density of the burnt gases are much smaller than the fresh gases coming above the mixing layer density differential further increases mixing and hence reaction causing the mixing layer to grow and create wrinkled structures. The shadowgraph calculated using LES results cannot be used to make direct comparisons with Schlieren photograph at downstream flow structures because these larger turbulent structures do not contain a consistent mean feature.

In Figure: 7.11 and Figure: 7.12 scalar contours and scalar values mapped on an iso-surface of reaction progress variable source term $\tilde{\omega}_c = 20$ are illustrated. The particular source term iso-surface is selected to represent an averaged reacting surface. Figure: 7.11a shows the instantaneous progress variable contours, and it can be seen that there exist a clear reaction zone separating the burned mixture from unburned gases and that pockets of reacting zones separate when large turbulence structures interfere the reaction zone. In Figure: 7.11b the progress variable reaction rate $\tilde{\omega}_c$ is shown, where it shows that close to the step the reaction rate is much smaller in magnitude because the high-temperature reaction zone occurs in the recirculation zone away from the wall (Figure: 7.11c). In addition, this view shows the breakaway reaction zone as a result of excessive flame wrinkling caused by larger eddies. In Figure: 7.12a, the temperature is plotted on an iso-contour of the reaction rate, and it shows that there exist two layers of iso-surfaces with same reaction rate magnitude, and the top iso-surface has lower temperature while the bottom iso-surface shows higher temperatures due to the reacted mixture. Figure: 7.12b and Figure: 7.12c show sub-grid velocity scale and the efficiency function mapped onto the same reaction rate iso-surface, and these figures show that efficiency function and sub-grid velocity scale shows a proportional relationship as theoretically expected.



(a) Iso surface of zero streamwise velocity - Non-reacting flow



(b) Iso surface of zero streamwise velocity - Reacting flow

Figure: 7.6 Recirculation flow in reacting and non-reacting backward facing step flow

7.1 Thickened Flame Model Performance

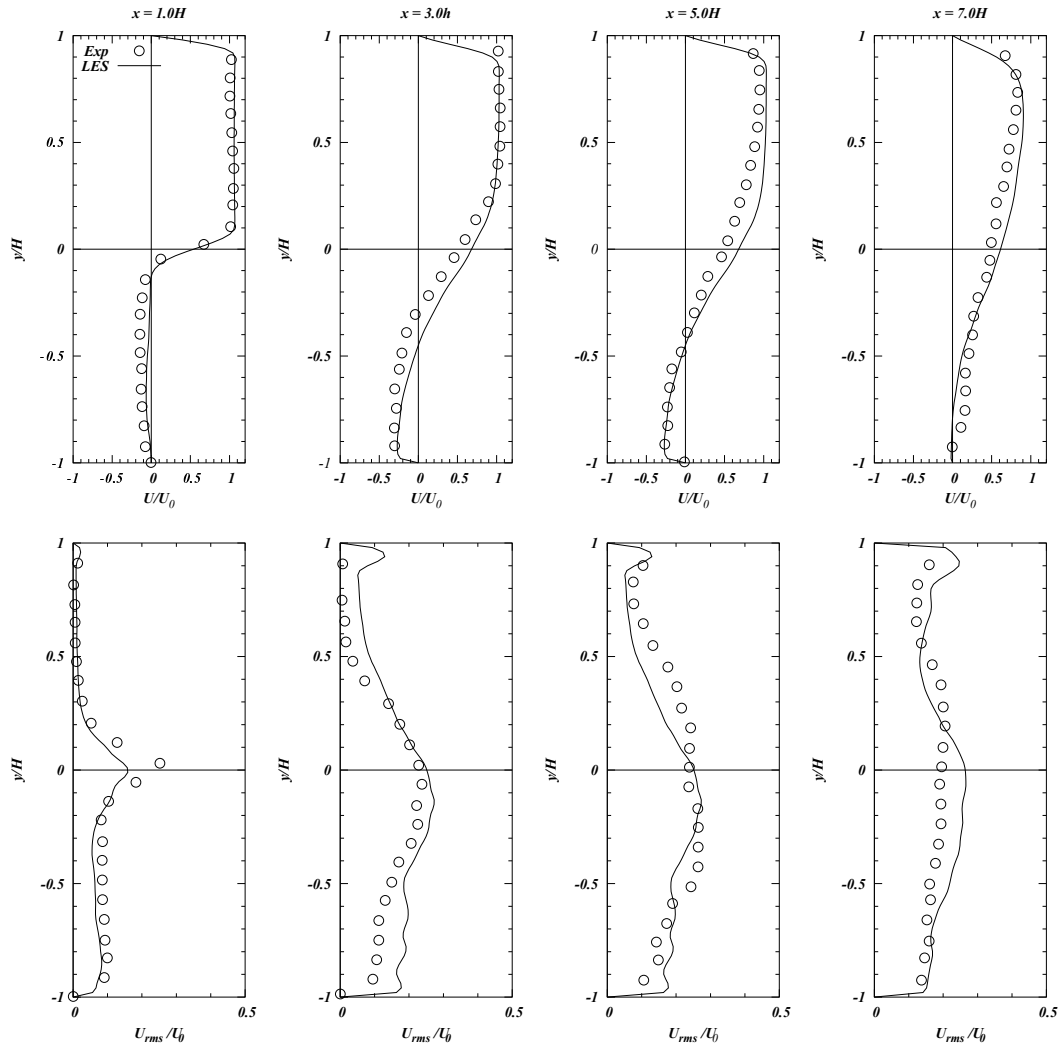


Figure: 7.7 Non-reacting flow velocity field, (— : LES, ○ : Experimental data [258])

7.1 Thickened Flame Model Performance

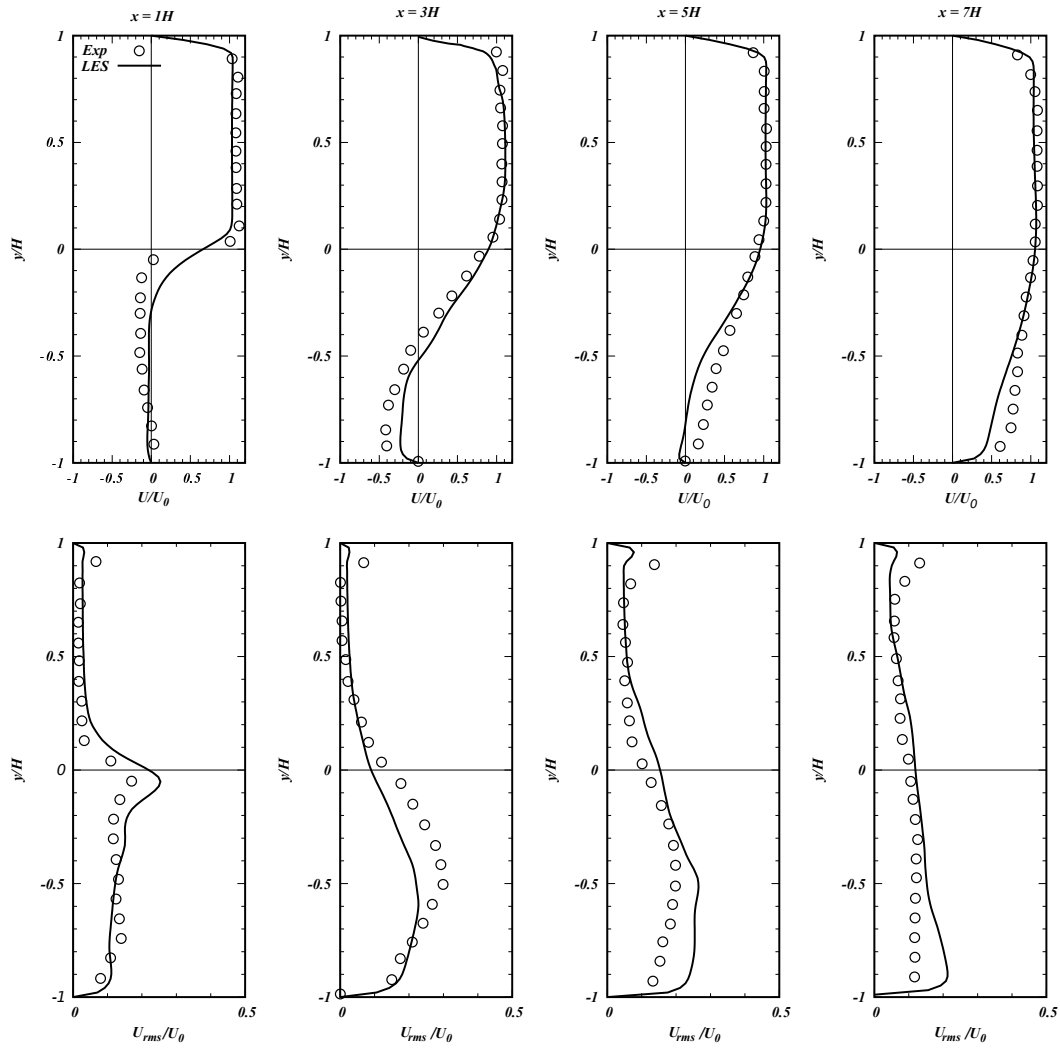


Figure: 7.8 Reacting flow velocity field, (— : LES, \circ : Experimental data [258])

7.1 Thickened Flame Model Performance

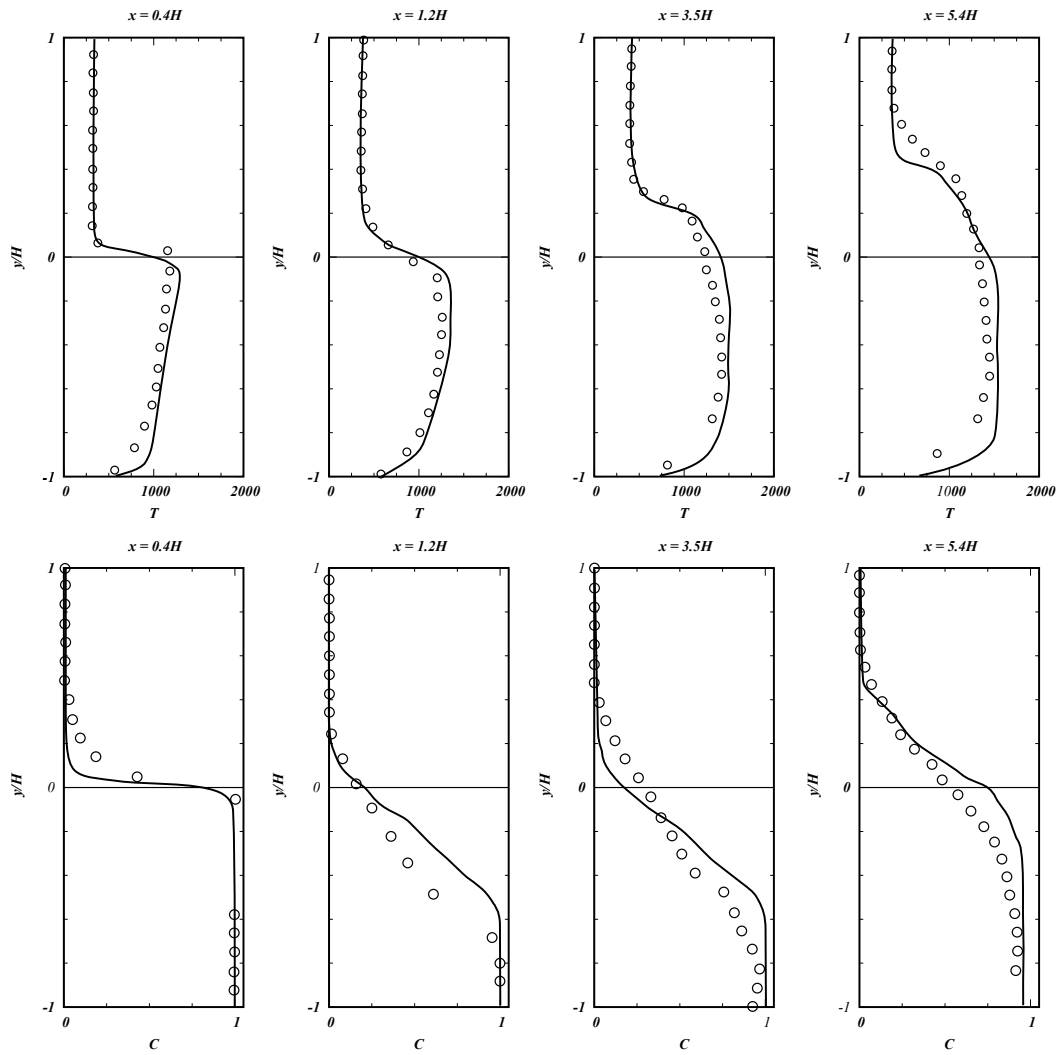
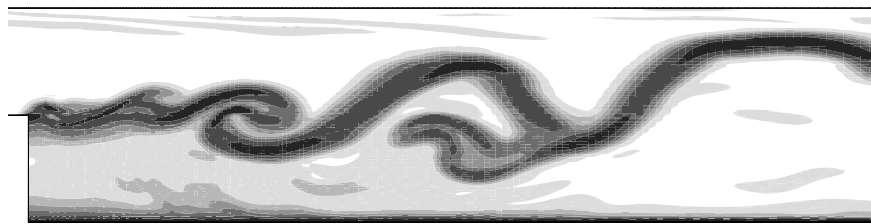


Figure: 7.9 Backward facing flame Temperature (T) and progress variable(c) variation, (— : LES, ○ : Experimental data [258])

7.1 Thickened Flame Model Performance



(a) Schlieren photograph from [258]



(b) Shadow intensity from LES results (magnitude of density gradient)

Figure: 7.10 Schlieren photograph and density differential from LES results

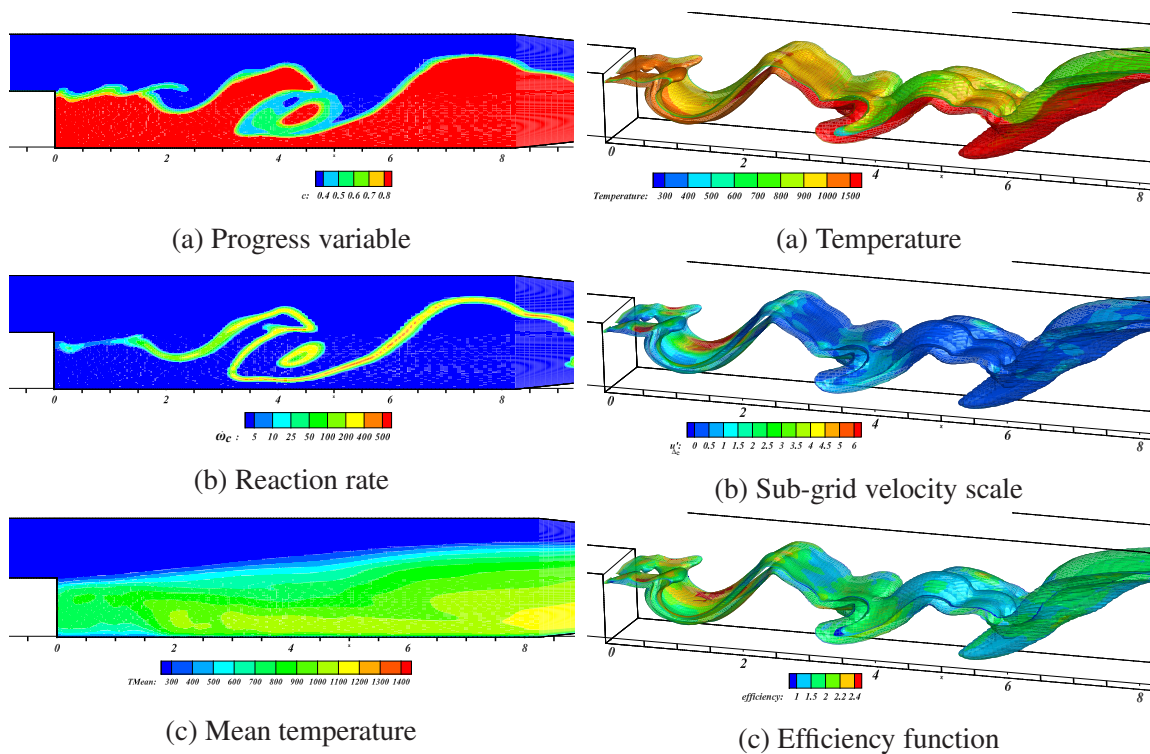


Figure: 7.11 Scalar contours on $z = 0$ plane for the backward facing step test

Figure: 7.12 Scalar mapped on to iso-contour of Reaction rate $\dot{\omega}_c = 20$

7.2 Flamelet Generated Manifold test cases

In this section, FGM model is tested using a canonical two-dimensional test case, and the experimental configuration of Cambridge Swirl burner for premixed/partially premixed flames. The objective is to test the FGM model implementation by Kröger [234] and to investigate the possibility of extending the implementation towards a combined FGM and Artificially thickened flame model.

7.2.1 2D Burner Stabilized Flame

The two-dimensional laminar burner stabilized flame has been used to compare the FGM results with detail chemistry analysis to evaluate the FGM model performance [259], and to compare the model implementation among different software [260]. The test burner in consideration was fed with a Methane air mixture of $\phi = 0.9$, and the burner geometry is shown in Figure: 7.13 where a portion of the symmetrical burner is shown. In numerical simulations inlet of the burner was placed $5mm$ away from the burner step, and a parabolic inlet velocity profile with a maximum velocity $U = 1.0m/s$ was provided. The burner walls were simulated at a constant temperature with $T_{wall} = 300K$. In burner stabilized flames, the flame is stabilized by the heat loss through wall and radiation effects for sooting flames. This test case that has been studied in previous literature as a laminar combustion of methane-air flame, however, the solver used in this work is a turbulent flow solver which contains eddy viscosity, and eddy diffusivity of other scalars resulting from turbulence model. Because the inflow introduces no velocity fluctuations and the velocities associated are smaller to introduce any significant effect from the eddy viscosity and eddy diffusivities, results from the turbulent flow solver were comparable with the results from literature where direct chemical simulations have been conducted with a laminar flow solver [259].

In Figure: 7.14 the progress variable source term variation with the progress variable is shown for a single flamelet. For adiabatic and fully premixed mixture a single flamelet is sufficient to describe the lower dimensional manifold. Non-adiabatic FGM laminar flamelets were generated with varying initial temperatures. In Figure: 7.15 the temperature manifold and progress variable source term manifold are shown against initial mixture enthalpy and progress variable (calculated from CO_2 mixture fraction). In this work, laminar flamelets were calculated using GRI-3.0 mechanism, and unity Lewis number assumption was used to solve 1D equations for a free propagating flame. Changing the initial temperature was required for non-adiabatic flamelet generation, and for this purpose starting from an adiabatic flame the enthalpy was changed until the flame extinguished and unable to achieve a solution. Flamelet solution fails when equilibrium temperature is very low, therefore to

7.2 Flamelet Generated Manifold test cases

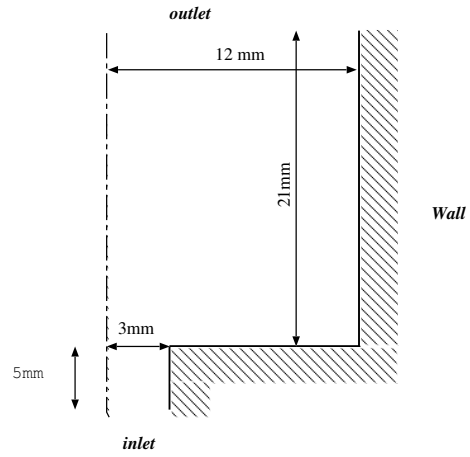


Figure: 7.13 2D burner stabilized flame test - geometry

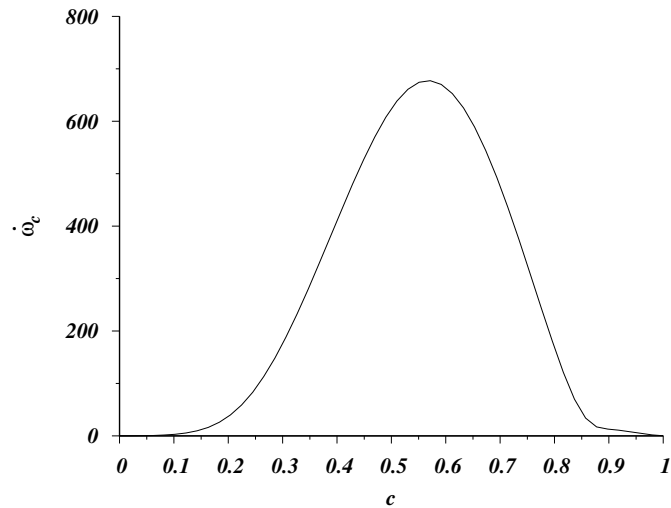


Figure: 7.14 Progress variable source term ($\dot{\omega}_c$) variation with progress variable (c) calculated from Y_{CO_2}

7.2 Flamelet Generated Manifold test cases

avoid these problems when initial temperature is less than 280K, a small amount of fuel is converted to products while keeping the mixture fraction constant. Figure: 7.15a shows that the magnitude of progress variable source term increases with the increase of progress variable as a result of reaction progress, simultaneously at the higher enthalpy region where fuel conversion has not started yet shows negligible progress variable source term magnitude which illustrates the cold flow behaviour. Similarly, at the other end when enthalpy is lowered similar to a burnt mixture the source term increases, however, the solution cease to exist quickly as enthalpy is lowered beyond $h = -1.2 \times 10^6 \text{ J/kg}$. Figure: 7.15b shows the temperature manifold against enthalpy and progress variable, and shows that at larger enthalpies which is cold flow unburned mixture, the temperature remains at initial mixture temperature as no reaction occurs. As enthalpy is reduced which is closer to fully burned mixture, the temperature can be seen to increase to the burn gas temperature. These lower dimensional manifolds are later read and integrated to generate assuming a $\beta - PDF$ distribution of integrated look-up table.

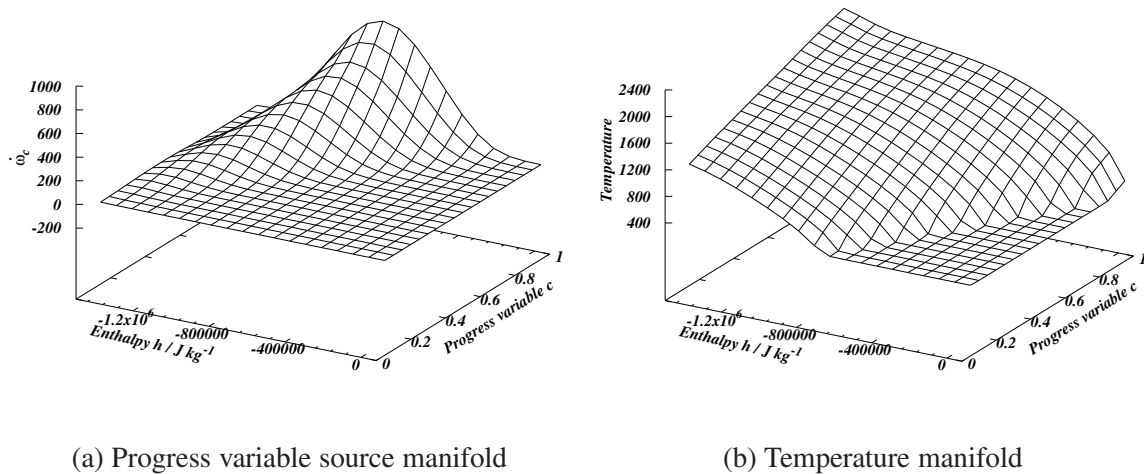


Figure: 7.15 Flamelet Generated Manifolds for $\text{CH}_4 - \text{Air}$ mixture with $\phi = 0.9$ for different initial temperatures

Figure: 7.16, shows a comparison between FGM results and two different detail chemistry results for the same problem used to compare the FGM model performance. In Figure: 7.16a results of the detail chemistry analysis by Van Oijen [139] are used to compare the temperature profiles. It can be seen that in general, the temperature profiles agree well, even though the analysis by Oijen was conducted by considering the differential diffusion of species and a different chemical kinetic mechanism (their work used Smooke mechanism [261]). However, the detail chemistry analysis showed little temperature diffusion while

7.2 Flamelet Generated Manifold test cases

FGM results showed more temperature diffusion thus produced a thicker reaction zone. This thicker high-temperature zone in FGM results may have been primarily caused because of the turbulence solver that spatially averaged the results, but the detail chemistry analysis was performed on a laminar flow solver. It can be seen that the maximum temperature profile location is predicted accurately by FGM results; therefore the flame height is also in good agreement with the detail chemical analysis results. Therefore, from these results, it can be confirmed that the implementation of FGM produced reliable results in solving the enthalpy transport equation and reaction progress variable equation. Furthermore, detail chemistry results show that close to the constant temperature wall the temperature iso-contours vary parallel to the wall, but in FGM results these contour lines come into contact with the wall surface. However, this difference is predominantly caused by an interpolation error because of the insufficient grid resolution near the wall. Figure: 7.16b shows a similar comparison between FGM results and detail chemistry simulation conducted using *reactingFoam* solver which employs the unity Lewis number approximation. The magnitude of CO_2 mass fraction is accurately predicted by the FGM method, however in the detail chemistry simulation by *reactingFoam* solver showed increased production of CO_2 in the high-temperature end of the reaction zone. However, CO_2 mass fraction prediction also shows reasonable agreement considering that two solvers used different approaches in the calculation of thermophysical and thermochemical properties.

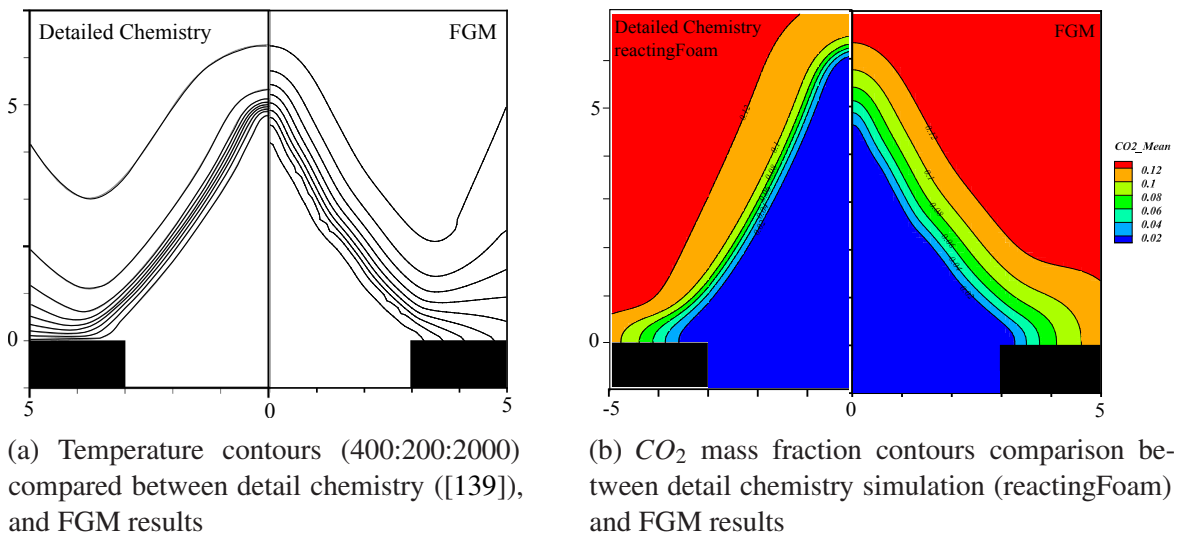


Figure: 7.16 Burner stabilized flame results validation

7.2.2 Cambridge Stratified Burner

Cambridge stratified burner provides experimental data for premixed/partially premixed flames with swirl/non-swirling flow conditions [262]. These experimental data have been used in numerical modelling endeavours in the literature using combined ATF-FGM methods [144] and PDF transport equation method [263]. In this section numerical simulations of the non-swirling flow premixed flame test case SwB1 and stratified test cases SwB5, SwB9 using FGM method are presented and discussed. Non swirling tests were selected for this thesis work because the swirling flow modelling requires additional computational resources to resolve the swirl flow.

Experimental details

Figure: 7.17 shows a cross-sectional view of the burner, in which a central bluff body is surrounded by an inner and outer annular, that feeds two air-fuel mixtures with two equivalence ratios ϕ_i and ϕ_o respectively. The burner is contained in a larger cylindrical container with 382mm that provides a co-flow air stream (U_{co}) to avoid entrainment. Velocity measurements were performed using LDA and two-dimensional PIV methods, and for comparison with numerical simulation data, PIV measurements were used. Measurements errors associated with PIV data for mean velocities and RMS components were 1.2% and 3.1% respectively. The temperature was measured using Rayleigh scattering with 2% error margin, and major species were measured using the simultaneous cross planar *OH* – *PLIF* technique with error margin less than 10%. According to these inlet flow parameters, the inner annulus flow was a turbulent flow of $Re_i = 5960$, and the outer flow measured a Reynolds number of $Re_o = 11500$.

Table: 7.2 shows the operating conditions for the test cases used in this section and inner annular flow and outer annular flow is denoted by subscripts *i* and *o* respectively. The mixing layer was defined as the locus of $\phi = 0.5(\phi_i + \phi_o) = 0.75$, and flame brush was defined as the locus of peak RMS fluctuation of temperature. Flames were categorized as lean flames because the region of interest (the mixing layer) always operated under lean conditions for all three experimental test cases. In addition according to the turbulence statistics measured at the intersection point of mean flame brush and layer, non-dimensional flame numbers were calculated as $Da = 0.17$, $Ka = 1165$, $u'/S_l = 17.6$, $l_t/\delta_l = 2$. According to these turbulent flame statistics, the flame can be placed in the thin reaction zone (Figure: 7.1).

7.2 Flamelet Generated Manifold test cases

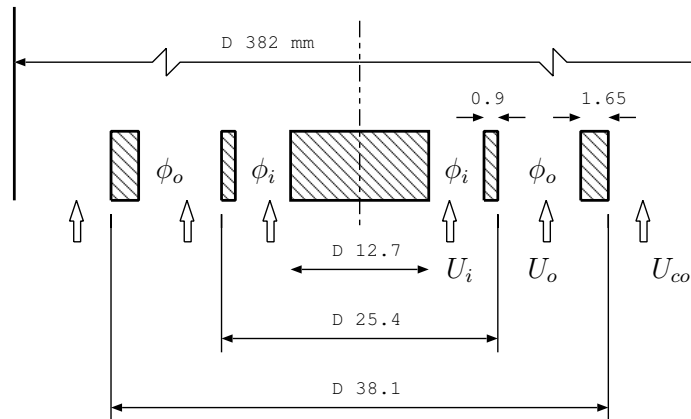


Figure: 7.17 Cambridge stratified burner geometry

Table 7.2 Boundary conditions of Cambridge stratified burner test cases

	ϕ_i	ϕ_o	Z_i	Z_o	$U_i/(ms^{-1})$	$U_o/(ms^{-1})$	$U_{co}/(ms^{-1})$
SwB1	0.750	0.750	0.041	0.041	8.31	18.7	0.4
SwB5	1.000	0.500	0.054	0.060	8.31	18.7	0.4
SwB9	1.125	0.375	0.038	0.021	8.31	18.7	0.4

Numerical Setup

A simplified computational geometry with a domain outer radius of $140mm$ was used for this study. To obtain proper inlet velocity, pre-calculated velocity profiles were imposed on the inlet boundaries from a priori simulation, and a random number generated fluctuations with turbulence intensities of (3%, 3%, 5%) were assumed for radial, tangential and axial directions. Computational grid consisted of 75000 hexagonal grids with the gradual increase in cell size in radial and axial directions. Outlet boundary was placed $200mm$ away from the inlet to reduce the computational memory consumption, and no-reflective pressure boundary condition was specified. Locally dynamic Smagorinsky model was used for turbulence modelling. Second order implicit time integration and TVD discretization schemes were used to assure second order spatial and temporal accuracy. Ignition sources were set by changing the local progress variable. LES results were time averaged for $200ms$ and Favre averaged scalar quantities are compared with LES results.

GRI-3.0 chemical mechanism was used to calculate 1D free propagating laminar flamelets for different mixture fractions, and from these flamelets, an adiabatic lower dimensional manifold was assembled by calculating the progress variable from normalized CO_2 mass fraction. Figure: 7.18a shows the chemical source term manifold in mixture fraction and

7.2 Flamelet Generated Manifold test cases

progress variable space, it shows beyond $Z \gtrsim 0.08$ rich flame extinction occurred and $Z \lesssim 0.015$ lean extinction occurred. Further, it shows that when reaction progresses the progress variable source term magnitude increases, and source term magnitude is greater near the stoichiometric mixture fraction ($Z \sim 0.054$). Similarly, Figure: 7.18a shows the temperature manifold and at the lean region (lower mixture fraction) temperature is smaller than in rich region, and with respect to the progress variable, temperature increase as progress variable increases and reaches a plateau towards the fuel-rich end of the mixture fraction space. Production of stable CO_2 is expected to increase with the reaction progress, similarly increase the temperature. Towards the fuel rich end, as the chemical reaction progress very quickly the CO_2 production can be assumed to have reached equilibrium state faster, therefore the chemical source term indicates a steep decline. The temperature manifold reaching a plateau can be explained by following this assumption that when a fuel-rich mixture is reacted adequately the CO_2 production is independent of temperature and vice versa. To calculate turbulent FGM lookup table, the properties are assumed to be varying in a $\beta - PDF$.

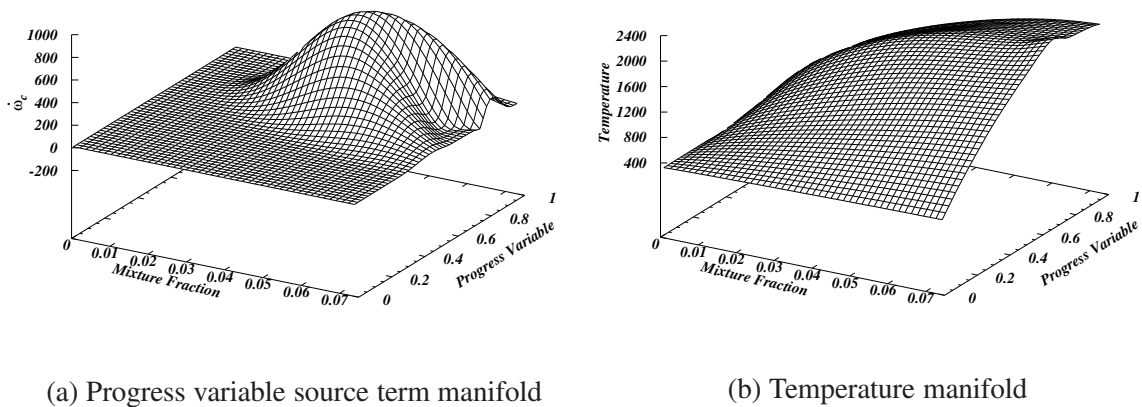


Figure: 7.18 Flamelet Generated Manifold structures for Cambridge stratified burner

Results

The test cases considered in this study are non-swirl flows, and hence only the axial flow velocity component is considered with the understanding that the used mesh resolution was insufficient to resolve radial and tangential velocity component. The fluctuating components results are excluded from the discussion because of the insufficient LES resolution to resolve velocity fluctuations accurately. Moreover, results beyond $50mm$ axial distance are also

7.2 Flamelet Generated Manifold test cases

omitted because the coarse grid induced numerical diffusion that caused erroneous results close to the outlet and circumferential boundary.

Three test cases SwB1, SwB5, SwB9 have similar inlet velocities, but the inner annular equivalence ratio increased in this order while the outer equivalence ratio decreased (Table: 7.2). Therefore, the SwB9 test case has the leanest outer annular flow and the richest inner annular flow, while SwB1 case had equal equivalence ratios for both flows. In Figure: 7.19 mean axial velocity components for the three test cases are compared, and in general LES results show good agreement with experimental velocity measurements at four different axial distances. The negative axial velocity measurements closer to the central axis shows the presence of a weak recirculation zone after the bluff body, and all three test cases show similar negative velocity measurements at $x = 2mm$. Both SwB1 and SwB5 simulations have predicted the negative axial velocity component at the centre of the bluff body, but the SwB9 results only show a nearly stagnant velocity at the central axis. As the SwB9 case had a richer inner annular composition compared to other, it can be considered that the increased heat release caused by this rich mixture might have caused this discrepancy in LES results. Velocity measurements on the central axis (y-axis intercept) at $x = 30mm$ and $x = 50mm$ heights show a gradual increase from SwB1 to SwB5. From that, it can be inferred that as the inner annular flow equivalence ratio increases from $\phi = 0.75$ to $\phi = 1$ the axial flow velocity of the burning zone slightly increases due to increased heat release, and this increase of axial flow velocity is reproduced by LES results. However LES results of SwB9 test case at $x = 50mm$ shows a significant underprediction closer to the central axis. From experimental measurements it can be seen that the SwB1 test case, the one with leanest inner annular flow produces the strongest negative velocity on the central axis, thus the strongest recirculation zone behind the bluff-body. Figure: 7.23d, Figure: 7.23h and Figure: 7.23i show axial velocity contours for three test cases. From velocity contours, it can be seen that the test case with the leanest inner annular flow (SwB1) produced the strongest recirculation zone above the bluff body, and LES results agree with experimental evidence on this phenomenon. It can be seen that even with a coarse grid resolution, the LES results have captured the essential flow dynamics for all three test cases.

Equivalence ratio measurements and LES results for the three test cases are compared in Figure: 7.20, and LES results show good overall agreement with experimental data. However, in all three test cases, equivalence ratio measurements in the recirculation zone ($r \lesssim 10mm$) are greater than both LES results and inlet boundary conditions, and this phenomenon is known to have been caused by differential species diffusion and bulk transport. It was hypothesised and experimentally supported [264] that H_2 and H_2O exhibit preferential diffusion in the direction of reactants and CO_2 in the direction of products, causing a

7.2 Flamelet Generated Manifold test cases

relatively lesser weight hydrogen atoms in reactants side compared to carbon atoms. Experimental determination of the equivalence ratio was done by using the Eqn: 7.4, which is the ratio of, the local demand of oxygen atoms (for the complete combustion of C and H atoms) to the local availability of oxygen. Therefore, the increase of C/H atom ratio increases the experimentally determined equivalence ratio in the reactants side. Furthermore, the recirculation zone aggravates this preferential diffusion effect causing to increase the equivalence ratio in the reactant recirculation zone. However, in the numerical simulation mixture fraction is solved and then converted to equivalence ratio using Eqn: 7.5. Since LES calculations used the equal species diffusivity assumption, numerical results exhibit under predicted equivalence ratio values in the reactants, especially in the recirculation zone.

$$\phi = \frac{X_{CO_2} + 2X_{CH_4} + X_{CO} + 0.5(X_{H_2O} + X_{H_2})}{X_{CO_2} + X_{O_2} + 0.5(X_{CO} + X_{H_2O})} \quad (7.4)$$

$$\phi = \frac{\frac{Z}{1-Z}}{\frac{Z_{st}}{1-Z_{st}}}, Z_{st} = 0.054 \quad (7.5)$$

Apart from the above difference, the LES results predict the time mean mixture fraction field accurately including the decay rate. Figure: 7.23a, Figure: 7.23e and Figure: 7.23i show equivalence ratio contours calculated using LES, and it can be seen that the test case SwB1 shows the least equivalence ratio stratification because both inlets had similar equivalence ratios, while SwB9 test case shows the greatest stratification. Therefore, from above evidence, it can be concluded that the mixture fraction field has been sufficiently represented by LES results regardless of the discrepancy in the recirculating zone.

Figure: 7.21 shows mean temperature predictions compared against experimental measurements, and for all three test cases, numerical results agreed very well with experimental measurements. Near the central axis where equivalence ratio is closer to unity, the temperature is greater and then gradually decays radially, and the decay rate is also accurately predicted for almost all three test cases. Only in the test SwB9, the maximum temperature is significantly overpredicted by LES results, and this can be explained by the experimental evidence of the local increase of equivalence ratio over $\phi = 1$ caused by preferential diffusion in the recirculation zone. Since the maximum temperature occurs at a slightly rich mixture a marginal increase of fuel mass fraction due to preferential diffusion results in an appreciable increase in temperature that cannot be reproduced using a unity Lewis number based mixture fraction transport equation based method. The temperature contours shown in Figure: 7.23b, Figure: 7.23f and Figure: 7.23j illustrate that high-temperature zone is nar-

rowest in the SwB1 test case and widest in the SwB9 test case. Therefore it can be inferred that the rich inner annular flow resulted in a more broader reacting zone and the effect of outer annular equivalence ratio has lesser influence over the reaction zone distribution.

In Figure: 7.22 the Favre averaged CO_2 mass fraction (\tilde{Y}_{CO_2}) is compared against experimental data, and it shows that for SwB1 test case the maximum mass fraction is underpredicted by LES results. The test case SwB5 case results show that the peak CO_2 concentration is accurately predicted by LES results. In SwB9 and SwB1 cases, the peak CO_2 concentration is underpredicted. It should be noted that in this work CO_2 mass fraction is used to calculate the progress variable. Therefore the underprediction of Y_{CO_2} can be explained as a result of lower reaction progress compared to experimental data, and vice versa. As a result, the need for a different linear combination of species to calculate progress variable is seen. However, the CO_2 mass fraction variation showed good qualitative overall agreement with experimental measurements, and Figure: 7.23c, Figure: 7.23g and Figure: 7.23k show that CO_2 mass fraction distribution is widest in the SwB5 test case and narrowest in the leanest mixture case SwB1. The instantaneous reaction progress variable source term which was looked up from the pre-computed table considering that $\dot{\omega}_c = \dot{Y}_{CO_2}$ is shown in Figure: 7.24. It shows that SwB9 test case, the test case with fuel richest inner annular flow, showed the greatest source term magnitude and the test case with the leanest inner annular flow SwB1 showed the smallest progress variable source term. Further SwB1 test case showed a narrower reaction zone compared to SwB5 and SwB9, and the SwB9 test case especially showed an extended reaction zone as it can be expected from a fuel rich inlet and more stratified mixture fraction field.

Therefore, it can be concluded that the FGM model captures the essential reacting flow variables for the stratified flame test cases. Improved results can be expected from a higher grid resolution numerical computation that would produce better agreement with second order statistics.

7.3 Chapter Summary

In this chapter two premixed combustion modelling approaches were tested using canonical problems and experimental configurations. The dynamically thickened flame model was only used for purely premixed homogeneous mixtures, and the FGM model was used in a purely premixed test case as well as a partially-premixed test case. The dynamic thickened flame model obtained very good results for the turbulent flame kernel growth speed and turbulent flame in a mixing layer formed behind a rearward facing step flow. The thickened flame model showed the ability to predict effects of turbulence on the increase

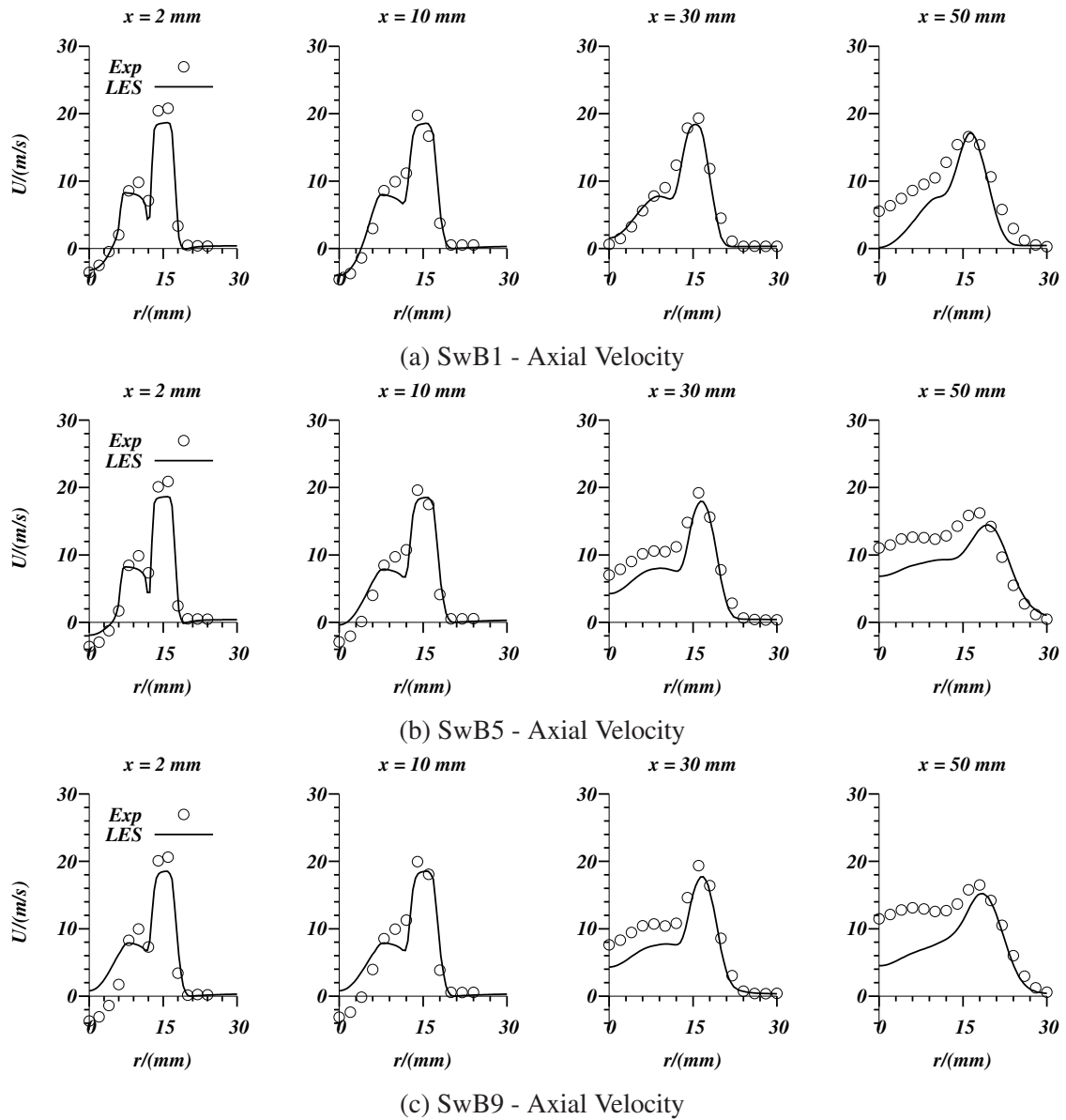
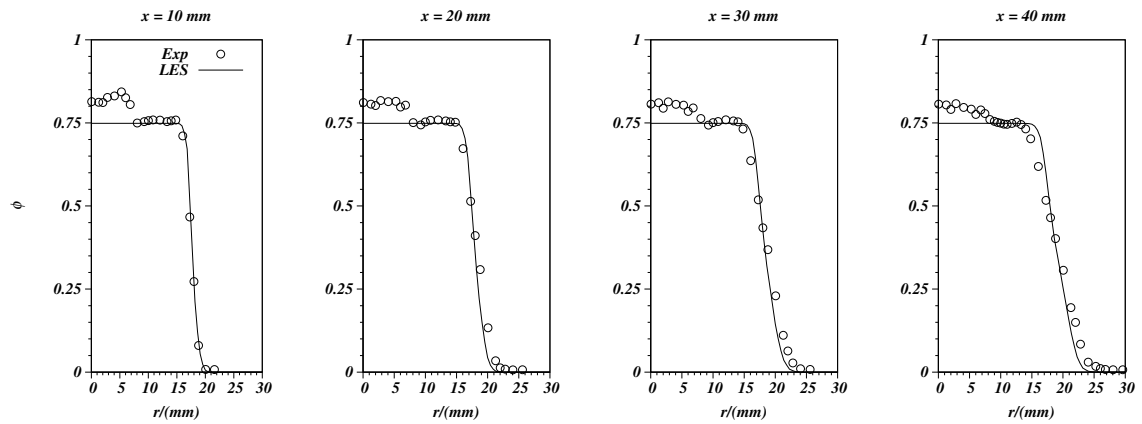
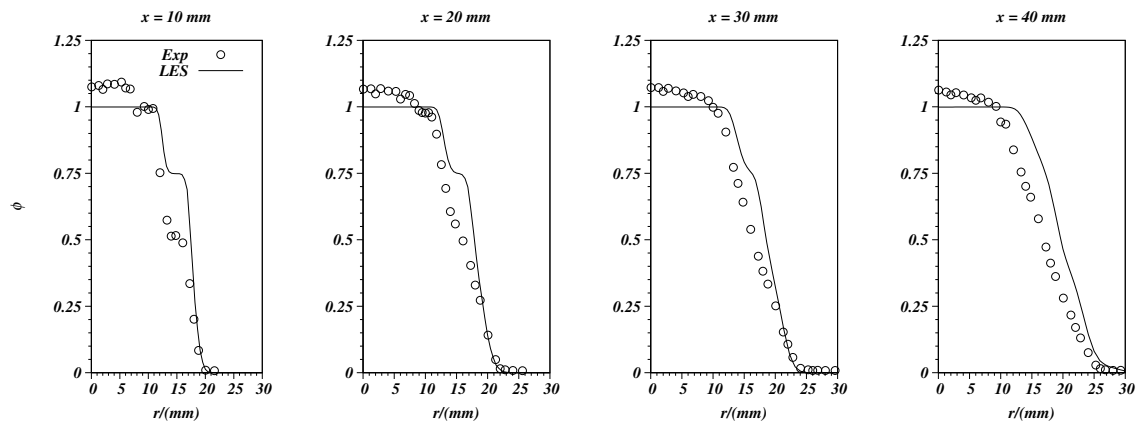


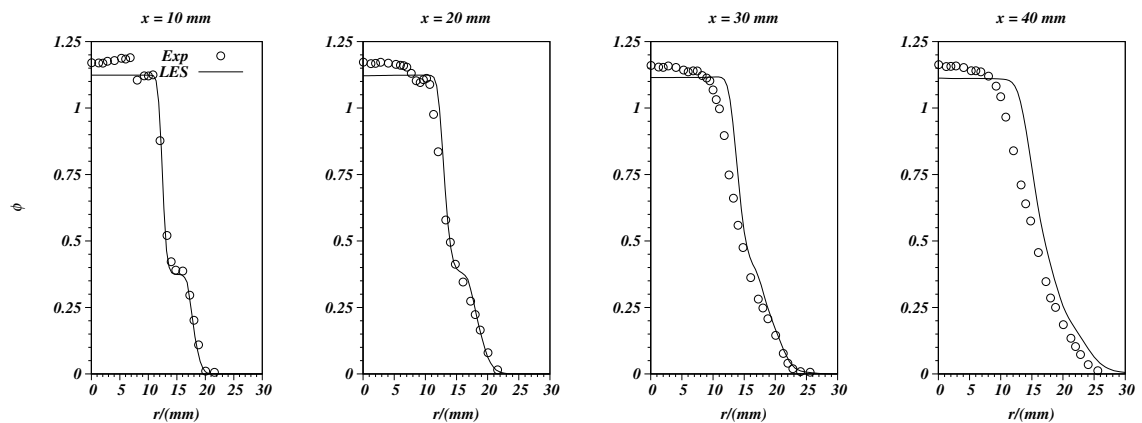
Figure: 7.19 Mean Axial velocity variation of the Cambridge stratified flames (Experimental data : [262]).



(a) SwB1 - Equivalence ratio

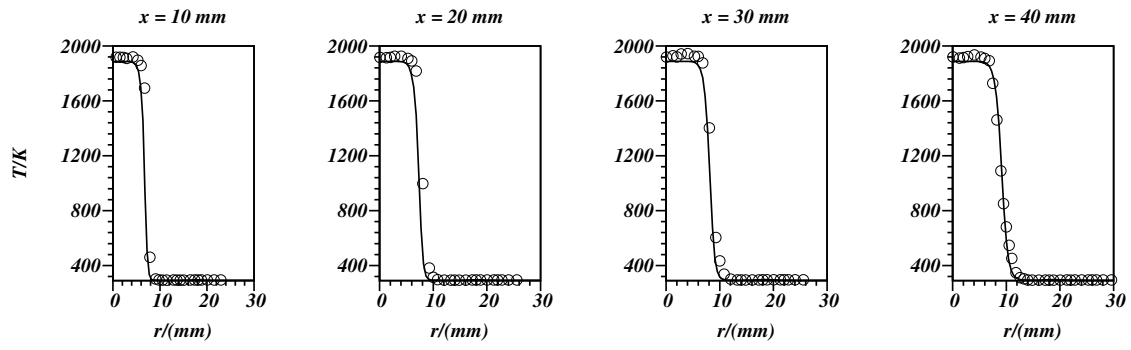


(b) SwB5 - Equivalence ratio

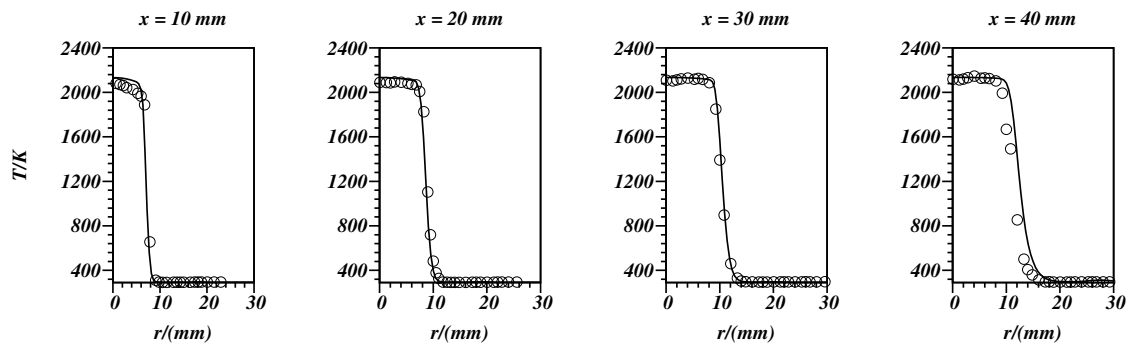


(c) SwB9 - Equivalence ratio

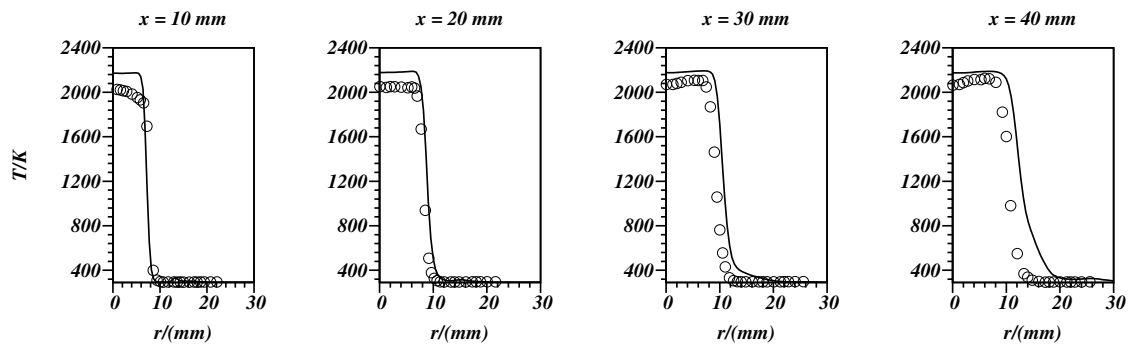
Figure: 7.20 Equivalence ratio ϕ distribution of the Cambridge stratified flames (Experimental data : [262]).



(a) SwB1 - Mean Temperature



(b) SwB5 - Mean Temperature



(c) SwB9 - Mean Temperature

Figure: 7.21 Temperature distribution of the Cambridge stratified flames

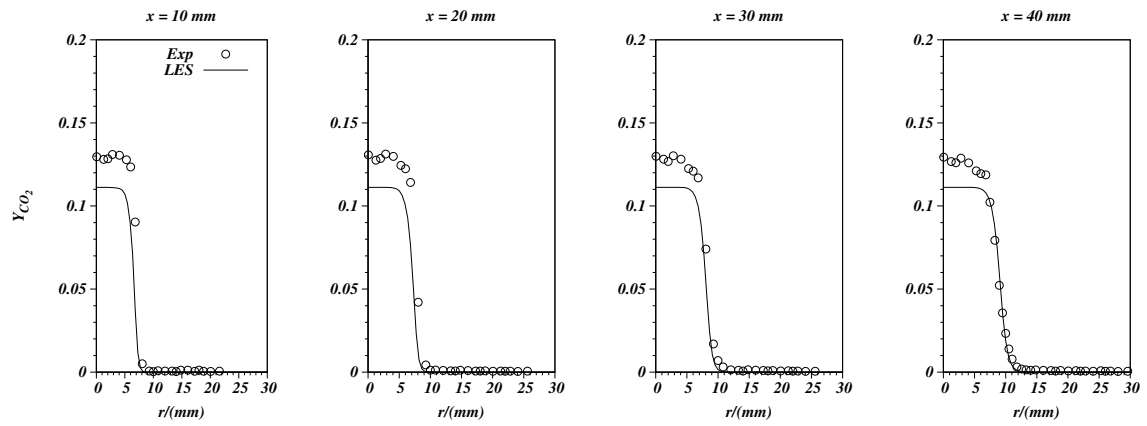
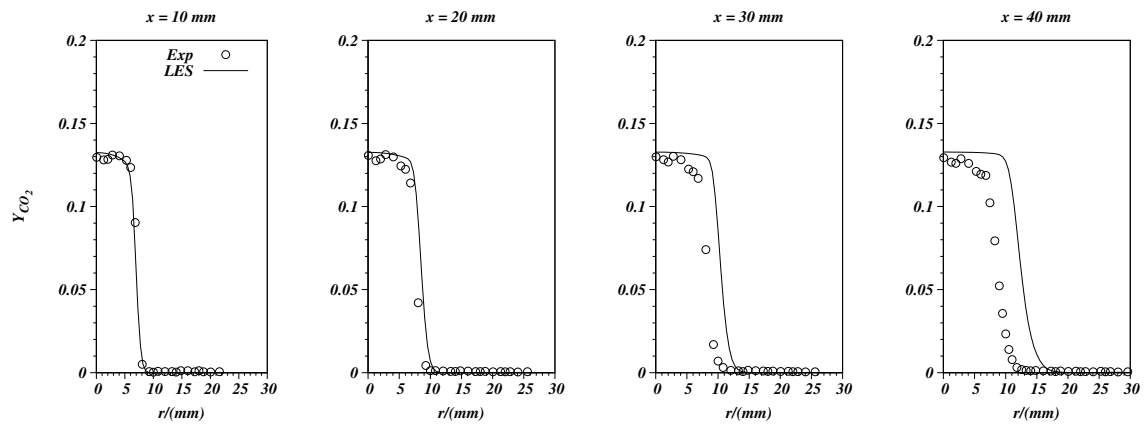
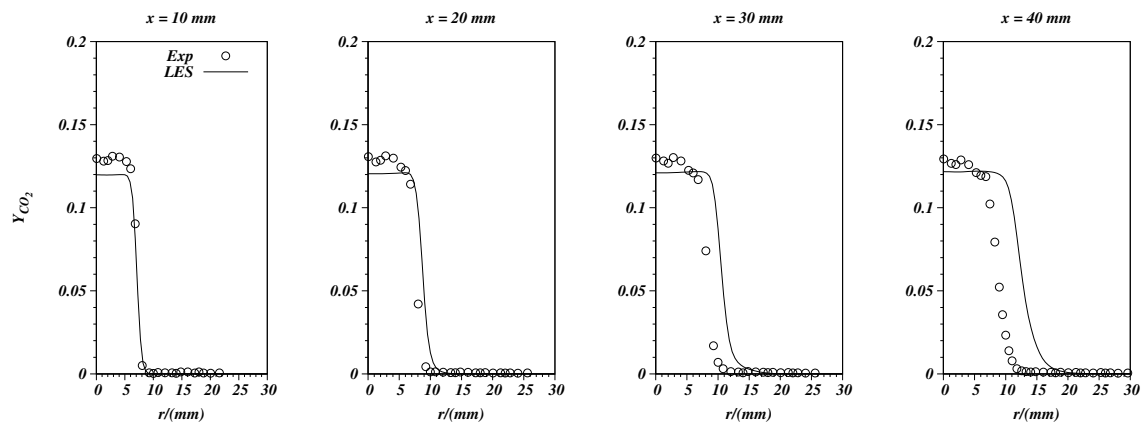
(a) SwB1 - \tilde{Y}_{CO_2} (b) SwB5 - \tilde{Y}_{CO_2} (c) SwB9 - \tilde{Y}_{CO_2}

Figure: 7.22 CO_2 Mass fraction variation of the Cambridge stratified flames (Experimental data : [262]).

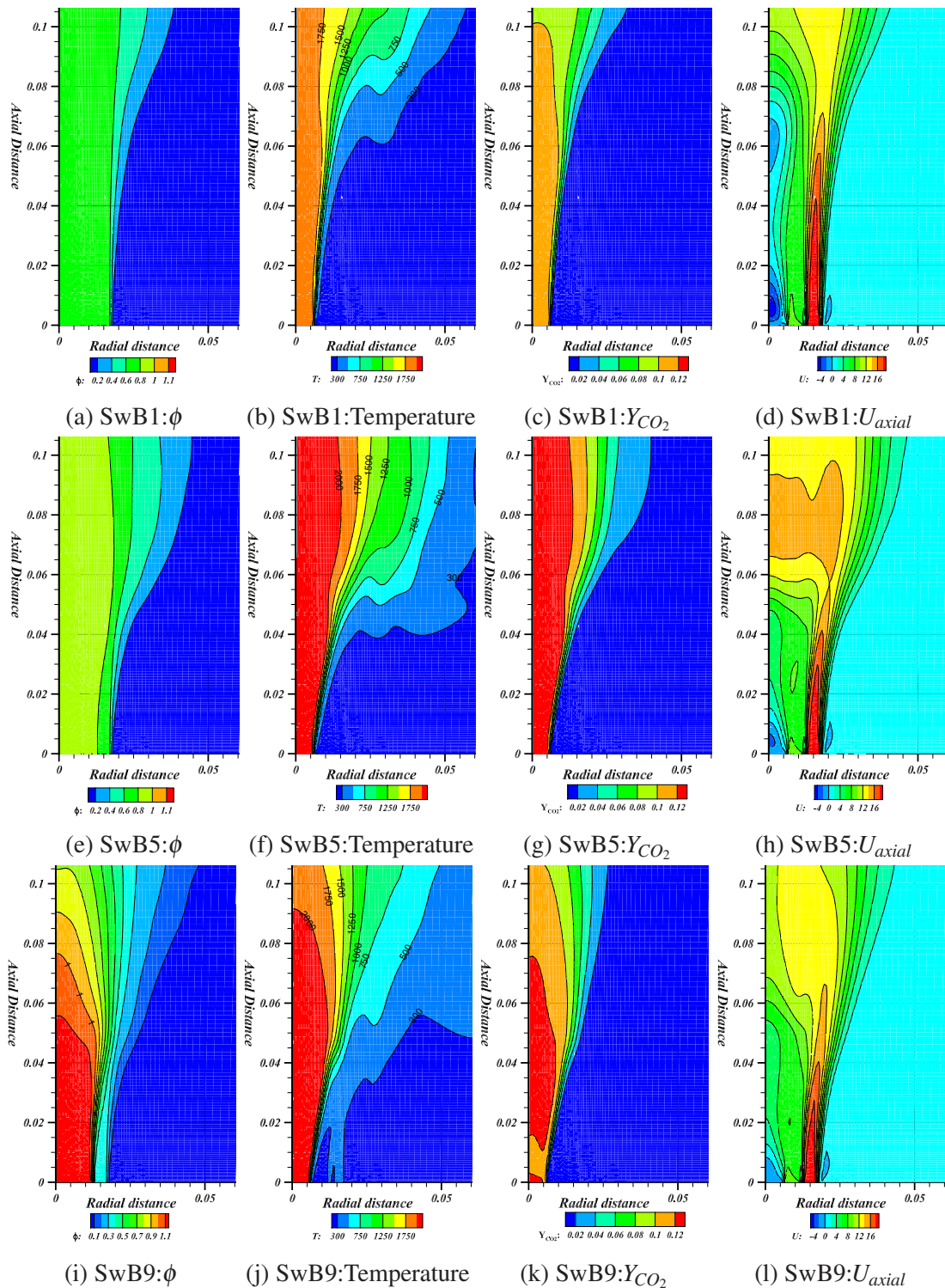


Figure: 7.23 Scalar and axial velocity contours for Cambridge stratified burner test cases.

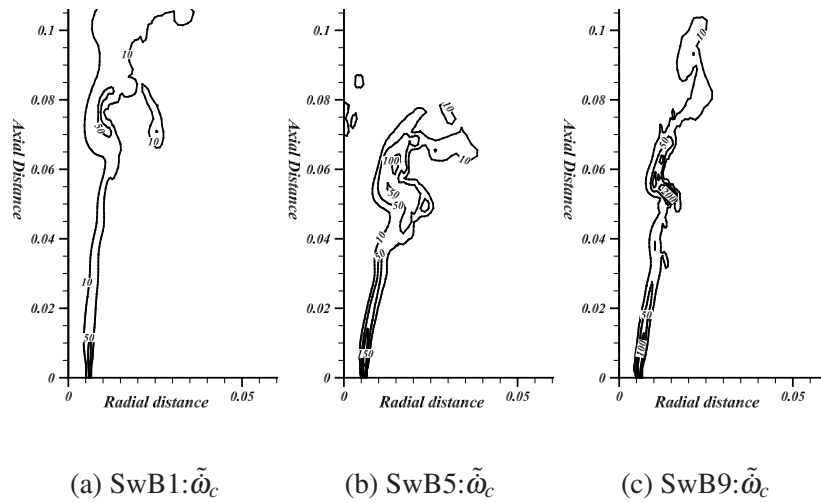


Figure: 7.24 Looked up progress variable source term $\tilde{\omega}_c$

of flame speed and the good results were obtained in the prediction of temperature field of the rearward mixing layer stabilised flame. Moreover, a solution of a reaction progress variable equation using a single step chemical reaction scheme, achieved good agreement between numerical predictions and experimental data for temperature and major species CO_2 prediction in the test case of flame behind the backwards-facing step. FGM model was tested using a canonical 2D test case and obtained comparable results with a detail chemical analysis. The Cambridge stratified burner was modelled using FGM model, and good agreement between numerical and experimental data were obtained. However, the effects of preferential diffusion of species were noticed experimentally; therefore the unity Lewis number based flamelet model appears unable to reproduce these effects in the recirculation zone. Further implementation and testing work is required to combine Flamelet Generated Manifold and dynamically thickened flame model and can be used to improve the turbulence premixed/partially premixed flame modelling using laminar flamelet based chemical reduction methods.

Chapter 8

Conclusion and Future Work

In this study, advanced turbulence and combustion modelling abilities are investigated for the modelling of air-fuel mixing and turbulent reacting flows which are the main contributory processes of stationary gas turbine combustion. Computational tools were developed and modified to model canonical problems of air-fuel mixing and reacting flows related to the gas turbine combustion process. However, the combustion process analysis was performed in an uncoupled manner, where the air-fuel mixing process and the combustion modelling methods were addressed separately. The developed tools and methods in this research can be used in a future study to numerically investigate the combined effects of air-fuel mixing on gas turbine combustion performance. In the following two sections the conclusions and future work related to air-fuel mixing and combustion modelling are discussed.

8.1 Jet in Cross-Flow modelling

Jet in Cross-Flow (JICF) mixing arrangement was identified as a more common method of achieving uniform air-fuel mixtures in stationary gas turbines. However, from the previous numerical and experimental modelling of JICF, a shortcoming of scalar mixing studies was identified, and in this thesis numerical simulations were performed and compared with comprehensive scalar mixing data. Numerical simulations of the turbulent jet in cross-flow were carried out using the RANS simulation technique in two software platforms STAR-CCM+, and OpenFOAM. Both CFD codes produced comparable results for mean momentum field and scalar field in RANS approach that agreed with comprehensive experimental data. Three RANS models namely the realizable $k - \epsilon$, $k - \omega$ -Shear Stress Transport (SST) and Launder-Gibson Reynolds Stress Transport Model (RSTM). However, the Reynolds stress components were underpredicted by all RANS models investigated in this work, and the Launder-Gibson RSTM showed severe Reynolds stress underprediction in both codes.

STAR-CCM+ simulations were conducted with an adaptive mesh refinement method to reduce mesh count, but OpenFOAM simulations were conducted on a hexahedral grid without adaptive mesh refinement. The two-equation models, realizable $k - \varepsilon$ and $k - \omega$ -SST model showed similar results in OpenFOAM context, but in STAR-CCM+ the realizable $k - \varepsilon$ model showed better agreement with experimental data in predicting mean velocity field. In scalar field modelling also realizable $k - \varepsilon$ model showed marginally better results than other two models. Although scalar mixing field results showed minor dependency on turbulent Schmidt number value between $Sc_t = 0.7 - 0.9$ was found to exhibit better agreement with experimental data. Therefore, in conclusion, the RANS modelling using the two-equation turbulence models showed better agreement than the Reynolds stress transport model. The realizable $k - \varepsilon$ model showed better agreement in mean velocity field and scalar field predictions with experimental data than other two models. Considering the performance of two-equation RANS models, the OpenFOAM code produced more consistent results from both models than STAR-CCM+. STAR-CCM+ simulations were performed using local mesh refinement. However, OpenFOAM simulations were performed in a hexahedral grid without local refinement, therefore in a future study, the local mesh refinement option of OpenFOAM can also be used to reduce the computational overload.

LES simulations of a jet in cross-flow mixing were performed using the OpenFOAM platform only, and the use of parallel computational facilities proved essential to carry out high-resolution LES computations. Several SGS models namely the dynamic Smagorinsky model (DSM), dynamic mixed model (DMM), and a dynamic one equation model (subgrid turbulent energy transport equation) were tested in this work. Previous numerical modelling work of JICF found in literature has been mostly limited to only Smagorinsky SGS model-based approach. The LES of the jet in cross-flow using different dynamic SGS models resulted in virtually indistinguishable results which agreed excellently with experimental data for both mean-field statistics and Reynolds stress component predictions. However, LES results showed significant improvement over the RANS simulation method in predicting Reynolds stress components. LES results also showed better agreement in scalar mixing field results when compared to RANS results. The LES results captured the coherent structures present in the near field jet cross-flow interaction zone. The LES method was successfully extended to model a twin-jet in cross-flow mixing application and obtained good agreement with limited experimental velocity measurements available. Twin-jet interaction revealed important information about the counter-rotating vortex pair interaction and the study showed that numerical simulations could be used to improve the air-fuel mixing arrangements. The study showed the LES simulation method using the dynamic Smagorinsky model could be successfully used for modelling multiple jet interactions in cross-flow

mixing applications with complicated geometries in future work. Twin jets were fed with passive scalar to observe the scalar mixing field and the passive scalar distribution also showed the effect of the vortex-pair merging. In a future experimental study, the distance of the vortex pair merging can be validated and will become useful in the design of air-fuel mixing arrangements with arrays of fuel nozzles. The LES simulations using OpenFOAM were carried out on block-structured grids, but to extend these methods into industrial mixing arrangements the use of unstructured grids with low dissipative numerical schemes for LES simulations should be investigated in future works. Furthermore, more realistic air-fuel mixing arrangements like fuel injection into swirling flow or fuel injection from swirl vanes can be studied using the developed methods.

8.2 Reacting flow modelling

Most low emission stationary gas turbines of today are operating under lean premixed combustion mode, however, during the full operational cycle of the gas turbine, other combustion regimes as non-premixed/ partially premixed flames also can be found. In addition, the industries have found increased interest in the inclusion of hydrogen as a fuel to both stabilize flames and to decrease C emissions. In this thesis work, numerical simulations of turbulent combustion in all three combustion regimes, non-premixed, premixed, and partially-premixed were carried out. Since the modelling approach was focused on gas-turbines combustion, the species concentration was an important modelling requirement. Therefore, the laminar flamelet assumption based chemical reduction models were used to model canonical stationary turbulent flames. Adiabatic Steady Laminar Flamelet method was used in modelling of swirl stabilized burner. Modelling of two non-reacting swirl flow test cases of this burner revealed interesting swirl flow dynamics; that contrary to the common understanding of stronger swirl flows create vortex breakdown structures, in this case low swirl strength flow produced bubble type vortex-breakdown structures. It showed that when vortex breakdown in swirl flows surrounding a central jet is considered; the swirl number can not only characterise the existence of vortex structures. Instead, more studies must be done to understand the relationship between swirl strength and central jet momentum and vortex-breakdown. In reacting flow modelling work, the well established steady laminar flamelet method using the *flameletFoam* was used in modelling the diffusion flame of Sydney swirl burner, which used a $CH_4 : H_2$ fuel mixture. The use of this method resulted in good agreement with experimental data for velocity field. Although the scalar field prediction showed reasonable agreement with experimental data, the disparity in mixture fraction field prediction affected other scalar predictions temperature and major species. To improve

these shortcomings of the radially expanding grid used in this study, a fully unstructured grid based computation can be used in a future study. In addition, further investigations are required to describe the reactions of $CH_4 : H_2$ fuel blends rather than using the natural gas based chemical reaction mechanisms.

In premixed/partially-premixed combustion modelling work preliminary work was conducted to develop a combined model of the Artificially Thickened Flame model and Flamelet Generated Manifold model. A thickened flame model was developed with dynamic flame thickening and tested using two test cases. A turbulent flame kernel growth was modelled using this model, and the computational model successfully reproduced the flame kernel growth speed. To validate the modelling of thermochemical properties using this model the flame behind a backwards-facing step was modelled using dynamic Smagorinsky model. The computational result showed excellent agreement in the prediction of velocity, temperature and CO_2 field data. Moreover, the numerically predicted the flow field structure was in very good agreement with experimental results by calculating the reattachment point of the flow behind the backward step to match with experimental measurements. Therefore, the implemented dynamic thickened flame model showed good performance in predicting turbulent flame propagation and thermochemical properties of the flame. Also in future work, the model can be extended in OpenFOAM platform to predict partially premixed combustion by incorporating a model to calculate laminar flame speed as a function of equivalence ratio. The Flamelet Generated Manifold (FGM) model implementation by Kroger [234] was updated to work with recent versions of OpenFOAM and validated in this work. A 2D validation test case showed excellent agreement between FGM model and results and detail chemistry analysis in predicting temperature and other CO_2 mass fraction. The FGM model was successfully used in simulating the Cambridge stratified burner flames. Even though a reasonably coarse grid was used, the numerical results showed very good agreement in velocity field and scalar field predictions. In a future study, the necessary steps to include preferential diffusion of chemical species into FGM modelling can be implemented to improve the scalar field predictions. More importantly in future work, the FGM model and Thickened flame model can be combined to model turbulence-chemistry interaction accurately. In a future study, these computational tools can be extended to model the air-fuel mixing and combustion process in a unified modelling approach.

References

- [1] Tim Lieuwen, Michael Chang, and Alberto Amato. Stationary gas turbine combustion: Technology needs and policy considerations. *Combustion and Flame*, 160(8):1311–1314, 2013.
- [2] World Energy Council. World Energy Resources 2013 Survey. Technical report, World Energy Council, 2013.
- [3] International Energy Agency. *World Energy Outlook 2013*. World Energy Outlook. International energy agency, 2013.
- [4] Paolo Chiesa, Giovanni Lozza, and Luigi Mazzocchi. Using Hydrogen as Gas Turbine Fuel. *Journal of Engineering for Gas Turbines and Power*, 127(1):73, jan 2005.
- [5] Arthur H. (Arthur Henry) Lefebvre and Dilip R. Ballal. *Gas turbine combustion : alternative fuels and emissions*. Taylor & Francis, 2010.
- [6] Suman Muppidi and Krishnan Mahesh. Direct numerical simulation of passive scalar transport in transverse jets. *Journal of Fluid Mechanics*, 598:335–360, 2008.
- [7] L. Y. M. Gicquel, G. Staffelbach, and T. Poinso. Large Eddy Simulations of gaseous flames in gas turbine combustion chambers. *Progress in Energy and Combustion Science*, 38(6):782–817, 2012.
- [8] ASME. The world’s first industrial gas turbine set at Neuchatel (1939), 1988.
- [9] A. H. Lefebvre. *Gas turbine combustion*. Taylor & Francis, New York, N.Y. ; Abingdon, Oxon, 1999.
- [10] Lefebvre H. A. Lean premixed/prevaporized combustion. Technical Report CP-2016, NASA, 1977.
- [11] Thomas Mikus, John B. Heywood, and R. Edward Hicks. *Nitric oxide formation in gas turbine engines: a theoretical and experimental study*, volume 2977. National Aeronautics and Space Administration, Scientific and Technical Information Office, 1978.
- [12] Valerie J. Lyons. Effect of Fuel and Air Ratio Nonuniformity on Emissions of Nitrogen Oxides. Technical Report TP-1798, NASA, 1981.
- [13] Thomas F. Fric. Effects of fuel-air unmixedness on NO(x) emissions. *Journal of Propulsion and Power*, 9(5):708–713, 1993.

-
- [14] J. C. Barnes and A. M. Mellor. Effects of Unmixedness in Piloted-Lean Premixed Gas-Turbine Combustors. *Journal of Propulsion and Power*, 14(6):967–973, nov 1998.
- [15] Hanno Krämer, Friedrich Dinkelacker, Alfred Leipertz, Gerwig Poeschl, Michael Huth, and Martin Lenze. Optimization of the Mixing Quality of a Real Size Gas Turbine Burner With Instantaneous Planar Laser-Induced Fluorescence Imaging. In *Volume 2: Coal, Biomass and Alternative Fuels; Combustion and Fuels; Oil and Gas Applications; Cycle Innovations*, page V002T02A027. ASME, jun 1999.
- [16] S. F. Frey, A. R. Eaton, D. M. Cusano, M. W. Plesniak, and P. E. Sojka. Effect of Inlet Turbulence and Premixer Length on Fuel Distribution in Swirling Gas-Turbine Premixer. *Journal of Propulsion and Power*, 16(5):837–844, 2000.
- [17] R. J. Margason, editor. *Fifty years of jet in cross flow research*. AGARD, November 1993.
- [18] North Atlantic Treaty Organization. Advisory Group for Aerospace Research and Development. Fluid Dynamics Panel. Symposium. *Computational and Experimental Assessment of Jets in Cross Flow*. AGARD conference proceedings. AGARD, 1993.
- [19] J. U. Schlüter and T. Schönfeld. LES of jets in cross flow and its application to a gas turbine burner. *Flow, Turbulence and Combustion*, 65(2):177–203, 2000.
- [20] R. M. Kelso, T. T. Lim, and A. E. Perry. An experimental study of round jets in cross-flow. *Journal of Fluid Mechanics*, 306:111–144, 1996.
- [21] R. M. Kelso and A. J. Smits. Horseshoe vortex systems resulting from the interaction between a laminar boundary layer and a transverse jet. *Physics of Fluids*, 7(1):153–158, 1995.
- [22] J. E. Broadwell and R. E. Breidenthal. Structure and mixing of a transverse jet in incompressible flow. *Journal of Fluid Mechanics*, 148:405–412, 1984.
- [23] Jannis Andreopoulos and Wolfgang Rodi. Experimental investigation of jets in a crossflow. *Journal of Fluid Mechanics*, 138:93–127, 1984.
- [24] L. Cortelezzi and A. R. Karagozian. On the formation of the counter-rotating vortex pair in transverse jets. *Journal of Fluid Mechanics*, 446:347–373, 2001.
- [25] Lester L. Yuan, Robert L. Street, and Joel H. Ferziger. Large-eddy simulations of a round jet in crossflow. *Journal of Fluid Mechanics*, 379:71–104, jan 1999.
- [26] J. F. Keffer and W. D. Baines. The round turbulent jet in a cross-wind. *Journal of Fluid Mechanics*, 15(4):481–496, 1963.
- [27] James W Ramsey and Richard J Goldstein. Interaction of a heated jet with a deflecting stream. *Journal of Heat Transfer*, 93(4):365–372, 1971.
- [28] Yasuhiro Kamotani and Isaac Greber. Experiments on a Turbulent Jet in a Cross Flow. *AIAA Journal*, 10(11):1425–1429, 1972.

-
- [29] D. Crabb, D. F. G. Durao, and J. H. Whitelaw. A round jet normal to a crossflow. *Journal of Fluids Engineering*, 103(1):142–153, 1981.
- [30] S. H. Smith, A. Lozano, M. G. Mungal, and R. K. Hanson. Scalar mixing in the subsonic jet in crossflow. In *In AGARD, Computational and Experimental Assessment of Jets in Cross Flow 13 p (SEE N94-28003 07-34)*, volume 1, 1993.
- [31] S. H. Smith and M. G. Mungal. Mixing, structure and scaling of the jet in crossflow. *Journal of fluid mechanics*, 357:83–122, 1998.
- [32] Shridhar Gopalan, Bruce M Abraham, and Joseph Katz. The structure of a jet in cross flow at low velocity ratios. *Physics of fluids*, 16(6):2067–2087, 2004.
- [33] L. K. Su and M. G. Mungal. Simultaneous measurements of scalar and velocity field evolution in turbulent crossflowing jets. *Journal of Fluid Mechanics*, 513:1–45, aug 2004.
- [34] N. Toy, E. Savory, S. McCusker, and P. J. Disimile. The interaction region associated with twin jets and a normal crossflow. In *AGARD, Computational and Experimental Assessment of Jets in Cross Flow 11 p (SEE N94-28003 07-34)*, pages No CP–534. AGARD, November 1993.
- [35] V.S. Naik-Nimbalkar, A.D. Suryawanshi, A.W. Patwardhan, I. Banerjee, G. Padmakumar, and G. Vaidyanathan. Twin jets in cross-flow. *Chemical Engineering Science*, 66(12):2616–2626, jun 2011.
- [36] Camilo Cárdenas, Rainer Suntz, Jordan A Denev, and Henning Bockhorn. Two-dimensional estimation of reynolds-fluxes and-stresses in a jet-in-crossflow arrangement by simultaneous 2d-lif and piv. *Applied physics B*, 88(4):581–591, 2007.
- [37] Flavio Cesar Cunha Galeazzo, Richard J Valdes, Werner Krebs, Georg Donnert, Peter Habisreuther, and Nikolaos Zarzalis. Measurement and Simulation of Turbulent Mixing in a Jet in Crossflow. *Journal of Engineering for Gas Turbines and Power*, 133(6):61504, 2011.
- [38] Flavio Cesar Cunha Galeazzo. *Simulation of turbulent flows with and without combustion with emphasis on the impact of coherent structures on the turbulent mixing*. PhD thesis, Kalsruher Institute of Technology, 2013.
- [39] Camilo Cárdenas, Julia Sedlmaier, Nikolaos Zarzalis, Richard J. Valdes, and Werner Krebs. Measurement of a Benchmarking Jet in Crossflow Configuration Under Highly Turbulent Conditions. In *Volume 3: Controls, Diagnostics and Instrumentation; Education; Electric Power; Microturbines and Small Turbomachinery; Solar Brayton and Rankine Cycle*, pages 51–60. ASME, 2011.
- [40] Elizaveta Ivanova, Berthold Noll, and Manfred Aigner. Unsteady Simulations of Turbulent Mixing in Jet in Crossflow. In *40th Fluid Dynamics Conference and Exhibit, Fluid Dynamics and Co-located Conferences*. American Institute of Aeronautics and Astronautics, 2010.

- [41] Elizaveta M. Ivanova, Berthold E. Noll, and Manfred Aigner. A Numerical Study on the Turbulent Schmidt Numbers in a Jet in Crossflow. *Journal of Engineering for Gas Turbines and Power*, 135(1):011505, nov 2012.
- [42] Flavio Cesar Cunha Galeazzo, Georg Donnert, Camilo Cárdenas, Julia Sedlmaier, Peter Habisreuther, Nikolaos Zarzalis, Christian Beck, and Werner Krebs. Computational modeling of turbulent mixing in a jet in crossflow. *International Journal of Heat and Fluid Flow*, 41:55–65, 2013.
- [43] Edmund E. Callaghan and Robert S. Ruggeri. Investigation of the penetration of an air jet directed perpendicularly to an air stream. Technical Report TN-1615, NASA, 1948.
- [44] S. V. Patankar, D. K. Basu, and S. A. Alpay. Prediction of the three-dimensional velocity field of a deflected turbulent jet. *Journal of Fluids Engineering*, 99(4):758–762, 1977.
- [45] J. Alvarez, W. P. Jones, and R. Seoud. Predictions of momentum and scalar fields in a jet in cross-flow using first and second order turbulence closures. In *In AGARD, Computational and Experimental Assessment of Jets in Cross Flow 10 p (SEE N94-28003 07-34)*, volume 1, 1993.
- [46] B.E. Launder and D.S.A. Samaraweera. Application of a second-moment turbulence closure to heat and mass transport in thin shear flows—I. Two-dimensional transport. *International Journal of Heat and Mass Transfer*, 22(12):1631–1643, 1979.
- [47] W. P. Jones and M. Wille. Large-eddy simulation of a plane jet in a cross-flow. *International Journal of Heat and Fluid Flow*, 17(3):296–306, jun 1996.
- [48] K. S. Chen and J. Y. Hwang. Experimental study on the mixing of one- and dual-line heated jets with a cold crossflow in a confined channel. *AIAA Journal*, 29(3):353–360, March 1991.
- [49] Lester L. Yuan, Robert L. Street, and Joel H. Ferziger. Large-eddy simulations of a round jet in crossflow. *Journal of Fluid Mechanics*, 379:71–104, 1999.
- [50] S. A. Sherif and R. H. Pletcher. Measurements of the Flow and Turbulence Characteristics of Round Jets in Crossflow. *Journal of Fluids Engineering*, 111(2):165, 1989.
- [51] B. Wegner, Y. Huai, and A. Sadiki. Comparative study of turbulent mixing in jet in cross-flow configurations using les. *International Journal of Heat and Fluid Flow*, 25(5):767–775, 2004.
- [52] J. Andreopoulos. Heat transfer measurements in a heated jet-pipe flow issuing into a cold cross stream. *Physics of Fluids*, 26(11):3201, 1983.
- [53] D. K. Lilly. A proposed modification of the Germano subgrid-scale closure method. *Physics of Fluids A: Fluid Dynamics*, 4(3):633, mar 1992.
- [54] Petri Majander and Timo Siikonen. Large-eddy simulation of a round jet in a cross-flow. *International Journal of Heat and Fluid Flow*, 27(3):402–415, 2006.

- [55] M. Salewski, D. Stankovic, and L. Fuchs. Mixing in Circular and Non-circular Jets in Crossflow. *Flow, Turbulence and Combustion*, 80(2):255–283, January 2008.
- [56] J. D. Holdeman, D. S. Liscinsky, V. L. Oechsle, G. S. Samuelson, and C. E. Smith. Mixing of Multiple Jets With a Confined Subsonic Crossflow: Part 1 Cylindrical Duct. *Journal of Engineering for Gas Turbines and Power*, 119(4):852, October 1997.
- [57] D. S. Liscinsky, B. True, and J. D. Holdeman. Crossflow mixing of noncircular jets. *Journal of Propulsion and Power*, 12(2):225–230, March 1996.
- [58] Dalibor Cavar and Knud Erik Meyer. LES of turbulent jet in cross-flow: Part 1 – A numerical validation study. *International Journal of Heat and Fluid Flow*, 36:18–34, 2012.
- [59] Dalibor Cavar and Knud Erik Meyer. LES of turbulent jet in cross flow: Part 2 – POD analysis and identification of coherent structures. *International Journal of Heat and Fluid Flow*, 36:35–46, 2012.
- [60] Oktay Öslash, Zcan, and Poul Scheel Larsen. Laser Doppler anemometry study of a turbulent jet in crossflow. *AIAA Journal*, 41(8):1614–1616, 2003.
- [61] C. Cárdenas, R. Suntz, J.A. Denev, and H. Bockhorn. Two-dimensional estimation of Reynolds-fluxes and -stresses in a Jet-in-Crossflow arrangement by simultaneous 2D-LIF and PIV. *Applied Physics B*, 88(4):581–591, aug 2007.
- [62] Flavio Cesar Cunha Galeazzo, Georg Donnert, Camilo Cárdenas, Julia Sedlmaier, Peter Habisreuther, Nikolaos Zarzalis, Christian Beck, and Werner Krebs. Computational modeling of turbulent mixing in a jet in crossflow. *International Journal of Heat and Fluid Flow*, 41:55–65, 2013.
- [63] E. M. Ivanova, B. E. Noll, and Manfred Aigner. Computational Modeling of Turbulent Mixing of a Transverse Jet. *Journal of Engineering for Gas Turbines and Power*, 133(2):021505, 2011.
- [64] J. A. Denev, J Fröhlich, and H Bockhorn. Evaluation of mixing and chemical reactions within a jet in crossflow by means of LES. In *European Combustion Meeting*, volume c, pages 3–6, 2005.
- [65] C. Prière, 4. Gicquel L.Y.M., P. Kaufmann, W. Krebs, and T. Poinso. Large eddy simulation predictions of mixing enhancement for jets in cross-flows. *Journal of Turbulence*, page N5, 2004.
- [66] Seonghyeon Hahn and Haecheon Choi. Unsteady simulation of jets in a cross flow. *Journal of Computational Physics*, 134(2):342–356, 1997.
- [67] Paul E. Dimotakis. Turbulent Mixing. *Annu. Rev. Fluid Mech*, 37:329–56, 2005.
- [68] R. S. Cant and E. Mastorakos. *An Introduction to Turbulent Reacting Flows*. Imperial College Press, 2008.
- [69] Daniel P. Combest, Palghat A. Ramachandran, and Milorad P. Dudukovic. On the Gradient Diffusion Hypothesis and Passive Scalar Transport in Turbulent Flows. *Industrial & Engineering Chemistry Research*, 50(15):8817–8823, aug 2011.

-
- [70] G. K Batchelor. Diffusion in a field of homogeneous turbulence. *Mathematical Proceedings of the Cambridge Philosophical Society*, 48(02):345–362, 1952.
- [71] Bart J. Daly and Francis H. Harlow. Transport Equations in Turbulence. *Physics of Fluids*, 13(11):2634, 1970.
- [72] Rodney O. Fox. *Computational models for turbulent reacting flows*. Cambridge University Press, 2003.
- [73] A.J. Reynolds. The prediction of turbulent Prandtl and Schmidt numbers. *International Journal of Heat and Mass Transfer*, 18(9):1055–1069, 1975.
- [74] Yanhu Guo, Guangbin He, Andrew Hsu, A. Brankovic, S. Syed, and N.-S. Liu. The development of a variable Schmidt number model for jet-in-crossflows using genetic algorithms. In *37th Aerospace Sciences Meeting and Exhibit*, Reston, Virginia, jan 1999. American Institute of Aeronautics and Astronautics.
- [75] Guangbin He, Yanhu Guo, and Andrew T. Hsu. The effect of Schmidt number on turbulent scalar mixing in a jet-in-crossflow. *International Journal of Heat and Mass Transfer*, 42(20):3727–3738, 1999.
- [76] Elizaveta M. Ivanova, Berthold E. Noll, and Manfred Aigner. A Numerical Study on the Turbulent Schmidt Numbers in a Jet in Crossflow. *Journal of Engineering for Gas Turbines and Power*, 135(1):11505, 2012.
- [77] Yoshihide Tominaga and Ted Stathopoulos. Turbulent Schmidt numbers for CFD analysis with various types of flowfield. *Atmospheric Environment*, 41(37):8091–8099, 2007.
- [78] B. Wegner, Y. Huai, and A. Sadiki. Comparative study of turbulent mixing in jet in cross-flow configurations using LES. *International Journal of Heat and Fluid Flow*, 25(5):767–775, 2004.
- [79] Arthur H. Lefebvre. *Gas turbine combustion: alternative fuels and emissions*. CRC press, 2010.
- [80] D Goodwin, N Malaya, H Moffat, and R Cantera Speth. An object-oriented software toolkit for chemical kinetics, thermodynamics, and transport processes. *Caltech, Pasadena*, 2009.
- [81] H. Pitsch. FlameMaster: A C++ computer program for 0-D combustion and 1-D laminar flame calculations, 2011. version-3.3.10.
- [82] Ömer L. Gülder. Turbulent premixed flame propagation models for different combustion regimes. In *Symposium (International) on Combustion*, volume 23, pages 743–750. Elsevier, 1991.
- [83] H.G. Weller, G. Tabor, A.D. Gosman, and C. Fureby. Application of a flame-wrinkling les combustion model to a turbulent mixing layer. *Symposium (International) on Combustion*, 27(1):899–907, jan 1998.

-
- [84] B. Hakberg and A.D. Gosman. Analytical determination of turbulent flame speed from combustion models. *Symposium (International) on Combustion*, 20(1):225–232, jan 1985.
- [85] R. Borghi. On the structure and morphology of turbulent premixed flames. In *Recent advances in the Aerospace Sciences*, pages 117–138. Springer, 1985.
- [86] R.W. Bilger. Some Aspects of Scalar Dissipation. *Flow, Turbulence and Combustion formerly 'Applied Scientific Research'*, 72(2-4):93–114, 2004.
- [87] Norbert Peters. *Turbulent Combustion*. Cambridge Monographs on Mechanics. Cambridge University Press, 2000.
- [88] John P. Longwell, Edward E. Frost, and Malcolm A. Weiss. Flame stability in bluff body recirculation zones. *Industrial & Engineering Chemistry*, 45(8):1629–1633, 1953.
- [89] David G Lilley. Swirl Flows in Combustion: A Review. *AIAA Journal*, 15:1063–1078, aug 1977.
- [90] N. Syred and J. M. Beér. Combustion in swirling flows: A review. *Combustion and Flame*, 23(2):143–201, 1974.
- [91] N. A. Chigier and J. M. Beer. Velocity and static-pressure distributions in swirling air jets issuing from annular and divergent nozzles. *Journal of basic Engineering*, 86(4):788–796, 1964.
- [92] Sidney Leibovich. The structure of vortex breakdown. *Annual review of fluid mechanics*, 10(1):221–246, 1978.
- [93] Turgut Sarpkaya. Vortex breakdown in swirling conical flows. *AIAA J*, 9(9):1792–1799, 1971.
- [94] N. Syred, W. Fick, T. O’doherly, and A. J. Griffiths. The effect of the precessing vortex core on combustion in a swirl burner. *Combustion science and technology*, 125(1-6):139–157, 1997.
- [95] Nicholas Syred. A review of oscillation mechanisms and the role of the precessing vortex core (pvc) in swirl combustion systems. *Progress in Energy and Combustion Science*, 32(2):93–161, 2006.
- [96] Turgut Sarpkaya. On stationary and travelling vortex breakdowns. *Journal of Fluid Mechanics*, 45(3):545–559, 1971.
- [97] J. H. Faler and S. Leibovich. Disrupted states of vortex flow and vortex breakdown. *Physics of Fluids*, 20(9):1385, 1977.
- [98] O Lucca-Negro and T O’Doherty. Vortex breakdown: a review. *Progress in Energy and Combustion Science*, 27(4):431–481, jan 2001.
- [99] Satoru Ishizuka. Flame propagation along a vortex axis. *Progress in Energy and Combustion Science*, 28(6):477–542, 2002.

-
- [100] Martin Kroner, Jassin Fritz, and Thomas Sattelmayer. Flashback limits for combustion induced vortex breakdown in a swirl burner. In *ASME Turbo Expo 2002: Power for Land, Sea, and Air*, pages 413–422. American Society of Mechanical Engineers, 2002.
- [101] R. M. Kopecky and K. E. Torrance. Initiation and structure of axisymmetric eddies in a rotating stream. *Computers & Fluids*, 1(3):289–300, 1973.
- [102] Xungang Shi. Numerical simulation of vortex breakdown. Technical Report TM-77951, NASA, 1985.
- [103] Robert E. Spall and Thomas B. Gatski. A computational study of the topology of vortex breakdown. *Proceedings of the Royal Society of London A: Mathematical, Physical and Engineering Sciences*, 435(1894):321–337, 1991.
- [104] A. S. Nejad, S. P. Vanka, S. C. Favaloro, M. Samimy, and C. Langenfeld. Application of laser velocimetry for characterization of confined swirling flow. *Journal of Engineering for Gas Turbines and Power*, 111(1):36–45, 1989.
- [105] R. Weber, B.M. Visser, and F. Boysan. Assessment of turbulence modeling for engineering prediction of swirling vortices in the near burner zone. *International Journal of Heat and Fluid Flow*, 11(3):225 – 235, 1990.
- [106] P. Wang and X. S. Bai. Large eddy simulations of turbulent swirling flows in a dump combustor: a sensitivity study. *International Journal for Numerical Methods in Fluids*, 47(2):99–120, 2005.
- [107] W. Malalasekera, K. K. J. Ranga Dinesh, S. S. Ibrahim, and M. P. Kirkpatrick. Large Eddy Simulation of Isothermal Turbulent Swirling Jets. *Combustion Science and Technology*, 179(8):1481–1525, 2007.
- [108] G. Bulat, W. P. Jones, and S. Navarro-Martinez. Large eddy simulations of isothermal confined swirling flow in an industrial gas-turbine. *International Journal of Heat and Fluid Flow*, 51:50–64, 2015.
- [109] F. di Mare, W.P. Jones, and K.R. Menzies. Large eddy simulation of a model gas turbine combustor. *Combustion and Flame*, 137(3):278–294, may 2004.
- [110] Won-Wook Kim, Suresh Menon, and Hukam C. Mongia. Large-eddy simulation of a gas turbine combustor flow. *Combustion Science and Technology*, 143(1-6):25–62, 1999.
- [111] Stephen B. Pope. PDF methods for turbulent reactive flows. *Progress in Energy and Combustion Science*, 11(2):119–192, 1985.
- [112] Jun Xu and Stephen B. Pope. PDF calculations of turbulent nonpremixed flames with local extinction. *Combustion and Flame*, 123(3):281–307, 2000.
- [113] D. B. Spalding. Mixing and chemical reaction in steady confined turbulent flames. *Symposium (International) on Combustion*, 13(1):649–657, jan 1971.

- [114] R. Saïd and R. Borghi. A simulation with a “cellular automaton” for turbulent combustion modelling. *Symposium (International) on Combustion*, 22(1):569–577, 1989.
- [115] B.F. Magnussen and B.H. Hjertager. On mathematical modeling of turbulent combustion with special emphasis on soot formation and combustion. *Symposium (International) on Combustion*, 16(1):719–729, jan 1977.
- [116] Inge R. Gran and Bjørn F. Magnussen. A Numerical Study of a Bluff-Body Stabilized Diffusion Flame. Part 2. Influence of Combustion Modeling And Finite-Rate Chemistry. *Combustion Science and Technology*, 119(1-6):191–217, oct 1996.
- [117] K. N. C. Bray, Paul A. Libby, and J. B. Moss. Unified modeling approach for premixed turbulent combustion—part i: General formulation. *Combustion and flame*, 61(1):87–102, 1985.
- [118] K. N. C. Bray, Paul A. Libby, and J. B. Moss. Flamelet Crossing Frequencies and Mean Reaction Rates in Premixed Turbulent Combustion. *Combustion Science and Technology*, 41(3-4):143–172, 1984.
- [119] K. N. C. Bray and Paul A. Libby. Passage times and flamelet crossing frequencies in premixed turbulent combustion. *Combustion Science and Technology*, 47(5-6):253–274, 1986.
- [120] K. N. C. Bray and R. S. Cant. Some applications of kolmogorov’s turbulence research in the field of combustion. In *Proceedings of the Royal Society of London A: Mathematical, Physical and Engineering Sciences*, volume 434, pages 217–240. The Royal Society, 1991.
- [121] F. C. Gouldin, K. N. C. Bray, and J-Y. Chen. Chemical closure model for fractal flamelets. *Combustion and flame*, 77(3-4):241–259, 1989.
- [122] S. B. Pope. The evolution of surfaces in turbulence. *International journal of engineering science*, 26(5):445–469, 1988.
- [123] Sebastien M Candel and Thierry J Poinso. Flame Stretch and the Balance Equation for the Flame Area. *Combustion Science and Technology*, 70(1-3):1–15, 1990.
- [124] Ronnie Knikker, Denis Veynante, and Charles Meneveau. A dynamic flame surface density model for large eddy simulation of turbulent premixed combustion. *Physics of Fluids*, 16(11):L91–L94, 2004.
- [125] Gaofeng Wang, Matthieu Boileau, Denis Veynante, and Karine Truffin. Large eddy simulation of a growing turbulent premixed flame kernel using a dynamic flame surface density model. *Combustion and Flame*, 159(8):2742–2754, 2012.
- [126] E. R. Hawkes and R. S. Cant. A flame surface density approach to large-eddy simulation of premixed turbulent combustion. *Proceedings of the Combustion Institute*, 28(1):51–58, 2000.
- [127] T Ma, O T Stein, N Chakraborty, and A M Kempf. Combustion Theory and Modelling A posteriori testing of algebraic flame surface density models for LES A posteriori testing of algebraic flame surface density models for LES. *Combustion Theory and Modelling Volvo Rig Laser Anemometry AIAA Journal*, 17(28):431–482, 2013.

-
- [128] V. Zimont, W. Polifke, M. Bettelini, and W. Weisenstein. An Efficient Computational Model for Premixed Turbulent Combustion at High Reynolds Numbers Based on a Turbulent Flame Speed Closure. *Journal of Engineering for Gas Turbines and Power*, 120(3):526, jul 1998.
- [129] P. Flohr and H. Pitsch. A turbulent flame speed closure model for les of industrial burner flows. In *Proceedings of the summer program*, pages 169–179, 2000.
- [130] Alan R. Kerstein, William T. Ashurst, and Forman A. Williams. Field equation for interface propagation in an unsteady homogeneous flow field. *Phys. Rev. A*, 37:2728–2731, Apr 1988.
- [131] H. Pitsch. A consistent level set formulation for large-eddy simulation of premixed turbulent combustion. *Combustion and Flame*, 143(4):587–598, dec 2005.
- [132] O. Colin, F. Ducros, D. Veynante, and T. Poinsot. A thickened flame model for large eddy simulations of turbulent premixed combustion. *Physics of Fluids*, 12(7):1843–1863, 2000.
- [133] T. D. Butler and P. J. O’rourke. A numerical method for two dimensional unsteady reacting flows. In *Symposium (International) on Combustion*, volume 16, pages 1503–1515. Elsevier, 1977.
- [134] J. P. Legier, T. Poinsot, and D. D. Veynante. Dynamically thickened flame LES model for premixed and non-premixed turbulent combustion. In *Proceedings of the Summer Program 2000*. Center for Turbulence Research, 2000.
- [135] Fabrice Charlette, Charles Meneveau, and Denis Veynante. A power-law flame wrinkling model for LES of premixed turbulent combustion Part I: non-dynamic formulation and initial tests. *Combustion and Flame*, 131(1):159–180, 2002.
- [136] Fabrice Charlette, Charles Meneveau, and Denis Veynante. A power-law flame wrinkling model for LES of premixed turbulent combustion Part II: dynamic formulation. *Combustion and Flame*, 131(1):181–197, 2002.
- [137] Ulrich Maas and Stephen B. Pope. Simplifying chemical kinetics: intrinsic low-dimensional manifolds in composition space. *Combustion and flame*, 88(3):239–264, 1992.
- [138] Dimitris A. Goussis and Ulrich Maas. Model reduction for combustion chemistry. *Turbulent Combustion Modeling*, pages 193–220, 2011.
- [139] J. A. Oijen. *Flamelet-generated manifolds : development and application to premixed laminar flames*. PhD thesis, Eindhoven University of Technology, 2002.
- [140] W. J. S. Ramaekers, J. A. van Oijen, and L. P. H. de Goey. A Priori Testing of Flamelet Generated Manifolds for Turbulent Partially Premixed Methane/Air Flames. *Flow, Turbulence and Combustion*, 84(3):439–458, apr 2010.
- [141] A. W. Vreman, B. A. Albrecht, J. A. Van Oijen, L. P. H. De Goey, and R. J. M. Bastiaans. Premixed and nonpremixed generated manifolds in large-eddy simulation of Sandia flame D and F. *Combustion and Flame*, 153:394–416, 2008.

-
- [142] Charles D. Pierce and Parviz Moin. Progress-variable approach for large-eddy simulation of non-premixed turbulent combustion. *J. Fluid Mech*, 504:73–97, 2004.
- [143] G. Kuenne, A. Ketelheun, and J. Janicka. LES modeling of premixed combustion using a thickened flame approach coupled with FGM tabulated chemistry. *Combustion and Flame*, 158:1750–1767, 2011.
- [144] Fabian Proch and Andreas M Kempf. Numerical analysis of the Cambridge stratified flame series using artificial thickened flame LES with tabulated premixed flame chemistry. *Combustion and Flame*, 161(10):2627–2646, 2014.
- [145] Hannes Kröger, Nikolai Kornev, Detlef Wendig, and Egon Hassel. Premixed flame propagation in a free straight vortex. *Forschung im Ingenieurwesen*, 72(2):85–92, Jun 2008.
- [146] A. Yu. Klimenko. Multicomponent diffusion of various admixtures in turbulent flow. *Fluid Dynamics*, 25(3):327–334, may 1990.
- [147] R. W. Bilger. Conditional moment closure for turbulent reacting flow. *Physics of Fluids A: Fluid Dynamics*, 5(436), 1993.
- [148] T. Poinso and D. Veynante. *Theoretical and Numerical Combustion*. R.T. Edwards, Inc., 2005, 2005.
- [149] P. T. Roberts and J. B. Moss. A wrinkled flame interpretation of the open turbulent diffusion flame. In *Symposium (International) on Combustion*, volume 18, pages 941–950. Elsevier, 1981.
- [150] Michael C. Drake and Richard J. Blint. Structure of laminar opposed-flow diffusion flames with co/h₂/n₂ fuel. *Combustion science and technology*, 61(4-6):187–224, 1988.
- [151] N. Peters. Laminar diffusion flamelet models in non-premixed turbulent combustion. *Progress in Energy and Combustion Science*, 10(3):319–339, 1984.
- [152] S. K. Liew, K. N. C. Bray, and J. B. Moss. A stretched laminar flamelet model of turbulent nonpremixed combustion. *Combustion and Flame*, 56(2):199–213, 1984.
- [153] D. Lentini. Assessment of The Stretched Laminar Flamelet Approach For Non-premixed Turbulent Combustion. *Combustion Science and Technology*, 100(1-6):95–122, oct 1994.
- [154] J. Carregal Ferreira. Steady and transient flamelet modelling of turbulent non-premixed combustion. *Progress in Computational Fluid Dynamics, An International Journal*, 1:29, 2001.
- [155] A. Vranos, B. A. Knight, W. M. Proscia, L. Chiappetta, and M. D. Smooke. Nitric oxide formation and differential diffusion in a turbulent methane-hydrogen diffusion flame. In *Symposium (International) on Combustion*, volume 24, pages 377–384. Elsevier, 1992.

- [156] J. P. H. Sanders and A. P. G. G. Lamers. Modeling and calculation of turbulent lifted diffusion flames. *Combustion and Flame*, 96(1-2):22–33, 1994.
- [157] Martin Schlatter, Jorge C. Ferreira, Matthias Flury, and Jürg Gass. Analysis of turbulence-chemistry interaction with respect to no formation in turbulent, non-premixed hydrogen-air flames. In *Symposium (International) on Combustion*, volume 26, pages 2215–2222. Elsevier, 1996.
- [158] J-Y Chen and Wei-Chen Chang. Flamelet and pdf modeling of co and nox emissions from a turbulent, methane hydrogen jet nonpremixed flame. In *Symposium (International) on combustion*, volume 26, pages 2207–2214. Elsevier, 1996.
- [159] Peters N. Bray K. N. C. Laminar flamelets in turbulent flames. In Williams F.A Libby P.A, editor, *Turbulent reacting flows*, chapter 2, pages 63–94. Academic Press, London, 1994.
- [160] B. Marracino and D. Lentini. Radiation modelling in non-luminous nonpremixed turbulent flames. *Combustion science and technology*, 128(1-6):23–48, 1997.
- [161] Mamdud Hossain. *CFD modelling of turbulent non-premixed combustion*. PhD thesis, Loughborough University, Loughborough, United Kingdom, 1999.
- [162] Ravikanti V. V. S. Murthy. *Advanced flamelet modelling of turbulent nonpremixed and partialy premixed combustion*. PhD thesis, Loughborough University, Loughborough, United Kingdom, 2008.
- [163] D.C. Haworth, M.C. Drake, S.B. Pope, and R.J. Blint. The importance of time-dependent flame structures in stretched laminar flamelet models for turbulent jet diffusion flames. *Symposium (International) on Combustion*, 22(1):589 – 597, 1989.
- [164] Heinz Pitsch, M. Chen, and Norbert Peters. Unsteady flamelet modeling of turbulent hydrogen-air diffusion flames. In *Symposium (international) on combustion*, volume 27, pages 1057–1064. Elsevier, 1998.
- [165] Andrew W. Cook, James J. Riley, and George Kosály. A laminar flamelet approach to subgrid-scale chemistry in turbulent flows. *Combustion and Flame*, 109(3):332–341, 1997.
- [166] Javier Jiménez, Amable Liñán, Michael M. Rogers, and Francisco J. Higuera. A priori testing of subgrid models for chemically reacting non-premixed turbulent shear flows. *Journal of Fluid Mechanics*, 349:149–171, 1997.
- [167] S. M. de Bruyn Kops, J. J. Riley, G. Kosály, and A. W. Cook. Investigation of modeling for non-premixed turbulent combustion. *Flow, Turbulence and combustion*, 60(1):105–122, 1998.
- [168] Charles D. Pierce and Parviz Moin. A dynamic model for subgrid-scale variance and dissipation rate of a conserved scalar. *Physics of Fluids*, 10(3041), 1998.
- [169] A. Kempf, F. Flemming, and J. Janicka. Investigation of lengthscales, scalar dissipation, and flame orientation in a piloted diffusion flame by LES. *Proceedings of the Combustion Institute*, 30:557–565, 2005.

- [170] Heinz Pitsch. Unsteady flamelet modeling of differential diffusion in turbulent jet diffusion flames. *Combustion and Flame*, 123(3):358–374, 2000.
- [171] K. K. J Ranga-Dinesh. *Large eddy simulation of turbulent swirling flames*. PhD thesis, Loughborough University, 2007.
- [172] A Kempf, W Malalasekera, K K J Ranga-Dinesh, and O Stein. Large Eddy Simulations of Swirling Non-premixed Flames With Flamelet Models: A Comparison of Numerical Methods. *Flow, Turbulence and Combustion*, 81(4):523–561, dec 2008.
- [173] Volker Sick, Frank Hildenbrand, and Peter Lindstedt. Quantitative laser-based measurements and detailed chemical kinetic modeling of nitric oxide concentrations in methane-air counterflow diffusion flames. In *Symposium (International) on Combustion*, volume 27, pages 1401–1409. Elsevier, 1998.
- [174] H.K. Versteeg and W. Malalasekera. *An Introduction to Computational Fluid Dynamics: The Finite Volume Method*. Pearson Education, Limited, 2011.
- [175] Joel H. Ferziger and Milovan Peric. *Computational methods for fluid dynamics*. Springer Science & Business Media, 2012.
- [176] P. Bradshaw. Possible origin of Prandtl’s mixing-length theory. *Nature*, 249(5453):135–136, may 1974.
- [177] P. Spalart and S. Allmaras. A one-equation turbulence model for aerodynamic flows. In *30th Aerospace Sciences Meeting and Exhibit*, Aerospace Sciences Meetings. American Institute of Aeronautics and Astronautics, jan 1992.
- [178] Barrett Baldwin and Timothy Barth. A one-equation turbulence transport model for high reynolds number wall-bounded flows. In *29th Aerospace Sciences Meeting*, page 610, 1991.
- [179] M. M. Gibson and B. E. Launder. Ground effects on pressure fluctuations in the atmospheric boundary layer. *Journal of Fluid Mechanics*, 86(03):491, jun 1978.
- [180] B.E. Launder and D.B. Spalding. The numerical computation of turbulent flows. *Computer Methods in Applied Mechanics and Engineering*, 3(2):269–289, mar 1974.
- [181] S. B. Pope. An explanation of the turbulent round-jet/plane-jet anomaly. *AIAA Journal*, 16(3):279–281, mar 1978.
- [182] Tsan-Hsing Shih, William W. Liou, Aamir Shabbir, Zhigang Yang, and Jiang Zhu. A new k-epsilon eddy viscosity model for high reynolds number turbulent flows. *Computers & Fluids*, 24(3):227–238, mar 1995.
- [183] David C. Wilcox. Reassessment of the scale-determining equation for advanced turbulence models. *AIAA Journal*, 26(11):1299–1310, nov 1988.
- [184] David C. Wilcox et al. *Turbulence modeling for CFD*, volume 2. DCW industries La Canada, CA, 1998.
- [185] F. R. Menter. Influence of freestream values on k-omega turbulence model predictions. *AIAA Journal*, 30(6):1657–1659, jun 1992.

-
- [186] F. R. Menter. Two-equation eddy-viscosity turbulence models for engineering applications. *AIAA Journal*, 32(8):1598–1605, aug 1994.
- [187] Florian R. Menter. Review of the shear-stress transport turbulence model experience from an industrial perspective. *International Journal of Computational Fluid Dynamics*, 23(4):305–316, apr 2009.
- [188] Florian Menter. Improved two-equation k-omega turbulence models for aerodynamic flows. Technical Report TM-103975, NASA, 11 1992.
- [189] Massimo Germano, Ugo Piomelli, Parviz Moin, and William H. Cabot. A dynamic subgrid-scale eddy viscosity model. *Physics of Fluids A: Fluid Dynamics*, 3, 1991.
- [190] J. Smagorinsky. General Circulation Experiments With The Primitive Equations. *Monthly Weather Review*, 91(3):99–164, mar 1963.
- [191] Douglas K Lilly. The representation of small-scale turbulence in numerical simulation experiments. In *Proc. IBM Sci. Compt. Symp. Environ. Sci., White Plains, IBM, 1967*, 1967.
- [192] Edward R. Van Driest. On turbulent flow near a wall. *J. Aeronaut. Sci*, 23(11):1007–1011, 1956.
- [193] J. Bardina, J. H. Ferziger, and W. C. Reynolds. Improved subgrid-scale models for large-eddy simulation. *American Institute of Aeronautics and Astronautics*, 1980.
- [194] Yan Zang, Robert L Street, and Jeffrey R Koseff. A dynamic mixed subgrid scale model and its application to turbulent recirculating flows. *Physics of Fluids A: Fluid Dynamics (1989-1993)*, 5(12):3186–3196, 1993.
- [195] Bert Vreman, Bernard Geurts, and Hans Kuerten. On the formulation of the dynamic mixed subgrid-scale model. *Physics of Fluids*, 6(12):4057, dec 1994.
- [196] Johann Turnow. *Flow Structures and Heat Transfer On Dimpled Surfaces*. PhD thesis, University of Rostock, 2012.
- [197] M. Wolfshtein C. Fureby, A.D. Gosman, G. Tabor, H.G. Weller, N. Sandham. Large Eddy Simulation Of Turbulent Channel Flows. *Turbulent shear flows*, 11:28–13, 1997.
- [198] Akira Yoshizawa and Kiyosi Horiuti. A Statistically-Derived Subgrid-Scale Kinetic Energy Model for the Large-Eddy Simulation of Turbulent Flows. *Journal of the Physical Society of Japan*, 54(8):2834–2839, aug 1985.
- [199] S. Ghosal and P. Moin. The Basic Equations for the Large Eddy Simulation of Turbulent Flows in Complex Geometry. *Journal of Computational Physics*, 118(1):24–37, apr 1995.
- [200] C Fureby, G Tabor, H G Weller, A D Gosman, and) G Tabor. A comparative study of subgrid scale models in homogeneous isotropic turbulence. *Physics of Fluids Physics of Fluids A: Fluid Dynamics*, 9(4):1416–1492, 1997.

-
- [201] H. Reichardt. Vollständige darstellung der turbulenten geschwindigkeitsverteilung in glatten leitungen. *ZAMM-Journal of Applied Mathematics and Mechanics/Zeitschrift für Angewandte Mathematik und Mechanik*, 31(7):208–219, 1951.
- [202] I. Hadzic. *Second-Moment Closure Modelling of Transitional and Unsteady Turbulent Flows*. PhD thesis, Technical University of Delft, 2 1999.
- [203] CD-adapco. Star-ccm+ user guide, 2013.
- [204] John Kim, Parviz Moin, and Robert Moser. Turbulence statistics in fully developed channel flow at low reynolds number. *Journal of fluid mechanics*, 177:133–166, 1987.
- [205] Helmut Eckelmann. The structure of the viscous sublayer and the adjacent wall region in a turbulent channel flow. *Journal of Fluid Mechanics*, 65(03):439, sep 1974.
- [206] Eugene de Villers. *The Potential of Large Eddy Simulation for the Modelling of Wall Bounded Flows*. PhD thesis, Imperial College of Science, Technology and Medicine, London, UK, 7 2006.
- [207] D. B. Spalding. A Single Formula for the “Law of the Wall”. *Journal of Applied Mechanics*, 28(3):455, sep 1961.
- [208] G.R. Tabor and M.H. Baba-Ahmadi. Inlet conditions for large eddy simulation: A review. *Computers & Fluids*, 39(4):553–567, apr 2010.
- [209] M. Lesieur, P. Begou, E. Briand, A. Danet, F. Delcayre, and J. L. Aider. Coherent-vortex dynamics in large-eddy simulations of turbulence. *Journal of Turbulence*, 4:N16, 2003.
- [210] A. Smirnov, S. Shi, and I. Celik. Random Flow Generation Technique for Large Eddy Simulations and Particle-Dynamics Modeling. *Journal of Fluids Engineering*, 123(2):359, 2001.
- [211] Jean-Luc Aider, Alexandra Danet, and Marcel Lesieur. Large-eddy simulation applied to study the influence of upstream conditions on the time-dependant and averaged characteristics of a backward-facing step flow. *Journal of Turbulence*, 8:N51, jan 2007.
- [212] M. Klein, A. Sadiki, and J. Janicka. A digital filter based generation of inflow data for spatially developing direct numerical or large eddy simulations. *Journal of Computational Physics*, 186(2):652–665, 2003.
- [213] N. Kornev and E. Hassel. Method of random spots for generation of synthetic inhomogeneous turbulent fields with prescribed autocorrelation functions. *Communications in Numerical Methods in Engineering*, 23(1):35–43, may 2006.
- [214] T. J. Poinso and S. K. Lelef. Boundary conditions for direct simulations of compressible viscous flows. *Journal of Computational Physics*, 101(1):104–129, jul 1992.
- [215] Sandip Ghosal. Analysis of discretization errors in LES. *Center for Turbulence Research Annual Research Briefs*, 1995.

-
- [216] Sandip Ghosal. An Analysis of Numerical Errors in Large-Eddy Simulations of Turbulence. *Journal of Computational Physics*, 125(1):187–206, apr 1996.
- [217] U Piomelli. Large-eddy simulation: achievements and challenges. *Progress in Aerospace Sciences*, 35:335–362, 1999.
- [218] Charles Meneveau, Thomas S. Lund, and William H. Cabot. A Lagrangian dynamic subgrid-scale model of turbulence. *Journal of Fluid Mechanics*, 319(-1):353, jul 1996.
- [219] Stephen B. Pope. Ten questions concerning the large-eddy simulation of turbulent flows. *New Journal of Physics*, 6(1):35–35, mar 2004.
- [220] A. K. M. Fazle Hussain. Coherent structures and turbulence. *J. Fluid Mech*, 173:303–356, 2017.
- [221] A. Roshko. Structure of Turbulent Shear Flows: A New Look. *AIAA Journal*, 14(10):1349–1357, oct 1976.
- [222] H. E. Fiedler. Coherent structures in turbulent flows. *Progress in Aerospace Sciences*, 25(3):231–269, jan 1988.
- [223] Hans J. Lugt. The dilemma of defining a vortex. In *Recent developments in theoretical and experimental fluid mechanics*, pages 309–321. Springer, 1979.
- [224] Jinhee Jeong and Fazle Hussain. On the identification of a vortex. *Journal of Fluid Mechanics*, 285(-1):69, apr 2006.
- [225] J. C. R. Hunt, A. A. Wray, and P. Moin. Eddies, streams, and convergence zones in turbulent flows. In *Proceedings of the Summer Program 1988*. Center for Turbulence Research, 1988.
- [226] S.H. El Tahry. k-epsilon equation for compressible reciprocating engine flows. *Journal of Energy*, 7(4):345–353, jul 1983.
- [227] OpenCFD Limited. OpenFOAM User Guide.
- [228] Robert J. Kee, Joseph F. Grcar, Mitchell D. Smooke, J. A. Miller, and E. Meeks. Premix: a fortran program for modeling steady laminar one-dimensional premixed flames. Technical Report SAND85-8249, Sandia National Laboratories, 1985.
- [229] G. D’Errico, D. Ettore, and T. Lucchini. Comparison of combustion and pollutant emission models for di diesel engines. In *8th International Conference on Engines for Automobiles*. Consiglio Nazionale delle Ricerche, sep 2007.
- [230] H. Pitsch and N. Peters. A consistent flamelet formulation for non-premixed combustion considering differential diffusion effects. *Combustion and Flame*, 1998.
- [231] R. W. Bilger. The structure of turbulent nonpremixed flames. *Symposium (International) on Combustion*, 22(1):475–488, 1989.
- [232] R. W. Bilger. Turbulent flows with nonpremixed reactants. *Turbulent reacting flows*, pages 65–113, 1980.

-
- [233] Michael Pfitzner Hagen Müller and Federica Ferraro. Implementation of a Steady Laminar Flamelet Model for non-premixed combustion in LES and RANS simulations. In *8th International OpenFOAM Workshop, Jeju, Korea*, 2013.
- [234] Hannes Kröger. *Large-Eddy Simulation of Combustion Induced Vortex Breakdown in an Unconfined Turbulent Vortex using a Presumed-PDF Combustion Model*. PhD thesis, Universität at Rostock, 2010.
- [235] C. Meneveau and T. Poinso. Stretching and Quenching of Flamelets in Premixed Turbulent Combustion. *COMBUSTION AND FLAME*, 86:311–332, 1991.
- [236] S. H. Smith and M. G. Mungal. Mixing, structure and scaling of the jet in crossflow. *Journal of Fluid Mechanics*, 357:83–122, 1998.
- [237] P. A. Durbin. On the k-3 stagnation point anomaly. *International Journal of Heat and Fluid Flow*, 17(1):89–90, feb 1996.
- [238] B. E. Launder and M. Kato. Modeling flow-induced oscillations in turbulent flow around a square cylinder. In *ASME Fluid Engineering conference, Washington*, page 189, June 1993.
- [239] W. C. Strahle. Stagnation point flows with freestream turbulence - The matching condition. *AIAA Journal*, 23(11):1822–1824, nov 1985.
- [240] A. O. Demuren. Modeling jets in cross flow. Technical Report CR-194965, NASA, 1994.
- [241] Paul A. Durbin and B. A. Pettersson Reif. *Statistical theory and modeling for turbulent flows*. Wiley, 2011.
- [242] A. Fric, T. F. Roshko. Vortical structure in the wake of a transverse jet. *Journal of Fluid Mechanics*, 279:1–47, nov 1994.
- [243] Matteo Gazzani, Paolo Chiesa, Emanuele Martelli, Stefano Sigali, and Iarno Brunetti. Using Hydrogen as Gas Turbine Fuel: Premixed Versus Diffusive Flame Combustors. *Journal of Engineering for Gas Turbines and Power*, 136(5):051504, jan 2014.
- [244] A. R. Masri, P. A. M. Kalt, and R. S. Barlow. The compositional structure of swirl-stabilised turbulent nonpremixed flames. *Combustion and Flame*, 137(1–2):1–37, 2004.
- [245] Yasir M. Al-Abdeli and Assaad R. Masri. Recirculation and flowfield regimes of unconfined non-reacting swirling flows. *Experimental Thermal and Fluid Science*, 27(5):655–665, may 2003.
- [246] K K J Ranga-Dinesh. *Large eddy simulation of turbulent swirling flames*. Doctoral thesis, Loughborough University, 2007.
- [247] Swirl flows and flames database, 2018. <http://web.aeromech.usyd.edu.au/thermofluids/swirl.php>.

- [248] R. Barlow, J. Frank, A. Karpetis, and J. Chen. Piloted methane/air jet flames: Transport effects and aspects of scalar structure. *Combustion and Flame*, 143(4):433–449, dec 2005.
- [249] Sandia/TUD Piloted CH₄/Air Jet Flames , 2018. <https://www.sandia.gov/TNF/DataArch/FlameD.html>.
- [250] G. P. Smith, D. M. Golden, M. Frenklach, B. Eiteener, M. Goldenberg, C. T. Bowman, R. K. Hanson, W. C. Gardiner, V. V. Lissianski, and Z. W. Qin. GRI-Mech 3.0, 2000.
- [251] Wm. E Wilson. A Critical Review of the Gas Phase Reaction Kinetics of the Hydroxyl Radical. *Journal of Physical and Chemical Reference Data*, 1(2):535–573, apr 1972.
- [252] Andrew W. Cook and James J. Riley. Subgrid-scale modeling for turbulent reacting flows. *Combustion and Flame*, 112(4):593–606, 1998.
- [253] Jean-Philippe Legier, Thierry Poinsot, and Denis Veynante. Dynamically thickened flame les model for premixed and non-premixed turbulent combustion. In *Proc. of the summer program*, pages 157–168, 2000.
- [254] I.K. Nwagwe, H.G. Weller, G.R. Tabor, A.D. Gosman, M. Lawes, C.G.W. Sheppard, and R. Wooley. Measurements and large eddy simulations of turbulent premixed flame kernel growth. *Proceedings of the Combustion Institute*, 28(1):59–65, jan 2000.
- [255] R. W. Pitz and J. W. Daily. Combustion in a turbulent mixing layer formed at a rearward-facing step. *AIAA Journal*, 21(November 1983):1565–1570, 1983.
- [256] A. R. Ganji and R. F. Sawyer. Experimental Study of the Flowfield of a Two-Dimensional Premixed Turbulent Flame. *AIAA Journal*, 18(7):817–824, jul 1980.
- [257] J. Janicka and A. Sadiki. Large eddy simulation of turbulent combustion systems. *Proceedings of the Combustion Institute*, 30(1):537–547, jan 2005.
- [258] Robert W Pitz. An experimental study of combustion: The turbulent structure of a reacting shear layer formed at a rearward-facing step. ph. d. thesis. final report. Technical Report CR-165427, NASA, 1981.
- [259] J.A. Van Oijen and L.P.H. De Goey. Modelling of Premixed Laminar Flames using Flamelet-Generated Manifolds. *Combustion Science and Technology*, 161(1):113–137, dec 2000.
- [260] Alessio Fancello. *Dynamic and turbulent premixed combustion using Flamelet-Generated Manifold in OpenFOAM*. Doctoral thesis, Eindhoven University of Technology, 2014.
- [261] Mitchell D. Smoke and Vincent Giovangigli. Formulation of the premixed and non-premixed test problems. In *Reduced Kinetic Mechanisms and Asymptotic Approximations for Methane-Air Flames*, pages 1–28. Springer, 1991.
- [262] Mark S. Sweeney, Simone Hochgreb, Matthew J. Dunn, and Robert S. Barlow. The structure of turbulent stratified and premixed methane/air flames I: Non-swirling flows. *Combustion and Flame*, 159:2896–2911, 2012.

- [263] T. Brauner, W. P. Jones, and A. J. Marquis. LES of the Cambridge Stratified Swirl Burner using a Sub-grid pdf Approach. *Flow, Turbulence and Combustion*, 96(4):965–985, 2016.
- [264] Robert S. Barlow, Matthew J. Dunn, Mark S. Sweeney, and Simone Hochgreb. Effects of preferential transport in turbulent bluff-body-stabilized lean premixed CH₄/air flames. *Combustion and Flame*, 159(8):2563–2575, aug 2012.

Appendix A

A.1 Potential Flow JICF

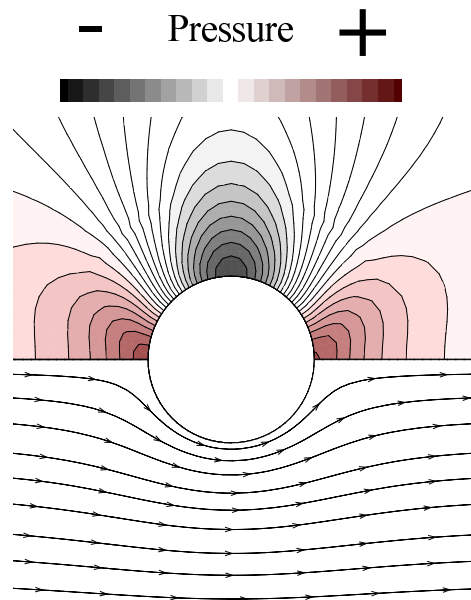


Figure: A.1 Pressure field distribution and stream lines in flow around cylinder calculated from potential flow

A.2 Turbulent Schmidt number sensitivity

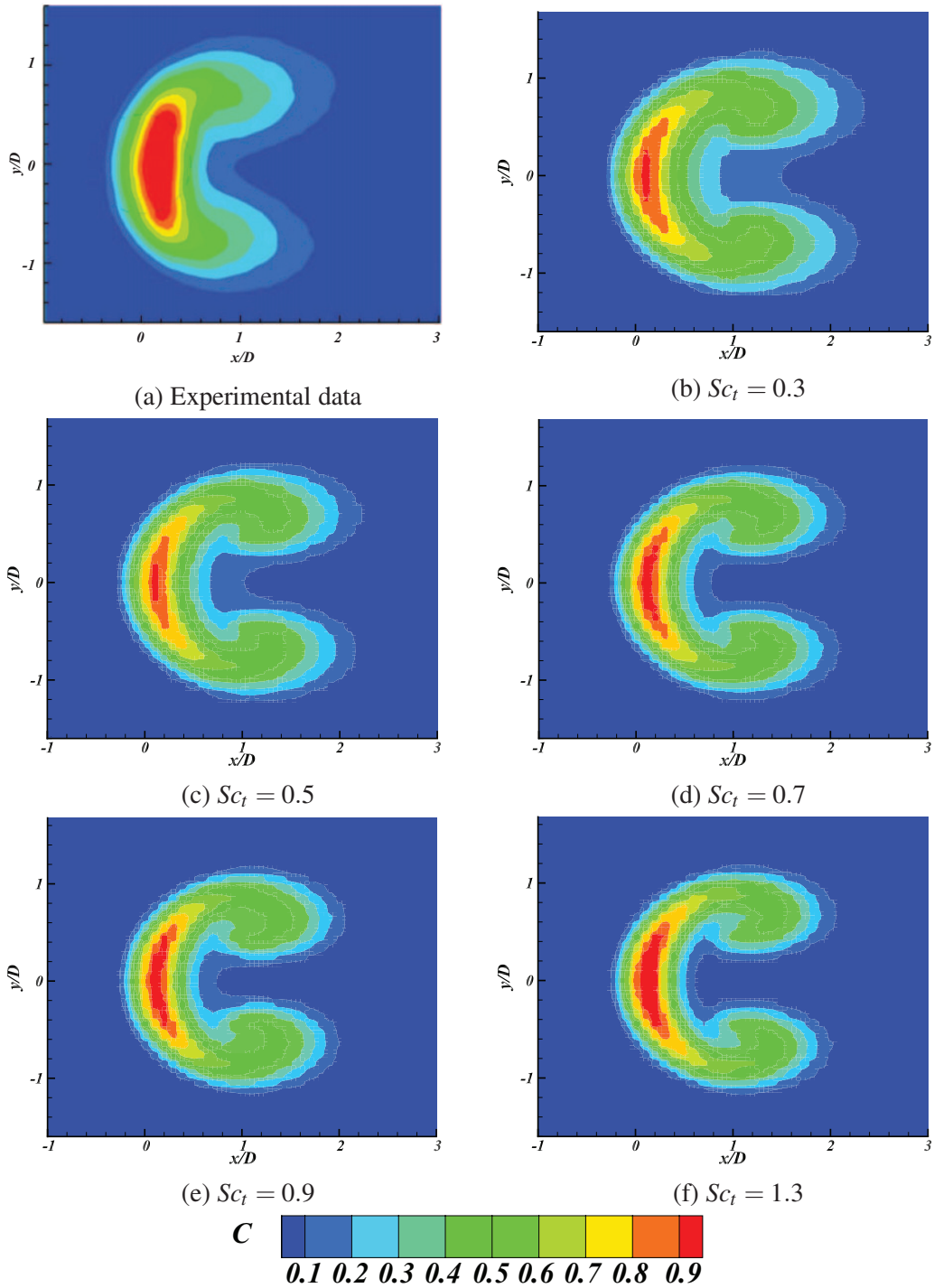


Figure: A.2 Sensitivity of turbulent Schmidt number (Sc_t) on passive scalar C at $z = 1.5D$ plane - STAR-CCM+, experimental data from [37] taken under permission.

A.3 LES and RANS results of JICF

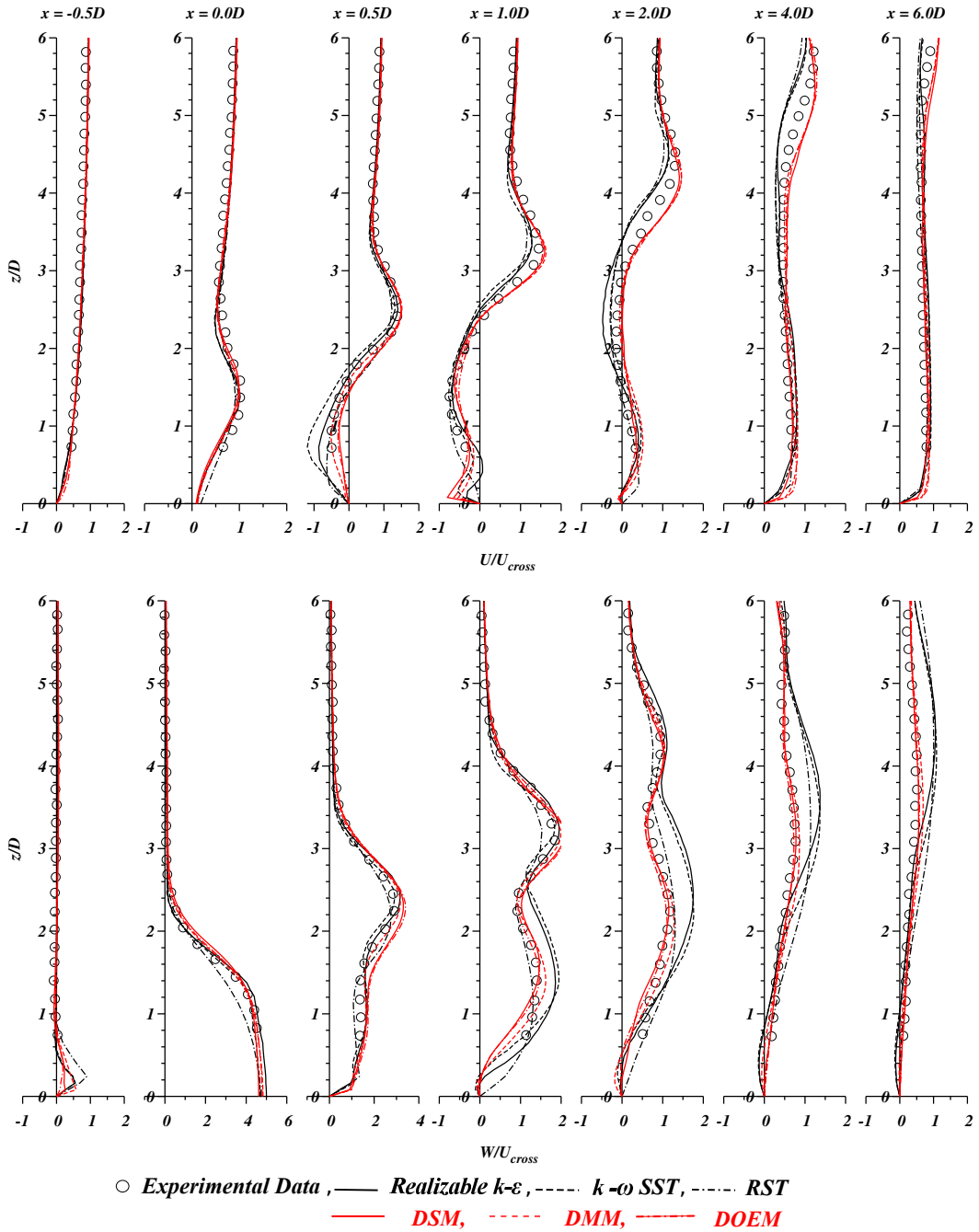


Figure: A.3 LES and RANS results comparison

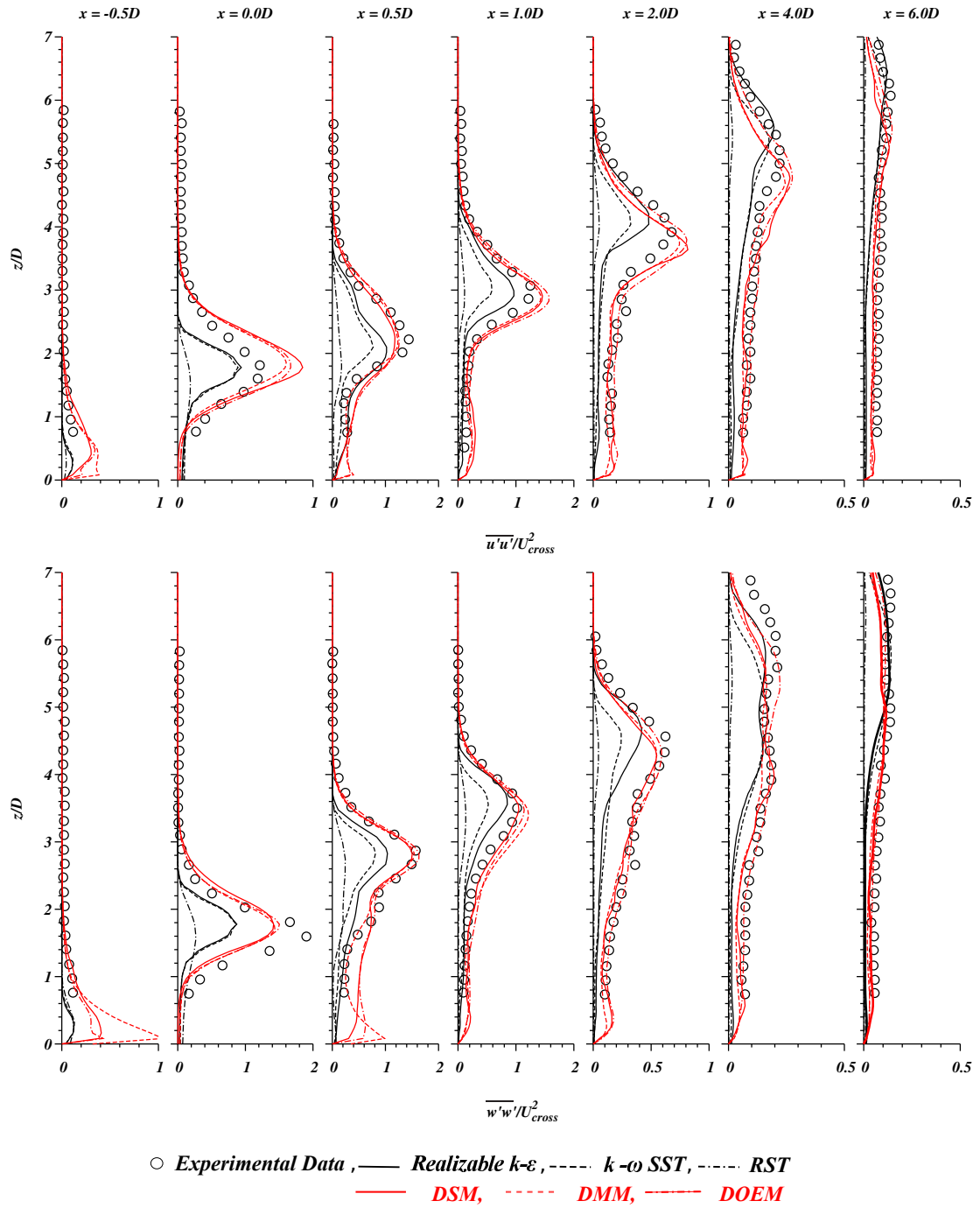


Figure: A.4 LES and RANS results comparison